The role of metamorphic reactions for strain localization in the middle and lower crust : Insights from field observations and deformation experiments

Nicolas Mansard

Centre Val de Loire UNIVERSITÉ Spirit of the Loire Valley

UNIVERSITÉ D'ORLÉANS

UNIVERSITE D'ORLEANS

ÉCOLE DOCTORALE ÉNERGIE, MATÉRIAUX, SCIENCES DE LA TERRE ET DE L'UNIVERS

Institut des Sciences de la Terre d'Orléans

THÈSE présentée par :

Nicolas MANSARD

Soutenue le : **3 décembre 2019**

Pour obtenir le grade de : **Docteur de l'université d'Orléans**

Discipline/Spécialité : **Sciences de la Terre**

The role of metamorphic reactions for strain localization in the middle and lower crust

Insights from field observations and deformation experiments

THÈSE dirigée par :

Holger STÜNITZ	Professeur, UiT, Tromsø et ISTO, Orléans
Hugues RAIMBOURG	Maître de conférences, ISTO, Orléans
Jacques PRECIGOUT	Ingénieur de recherche, ISTO, Orléans

RAPPORTEURS :

Misha BYSTRICKY	Maître de conférences, IRAP, Toulouse
Petr JERABEK	Professeur associé, IPSG, Prague

JURY :

Caroline MARTEL	Directrice de recherche, ISTO, Orléans, Présidente du jury
Misha BYSTRICKY	Maître de conférences, IRAP, Toulouse
Petr JERABEK	Professeur associé, IPSG, Prague
Philippe AGARD	Professeur, ISTeP, Paris
Claudio ROSENBERG	Professeur, ISTeP, Paris

« La véritable science enseigne, par-dessus tout, à douter et à être ignorant. »

Miguel de Unamuno (1864-1936)

« Les machines un jour pourront résoudre tous les problèmes, mais jamais aucune d'entre elles ne pourra en poser un ! »

Albert Einstein (1879-1955)

Remerciements

Le délicat chapitre de ma vie « d'apprenti chercheur » s'achève par l'écriture de ces remerciements. Ces remerciements, j'y pense depuis longtemps, depuis les premières heures du projet. Pour autant, quand vient l'heure de trouver les mots justes pour chacun, les mots permettant d'exprimer ma sincère gratitude, l'écriture s'avère être un exercice difficile.

Je tiens évidemment à remercier, en premier lieu, Holger Stünitz, Hugues Raimbourg et Jacques Précigout pour avoir encadré ce projet de recherche. Merci à eux pour la confiance qu'ils m'ont accordée, leurs rigueurs intellectuelles, leurs dynamismes, leurs franchises et leurs gentillesses. Je suis reconnaissant pour le temps qu'ils ont pris pour m'aider, me guider et même parfois me pousser à mettre un « bon coup de collier ».

Je tiens également à remercier l'ensemble des membres du jury (Caroline Martel, Misha Bystricky, Petr Jerabek, Philippe Agard et Claudio Rosenberg) d'avoir accepté d'évaluer ce travail de thèse. Merci pour votre bienveillance, vos commentaires et retours, ainsi que vos remarques constructives et l'enrichissante discussion s'étant poursuivie après la soutenance.

Bien qu'extérieur à ce projet de thèse, je souhaite également exprimer ma sincère gratitude à Laurent Jolivet qui a su transmettre sa passion et son amour des cailloux dès mon arrivée en Master 1 à Orléans. N'ayant pas intégré ce Master dans l'optique d'y poursuivre un parcours recherche, c'est bien au travers de son enseignement, sa pédagogie et sa bienveillance que cette envie est née. Tout simplement merci.

Que serait un chapitre de remerciement sans parler de ces collègues et amis qui partagent au quotidien les joies, les satisfactions, les doutes et les peines de cette merveilleuse aventure qu'est la thèse. Par crainte d'oublier quelqu'un, ou peut-être par fainéantise de tous les citer, je tiens à remercier tout ce beau monde qui se reconnaitra dans ce paragraphe :D. Un grand MERCI pour votre compagnie, votre amitié, votre bonne humeur, votre soutien au quotidien et tous ces bons moments passés ensemble.

J'exprime également toute ma gratitude à ces « petites mains », si je puis dire, qui ont contribué au bon déroulement de la thèse. Je pense évidemment aux services

informatique, analytique, administratif et par-dessus tout aux gars de l'atelier mécanique.

Un grand Merci à ma famille, mes parents, mes 10 000 frères et sœurs (en vrai j'en ai 8, mais c'est tout de même beaucoup), et évidemment mes grands-parents qui m'ont apporté un soutien indéfectible. Merci à eux de m'avoir transmis l'amour de l'apprentissage et ont su éveiller en moi la curiosité scientifique dès le plus jeune âge. Un grand Merci également à ma belle-famille pour le soutien qu'ils m'ont apporté, à l'intérêt qu'ils ont pu avoir pour ma thèse et les curieuses discussions qui en ont découlé :

« Tu es encore à l'école à 26 ans Nico ? »

« Une thèse sur la déformation des roches ? … Hmmm, ça sert à quoi ? »

« Tu vas en Norvège dans un laboratoire de déformation ? ..[silence].. Parce que tu es trop formé ? ».

Je souhaite également remercier mes petits monstres à quatre pattes, Melba, Nina et Oups. Mention spéciale pour Melba qui a tenté de m'aider dans l'écriture de cette thèse, malheureusement je n'ai pas souhaité intégrer sa théorie : « gfzehmRUAdùàprtv=zà(d », car je ne l'ai toujours pas comprise.

Pour finir, merci à toi, Chloé, jamais je ne pourrais te remercier assez ! Tu as toujours été à mes côtés, dans les bons moments comme dans les moins bons, tu as su m'apporter le soutien dont j'avais besoin, tu m'encourages quand je baisse les bras et me remonte le moral dans les moments de creux. Au moment où j'écris ces lignes, bébé n'est encore que crevette dans ton ventre, mais bientôt il pointera le bout de son nez. Il m'a fallu trois ans pour accoucher cette thèse, j'espère que ça ira plus vite pour toi ! Moi qui pensais pouvoir me reposer après cette thèse et perdre cette habitude de me lever la nuit, c'est raté !

Abstract

Shear zones arise from strain localization into rocks of the crust and uppermost mantle during deformation of the lithosphere. Accommodating a large amount of strain, these shear zones are thus critical to be addressed to understanding the dynamics of the lithosphere. In the present study, we aim at extending the current knowledge about the rheology and development of shear zones using a multi-scale approach, which includes field observations and deformation experiments.

First, we investigated the South Armorican Shear Zone (SASZ), which corresponds to a crustal-scale shear zone that deforms granitoid rocks at mid-crustal conditions. With increasing strain from weakly deformed (protolith) to highly deformed (ultramylonite) rocks, this shear zone is characterized by (1) a significant grain size reduction, (2) the development of monophase layers of mica in moderately (protomylonite) and further deformed (mylonite) rocks, and (3) their subsequent replacement by fine-grained mixed-phase zones in ultramylonite. Microstructural features also indicate that grain size has triggered a transition from grain size insensitive (GSI) to grain size sensitive (GSS) creep, including grain boundary sliding (GBS). Altogether, our findings identify a succession of weakening processes responsible for large-scale strain localization and the development of the SASZ. This starts with the nucleation of mica as a first weakening material, and then evolves with the formation of weak zones of fine-grained and mixed phases.

Second, we performed shear experiments on fine-grained two-phase assemblages representative of the lower crust (plagioclase—pyroxene) to study how shear zones develop and how the interplay between deformation and mineral reactions influence rock rheology. We first investigated and compared the evolution of microstructures, deformation mechanisms and rheology in two-phase and pure phase experiments. Our experiments reveal that the peak stress of plagioclase + pyroxene assemblages lies in between the ones of the end-member phases. However, the strength drops significantly after the peak stress and reaches flow stresses that stabilize far below those of the weaker end-member (plagioclase). This weakening correlates with the coeval development of interconnected shear bands filled by intimately mixed, fine-grained reaction products. Our study demonstrates that deformation significantly enhances the kinetics of mineral reactions, which in turn strongly weaken the deforming sample through strain localization and phase nucleation, both probably driven by GSS dissolution-precipitation creep

(DPC). Such an interplay between deformation and mineral reactions may have strong implications for the development and durability of crustal shear zones.

Third, shear experiments on mafic assemblages were performed to address the influence of minor compositional changes on the strength and deformation of crustal rocks. Starting with the same mineralogical mixture (plagioclase—pyroxene), we used two types of orthopyroxene, the composition which is enriched in either Magnesium (Mg) or Iron (Fe). At a first order, each sample reacts differently in terms of strain localization and resistance, depending on the degree of metastability. While the Fe-rich assemblages react quickly and record a weak strength, the Mg-rich assemblages are slower to react and document a high strength at peak stress conditions. However, unlike to the Fe-rich assemblages, a pronounced weakening is recorded after peak stress for the Mg-rich assemblages. Such a weakening is coeval with the development of highly connected shear bands of polyphase, fine-grained material. In contrast, the Fe-rich samples only produce partially connected, coarse-grained aggregates of monophase material, which may account for the absence of significant weakening. These results confirm that strongly connected, fine-grained mixed zones (e.g. ultramylonite) are weaker than poorly connected, coarse-grained monophase domains (e.g. mylonite). This accounts therefore for the long-term, quasi-permanent weakness of highly deformed shear zone (i.e., ultramylonite) where fine-grained, phase mixing occurs upon mineral reactions, provided that the reaction kinetics remains limited enough.

To conclude, our study illustrates that the rheology of rocks cannot be summarized as being controlled by monophase materials. In order to use rheological models to predict the lithospheric strength, it seems therefore required to use appropriate laws that consider both, the complexity of regional structures (such as shear zone areas) and the complete nature of rocks that compose them, including the rheology of polyphase material in presence—or in absence—of feedback between deformation and reactions.

Résumé

Les zones de cisaillement résultent de la localisation de la déformation dans les roches de la croûte et du manteau supérieur au cours de la déformation de la lithosphère. Accommodant une importante quantité de déformation, ces zones de cisaillement s'avèrent ainsi déterminantes pour la compréhension de la dynamique globale de la lithosphère. Dans la présente étude, nous aspirons à élargir les connaissances actuelles sur la rhéologie et le développement des zones de cisaillement par une approche multi-échelle, qui inclut des observations de terrain et des expériences de déformation.

Premièrement, nous avons étudié la zone de cisaillement sud Armoricaine (CSA), qui correspond à une zone de cisaillement d'échelle crustale qui déforme des roches granitiques dans les conditions de la croûte moyenne. Avec l'augmentation de la déformation depuis des roches faiblement déformées (protolithe) à fortement déformées (ultramylonite), cette zone de cisaillement se distingue par (1) une réduction significative de la taille des grains, (2) le développement de bandes monophasées à mica dans des roches modérément (protomylonite) et davantage déformées (mylonite), et (3) leur remplacement ultérieur par des zones de mélange à grains fins dans les ultramylonites. Les caractéristiques microstructurales indiquent également que la taille des grains a amorcé une transition entre le fluage insensible à la taille des grains (GSI pour *grain size insensitive*) et le fluage sensible à la taille des grains (GSS pour *grain size sensitive*), dont le glissement aux joints de grains (GBS pour *grain boundary sliding*). Dans l'ensemble, nos résultats identifient une succession de processus affaiblissants responsables de la localisation de la déformation à grande échelle et du développement du CSA. Cela débute par la nucléation du mica comme premier matériau affaiblissant, puis évolue avec la formation de zones de mélange de phases à grains fins.

Deuxièmement, nous avons effectué des expériences de déformation en cisaillement sur des assemblages à deux phases représentatifs de la croûte inférieure (plagioclase – pyroxène) afin d'étudier comment les zones de cisaillement se développent et comment l'interaction entre déformation et réactions minérales influence la rhéologie de la roche. Nous avons initialement étudié et comparé l'évolution des microstructures, des mécanismes de déformation et de la rhéologie des assemblages polyphasés et monophasés. Nos expériences révèlent que la contrainte maximale (pic de contrainte) des assemblages à plagioclase + pyroxène se situe entre celles des assemblages monophasés. Cependant, la résistance décroît significativement après le pic de contrainte, jusqu'à

atteindre une résistance bien inférieure à celle de la phase la plus faible, le plagioclase. Cet affaiblissement coïncide avec l'apparition simultanée de bandes de cisaillement interconnectées, composées de produits de réaction à grains fins et intimement mélangés. Notre étude démontre que la déformation amplifie significativement la cinétique des réactions minérales, ce qui affaiblit fortement la résistance des assemblages déformés du fait de la localisation de la déformation et de la nucléation de phase. Une telle interaction entre la déformation et les réactions minérales peut avoir de fortes répercussions sur le développement et la durabilité des zones de cisaillement de la croûte terrestre.

Troisièmement, des expériences de déformation en cisaillement sur des assemblages mafiques ont été effectuées dans le but de déterminer l'influence de faibles variations de la composition sur la résistance et la déformation des roches crustales. À partir du même mélange minéralogique (plagioclase - pyroxène), nous avons utilisé deux types d'orthopyroxène, dont la composition est soit enrichie en magnésium (Mg) soit enrichie en fer (Fe). Dans un premier temps, chaque échantillon réagit différemment en en termes de localisation de la déformation et de résistance, selon son degré de métastabilité. Alors que les assemblages riches en Fe réagissent rapidement et se caractérisent par une faible résistance, les assemblages riches en Mg réagissent plus lentement et présentent une résistance plus élevée au pic de contrainte. Toutefois, contrairement aux assemblages riches en Fe, un affaiblissement prononcé est enregistré après le pic de contrainte pour les assemblages riches en Mg. Un tel affaiblissement est concomitant avec le développement de bandes de cisaillement à grains fins fortement connectées. En revanche, les échantillons riches en Fe ne produisent que des agrégats de matériaux monophasés à gros grains partiellement connectés, ce qui pourrait justifier l'absence d'affaiblissement significatif. Ces résultats confirment que les zones polyphasées fortement connectées à grains fins (e.g. ultramylonite) sont plus faibles que les domaines monophasés à grains plus grossiers dont la connectivité est faible (e.g. mylonite). Cela rend donc compte de la faiblesse quasi permanente à long terme d'une zone de cisaillement fortement déformée (i.e. ultramylonite) où le mélange de phases à grains fins se forme au cours des réactions minérales, sous réserve que la cinétique de réaction demeure suffisamment limitée.

Pour conclure, notre étude montre que la rhéologie des roches ne peut se résumer au comportement rhéologique des matériaux monophasés. Afin de recourir à l'utilisation de modèles rhéologiques pour prédire la résistance de la lithosphère, il semble nécessaire

d’utiliser des lois appropriées qui tiennent compte à la fois de la complexité des structures régionales (comme les zones de cisaillement) et de la nature complète des roches qui les composent, notamment la rhéologie des matériaux polyphasés en présence — ou non — de la rétroaction entre la déformation et les réactions.

Contents

Résumé étendu

1. Introduction et cadre d'étude

La planète Terre est en perpétuel changement dans la mesure où sa surface est constamment remaniée par un ensemble de processus endogènes et exogènes. Tandis que certains phénomènes tels que les tremblements de terre, les éruptions volcaniques et les glissements de terrain provoquent des modifications presque instantanées de la surface de la Terre, d'autres, bien plus discret à l'échelle humaine, n'en sont pas moins importants.

Les connaissances actuelles de la déformation des masses continentales à grande échelle se basent largement sur la théorie scientifique de la tectonique des plaques formulée dans les années 60 (McKenzie and Parker, 1967; Morgan, 1968; Le Pichon, 1968). Cette théorie est l'aboutissement d'une série d'hypothèses, dont celle proposée par Alfred Wegener en 1912 sur la dérive des continents, et celle sur l'expansion des fonds océaniques (Vine and Matthews, 1963; Morley and Larochelle, 1964). Selon la théorie de la tectonique des plaques, la partie superficielle de la Terre, connue sous le nom de lithosphère (du Grec *lithos*, signifiant « roche »), constitue une enveloppe au comportement rigide, qui est discontinue et fragmentée en grandes calottes sphériques appelées « plaques tectoniques ». La lithosphère repose sur un milieu qui se déforme lentement par fluage sous l'effet de contraintes faibles, mais durables : l'asthénosphère (du Grec *asthenos*, signifiant « faible »). En perpétuels mouvements, les plaques tectoniques peuvent être de différente nature (océanique et continentale) et de taille variable. Selon la nature du déplacement des plaques les unes par rapport aux autres, 3 types de limites de plaques se distinguent : les plaques convergentes (cordillère des Andes, Himalaya), divergentes (Rift est-africain, basin and range) et transformantes (faille de San Andreas, faille nord anatolien). Les plaques lithosphériques sont donc soumises à d'importantes contraintes tectoniques qui se localisent principalement le long des limites de plaque, générant ainsi une activité géologique intense dans ces régions du globe.

En fournissant un modèle cinématique remarquable des mouvements horizontaux à grande échelle de la surface de la Terre, la théorie de la tectonique des plaques a

significativement modifié notre compréhension de la dynamique terrestre. Cette théorie

fournit un cadre d'interprétation cohérant pour tous les phénomènes et structures géologiques, telles que la formation des chaînes de montagnes, la topographie des fonds marins, la formation de gisements minéraux, la distribution et la cause des tremblements de terre.

La lithosphère se compose de deux couches superposées qui diffèrent notamment par la nature des matériaux qui les composent, à savoir la croûte, qui se compose largement de granite (pour la croûte continentale), et la partie supérieure du manteau, autrement dit le manteau lithosphérique, qui se compose principalement de péridotite (e.g. Ringwood and Hart, 1969). Suite à l'identification de ces matériaux naturels, de nombreuses études de déformation expérimentales ont été réalisées afin de comprendre leurs mécanismes de déformation (e.g. Byerlee, 1978; Kirby, 1985; Kohlstedt et al., 1995). Parmi elles, plusieurs observations ont mis en exergue le lien entre la déformation d'un matériau et sa résistance, identifiant ainsi deux principaux modes de comportement rhéologique : le comportement fragile et le comportement visqueux. Ces observations ont aussi permis d'instaurer le concept d'enveloppe rhéologique afin de prédire le comportement des matériaux associé à l'augmentation de la température et de la pression en fonction de la profondeur (Fig. 1; e.g. Sibson, 1977; Goetze and Evans, 1979; Kirby, 1980).

Cependant, les incertitudes de premier ordre liées à la construction des enveloppes rhéologiques restreignent considérablement l'évaluation de la rhéologie de la lithosphère. L'une des hypothèses majeures repose sur le fait que les principaux constituants des assemblages rocheux régissent la rhéologie des couches de la lithosphère. Les roches sont ainsi simplifiées à leurs constituants majeurs tels que le quartz, le feldspath et le pyroxène pour les roches crustales et l'olivine pour les roches mantelliques (Kohlstedt et al., 1995). Cependant, cette approximation s'affranchit du fait que les enveloppes de la lithosphère sont principalement composées d'assemblages polyphasés (e.g. Handy, 1990; Handy et al., 1999), ce qui réduit artificiellement l'importance des autres phases minérales. Or, de nombreuses études ont montré que le comportement mécanique des matériaux polyphasés peut être fortement influencé par la proportion des phases, leurs contrastes rhéologiques, leurs tailles et leurs arrangements spatiaux et géométriques (e.g. Handy, 1990; Tullis and Wenk, 1994; Dimanov and Dresen, 2005; Takeda and Griera, 2006). Ces observations suggèrent que la vision actuelle de la lithosphère peut donc être sensiblement différente

si l'on considère l'interaction complexe entre les phases minérales.

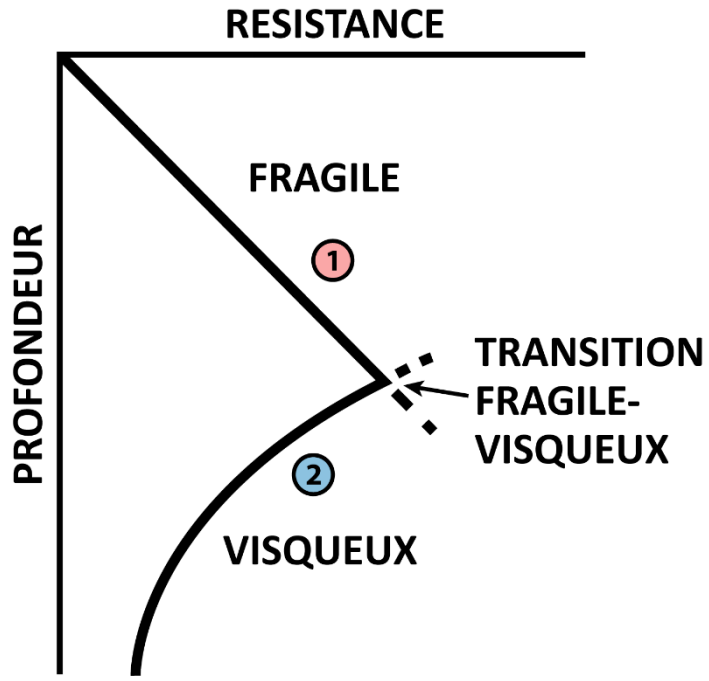

Fig 1: Profil schématique de résistance de la croûte continentale montrant un comportement fragile dans la partie supérieure et un comportement visqueux dans la partie inférieure (modifié à partir de Scholz, 1988). (1) La résistance augmente linéairement avec la pression de confinement et la profondeur. (2) La résistance diminue exponentiellement avec la température et la profondeur.

Les mouvements de la croûte et du manteau supérieur issus de la déformation de la lithosphère sont largement accommodés par les failles et leurs équivalents en profondeur, à savoir les zones de cisaillements. Ces dernières correspondent à des zones de forte localisation de la déformation, qui résultent d'une chute locale de viscosité au sein d'un matériau cohésif. Les failles quant à elles caractérisent la déformation d'un matériau fragile et qui n'est donc plus cohésif. Cette accumulation préférentielle de la déformation dans les zones de cisaillement prouve que ces structures peuvent avoir une incidence majeure sur la résistance globale de la lithosphère (e.g., Bürgmann and Dresen, 2008; Fossen and Cavalcante, 2017). La présence en elle-même des zones de cisaillement dans un volume donné de roche est la signature d'une distribution hétérogène de la déformation (e.g. Ramsay, 1980; Vauchez et al., 2012). L'une des expressions marquantes de la localisation de la déformation dans les zones de cisaillements ductiles

est le développement progressif de protomylonite, mylonite et ultramylonite, qui traduisent une déformation de plus en plus intense (Fig. 2) (e.g. Tsurumi et al., 2003; Baratoux et al., 2005; Linckens et al., 2015; Farkašovský et al., 2016).

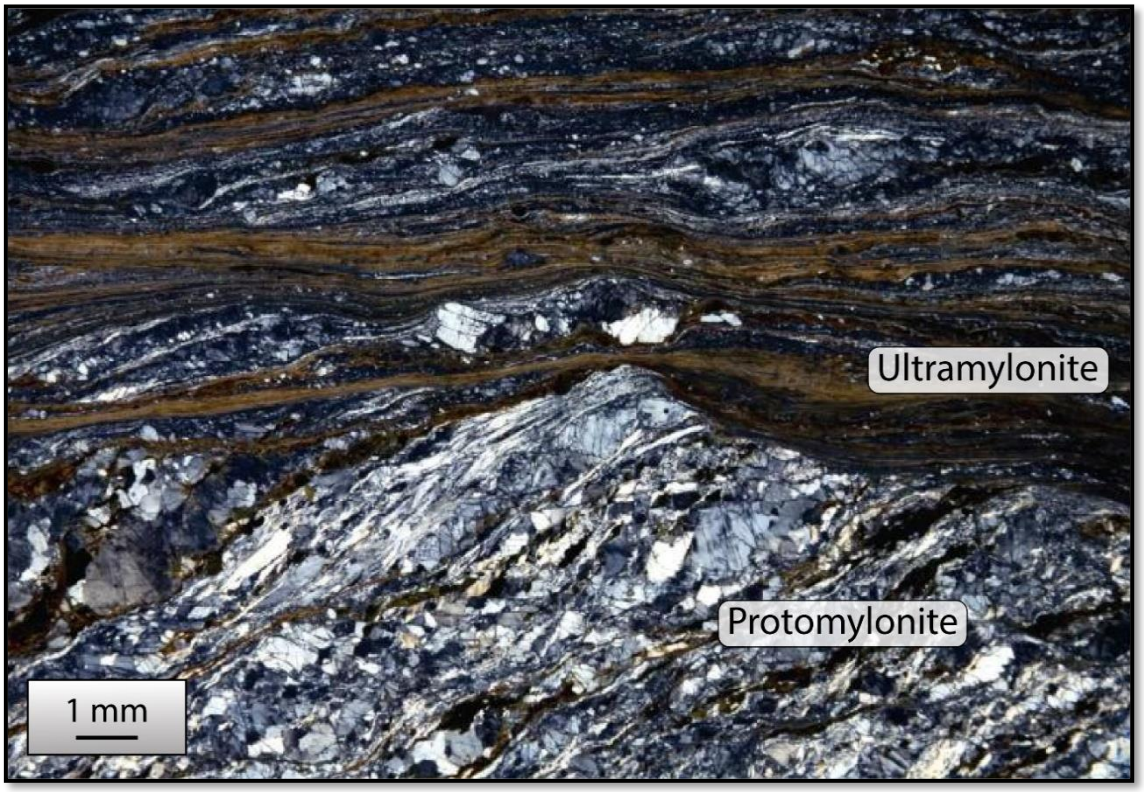

Fig 2: Photo au microscope optique montrant le contraste entre un domaine protomylonitique dans la partie inférieure et le domaine ultramylonique dans la partie supérieure (extrait de Trouw et al., 2010).

Comprendre le comportement rhéologique des zones de cisaillements, qui représentent des zones de faiblesses lithosphériques où la déformation est fortement localisée, s'avère ainsi essentiel pour mieux appréhender le comportement géodynamique global de la lithosphère. Cependant, l'étude des zones de cisaillements s'avère être un exercice complexe, car cela requiert une quantification de paramètres fondamentaux tels que la contrainte, la vitesse de déformation et la taille des grains des matériaux, et ce à partir d'observations de terrains et d'expériences de déformation. De plus, les zones de cisaillement naturelles ne fournissent généralement qu'un aperçu de l'histoire rhéologique, car ces zones ont pu enregistrer différentes conditions de pression, de température, de vitesse de déformation, etc. au cours des temps géologiques. Ainsi, les

traces d'épisodes précoces de déformation enregistrés par la roche ont pu être partiellement effacées par des épisodes de déformation postérieurs. Une façon de remédier à ce problème est de reproduire expérimentalement la déformation des roches en question, permettant d'analyser l'évolution de leur résistance mécanique en fonction des processus actifs responsables du développement des zones de cisaillement. Le défi lié à la réalisation d'expériences de déformation sur des assemblages rocheux repose, d'une part, sur la capacité technique à reproduire les conditions naturelles de déformation (pression, température, teneur en eau, etc.), mais aussi sur la validité de l'extrapolation des résultats obtenus. En effet, l'une des principales difficultés est la rapidité avec laquelle les conditions de pression (P) et de température (T) expérimentales sont atteintes au cours d'une expérience (~ 4 à 8 h), et comment cela peut favoriser la métastabilité d'un assemblage rocheux porté à de telles conditions. Dans la nature, ces changements de conditions P-T s'effectuent plus lentement, ce qui induit des changements bien plus progressifs dans les assemblages minéraux (e.g. Herwegh et al., 2011). Ce gap entre nature et expériences est quasi inévitable, puisque les conditions géologiques exigent des forces impraticables et des durées expérimentales irréalistes pour être appliquées (e.g., Kohlstedt et al., 1995; Précigout et al., 2018). Néanmoins, la similitude entre les microstructures des échantillons naturels et expérimentaux suggère fortement que des processus similaires ont agi mutuellement dans la nature et les expériences.

Ce travail de thèse vise à approfondir les connaissances actuelles sur le comportement rhéologique des zones de cisaillement. Pour cela, une approche multi-échelle est proposée, en combinant à la fois des observations de terrains et des observations expérimentales sur les processus de localisation de la déformation et d'adoucissement dans les conditions de la croûte moyenne à inférieure. Le cas d'étude naturel que nous présentons s'intéresse aux granitoïdes du Massif Armoricain français, déformés par une importante zone de cisaillement d'échelle crustale. Parallèlement, une étude approfondie de déformation expérimentale sur des assemblages biphasés représentatifs de la croûte inférieure a été menée.

2. Le cisaillement sud Armoricain : témoin d'une succession de processus adoucissants qui localisent la déformation

Le cas naturel présenté dans cette thèse nous amène en Bretagne sud dans le massif sud Armoricain pour étudier le granite de Questembert, granite affecté par des intensités de déformation variables qui donnent naissance localement à des mylonites et des ultramylonites. Nous avons décidé de travailler le long de la zone de cisaillement sud Armoricaine (CSA), car cette importante zone de cisaillement crustale préserve un gradient de déformation à grande échelle allant des domaines de faible déformation (protolithe et protomylonite) aux domaines de plus forte déformation (mylonite et ultramylonite) (Fig. 3). Le CSA est donc un exemple idéal pour l'étude de la localisation de la déformation visqueuse amenant au développement de mylonites et ultramylonites. Les échantillons étudiés ont été prélevés par Romain Augier lors d'une précédente campagne de terrain le long d'une coupe orthogonale au gradient de déformation. Les observations et les analyses ont été effectuées sur des lames minces orientées parallèlement à la linéation et perpendiculairement à la foliation (plan XZ).

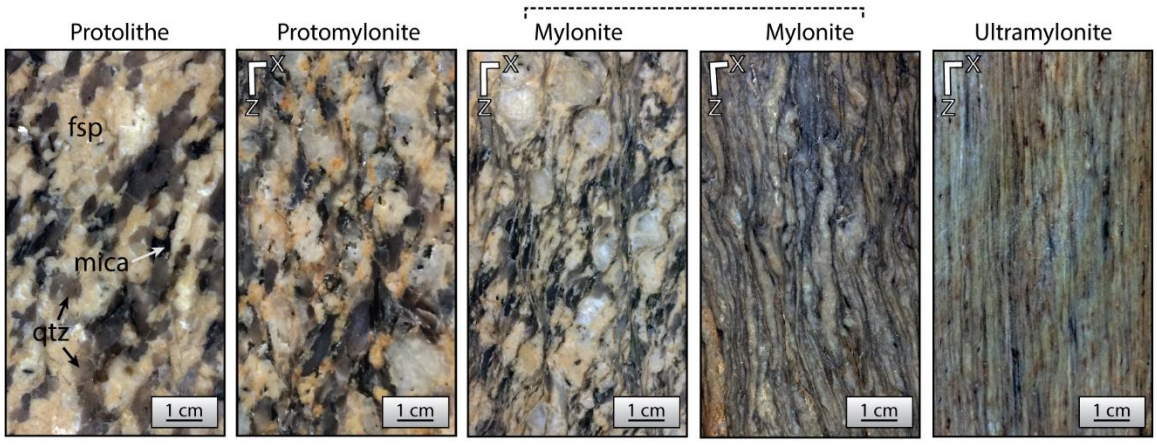

Fig 3: Photographies des échantillons analysés dans l'étude du cas naturel, montrant les différents gradients de déformation, du protolithe à l'ultramylonite. Qtz = quartz, fsp = feldspar.

L'augmentation de la déformation du protolithe à l'ultramylonite s'accompagne d'une évolution des microstructures, marquée notamment par : (1) une réduction importante de la taille des grains, (2) le développement de bandes monophasées et partiellement connectées de micas dans la protomylonite et la mylonite, et (3) leurs remplacements ultérieurs par des zones de mélange à grains fins dans l'ultramylonite.

La transition du protolithe à l'ultramylonite se traduit également par une forte dispersion de l'orientation préférentielle de réseau du quartz. Nous suggérons que l'interconnexion des bandes monophasées à micas est liée à la formation de fissures dans le protolithe et à la nucléation de phase assistée par les fluides (Mansard et al., 2018). La nucléation joue également un rôle majeur dans le mélange des phases, comme en témoigne notamment la précipitation du feldspath potassique au niveau (1) de points triples dans les agrégats de quartz et (2) des ombres de pression à grains fins, situées aux abords des porphyroclastes hérités de feldspaths potassiques dans l'ultramylonite (Fig. 4). Nos observations attestent que la nucléation de phase est le principal processus responsable du mélange de phases, dont la force motrice implique une combinaison de réactions chimiques et de glissement aux joints de grains (GBS, pour *Grain boundary Sliding*) permettant d'ouvrir des cavités au cours de la déformation. La transition du protolithe à l'ultramylonite est ainsi marquée par une transition dans le mécanisme de déformation dominant qui devient, dans les zones à grains fins, extrêmement sensibles à la taille des grains.

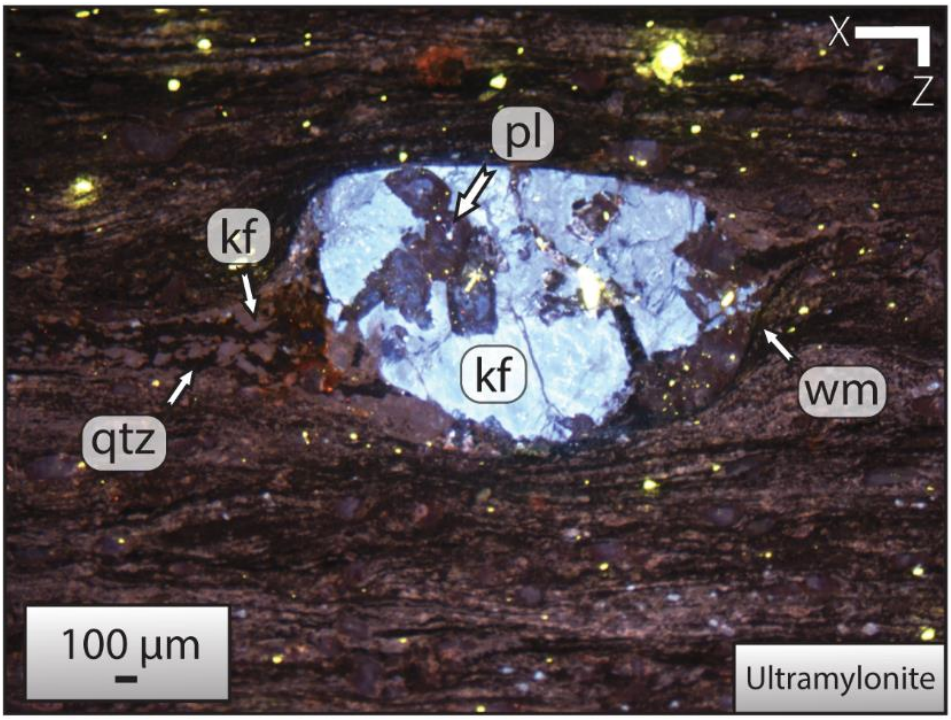

Fig 4: Photo au microscope optique cathodoluminescent illustrant la nucléation de quartz et de feldspath potassique dans les ombres de pression d'un grain hérité de feldspath potassique dans l'ultramylonite. Qtz = quartz, pl = plagioclase, kf = feldspath potassique, wm = mica blanc.

Cette étude met ainsi en évidence une succession de processus qui adoucissent la roche avec la diminution de la température et la localisation de la déformation, en commençant par la nucléation du mica comme premier matériau affaiblissant (phase la plus faible au sein des roches granitiques, e.g. Tullis and Wenk, 1994), puis évoluant avec

la formation de zone de mélange à grains fins qui peuvent se déformer sous l'effet du fluage diffusion et du GBS. Se développant en remplacement du réseau interconnecté de mica, le mélange polyphasé à grains fins est considéré comme la géométrie la plus faible de la zone de cisaillement. La réduction de la taille des grains joue ainsi un rôle majeur dans la localisation de la déformation et la formation des zones de cisaillement.

3. Impact rhéologique lié au développement des zones de cisaillement : approche expérimentale

Afin d'étudier l'effet rhéologique lié au développement des zones de cisaillement, nous avons dans un deuxième temps effectué des expériences de cisaillement en laboratoire à l'aide d'un dispositif de déformation de type Griggs (Fig. 5). Cette presse tri-axiale à confinement solide permet de créer un environnement à haute pression (HP) et haute température (HT), tout en déformant un échantillon de roche donné. L'enregistrement continu de la contrainte appliquée sur l'échantillon et de la déformation résultante nous permet de déterminer ses propriétés rhéologiques.

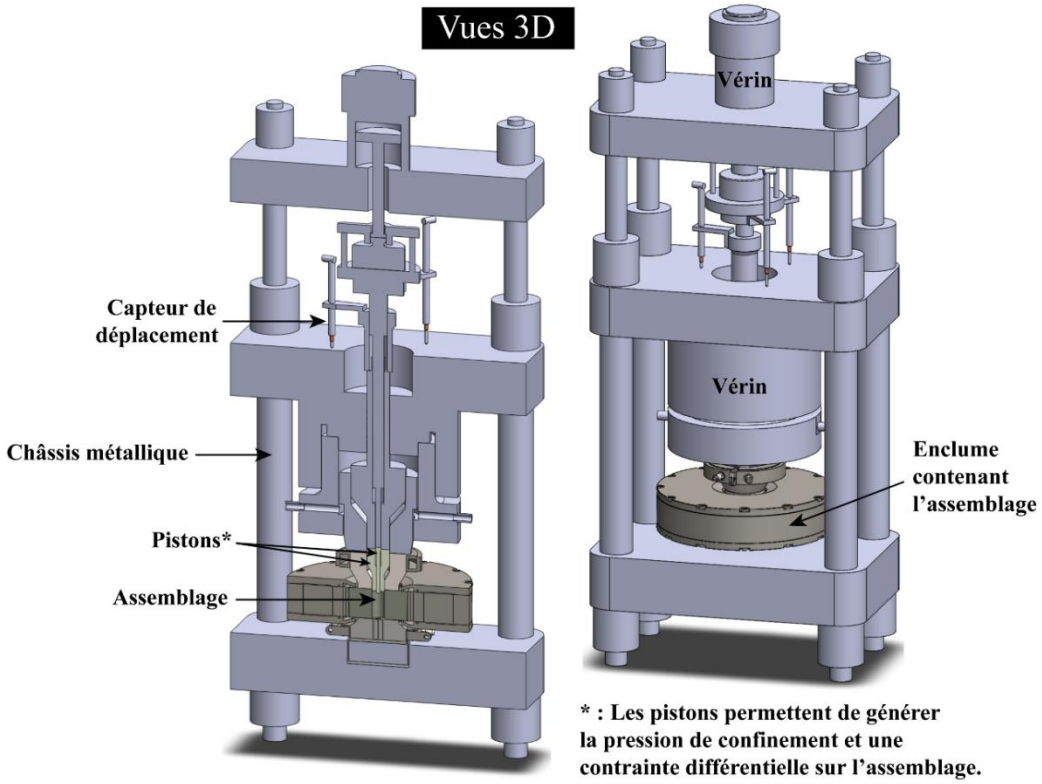

Fig 5: Représentation schématique en 3D de la presse de type Griggs disponible à l'Institut des Sciences de la Terre d'Orléans (ISTO, France) (modifié d'après Précigout et al., 2018).

Au cours de cette étude expérimentale, nous avons souhaité étudier l'interaction entre la déformation, les réactions minérales et la taille des grains, mais également l'influence que peut avoir la composition chimique des produits de départ sur les processus de déformation et de réaction. Ces expériences ont été réalisées sur des assemblages biphasés de plagioclase-pyroxène, plagioclase-amphibole et, à titre de comparaison, sur des assemblages monophasés de plagioclase, pyroxène et amphibole. Plusieurs matériaux ont permis d'extraire la poudre initiale nécessaire à la réalisation des expériences (Fig. 6), à savoir (1) du plagioclase (labradorite) issu de gemmes provenant de Sonora au Mexique (An60-Ab37-Or3), (2) de l'orthopyroxène (mentionné sous le terme Mg-Opx) issu d'une péridotite et provenant de Chine (Wo1-En89-Fs10), (3) un autre plagioclase (labradorite; An55-Ab44-Or1) et un autre orthopyroxène (Wo2-En62-Fs36 – mentionné sous le terme Fe-Opx) issus tous deux d'une granulite d'Hidaka au Japon, et (4) de l'amphibole (magnesio-hornblende) issue d'une amphibolite du Massif Central en France. Les expériences présentées dans cette thèse ont été réalisées à une pression de 1 GPa, des températures comprises entre 800 et 900 °C et à une vitesse de déformation cisaillante de 10^{-5} s^{-1}.

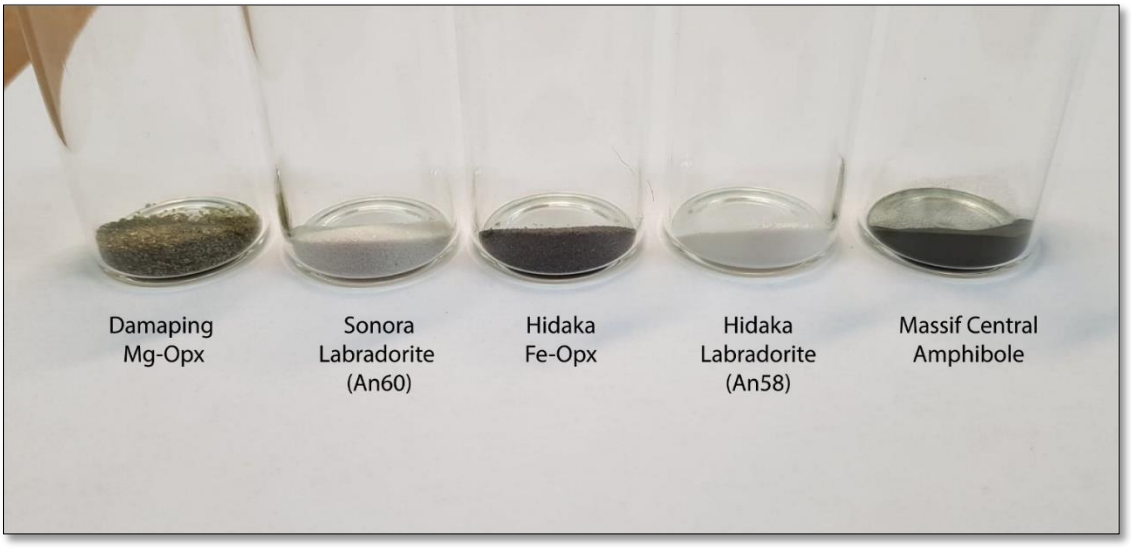

Fig 6: Image des différents matériaux de départ utilisés pour réaliser les expériences.

3.1 Influence de la composition minéralogique sur la localisation de la déformation et l'adoucissement à faible contrainte cisaillante

La déformation d'assemblages biphasés (pyroxène et plagioclase) montre une étroite corrélation entre la capacité des minéraux à interagir, la proportion de produit de réaction

et la résistance des matériaux. En ce qui concerne la quantité de produits de réaction, nous avons remarqué que deux expériences peuvent atteindre un pic de résistance différent selon la proportion de produits de réactions. Plus la proportion de produits de réactions est importante, plus l'échantillon est faible. Par conséquent, les réactions minérales ont un contrôle direct sur la rhéologie des roches.

Lorsque l'on considère deux assemblages qui diffèrent essentiellement par la nature plutôt ferreuse (Fe-Opx) ou magnésienne (Mg-Opx) du pyroxène que l'on mélange à un plagioclase, on s'aperçoit que (1) la nature des produits de réaction, (2) la localisation initiale de la déformation, et (3) la cinétique de réaction sont significativement différentes. Dans l'assemblage à Fe-Opx + Plag, la nature ferreuse de l'Opx initial (Opx_1) privilégie la formation d'Amph alors que dans l'assemblage à Mg-Opx + Plag, la nucléation d'un nouvel Opx (Opx_2) est favorisée. De plus, dans l'assemblage à Mg-Opx + Plag, la localisation initiale de la déformation s'effectue aux abords des grains originaux d'Opx_1 via la nucléation de zones de mélange à grains fins (Fig. 7a). En revanche, dans l'assemblage à Fe-Opx + Plag, la localisation de la déformation s'effectue via le développement de bandes globalement monophasées ou via le développement de zones légèrement mélangées et à grains plus grossiers par rapport aux assemblages à Mg-Opx + Plag (Fig. 7b).

L'étude de l'évolution de la composition révèle que celle des produits de réaction (plagioclase et pyroxène) documentée dans les assemblages à Fe-Opx + Plag est plus éloignée de la composition du matériau de départ par rapport aux assemblages à Mg-Opx + Plag. Étant donné que la composition du matériau de départ est plus éloignée de l'équilibre dans l'assemblage à Fe-Opx + Plag, l'énergie libre totale est supposée supérieure à celle des produits finaux. Ainsi, l'assemblage à Fe-Opx + Plag réagit plus rapidement que l'assemblage à Mg-Opx + Plag. Le comportement rhéologique étant contrôlé par les réactions minérales, l'assemblage à Fe-Opx se déforme donc sous des contraintes plus faibles.

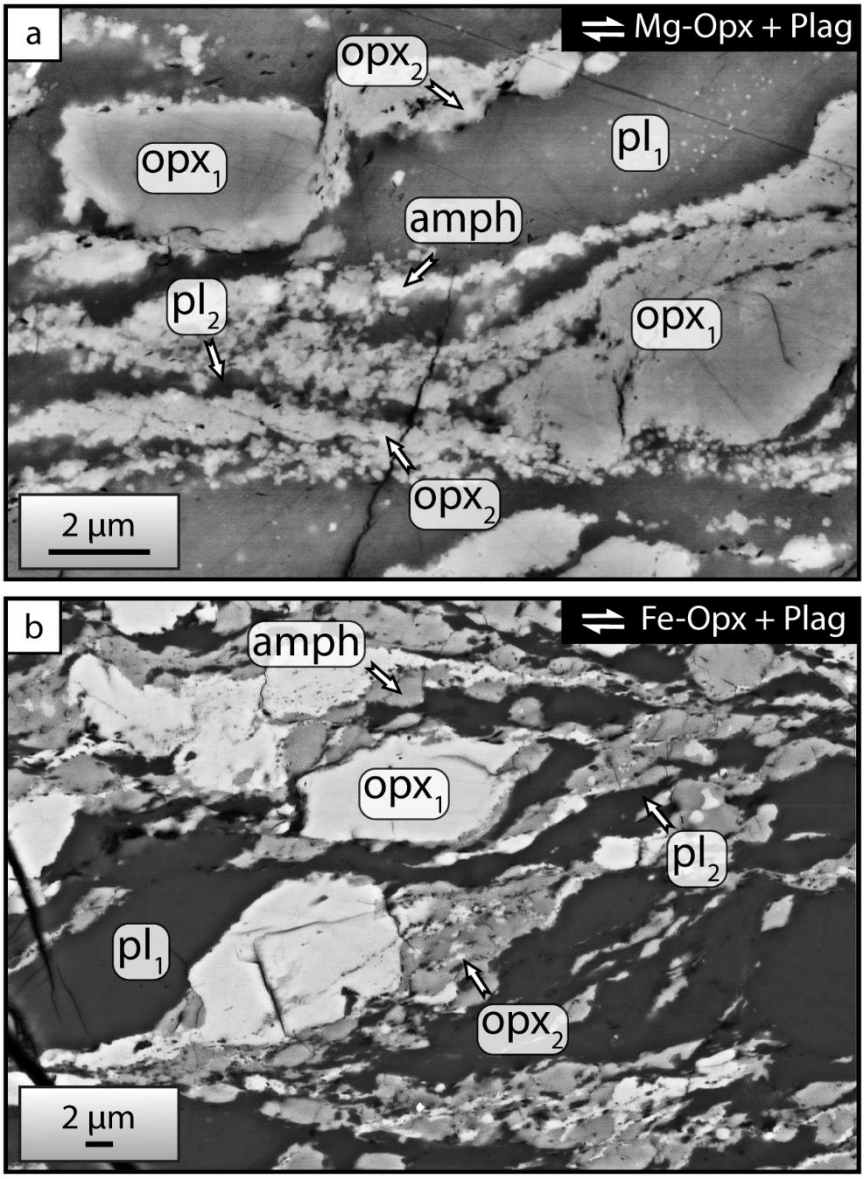

Fig 7: Image au microscope électronique (électrons rétro-diffusés) de la nucléation précoce et de la localisation de la déformation. (**a**) Dans l'assemblage à Mg-Opx + Plag des zones de mélange à grains fins nucléés aux abords des grains originaux. (**b**) Dans l'assemblage à Fe-Opx + Plag, la nucléation est essentiellement monophasée avec le développement de couronnes de réaction et de bandes riches en Amph. Opx = orthopyroxène, pl = plagioclase, amph = amphibole.

Ces observations révèlent que le comportement rhéologique des assemblages biphasiques à plagioclase et pyroxène est extrêmement sensible à leur composition minéralogique et que de faibles variations chimiques peuvent initier la localisation de la déformation — même à faible contrainte de cisaillement — et induire de larges différences de résistance. Ces différences de résistances à faible contrainte dépendent ainsi de la capacité des mélanges à réagir et donc de la proportion variable des phases faibles et secondaires générées par cette réaction.

3.2 Influence de l'interaction mutuelle entre déformation et réaction minérale sur la rhéologie des zones de cisaillement

Les expériences de déformation montrent une forte interaction entre déformation et réaction minérale dans la mesure où les réactions se localisent essentiellement le long des zones les plus déformées. La comparaison d'échantillons maintenus sans déformation aux conditions expérimentales et les échantillons faiblement déformés jusqu'au pic de contraintes (à période de temps similaire) révèlent que la déformation a un effet significatif sur le développement de produit de réaction en influant sur la cinétique des réactions.

Alors que le pic de contrainte des assemblages à plagioclase + pyroxène se situe entre celui des assemblages monophasés, la résistance des matériaux polyphasés diffère fortement avec l'augmentation de la déformation. Dès lors que la déformation s'initie, une succession de processus syn-cinématiques se succèdent et induisent une grande variété de comportements, basés notamment sur le type d'assemblage rocheux et la façon dont la déformation se distribue (Fig. 8). La résistance des assemblages à Mg-Opx + Plag (cas 1) s'affaiblit fortement après le pic de contrainte et atteint des contraintes de fluage qui se stabilisent bien en dessous de celle de la phase la plus faible (le plagioclase). Cet affaiblissement est en corrélation avec le développement concomitant de zones de cisaillement fortement déformées où le Plag original est entièrement remplacé au profit de produits de réaction à grains fins composés d'Opx_2, $Plag_2$ et Amph.

Les mécanismes de déformation dominants dans ces zones de forte déformation sont sensibles à la taille des grains. Cela inclut notamment le fluage diffusion, le fluage par pression-dissolution (DPC) et/ou le glissement aux joints de grains (GBS). La réduction de la taille des grains due à la nucléation des produits de réaction favorise l'activation de ces mécanismes. Dans ces assemblages, la viscosité des produits de réaction est très faible (zones de mélange à grains fins) par rapport aux assemblages de départ, ainsi les zones ayant réagi vont concentrer la déformation, induire des chutes de viscosité dans les zones adjacentes et propager la réaction jusqu'à former des zones connectées. Des expériences réalisées sur des assemblages monophasés à Amph montrent également une concomitance étroite entre la présence de zones de mélange à grains fins et un affaiblissement prononcé de la résistance de l'assemblage après le pic de contrainte.

En revanche, le comportement des assemblages à Fe-Opx + Plag et Amph + Plag

(cas 2) n'est pas comparable à celui des assemblages précédents, car ces derniers ne s'affaiblissent pas (Fe-Opx + Plag à 850 °C) ou difficilement (Amph + Plag à 800°C). Ils peuvent aussi durcir (Fe-Opx + Plag à 900 °C), mais dans tous les cas, ces assemblages se déforment à des contraintes considérablement plus faibles par rapport aux assemblages à Mg-Opx + Plag. D'ailleurs, les produits de réaction sont beaucoup moins intensément mélangés dans les assemblages à Fe-Opx + Plag par rapport aux assemblages à Mg-Opx + Plag, comme en atteste le développement de bandes de cisaillement globalement monophasées et partiellement interconnectées. Ces microstructures ont également été documentées dans l'assemblage à Amph + Plag. L'absence d'affaiblissement majeur dans les échantillons du cas 2 est imputable à trois facteurs : (i) l'absence d'interconnexion significative des agrégats faibles de produits de réaction, comme ceux observés dans les assemblages du cas 1, (ii) la taille des produits de réaction est considérablement plus grande (1 à 2 ordres de grandeur) et intensément moins mélangés, et (iii) la viscosité des produits de réactions (Amph) qui est plus élevée par rapport aux mélanges à grains fins des assemblages du cas 1. Cette viscosité limite la propagation de proche en proche de la réaction. Bien que le mécanisme de déformation dominant soit également le DPC avec le fonctionnement du GBS dans les assemblages du cas 2, les différences de microstructures suggèrent une différence dans l'importance respective de ces mécanismes dans les 2 cas étudiés. En effet, dans les assemblages du cas 2, les produits de réaction (Amph) présentent des rapports de forme plus grands, sous forme de grains fibreux, autour des grains de pyroxènes et dans les bandes de cisaillement. Ces microstructures représentent un type de fluage par DPC qui tend davantage vers un DPC à l'échelle du grain, où idéalement la forme des grains refléterait la contrainte finie (Fig. 8). Au contraire, les bandes de cisaillements à grains fins intensément mélangés dans les assemblages du cas 1 présentent des grains assez arrondis, où le DPC est probablement dominé par le GBS (Fig. 8).

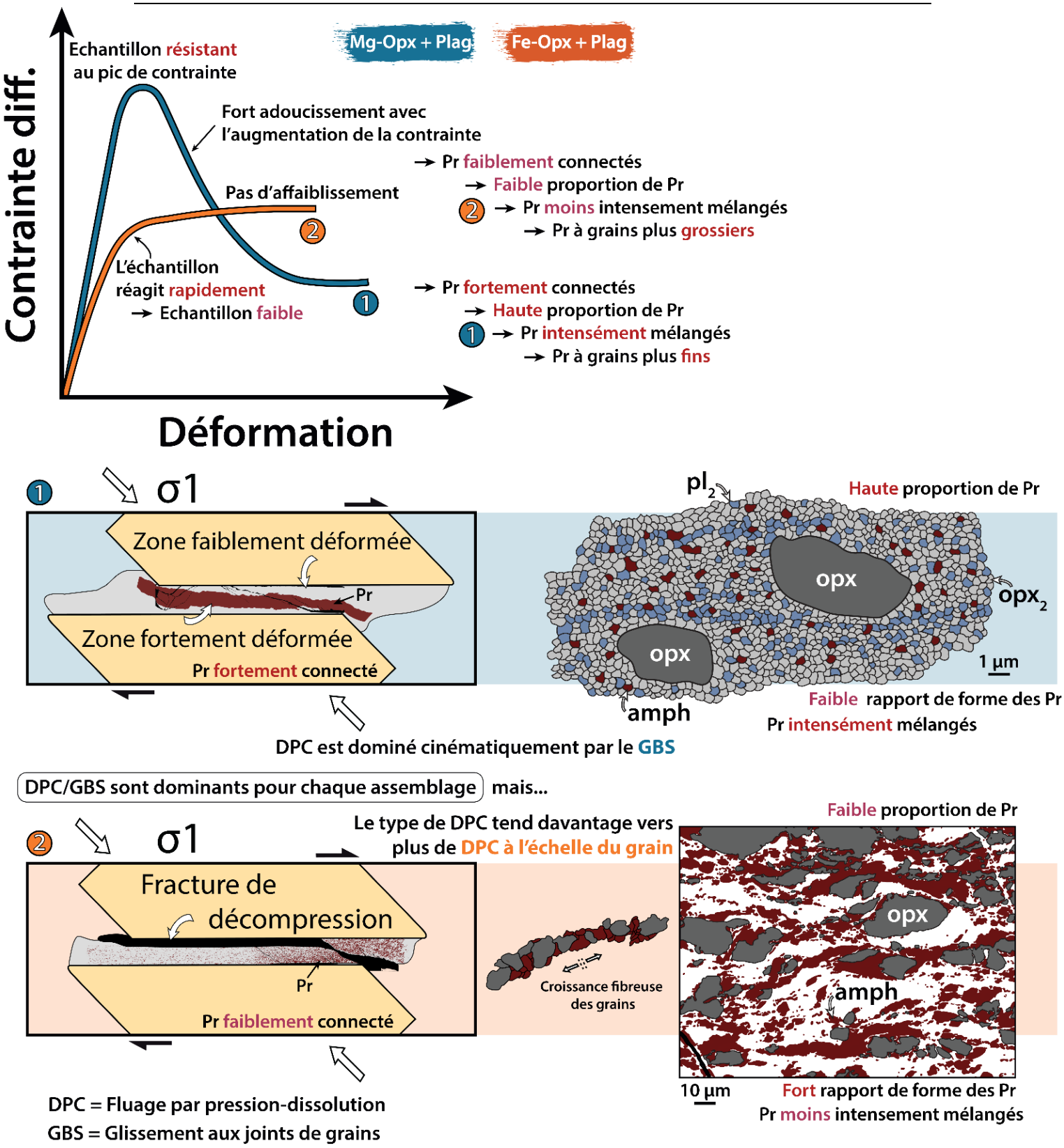

Fig 8: Schéma synthétique de l'évolution microstructurale et du comportement mécanique des assemblages déformés à Mg-Opx + Plag et Fe-Opx + Plag. Contrainte diff. = contrainte différentielle, Pr = produits de réaction, opx = orthopyroxène, pl = plagioclase, amph = amphibole.

• Nos observations illustrent deux chemins très contrastés dans l'évolution des matériaux, selon les propriétés de la réaction : dans un cas (assemblages à Fe-Opx + Plag et Amph + Plag), les produits de réaction ont une granulométrie relativement importante et leurs nucléations n'entraînent pas d'affaiblissement significatif (principalement des amphiboles monophasées). Dans un tel cas, les produits de réaction ne sont que partiellement connectés, la résistance globale est stable et l'effet de rétroaction de la déformation sur la réaction est limité.

• Dans l'autre cas (assemblages à Mg-Opx + Plag et pure Amph), les produits de réaction à grains fins intensément mélangés sont beaucoup plus faibles que le matériau initial. Dans ce cas, la zone mécaniquement faible tend à former une zone interconnectée qui conduit à un affaiblissement macroscopique important, et l'augmentation drastique de la proportion des produits de réaction avec l'augmentation de la déformation suggère un effet de rétroaction important.

• Globalement, la valeur du pic de contrainte initial (qui détermine où la déformation se localise initialement) et l'affaiblissement important de la rhéologie associé au développement de zones mélangées à grains fins (qui détermine si les bandes de cisaillement s'épaississent ou non) semblent être largement contrôlés par les réactions minérales.

3.3 Discussion et conclusion

Dans notre étude de cas expérimental, les matériaux de départ composés de plagioclase et de pyroxène ont délibérément été choisis pour être en déséquilibre aux conditions expérimentales de pression et de température. Ce déséquilibre permet de favoriser les réactions minérales. Néanmoins, nos expériences montrent qu'en l'absence de réactions minérales, les matériaux de départ (plagioclase et pyroxène) sont trop résistants pour être déformé par fluage dislocation à la vitesse de déformation appliquée. Ces observations sont cohérentes avec les études expérimentales sur la rhéologie du feldspath (e.g. Rybacki and Dresen, 2000; Dimanov et al., 2003), du pyroxène (e.g. Bystricky and Mackwell, 2001), et d'assemblages polyphasés à plagioclase et pyroxène (Dimanov and Dresen, 2005), qui démontrent que ces phases sont mécaniquement résistantes. De plus, ces observations s'avèrent également cohérentes avec des études

naturelles montrant qu'en dessous de ~700 °C, le plagioclase et le pyroxène n'exhibent pas de déformation plastique cristalline significative (e.g. Rutter and Brodie, 1985, 1992).

Au contraire, dès l'apparition de réactions minérales, les échantillons sont déformés visqueusement et la résistance s'affaiblit. Similairement, la déformation des roches mafiques semble aussi dépendre des réactions minérales, qui peuvent induire la nucléation de phases rhéologiquement plus faibles, ou la formation d'agrégats à grains fins déformés par un fluage sensible à la taille des grains, ou les deux (e.g. Rutter and Brodie, 1992; Stünitz, 1993; Kenkmann and Dresen, 2002; Brander et al., 2012; Okudaira et al., 2017). Les résultats expérimentaux mettent en exergue que la capacité des matériaux à interagir a un impact significatif sur la résistance mécanique des assemblages soumis à de faibles contraintes cisaillantes. Notons d'ailleurs que cette résistance semble, du moins dans un premier temps, indépendante à la résistance intrinsèque des produits de réactions. En effet, bien que les assemblages à Fe-Opx + Plag favorisent la nucléation de phases relativement résistante (Amph) par rapport aux mélanges de phases à grains fins (Mg-Opx + Plag), ces assemblages se déforment à de plus faibles contraintes, car ils réagissent plus rapidement. Ces observations sont instructives, car elles mettent en évidence l'importance des réactions minérales dans le développement initial des zones de cisaillement, en déterminant tout simplement quelles portions de roches vont se déformer. Avec l'augmentation de la déformation, les assemblages déformés présentent des microstructures distinctes, avec dans un cas la formation d'agrégats monophasés à grains relativement grossiers et des bandes de cisaillement qui n'induisent pas d'adoucissement rhéologique significatif (assemblage à Fe-Opx + Plag), et dans l'autre cas, le développement de zones de mélange à grains fins fortement localisées et responsables d'un adoucissement rhéologique prononcé après le pic de contrainte (assemblage à Mg-Opx + Plag).

• Lorsqu'ils sont appliqués à des zones de cisaillement naturelles, nos résultats suggèrent que (1) les portions de roche qui se déforment sont grandement dépendantes de la capacité des minéraux à interagir, et que (2) de petites variations chimiques et minéralogiques peuvent modifier considérablement la résistance des assemblages déformés. La localisation conséquente de la déformation dans les échantillons fortement déformés montre que les zones de mélange à grains fins fortement connectées peuvent être considérablement plus faibles que les domaines monophasés partiellement connectés à grains relativement plus grossiers.

• Dans l'optique d'une meilleure compréhension du comportement rhéologique de la croûte inférieure, ces observations sont notables, car une grande proportion de domaines à grains fins permet de préserver le comportement adouci et faible à long terme d'une zone de cisaillement. En d'autres termes, l'affaiblissement n'est pas limité à la phase de réaction mais est acquis en permanence.

• Ces observations soulignent également l'importance du partitionnement de la déformation, de la réduction de la taille des grains et du degré d'interconnectivité des phases faibles comme principaux facteurs contrôlant la résistance de la lithosphère. L'interaction complexe entre les phases minérales au cours de la déformation suggère que la rhéologie des roches polyphasées, telles que les roches mafiques, qui constituent une grande partie de la croûte océanique et peuvent être l'une des principales composantes de la croûte continentale inférieure, ne peuvent difficilement pas être simplifiée au comportement rhéologique des matériaux monophasés. Les complexités structurelles régionales et leur évolution, ainsi que des lois rhéologiques d'affaiblissement de la viscosité doivent donc être prises en compte pour continuer à utiliser les modèles d'enveloppes rhéologiques comme outil prédictif de la rhéologie de la lithosphère.

CHAPTER I

General Introduction
Scientific context and motivations

CONTENTS

1. The Theory of plate tectonics: The paradigm of Earth Sciences

Planet Earth is continually changing as its surface is constantly reworked by endogenous and exogenous processes. While some phenomena like earthquakes, volcanoes and landslides cause almost instantaneous changes on the face of the Earth, others, more unobtrusive on the human time scale, are no less important and result from slow geological processes. This includes, in particular, the movement of large-scale lithosphere masses that reconfigures oceans and continents over geological periods of time. These changes, which occur at all spatial and temporal scales, impose an obvious truth: what lies beneath our feet is as familiar as it is mysterious. The knowledge of the Earth and current geological processes held and still holds the attention of many scientists.

What we know about the deformation of large-scale continental mass is largely based on the theory of plate tectonics which was formulated in the late 1960s (McKenzie and Parker, 1967; Morgan, 1968; Le Pichon, 1968). From these years, a corpus of hypotheses began to emerge as a result of the accumulation of data provided by the exploration of the ocean floor (Fig. 1).

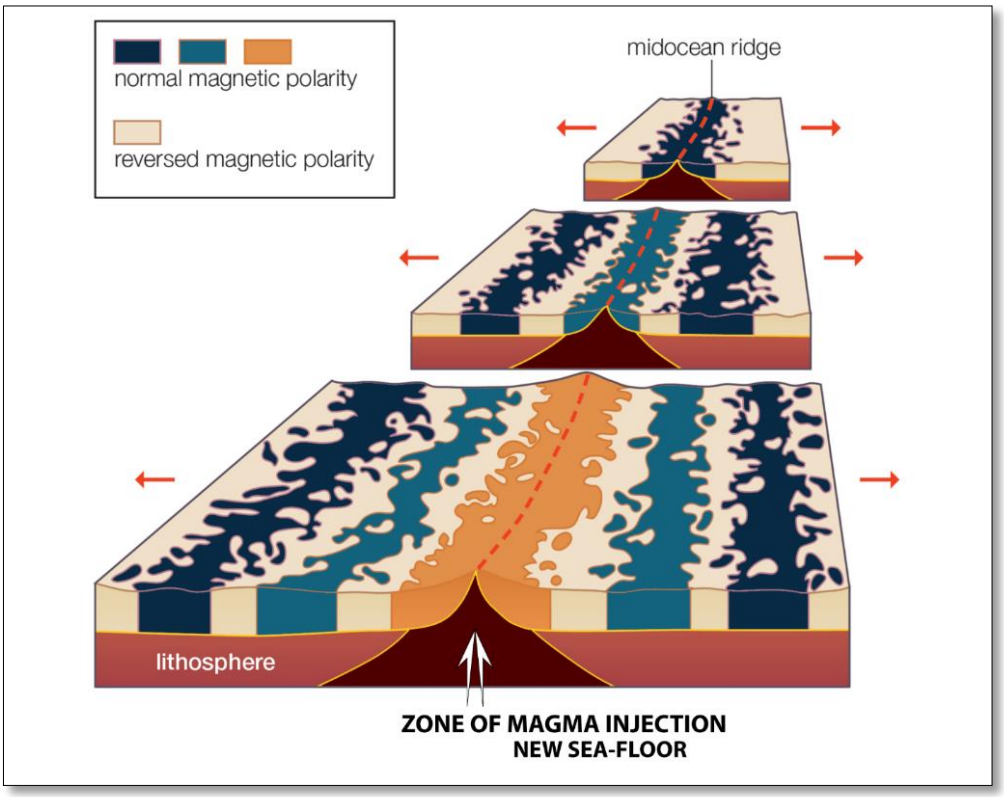

Fig 1: Seafloor spreading and magnetic striping. Figure modified from Copyright © 2012 Encyclopædia Britannica, Inc. Retrieved from https://www.britannica.com/science/seafloor-spreading/media/1/530828/155524

Indeed, scientists discovered that the rocks making up the ocean floor contained fossilized magnetic stripes that recorded the successive inversions of the Earth's magnetic field. Symmetrically arranged on either side of ocean ridges, this revelation clearly supported the hypothesis of seafloor spreading (Vine and Matthews, 1963; Morley and Larochelle, 1964), and reinforced the Wegener's mobilist conceptions of continental drift, proposed in 1912. According to the plate tectonics theory, Earth has a rigid outer shell known as the lithosphere (from the Greek *lithos*, meaning "rock"), which is discontinuous and fragmented into large domains called "plates" (Fig. 2). The lithosphere rests on a weaker medium that slowly deforms by creep ("time-dependent" deformation) under the effect of small but long-lasting stresses: this is the asthenosphere (from the Greek *asthenos*, meaning "weak"). The lithospheric plates of varying size and natures (oceanic and continental) continuously move relative to each other across Earth's surface and interact along their boundaries.

Three types of plate tectonics boundaries are defined: convergent (e.g. Cordilleran mountain belt, the Himalayas), divergent (e.g. East African Rift Valley) and transform (e.g San Andreas Fault, North Anatolian Fault). As a result, the lithospheric plates are subjected to tectonic stresses and deform mainly along their boundaries, where geological activity is intense.

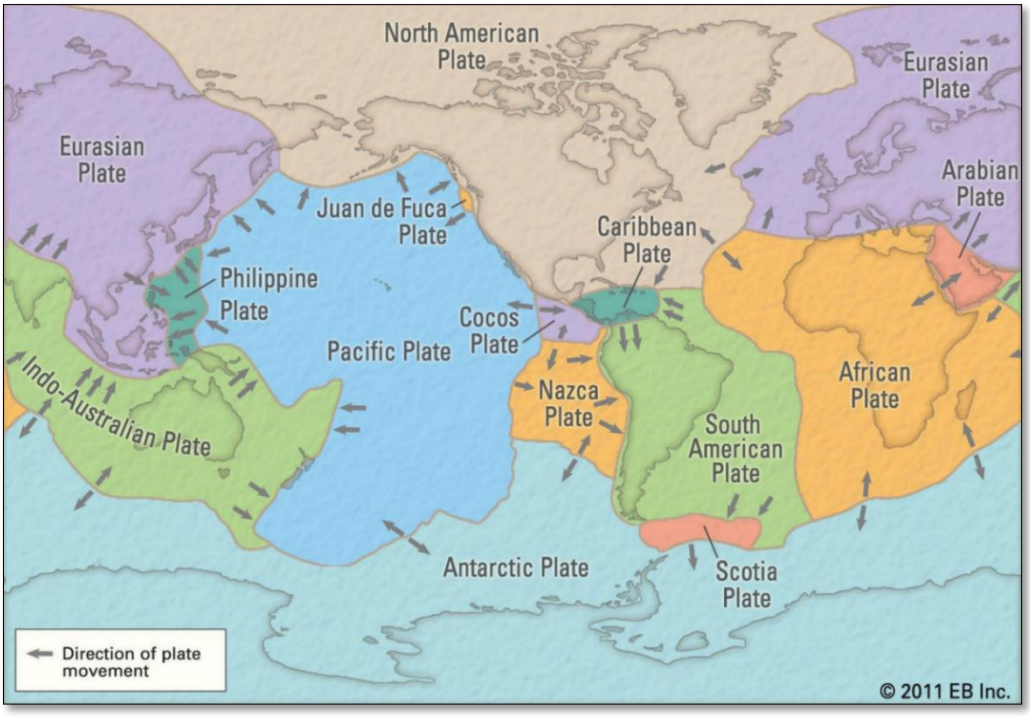

Fig 2: Map showing Earth's major tectonic plates with arrows depicting the directions of plate movement. Copyright © 2011 Encyclopædia Britannica, Inc. Retrieved from https://www.britannica.com/science/plate-tectonics/media/1/463912/172045

• By providing a remarkable kinematic model of large-scale horizontal movements at the Earth's surface, the theory of plate tectonics has changed our understanding of the Earth's dynamics. This theory is part of the new Earth Sciences paradigm, as it is no longer possible to study any geological phenomenon outside the framework that this theory proposes.

• This theory also provides a coherent interpretative framework for all geological phenomena and structures such as mountain range formation, ocean floor topography, mineral deposit formation, distribution and cause of earthquakes and volcanism.

2. Rheological behavior of the lithosphere

Following a large number of geological studies, in a broad sense, a global view of the composition and the structure of the lithosphere has gradually emerged. The lithosphere consists of two superposed layers, which differ, in particular, by the nature of the materials that compose them: a crust of variable thickness and the upper part of the mantle (i.e. lithospheric mantle). The continental crust is composed largely of granitoid-type material, while the underlying lithospheric mantle is composed mainly of peridotite (e.g. Ringwood and Hart, 1969).

After the identification of these natural materials, numerous experimental deformation studies have been carried out to understand their deformation mechanisms (e.g. Byerlee, 1978; Kirby, 1985; Kohlstedt et al., 1995). To explore the mechanical properties of rocks, a variety of stress conditions, which reflect different depths and stress regimes in the crust, are applied to the samples. These experiments have shown that there is a link between the deformation of a material and its strength, and that the mode of deformation of rocks is controlled by two types of rheological behavior when the deformation is non-elastic (i.e. the strain is non-recoverable): brittle and viscous behavior. Under low confining pressures and temperatures (e.g. in the upper levels of the lithosphere), the brittle behavior is dominant. A rock may deform by fracturing when subjected to stress beyond its yield strength, and this is concomitant with a sudden stress drop. The brittle behavior is sensitive to confining pressure, because it affects brittle fracture strength in particular by suppressing the growth of dilatant microcracks (Lockner and Beeler, 2002). The increase in pressure and temperature with depth leads to a transition from brittle to viscous behavior. In the viscous regime, a rock has the capacity

to accumulate permanent strain without fracturing, at least where its maximum resistance is exceeded.

From these observations, the concept of lithospheric strength profile emerged in order to predict the behavior of the materials as a function of depth for both the brittle and viscous regimes, by assuming a geothermal gradient (rate of temperature increase with depth) (e.g. Sibson, 1977; Goetze and Evans, 1979; Brace and Kohlstedt, 1980; Kirby, 1980; Kohlstedt et al., 1995). The concept of lithospheric strength profile was initially advanced for the oceanic lithosphere by Goetze and Evans (1979), and then adapted to the continental lithosphere by Brace and Kohlsted (1980). According to the Byerlee's law (empirical relation derived from experiments to describe the frictional behavior of rocks), the strength of rocks in the brittle domain increases linearly with depth and is independent of the material (Fig. 3). In contrast, in the viscous domain, the strength of rocks, that is determined from the extrapolation of high temperature steady-state flow laws, decreases with increasing depth (Fig. 3; Scholz, 1988). Although these flow laws are dependent on other parameters such as deformation rate or grain size (e.g. Handy, 1989), the strength profile indicates at first order an increase in resistance with depth in the brittle regime, and then a decrease in the viscous regime. The intersection region at which brittle domain gives way to viscous domain is known as the brittle-viscous transition (Kohlstedt et al., 1995).

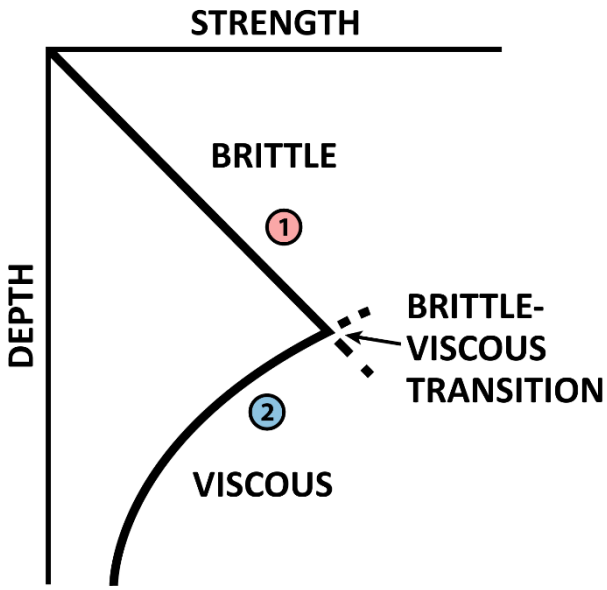

Fig 3: Schematic strength profile of the continental crust showing brittle behavior in the upper part and viscous behavior in the lower part (modified from Scholz, 1988). (1) The strength increases linearly with confining pressure and depth. (2) The strength decreases with temperature and depth.

Although models on lithosphere rheology have been constantly enriched with new data since its introduction in the 1970s (e.g. Sibson, 1977; Goetze and Evans, 1979; Kirby, 1980), the absence of directly measurable data beyond a few kilometers makes estimation of the rheology of the lithosphere very complex and is subject to drastically different interpretations (Fig. 4).

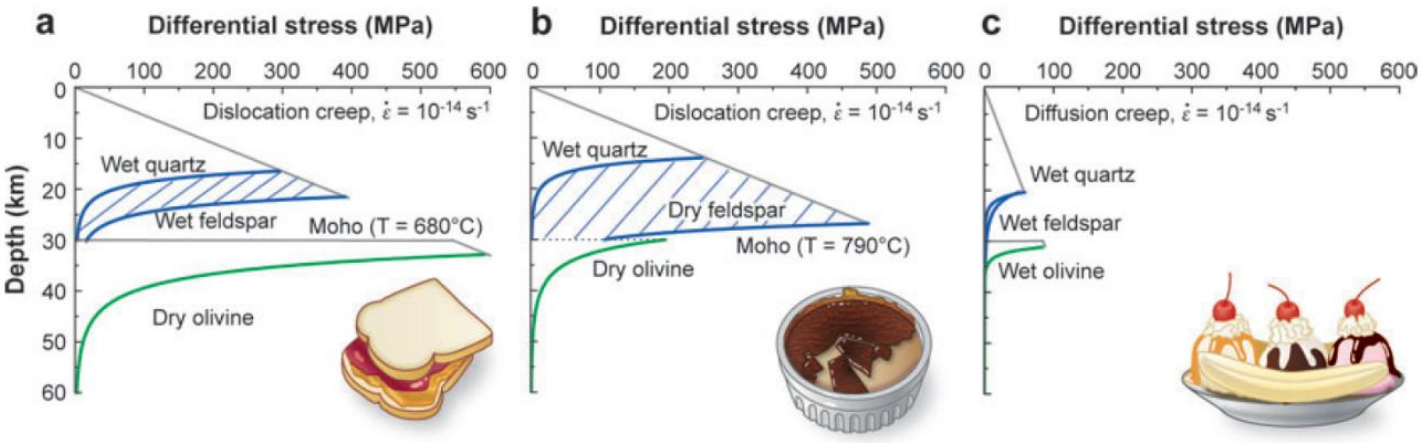

Fig 4: Models of strength through continental lithosphere (retrieved from Bürgmann and Dresen, 2008). Three main models are proposed as models of the layered earth. These models, which provide a visual description of how the lithosphere is structured, are as follows: the "jelly sandwich" (a), the "crème brûlée" (b) and the "banana split" (c) models.

MODELS OF STRENGTH OF THE CONTINENTAL LITHOSPHERE

- The first model considers the upper crust and upper mantle as the most mechanically resistant portions of the lithosphere. This model is known as the "*jelly sandwich*" with a weak lower crust, referring to jam, sandwiched between two slices of bread, the strong upper crust and lithospheric mantle (Fig. 4a; Kirby and Kronenberg, 1987; Burov and Watts, 2006). Analog models reveal that a weak lower crust and a strong mantle lithosphere are required for plate tectonics to operate (Handy and Brun, 2004). Lithospheric elastic thickness estimates also reveal that the lower continental crust is weaker than the underlying mantle (e.g. Burov and Watts., 2006). In this model, the long-term strength of the lithosphere resides in the lithospheric mantle. This model, which was very attractive in the 1980s, is still in use today (e.g. Sawyer, 1985; Kirby and Kronenberg, 1987; Gueydan et al., 2008), but since then it has been the subject of some criticism and debate (e.g. England, 1986; Maggi et al., 2000; Jackson et al., 2002).

- One of the criticisms against the "*jelly sandwich*" model is based on the rheological contrast that can be obtained between the lithospheric envelopes according to the presence or absence of fluid. Indeed, since the emergence of the "*jelly sandwich*" model, many studies have shown the significant impact that the presence of aqueous fluid can have on the viscosity of rocks, particularly on quartzite (e.g. Kronenberg and Tullis, 1984; Mainprice and Paterson, 1984; Paterson and Luan, 1990). Based on gravity anomalies and seismic depth distribution (Maggi et al., 2000), Jackson et al. (2002) showed that the crust is strong and override a weak lithospheric mantle. Unlike the "*jelly sandwich*" model, the upper mantle seems to be, according to this second model, aseismic and therefore essentially viscous. This second model is called "*crème brûlée*" because the rigid crust (caramel) rests on the underlying mantle, considered viscous and weak (cream) (Fig. 4b). The long-term strength of the lithosphere lies in the crust.

- Finally, Burgmann and Dresen (2008) proposed a model that considers the lithosphere as a whole that contains areas of weakness (shear zones). This model, commonly referred to as "*banana split*", considers ice balls as portions of crust and lithospheric mantle separated by large, relatively deep fault zones (Fig. 4c). The rheology of the lithosphere in this model is much weaker than the previous

These lithospheric strength profiles present some limitations insofar as their constructions require many assumptions and simplifications. One of them includes the use of a single mineral, usually the most abundant mineral, to represent a portion of the lithosphere, such as quartz for the crust and olivine for the lithospheric mantle (Kohlstedt et al., 1995). While it may appear, at first sight, appropriate to summarize the behavior of the upper mantle to that of olivine because this mineral represents nearly 80% of its volume, it seems less appropriate to characterize the behavior of the continental crust with that of quartz. Indeed, although the latter is dominant near the surface (also with feldspar), a mafic composition may predominate the lower crust, and this portion of the lithosphere would then be dominated by plagioclase and pyroxene assemblages (Rudnick and Taylor, 1987). In any case, all assumptions are a natural starting point that simplify strength profiles and provide first-order models for the rheology of the lithosphere.

However, the simplification of a single phase rheology ignores the fact that the layers of the lithosphere are mainly composed of polyphase assemblages (e.g. Handy, 1990; Handy et al., 1999) and consequently neglects the potential interaction within a multiphase assemblage. A growing body of literature has examined the rheology of two-phase assemblages (e.g. Handy, 1990; Tullis and Wenk, 1994; Dimanov and Dresen, 2005; Takeda and Griera, 2006; Dimanov et al., 2007), and it is rather well accepted that the mechanical behavior of polyphase materials can be strongly influenced by the proportion of phases, their rheological contrast, their size, their spatial and geometric arrangement, suggesting that the current view of the lithosphere may be completely different if we consider the complex interaction between mineral phases.

• The study of the rheological models is very instructive because we observe that the vision we have of the rheology of the lithosphere is very diverse according to whether we use one or other flow law, with different geothermal gradient, and so on.

• In order to further use the rheological models as a predictive tool for lithospheric rheology, which was most certainly originally used to obtain a qualitative and simplified view of lithospheric strength, it is necessary to use appropriate laws that are consistent with regional structural complexities and their evolution. This includes in particular (1) the polyphase nature of the lithospheric envelopes, (2) the complex interaction between mineral phases, and (3) the heterogeneous deformation of the lithosphere, which contains areas of intense strain localization.

• It is in this sense that the model proposed by Burgmann and Dresen (2008) is very enlightening because it shows that weak zones with intense strain localization (shear zone) can considerably weaken the rheology of the lithosphere. Moreover, shear zones are an expression of the finite state of the phenomenon of strain localization that accommodates the movements of the crust and mantle during the deformation of the lithosphere. This preferential accumulation of strain in shear zones serves as evidence that these structures can substantially affect the overall strength of the lithosphere (e.g. Bürgmann and Dresen, 2008; Fossen and Cavalcante, 2017).

3. Shear zones as major strain localization features in the lithosphere

While the upper crust is generally seen to deform brittlely (faults), beyond the brittle-ductile transition zone rocks may deform ductilely and form shear zones, because the brittle deformation is suppressed by large confining pressure. It is generally accepted that active shear zones, present into the ductile regime of the mid-lower crust, are the deeper counterparts to upper crustal faults visible at the surface (Fig. 5) (Sibson, 1977; Ramsay, 1980; Fossen and Cavalcante, 2017).

SHEAR ZONES

- At first sight, shear zones can be described as tabular zones of defined width marked by an astonishing concentration of deformation in relation to adjacent zones. The existence in itself of a shear zone in a given volume of rock is the signature of a heterogeneous distribution of deformation, i.e., strain is localized (e.g. Ramsay, 1980; Vauchez et al., 2012).

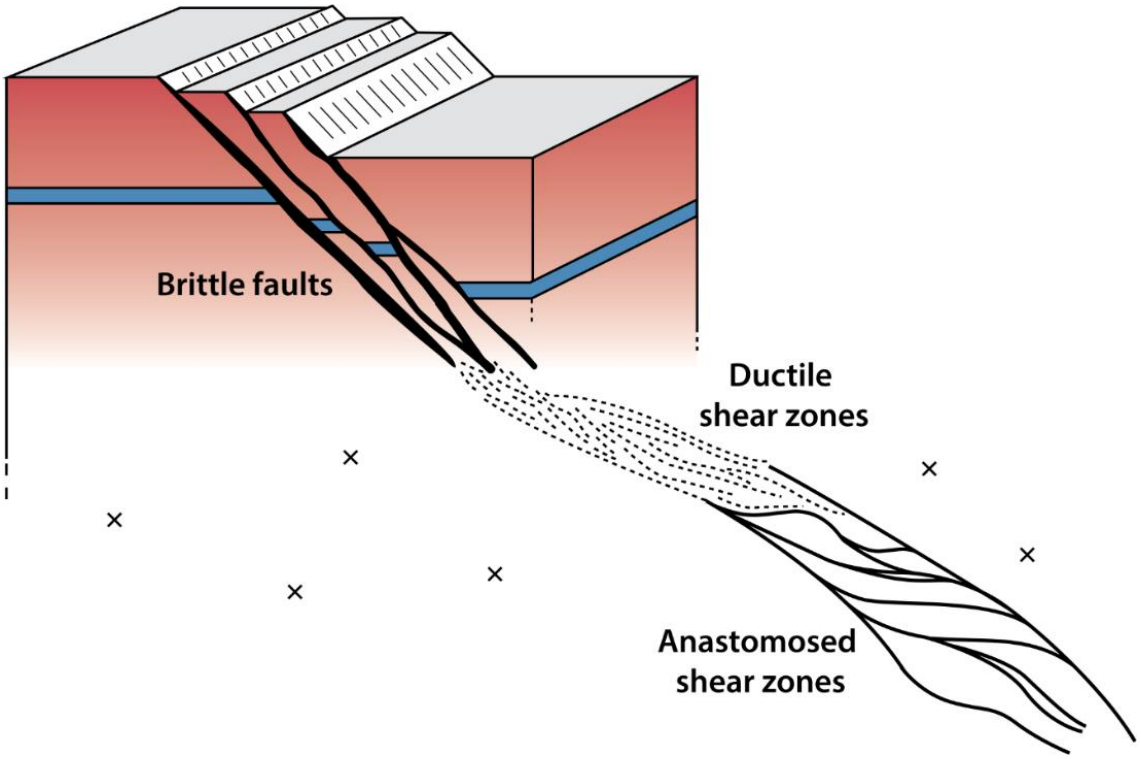

Fig 5: Conceptual model of a major fault zone and relationship between the upper-crustal brittle faults and the deeper-crustal ductile shear zones (adapted from Sibson, 1977).

Shear zones operate at all scales from the mineral to the lithosphere, and the shear zones form an anastomosed network that separates less deformed domains (Fig. 6).

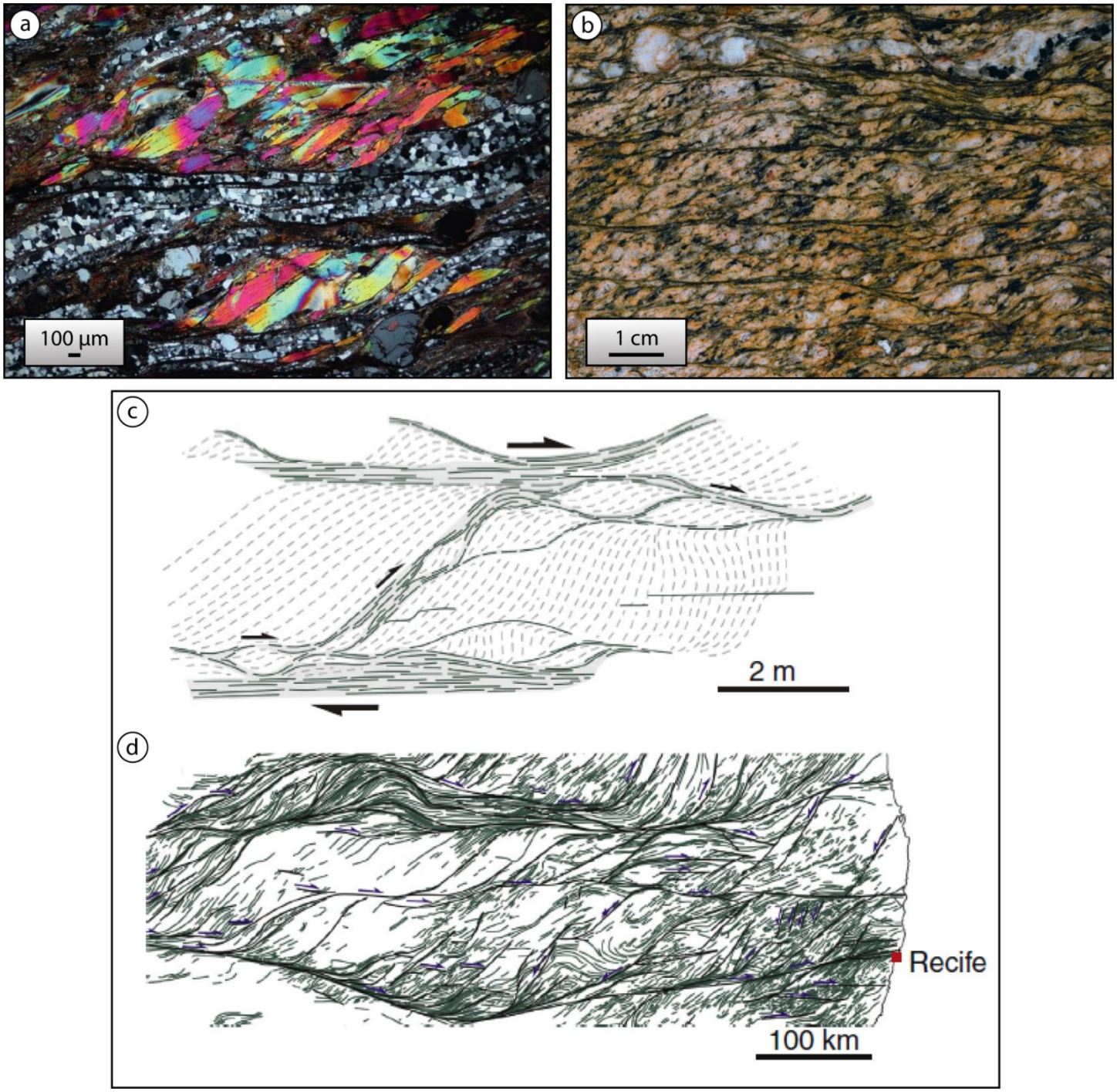

Fig 6: Shear zones occur at all scales, from micron (**a**), to centimeter (**b**), to meter (**c**) and to kilometer (**d**). (**a**) Mylonite derived from a quartz-mica schist. Dextral sense of shear (retrieved from Trouw et al., 2010). (**b**) Mylonite derived from a granite (retrieved from Trouw et al., 2010). (**c**) Meter-scale anastomosing shear zone system from Cap Creus (retrieved from Fusseis et al., 2006 and Fossen and Cavalcante, 2017). (**d**) Kilometer-scale anastomosing shear zone system of NE Brazil (retrieved from Trouw et al., 2010).

Shear zones thus accommodate large amounts of deformation and the expression of its localization in ductile shear zones is expressed by the progressive development of protomylonites, mylonites and ultramylonites with increasing strain (e.g. Tsurumi et al., 2003; Baratoux et al., 2005; Linckens et al., 2015; Farkašovský et al., 2016). The transition from protomylonite to ultramylonite is usually accompanied by a grain size refinement and a partitioning of phases in mylonites, then by a mixing of these fine-grained phases in ultramylonite (Fig. 7). The deformation within these shear zones is thus highly heterogeneous and the strain across the shear zone is associated with microstructural gradients. As each type of mineral is characterized by a specific deformation mechanism within polyphase aggregates, the deformation of rocks within shear zones is thus a complex combination of several deformation mechanisms that evolve with the evolution of microstructures.

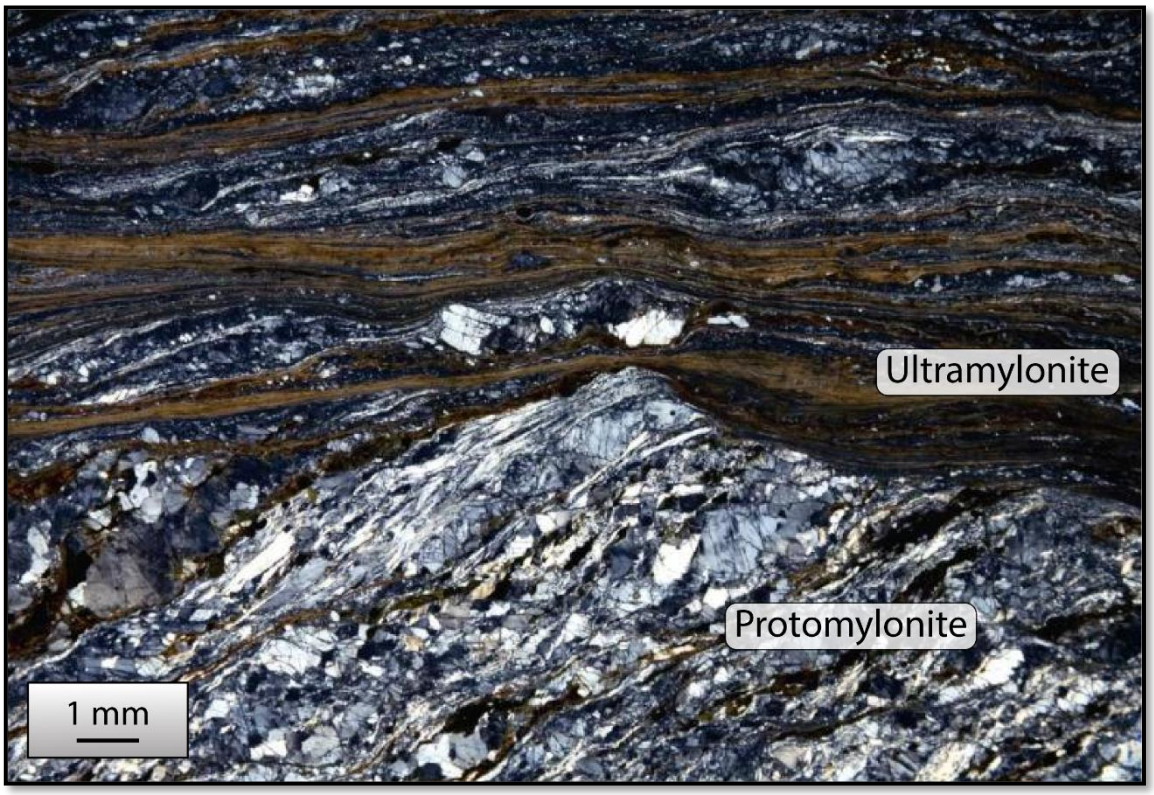

Fig 7: Picture showing the contrast between an inclined protomylonite in the lower part and an ultramylonite in the upper part (retrieved from Trouw et al., 2010).

To ensure that strain localization predominates over the homogeneous deformation in shear zones, the rock has to soften and deform as the strain progressively increases. This “strain weakening” is thus the case if less stress is required to keep the deformation going. On the contrary, when the stress increases as the rock deforms, it hardens. The

rock becomes harder to deform. This phenomenon is called “strain hardening”.

At present, the study of presently active shear zones is complex due to the depth of emplacement, preventing direct geological analyses. This is a major and limiting point because these active crustal-scale shear zones play a major role in the large-scale evolution of geological structures. As examples, we can mention the role of these shear zones in the burial and exhumation of materials, by accommodating the strike-slip component of subduction (e.g. Scheuber and Gonzalez, 1999), the development of large-scale detachment (e.g. Sidman et al., 2005) and by accommodating continental collision, such as the North Anatolian and Tibetan Fault systems (e.g. Bozkurt, 2001; Murphy et al., 2002). To understand the behavior of these active shear zones, inaccessible at the surface, it is necessary to study fossil shear zones that outcrop at the surface. As a complementary alternative, deformation experiments in the laboratory can be performed to understand deformation mechanisms, strain localization and weakening processes related to the development of shear zones.

The first three parts highlight that rock deformation is one of the most important geological processes and direct observations necessary to reconstruct the tectonic evolution of the lithosphere. When studied at a given scale of observation, the deformation of rocks is always a representation of processes acting at other scales. From mineral to shear zone scale and to lithospheric plates, the deformation mechanisms involved, only become understandable by transposing the reasoning from one level to another: a shear zone only makes sense once we have understood how strain is localized, which can only be understood once one has clarified which mechanisms are localizing and weakening within the materials of the shear zone. These mechanisms, which are discussed in the following section, include in particular mineral reactions, grain size reduction and interconnection weak materials. As microstructures evolve in space and time, they greatly influence the mechanical behavior of materials, of large-scale shear zones and finally that of the lithosphere.

4. Mechanisms of strain localization and weakening in shear zones

A number of processes are thought to contribute to strain localization in shear zones such as: (1) grain size reduction (e.g. White, 1976; Rutter and Brodie, 1988; De Bresser et al., 2001; Montési and Hirth, 2003), (2) mineral reactions (e.g. White and Knipe, 1978; Wintsch et al., 1995), (3) mixing of phases (e.g. Fliervoet et al., 1997; Kenkmann and Dresen, 1998; Kilian et al., 2011), (4) fabric-related "geometric" softening (e.g. Handy, 1990), (5) formation of interconnected weak layers (e.g. Handy, 1994; Holyoke and Tullis, 2006b), and (6) shear heating (e.g. Hutton et al., 1990). These physico-chemical or microstructural effects lead to a weakening of the rock, which in turn further localizes it, and can lead to long-term weakening in the lithosphere. We propose to discuss some of these processes below.

4.1 Mineral reactions

Shear zones can be effective for a long period of time and the materials they contain are likely to be carried in environments with highly variable P-T conditions. The thermodynamic disequilibrium produced by these changes in P-T conditions promotes the growth of new stable minerals (e.g. Newman et al., 1999; Stünitz and Tullis, 2001; Gerya et al., 2002; Jamtveit et al., 2016). Mineral reactions can also be achieved through fluid-rock interactions (hydrous fluids or melt), as shear zones represent "permeable" pathways for fluids that enhance diffusion and strongly catalyze the reactions (e.g. Brodie, 1980; Fitz Gerald and Stünitz, 1993; Newman and Mitra, 1993). These mineral reactions can induce a significant weakening, especially if the new phases formed are easier to deform compared to the minerals of the host rock (e.g. Mitra, 1978; White et al., 1980). One of the most relevant examples is the formation of mechanically weaker sheet silicates, such as mica (e.g. Tullis and Wenk, 1994). It has been shown in the study of e.g. Fitz Gerald and Stünitz, (1993), Park et al., (2006) and Menegon et al., (2008) that mica could extensively replace original strong phases, such as plagioclase. Other examples include the replacement of olivine by serpentine (e.g. Kelemen and Hirth, 2012), and these mechanically weak phases may notably reduce friction on geological faults (Rutter et al., 2013). These phase replacements have a significant effect on the weakening of the materials, not only because a strong phase is replaced by a weak phase, but also because it leads to a reduction in grain size (e.g. Stünitz and Tullis, 2001; Gueydan et al., 2003; Holyoke and Tullis, 2006). Grain size reduction may promote indeed a possible switch

from grain-size-insensitive (GSI) to grain-size-sensitive (GSS) deformation mechanism, giving rise to substantial weakening (e.g. Rutter and Brodie, 1988; Kruse and Stünitz, 1999; Newman et al., 1999). The role of grain size reduction in strain localization and weakening in shear zones will be discussed in the following section.

4.2 Grain size reduction and phase mixing

A close relationship between grain size reduction and significant deformation is commonly reported in ductile shear zones (e.g. White et al., 1980; Behrmann and Mainprice, 1987; Handy, 1989; Warren and Hirth, 2006; Precigout et al., 2007). This led many authors to investigate the evolution of grain size and related deformation mechanisms (e.g. Rutter and Brodie, 1988; Platt and Behr, 2011). It is now admitted that grain size is one of the most important microstructural parameters that cause rheological weakening and strain localization. The concept behind this model is that a reduced grain size can induce a switch from GSI to GSS creep, so that the rock strength decreases (i.e., weakens) with decreasing grain size at a given strain rate (Fig. 8) (e.g. Schmid, 1982; Rutter and Brodie, 1988). For instance, if we consider the deformation mechanism maps for olivine at 600 °C and 800 °C proposed by Rutter and Brodie (1988), the reduction of the average grain size of a deforming assemblage during dynamic recrystallization may take the material into the diffusion creep field and weaken it locally and localize strain (Fig. 8). In this example, strain localization could not occur at 800 °C, under geological deformation conditions (strain rate of 10^{-15} s^{-1}), but could be considerable at lower temperatures of 600 °C (Fig. 8). GSS creep mechanisms include so far diffusion creep (Coble or Nabarro-Herring creep; e.g. Nabarro, 1948; Herring, 1950; Coble, 1963), dislocation—(e.g. Miranda et al., 2016) or diffusion assisted grain-boundary sliding (GBS; e.g. Langdon, 2006) and dissolution precipitation creep (DPC; e.g. Berger and Stünitz, 1996).

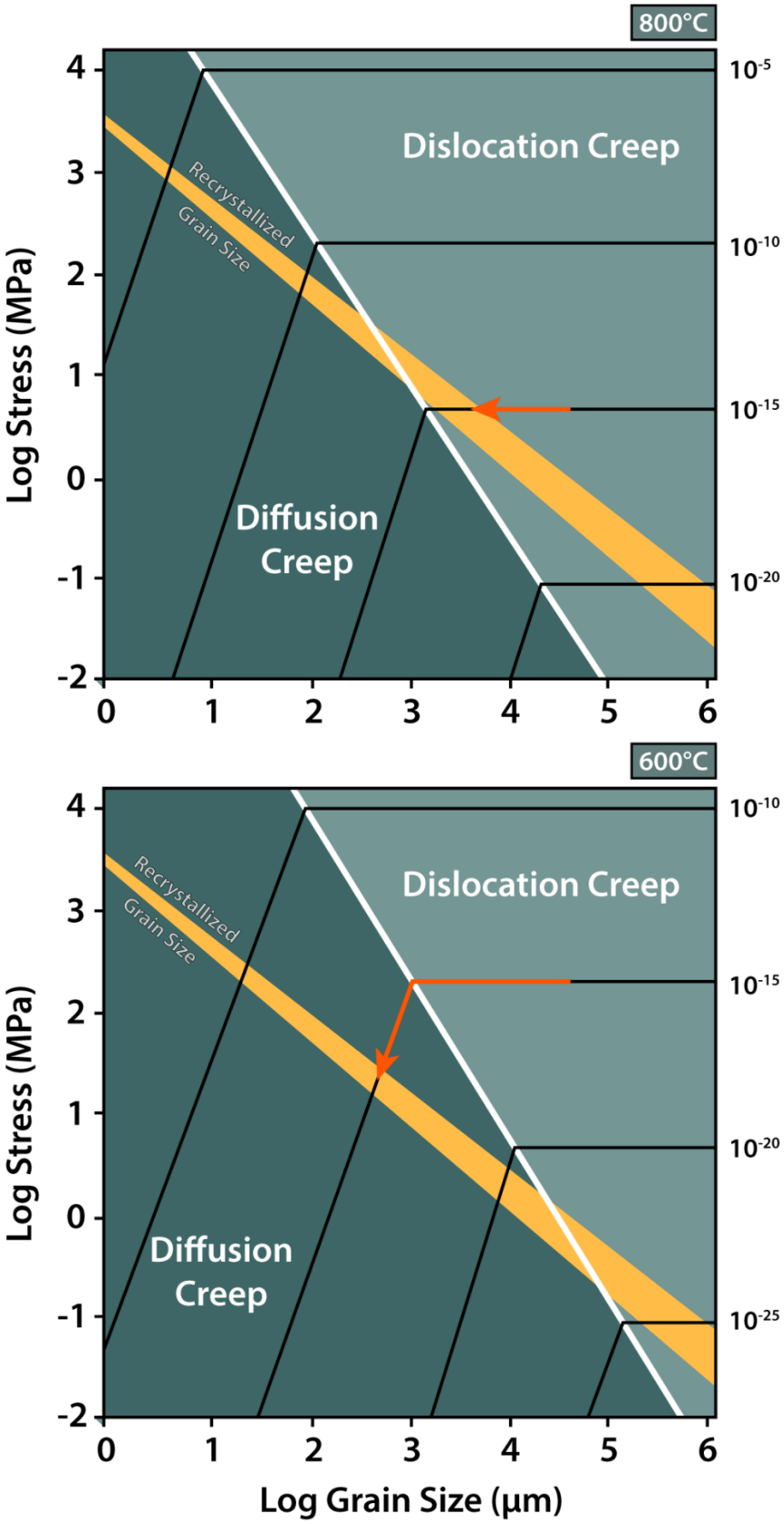

Fig 8: Stress/grain-size deformation mechanism maps for olivine at 600 °C and 800 °C (adapted from Rutter and Brodie, (1988)), using the parameters for dislocation creep of Karato et al., (1986) and the parameters for diffusion creep of Karato et al., (1986) and Rutter and Brodie, (1988). The grain size piezometer for olivine (yellow band) is taken from the study of Karato et al., (1986).

In relation to this, dynamic recrystallization is a significant process for grain size reduction to occur during plastic flow (Fig. 9) (e.g. Etheridge and Wilkie, 1979; Behrmann, 1985; De Bresser et al., 2001), as long as the deformation conditions in terms of grain size, temperature, pressure and differential stress are such that the rock deform in the GSI dislocation creep regime (e.g. Hirth and Tullis, 1992; Passchier and Trouw, 2005).

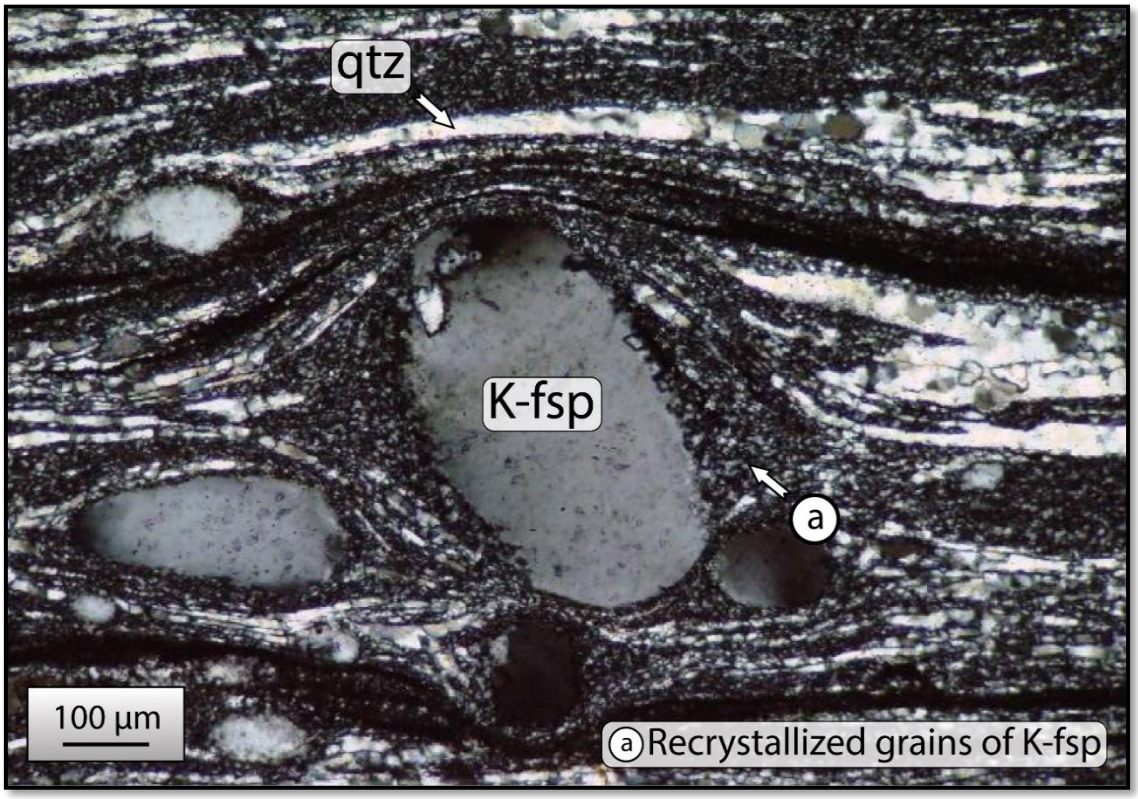

Fig 9: Mylonitized granite showing small recrystallized grains of K-feldspar in strain shadows of K-feldspar porphyroclast. Quartz shows minor recrystallization by bulging (adapted from Trouw et al., 2010). Mount west, Australia.

The heterogeneous nucleation of new grains of different composition is another common process invoked for grain size reduction (e.g. Kenkmann and Dresen, 2002; Kruse and Stünitz, 1999a; Précigout and Stünitz, 2016). This nucleation has the potential to affect the viscosity of the deforming material in two ways. First, the nucleation of new strain-free grains has the potential to lower the dislocation density of a material and therefore reduce the viscosity. Then, when the extent of grain size reduction is sufficiently important, the dominant deformation mechanism could change to a grain-size sensitive one, such as diffusion creep and GBS (e.g. Behrmann and Mainprice, 1987; Fliervoet et

al., 1997; Platt, 2015). When the displacement along grains is not fully accommodated by intra-grain deformation or due to the incompatibility in elastic deformation of adjacent grains (Benson et al., 2001; Meyersm and Ashworth, 1982), some loss of cohesion is expected to open cavities into which fluid-assisted precipitation of new phases may occur (e.g. Fusseis et al., 2009; Précigout and Stünitz, 2016; Précigout et al., 2017; 2019). Because of the varying nature of nucleated phases, some phase mixing arises and inhibits grain growth, The latter process is called Zener pinning: the presence of a given phase (A) inhibits the motion of the grain boundaries of the second phase (B), and reciprocally (Fig. 10) (e.g. Olgaard, 1990; Evans et al., 2001; Herwegh et al., 2011; Gilgannon et al., 2017). As a result, phase mixing contributes to weaken mineral aggregates (e.g. Evans et al., 2001).

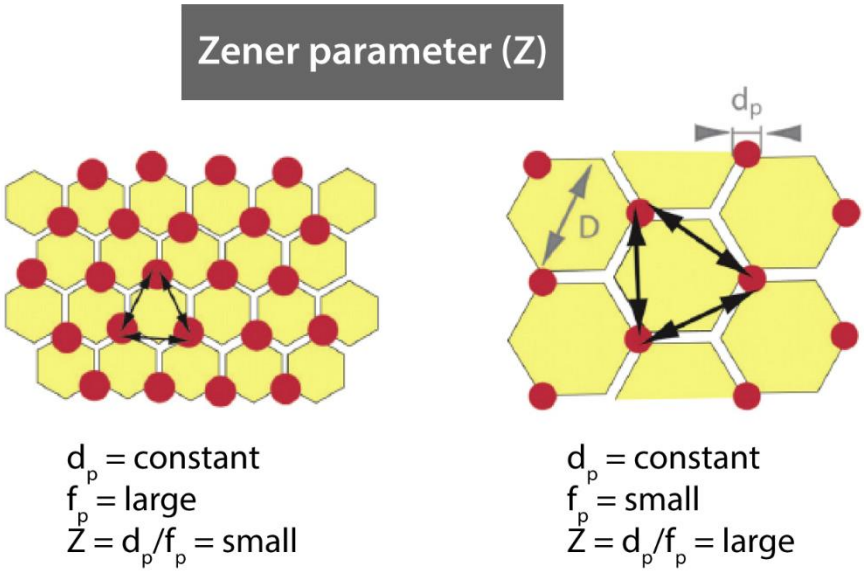

Fig 10: Effect of the Zener parameter (Z) (from Herwegh et al., 2011). d_p = size of the second phase; f_p = volume fraction of the second phase.

4.3 Formation of interconnected weak layers

In addition to the nature of phases, grain size and dominant deformation mechanisms, major determinants parameters for the material strength and strain localization in shear zones include the abundance of weak phases and their interconnection (e.g. Holyoke and Tullis, 2006). Tullis and Wenk, (1994) have shown that the increase in mica content, which is typically viewed as the weakest phase in granitoid rocks, causes decrease in the sample strength and anisotropy. Moreover, Montési (2013) proposed in a numerical study that the coalescence of weak

layers has a higher potential for strain localization and weakening in rocks compared to syn-tectonic reactions in themselves, although the reactions significantly contribute to this weakening as well.

Obviously, a higher proportion of weak phases reduces the spacing between them and thus increases the likelihood of these phases to be interconnected (e.g. Bons and Den Brok, 2000). In major contributions in 1990 and 1994, Handy provided a scheme for rocks that contained minerals of contrasting rheology, and emphasized that the rheology of a material is influenced by whether or not it contains a strong load-bearing framework (LBF), or interconnected weak layers (IWL). Numerous studies have followed and shown the importance of the proportion, spatial distribution of strong and weak phases and their variation in shape to induce significant strength drop of the material (e.g. Dell'Angelo and Tullis, 1996; Handy et al., 1999; Takeda and Griera, 2006; Gerbi, 2012; Montési, 2013; Gueydan et al., 2014).

Shear zones commonly expose two types of weak layers that can develop together: (1) monophase aggregates and layers of weak phases, such as quartz (e.g. Dell'Angelo and Tullis, 1996) and mica (Fig. 11a) (e.g. Berthé et al., 1979; Holyoke and Tullis, 2006), and (2) polyphase mixed zones and layers of reaction products (Fig. 11b) (e.g. Fliervoet et al., 1997; Keller et al., 2004). Once these weak layers have coalesced, strain strongly localized into them (Gerbi et al., 2016). The development of these layers is strongly dependent on the deformation mechanisms that prevail, because the spatial and temporal variation of geometry induces changes in grain size, degree of mixing and metamorphic reactions (e.g. Behrmann and Mainprice, 1987; Fitz Gerald and Stünitz, 1993; Wintsch et al., 1995; Kruse and Stünitz, 1999; Kenkmann and Dresen, 2002; Warren and Hirth, 2006; Svahnberg and Piazolo, 2010; Herwegh et al., 2011; Platt, 2015). In fact, the grain size reduction enhances the kinetics of metamorphic reactions due to a relative increase in surface area (Kenkman et al., 2002), and if the grain size is sufficiently reduced, the phases may deform more rapidly by GSS creep rather than GSI creep (Platt, 2015). As mentioned above, one important accommodation process in GSS creep is GBS (e.g. Langdon, 2006), and GBS is hypothesized to promote phase mixing by opening potential voids between the grains (e.g. Zhang et al., 1996), and therefore increase the proportion of weak phases (e.g. Menegon et al., 2015). Thus, by increasing the proportion of weak phases, this case of succession of mechanisms can reduce the space between them and increase the ability of these phases to connect.

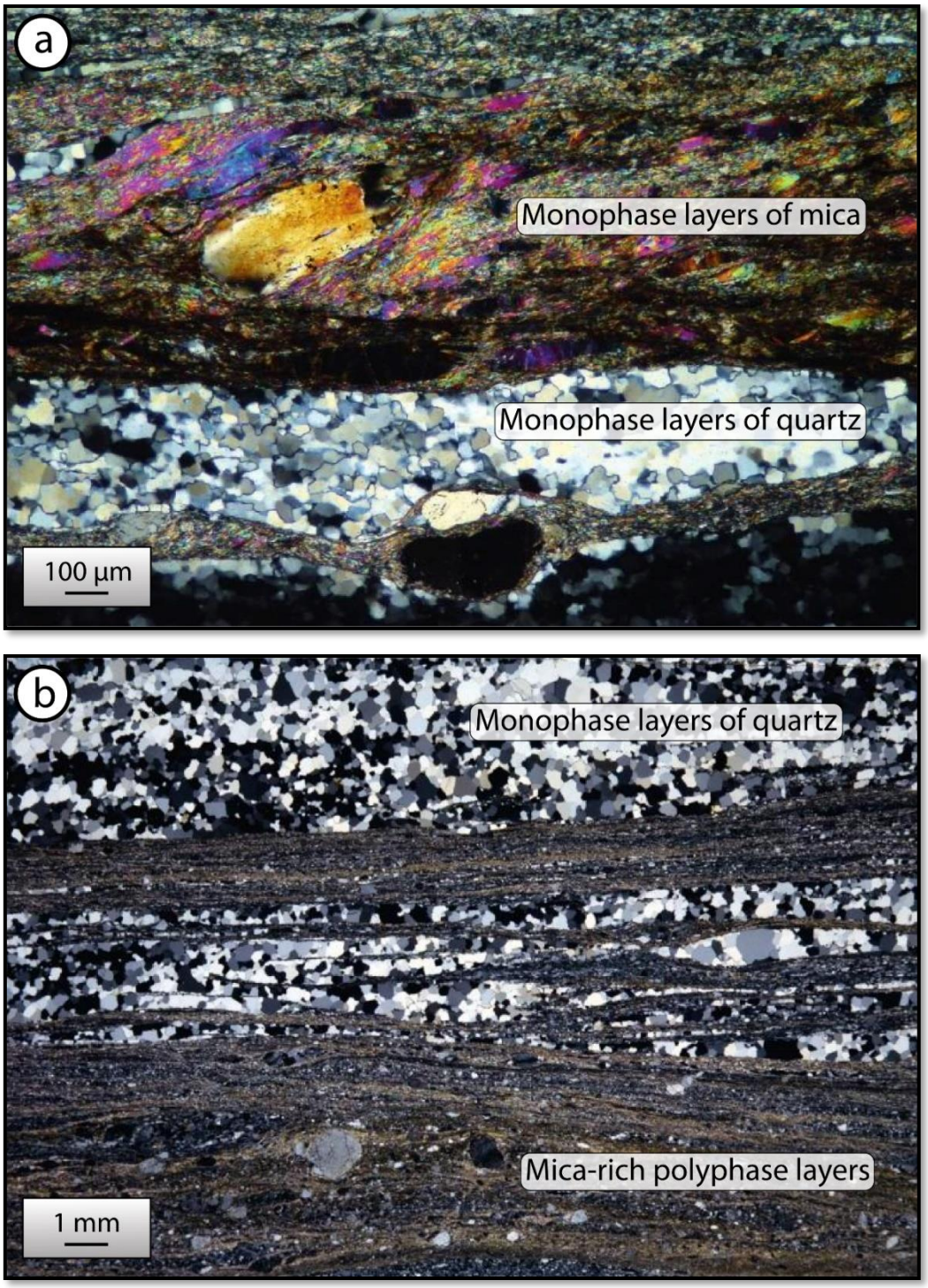

Fig. 11 (**a**) Mylonitized pegmatitic granite showing alternating layers of quartz and mica. (adapted from Trouw et al., 2010). Cadaquez, NE Spain. (**b**) Greenschist facies mylonite showing monophase layers of quartz and polyphase layers rich in mica, quartz and K-feldspar that occur in the same shear zone in alternating layers (adapted from Trouw et al., 2010). Southern Minas Geras State, SE Brazil.

5. Thesis outline

The present study aims at extending the current knowledge about the rheological behavior of shear zones. This goal is not a straightforward exercise because it requires to quantify fundamental parameters, such as stress, strain rate and grain size of the rocks involved based on field observations and deformation experiments. In addition, natural shear zones provide access only to the final stage of deformation and many early-stage features, relevant for deep crust rheology, have been obliterated by late-stage deformation. Major shear zones may have indeed recorded different conditions of pressure, temperature, strain rate, etc. over geological times. One way to tackle this issue is to perform deformation experiments, which have the ability to analyze the mechanical strength evolution of rocks according to the active processes responsible for the development of shear zones.

The challenge of performing deformation experiments on rock assemblages is to extrapolate the results obtained and compare them to natural systems. One of the key problems is how quickly the P-T conditions are reached during an experiment (~4–8 h), and how it promotes the metastability of the rock assembly brought to these conditions. In nature, these changes of P-T conditions occur at far lower rates, inducing progressive changes in mineral assemblages (e.g. Herwegh et al., 2011). This is an inevitable gap between nature and deformation experiments, but the similarity between the microstructures of their deformed samples is often taken as an argument that similar processes act mutually in nature and experiments.

In this study, we have combined field and experimental observations of processes associated with strain localization and weakening in mid- to lower-crustal shear zones. As a natural case, we chose to focus on granitoids from the French Armorican massif deformed by a major crustal-scale shear zone at mid-crustal conditions. In the meantime, we performed deformation experiments focusing on two-phase assemblages representative of the lower crust. Although **chapters III, IV** and **V** are written as manuscripts for publication, they have been modified to avoid repetition, particularly on the methodology of the experimental chapters. This thesis is thus organized as follows:

- The **chapter II** describes the methods of all different investigations, including a brief background overview of the strategy employed for the natural case study presented in **chapter III**. Then, the experimental framework including the

- apparatus, the starting material, the sample assembly and the experimental procedure are described. This part of the method is only relevant for the two chapters of experimental results that are presented in **chapters IV** and **V**. Finally, the analytical procedure is presented and concerns all chapters of results.

- In the **chapter III**, the natural case study of a granitoid mylonitized within a major crustal shear zone of South Brittany (Western France) is presented. This shear zone corresponds to the historical place of first recognition of S-C and S-C' fabrics (Berthé et al., 1979) and serves as a natural example of strain localization and weakening. This chapter was published as:

***Mansard, N.**, Raimbourg, H., Augier, R., Précigout, J., Le Breton, N. (2018). Large-scale strain localization induced by phase nucleation in mid-crustal granitoids of the south Armorican massif. **Tectonophysics**, 745, 46–65. doi: 10.1016/j.tecto.2018.07.022.*

- **Chapter IV** investigates the evolution of microstructures in two-phase plagioclase-pyroxene shear experiments, which provide important insights on weakening mechanisms and localization of deformation during shear zone development. This study is an ideal example of how deformation can facilitate metamorphic reactions, nucleation of new phases, formation of fine-grained phase mixtures, and how such an evolution in microstructures eventually results in strain localization and weakening of polyphase aggregates. This chapter was submitted as:

***Mansard, N.**, Stünitz, H., Raimbourg, H., Précigout, J. Strain localization and weakening induced by feedback of deformation and mineral reactions: experimentally deformed plagioclase-pyroxene assemblages. **Journal of Structural Geology**. Under review.*

- **Chapter V** explores the interplay between chemical reactions and deformation processes during deformation of two-phase assemblages. By studying the rheological behavior of two-phase assemblages deformed to varying amount of strain, we suggest that ductile strain localization is primarily dependent on the

- ability of minerals to react, and that even small initial differences in composition can lead to very large differences in mechanical strength. This chapter will be submitted as:

Mansard, N.**, Stünitz, H., Raimbourg, H., Précigout, J. Experimental evidence of weakening and strain localization induced by minor metastability of mafic rocks.* ***Journal of Geophysical Research*. In preparation.*

- **Chapter VI** ends this work by providing a general discussion, conclusions and opportunities for future work.

CHAPTER II

Methods

CONTENTS

1. Natural case study strategy

The natural case study presented in this thesis (**chapter III**) focuses on a granitoid that is affected by variable intensities of strain, giving rise to local mylonites and ultramylonites along the South Armorican Shear Zone (SASZ) of South Brittany, Western France. We have decided to work on this major crustal shear zone because it preserves a large-scale deformation gradient from low-strain (protolith and protomylonite) to high-strain domains (mylonite and ultramylonite). The SASZ is thus an ideal example for studying the progressive localization of deformation with increasing strain, including the development of meso-scale shear zones. The samples studied were collected by Romain Augier during a previous field campaign along a cross-section shown in **Fig. 1** (**chapter III**). This section is orthogonal to a strain gradient that ranges from undeformed or slightly deformed rocks to highly deformed ones, including ultramylonitic samples in the core of the SASZ (Augier et al., 2011). Observations and analyzes have been performed on thin sections parallel to the stretching lineation and perpendicular to the foliation (XZ plane). The analytical instrumentation and techniques required to analyze these thin sections are presented in Part 3 (analytical procedure) of this chapter.

2. Experimental strategy

2.1 Solid-medium Griggs-type apparatus

All experiments were carried out using several solid-medium Griggs-type deformation apparatuses, including an "old-fashion" Tullis-modified one at the University of Tromsø (Norway) and a new generation one at the University of Orléans (France). A detailed description of these deformation apparatuses is presented in Pec et al., 2012, Richter's thesis (2017) and Marti's thesis (2017) (apparatus at the University of Tromsø), and Précigout et al., 2018 (apparatus at the University of Orléans). For the sake of simplicity, we will mainly focus in the newly designed Griggs-type apparatus, which has been very recently implemented in the rock deformation laboratory at the ISTO (Orléans). The reader is referred to the previous references to inquire about additional information regarding one or the other apparatus. Also, the video that describes the procedure to perform deformation experiments in the newly designed solid-medium Griggs-type apparatus can be found at https://www.jove.com/video/56841/.

2.1.1 Deformation apparatus

The Griggs-type apparatus, which has been formerly designed by David T. Griggs in the 60's, is an adaptation of the solid confining medium piston-cylinder apparatus. This apparatus is an appropriate technique to study deformation processes in an environment of high pressure (<4 GPa) and high temperature (≤ 1200 °C). The Griggs-type apparatus consists of a metal frame characterized by three horizontal platens connected by vertical columns (Précigout et al., 2018). The middle platen holds the main hydraulic cylinder (confining pressure ram) while the upper platen supports the deformation ram (Fig. 1). These ram are connected to individual pistons. The confining pressure ram is connected to a confining pressure piston (σ_3-piston), while the deformation ram is connected to a deformation piston (σ_1-piston) (Fig. 2). A pressure vessel containing the sample assembly is placed on top of a base plate at the lowermost platen. The above-mentioned WC-removable σ_1 piston and σ_3 piston, as well as an end-load piston (that homogenizes the pre-stress in the pressure vessel), are placed above the pressure vessel for transmitting forces to the sample assembly (Fig. 2) (Précigout et al., 2018).

The confining pressure is generated by moving down the confining pressure ram which presses the σ_3-piston into the pressure vessel chamber (Fig. 2). The confining pressure is measured by a pressure transducer. The temperature inside the pressure vessel is increased by Joule effect, injected from below the assembly through a resistive graphite furnace and controlled by S-type thermocouples (TC) (Précigout et al., 2018). The force is generated by the deformation ram which pushes the σ_1-piston through the σ_3-piston onto the sample assembly. This force is measured by the relative displacement of the σ_1-piston with respect to the middle plate of the apparatus using a linear-variable-displacement-transducer (σ_1-LVDT), while the stress is measured with a force transducer, commonly referred to as a load cell (Fig. 1, 2). During an experiment, the pressure vessel is water-cooled and the confining pressure ram is also cooled by silicon oil flow in order to reduce the confining pressure variations due to ambient temperature variations.

Fig 1: Overview of the deformation apparatus available at the Institut des Sciences de la Terre d'Orléans (ISTO, France).

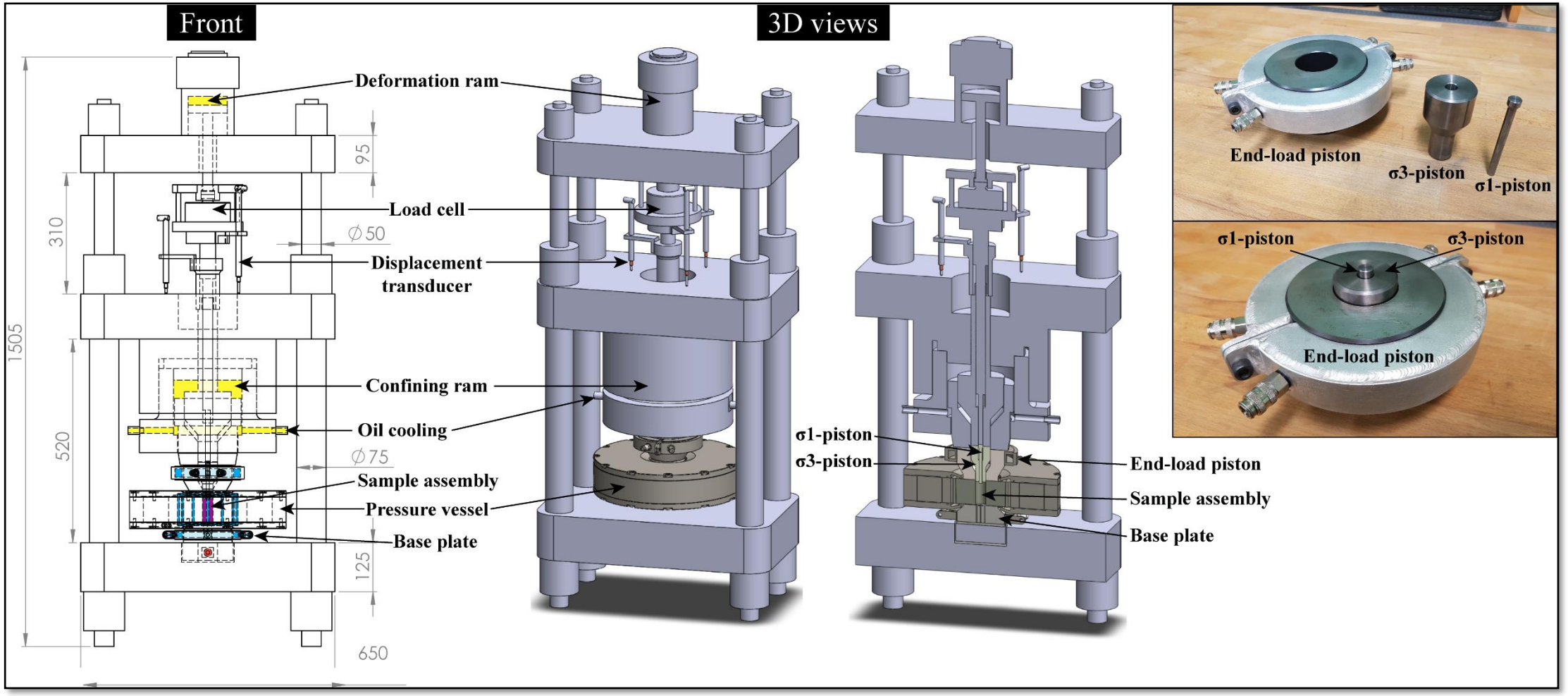

Fig 2: Schematic drawings of the new generation Griggs-type apparatus and photographs of the WC-removable pistons. Adapted from Précigout et al., 2018.

2.2 Starting material

Experiments were performed on two-phase plagioclase-pyroxene assemblages, plagioclase-amphibole assemblages and for comparison, pure plagioclase, pure pyroxene and pure amphibole material. Experiments were conducted on mineral powders separated from natural materials. The starting material was prepared from several sources: (1) Gem-quality labradorite from Sonora, Mexico (An60-Ab37-Or3), (2) Orthopyroxene from Damaping peridote, China (Wo1-En89-Fs10—here referred to as Mg-Opx), (3) Labradorite (An55-Ab44-Or1) and orthopyroxene (Wo2-En62-Fs36—here referred to as Fe-Opx) from Hidaka granulite, Japan, and (4) Amphibole from Massif Central amphibolite (magnesiohornblende), France. (Fig. 3). The initial mineral compositions are presented in Table. 1. The peridotite material was kindly provided by Mark Zimmerman (University of Minnesota), the amphibolite by Laurent Arbaret (University of Orléans), the gem-quality Sonora labradorite by Holger Stünitz (University of Tromsø and Orléans), and the granulite by Hugues Raimbourg (University of Orléans). The gem-quality Sonora labradorite derived from basaltic deposits in Mexico and was used in previous studies on simple shear deformation experiments (e.g. Stünitz and Tullis, 2001; Marti et al., 2017; 2018). The Damaping Mg-Opx are derived from a peridotite xenolith (Cranberry Lake, United States) and was also used in the recent studies of Sina Marti (Marti et al., 2017; 2018). The Hidaka material derived from a granulite-facies shear zone in the Hidaka Metamorphic Belt (Japan), the microstructures of which have described by Raimbourg et al., (2008).

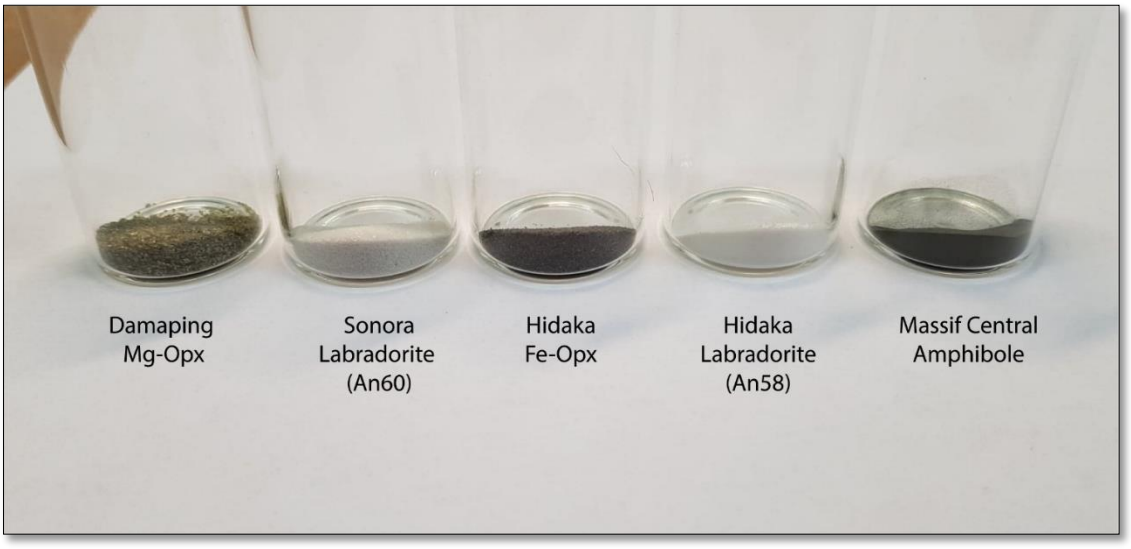

Fig 3: Picture of the different starting materials used to carry out the experiments.

	***Sonoran* Plag**		***Damaping* Mg-Opx**	
	Wt. % oxides	Ions per 8 O	Wt. % oxides	Ions per 6 O
SiO_2	53,37	2,423	56,31	1,929
Al_2O_3	29,41	1,574	3,80	0,153
CaO	11,88	0,578	0,45	0,017
Na_2O	3,96	0,349	0,07	0,005
K_2O	0,46	0,027	0,02	0,001
MgO	0,09	0,006	33,42	1,707
TiO_2	0,08	0,03	0,07	0,002
FeO	0,38	0,014	6,31	0,181
MnO	0,05	0,002	0,18	0,005
Total	99,68	4,975	100,63	4,000
	An60		**Wo**1	
	Ab37		**En**89	
	Or3		**Fs**10	

	***Hidaka* Plag**		***Hidaka* Fe-Opx**	
	Wt. % oxides	Ions per 8 O	Wt. % oxides	Ions per 6 O
SiO_2	54,71	2,448	52,86	1,952
Al_2O_3	29,28	1,544	1,00	0,044
CaO	11,42	0,548	1,23	0,049
Na_2O	4,94	0,429	0,06	0,004
K_2O	0,22	0,013	0,02	0,001
MgO	0,01	0,001	22,41	1,234
TiO_2	0,00	0,000	0,21	0,006
FeO	0,39	0,015	22,55	0,696
MnO	0,09	0,003	0,46	0,014
Total	100,06	5,000	100,80	4,000
	An55		**Wo**2	
	Ab44		**En**62	
	Or1		**Fs**36	

	***Massif Central* Amph**	
	Wt. % oxides	Ions per 23 O
SiO_2	43,99	6,646
Al_2O_3	9,91	1,765
CaO	11,12	1,800
Na_2O	1,67	0,489
K_2O	0,47	0,091
MgO	10,87	2,448
TiO_2	1,21	0,138
FeO	17,79	2,248
MnO	0,38	0,000
Total	97,41	15,625
	Magnesiohornblende	

Tab 1: Chemical composition of the starting materials.

The rocks were crushed using a hammer and sieved to sizes grains diameter between 100 to 200 µm. Minerals were pre-separated with a Frantz magnetic separator and hand-picked. They were subsequently crushed into an alumina mortar, and then sorted by settling in a distilled water column to extract a powder ranging from 10 to 20 µm grain size. (Fig. 4). Based on the density of the starting material and density of the fluid, among others, one can indeed easily calculate with the Navier-Stokes equation the travel time of the particles of a certain size over a defined distance. This makes it possible to isolate desired grain size ranges. The powders were then mixed at a ratio of 50:50% (by volume) as a slurry in acetone using an ultrasonic stirrer to avoid density/grain size separation (De Ronde et al., 2004, 2005). When the acetone has completely evaporated, the slurry was dried in an oven at ~110 °C.

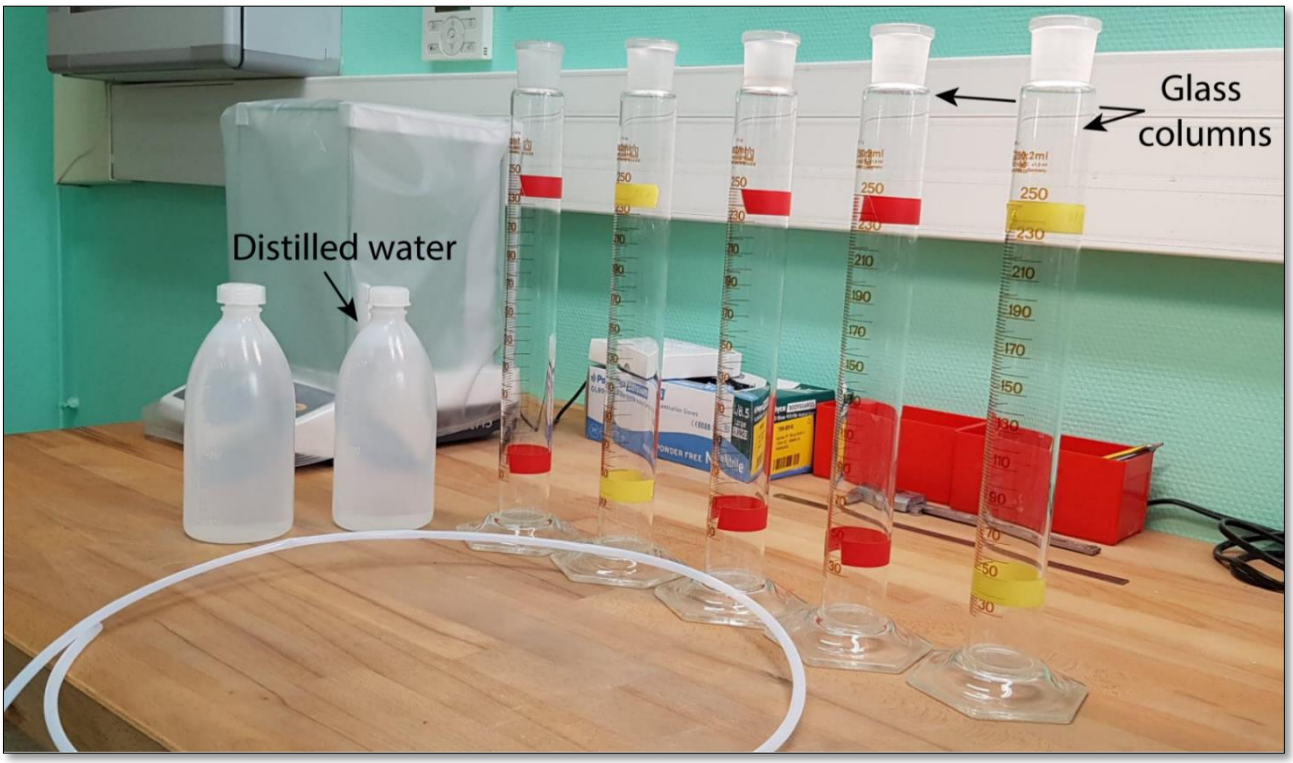

Fig 4: Picture of the distilled water columns used to extract mineral powders with a grain size ranging from 10 to 20 µm.

The mixed powder was placed between 45° pre-cut alumina forcing blocks (Fig. 5). An amount of ~0.12 g powder for 6.33 mm diameter samples (at Tromsø University) and 0.25 g for 8 mm diameter samples (at Orléans University) were used with 0.1 wt% H_2O added, so that we end up with a shear zone of ~1 mm thick. A nickel foil of 0.025 mm

thickness was wrapped around the pistons and all inserted into a weld-sealed platinum jacket (Fig. 5). During welding using a Lampert apparatus (PUCK), the jacket is held in a brass piece to minimize heating.

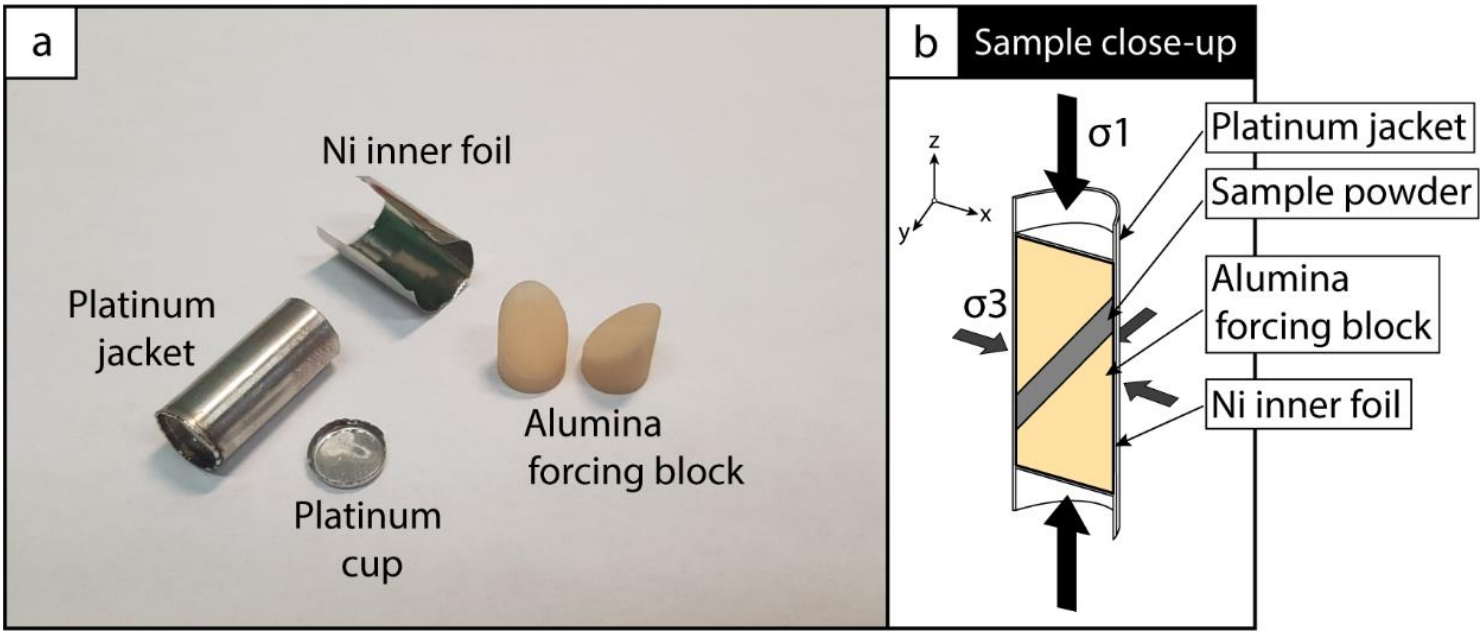

Fig 5: (**a**) Pieces of the sample assembly. (**b**) Sample geometry in a 3D view (modified after Tarantola et al., 2010, Pec et al., 2012 and Richter's thesis, 2017).

2.3 Sample assembly

The jacketed sample is placed in between two alumina pistons (Fig. 6a). NaCl was used as solid confining medium and prepared from sodium chloride (NaCl). These salt pieces surrounded both, the Pt jacket and two alumina pistons (Fig. 6b-c). This assembly was then placed inside a graphite furnace, itself surrounded by two outer salt pieces. Holes were drilled in the graphite furnace and salt pieces in order to place in contact with the sample two S-type (Pt/Pt-Rh) thermocouples. As the success of an experiment depends on the quality of the thermocouple used, we decided to use two thermocouples, although this makes more complex the sample assembly. The two copper discs placed on top and bottom of the furnace permit to connect the furnace to the outer electric circuit (Fig. 6b). Below the bottom copper disc, a tungsten carbide plug is surrounded by a piece of pyrophyllite drilled and filled by a crushable alumina to hold the thermocouple in place. Except for the tungsten carbide plug, each of the pieces mentioned above must be renewed (Richter's thesis, 2017).

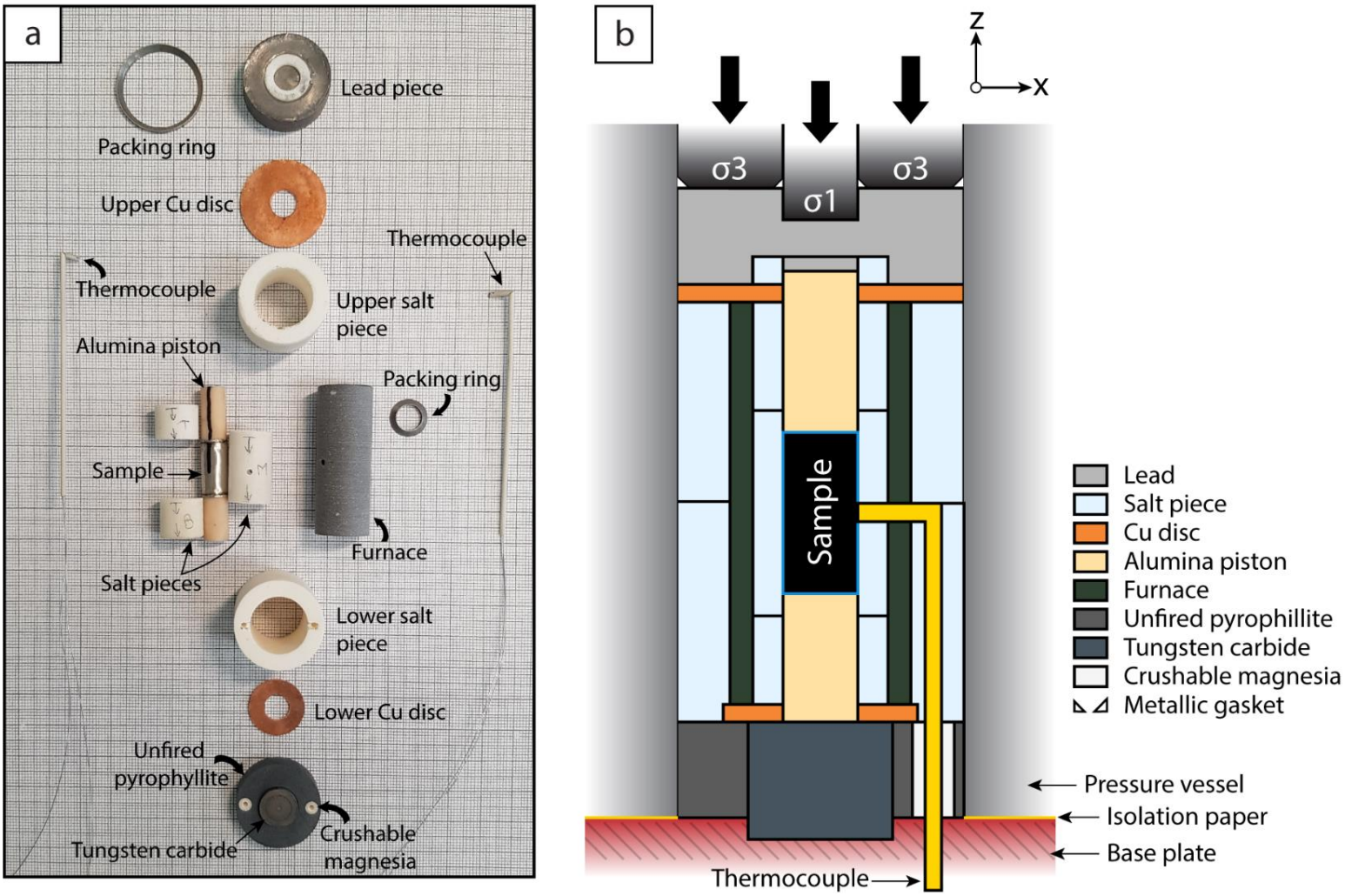

Fig 6: Sample assembly (**a**) Individual pieces of the sample assembly (Based on Richter's thesis 2017). (**b**) Schematic cross-section of the sample assembly inside the pressure vessel (modified after Tarantola et al., 2010, Pec et al., 2012 and Marti et al., 2018).

2.4 Experimental procedure

2.4.1 Charging the sample assembly

After the pieces are fitted together (Fig. 7a), the sample assembly is wrapped with Teflon (except for the top copper disc and packing rings), before to be placed on the center of the base plate in an arbor press (Fig. 7b). Before to carefully lower the pressure vessel onto the base plate, a foil of Mylar is placed around the sample assembly to isolate the base plate from the pressure vessel, so that any short circuit is prevented from occurring during the experiment (Fig. 7b). The sample assembly is finally covered by the top copper disc (Fig. 7c), lead piece (Fig. 7d) and σ_3 packing ring (Fig. 7e). After insulating the thermocouple wires from any metal pieces using sliding plastic tubes, the end-load piston,

σ_3 WC piston, and σ_1 WC piston are placed on top of the lead piece. The complete assembly can finally be placed onto the bottom platen of the Griggs apparatus below the

hydraulic ram. The thermocouples are plugged and the water tubes are connected to cooled down the system.

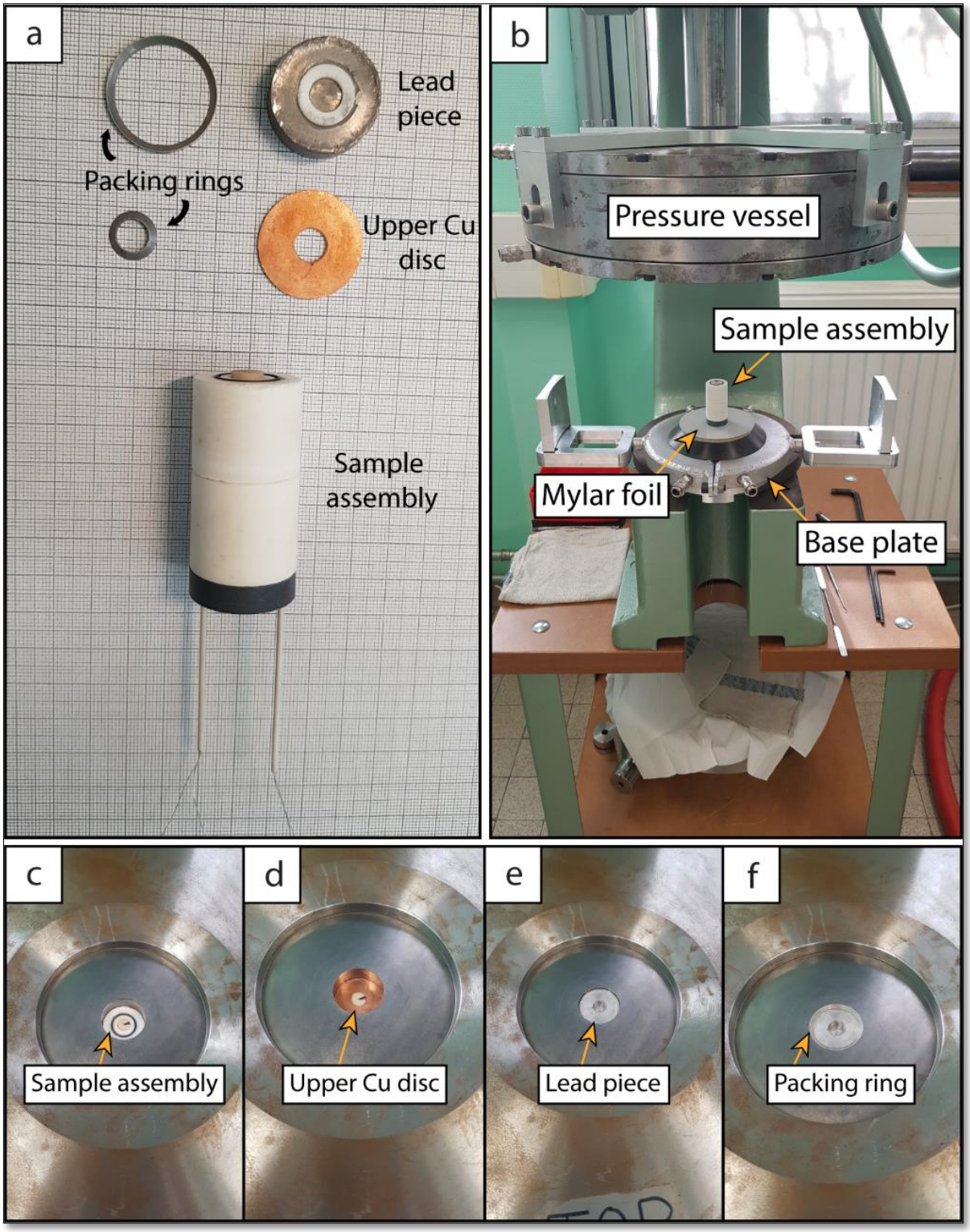

Fig 7: (**a**) Individual pieces assembled together by hand, except for the lead piece, upper Cu disc and packing rings. (**b**) Sample assembly inserted at the center of the base plate and a foil of Mylar is added around the assembly. (**c**) Once the sample is fitted into the borehole of the pressure vessel, we added the upper Cu disc (**d**), lead piece (**e**) and σ3 packing ring (**f**) on top of the sample assembly (Précigout et al., 2018).

2.4.2 Performing the experiment

Samples were deformed at constant shear strain rate of 2×10^{-5} s^{-1} to varying amounts of shear strain (Fig. 8). Pressures and temperatures were increased alternatingly over several hours to achieve the target values of 800, 850, and 900 °C and confining pressures of 1.0 GPa (Précigout et al., 2018). The temperature increased at a rate of 0.3 °C/s. The last increment of heating was performed at the desired confining pressure. The whole pressurization procedure was accomplished in 5–8 hours. At the desired P-T conditions, a period of hydrostatic hot-pressing was applied. The deformation part of the experiment was started by advancing the deformation piston first through the lead piece ("run-in" section) and then touching the top alumina piston (hit point), indicating the starting point of sample deformation (Précigout et al., 2018).

The displacement of the deformation piston within the lead piece is characterized by a slow increase of differential stress (Précigout et al., 2018), which has a different duration depending on the experiment. The run-in period is indeed dependent on the amount of lead material between the top alumina piston and σ_1 piston. We thus separated the experiments based on the duration of the "run-in" curve, those shorter than 65 hours and the other ones longer than 65h. Following this period, samples were deformed to bulk shear strains of up to $\gamma = 8$ (high shear strain experiments). Several experiments were also carried out without deformation (hot-pressing experiments) or with deformation only up to the peak stress at $\gamma \sim 1$ (peak stress experiments) in order to study the early stages of deformation (Table. 2).

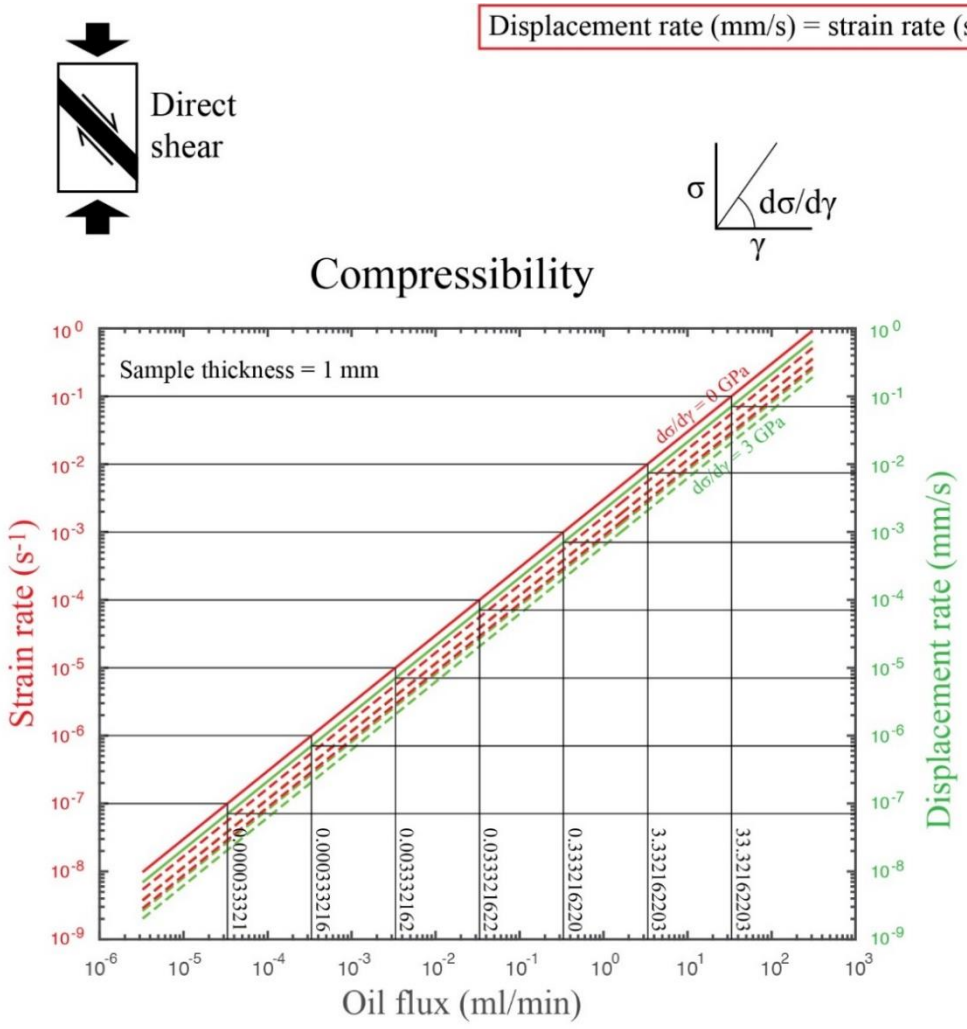

Displacement rate (mm/s)	Oil flux (ml/min)
$7.07*10^{-10}$	**0.000000333216220**
$1.41*10^{-09}$	0.000000666432441
$2.12*10^{-09}$	0.000000999648661
$2.83*10^{-09}$	0.000001332864881
$3.54*10^{-09}$	0.000001666081102
$4.24*10^{-09}$	0.000001999297322
$4.95*10^{-09}$	0.000002332513543
$5.66*10^{-09}$	0.000002665729763
$6.36*10^{-09}$	0.000002998945983
$7.07*10^{-09}$	**0.000003332162204**
$1.41*10^{-08}$	0.000006664324407
$2.12*10^{-08}$	0.000009996486611
$2.83*10^{-08}$	0.000013328648814
$3.54*10^{-08}$	0.000016660811018
$4.24*10^{-08}$	0.000019992973222
$4.95*10^{-08}$	0.000023325135425
$5.66*10^{-08}$	0.000026657297629
$6.36*10^{-08}$	0.000029989459833
$7.07*10^{-08}$	**0.000033321622036**
$1.41*10^{-07}$	0.000066643244072
$2.12*10^{-07}$	0.000099964866109
$2.83*10^{-07}$	0.000133286488145
$3.54*10^{-07}$	0.000166608110181
$4.24*10^{-07}$	0.000199929732217
$4.95*10^{-07}$	0.000233251354253
$5.66*10^{-07}$	0.000266572976290
$6.36*10^{-07}$	0.000299894598326
$7.07*10^{-07}$	**0.000333216220362**
$1.41*10^{-06}$	0.000666432440724
$2.12*10^{-06}$	0.000999648661086
$2.83*10^{-06}$	0.001332864881448
$3.54*10^{-06}$	0.001666081101809
$4.24*10^{-06}$	0.001999297322171
$4.95*10^{-06}$	0.002332513542533
$5.66*10^{-06}$	0.002665729762895
$6.36*10^{-06}$	0.002998945983257
$7.07*10^{-06}$	**0.003332162203619**
$1.41*10^{-05}$	0.006664324407238
$2.12*10^{-05}$	0.009996486610856
$2.83*10^{-05}$	0.013328648814475
$3.54*10^{-05}$	0.016660811018094
$4.24*10^{-05}$	0.019992973221713
$4.95*10^{-05}$	0.023325135425331
$5.66*10^{-05}$	0.026657297628950
$6.36*10^{-05}$	0.029989459832569
$7.07*10^{-05}$	**0.033321622036188**
$1.41*10^{-04}$	0.066643244072375
$2.12*10^{-04}$	0.099964866108563
$2.83*10^{-04}$	0.133286488144751
$3.54*10^{-04}$	0.166608110180939
$4.24*10^{-04}$	0.199929732217126
$4.95*10^{-04}$	0.233251354253314
$5.66*10^{-04}$	0.266572976289502
$6.36*10^{-04}$	0.299894598325690
$7.07*10^{-04}$	**0.333216220361877**
$1.41*10^{-03}$	0.666432440723755
$2.12*10^{-03}$	0.999648661085632
$2.83*10^{-03}$	1.332864881447510
$3.54*10^{-03}$	1.666081101809387
$4.24*10^{-03}$	1.999297322171265
$4.95*10^{-03}$	2.332513542533142
$5.66*10^{-03}$	2.665729762895019
$6.36*10^{-03}$	2.998945983256897
$7.07*10^{-03}$	**3.332162203618775**
$1.41*10^{-02}$	6.664324407237549
$2.12*10^{-02}$	9.996486610856325
$2.83*10^{-02}$	13.328648814475098
$3.54*10^{-02}$	16.660811018093874
$4.24*10^{-02}$	19.992973221712649
$4.95*10^{-02}$	23.325135425331425
$5.66*10^{-02}$	26.657297628950197
$6.36*10^{-02}$	29.989459832568969
$7.07*10^{-02}$	**33.321622036187748**

Fig 8: Graphs showing the values of displacement rate (mm/s) and strain rate (s^{-1}) as a function of oil flux (ml/min) injected in the deformation pump, for a sample thickness of 1 and 0.5 mm in shear experiments.

Exp. Nr	Material	Type	T	P	H_2O	τ_{peak}	τ_{flow}	τ_{end}	γ	th_0	th_f	notes
			[°C]	[GPa]	µL	[MPa]	[MPa]	[MPa]		[mm]	[mm]	
535NM	Pure Plag	D	900	1	0,12	620	524	524	2,9	0,75	0,57	
563NM	Pure Plag	D	850	1	0,12	255	200	200	3,6	0,75	0,51	Slip at SPI*
OR17NM	Pure Plag	D	800	1	0,25	295	-	390	4,6	1,1	0,76	Slip at SPI*
OR53NM	Pure Plag	D	800	1	0,25	904	746	746	4,7	1,1	1,0	
537NM	Pure Opx	PS	900	1	0,12	1600	-	1546	0,9	0,75	0,69	
534NM	Pure Opx	F	900	1	0,12	-	-	-	-	-	-	Jacket leak
561NM	Pure Opx	D	900	1	0,12	1050	590	583	2,0	0,75	0,62	High porosity
OR20NM	Pure Opx	D	800	1	0,25	990	550	545	5,2	1,1	0,67	Min. separation*
OR46NM	Pure Opx	D^x	900	1	0,25	817	-	592	2,5	1,1	0,63	High porosity
539NM	Mg-Opx + Plag	D	900	1	0,12	590	-	1240	4,2	0,75	0,72	Slip at SPI*
554NM	Mg-Opx + Plag	D	900	1	0,12	300	291	291	2,4	0,75	0,61	Slip at SPI*
557NM	Mg-Opx + Plag	PS^x	850	1	0,12	1067	-	577	0,4	0,75	0,59	
559NM	Mg-Opx + Plag	PS^x	800	1	0,12	1111	-	350	0,5	0,75	0,67	
OR24NM	Mg-Opx + Plag	D	800	1	0,25	1280	-	866	3,1	1,1	0,87	
OR34NM	Mg-Opx + Plag	D	900	1	0,25	781	114	126	7,6	1,1	0,68	
OR38NM	Mg-Opx + Plag	D	850	1	0,25	1037	339	339	8,0	1,1	0,63	
OR40NM	Mg-Opx + Plag	PS	900	1	0,25	379	-	-	1,2	1,1	1,0	
OR41NM	Mg-Opx + Plag	D	900	1	0,25	1094	542	542	7,0	1,1	0,72	
OR43NM	Mg-Opx + Plag	HP	900	1	0,25	-	-	-	-	1,1	1,1	
OR47NM	Mg-Opx + Plag	PS	900	1	0,25	989	-	989	0,6	1,1	0,91	
OR49NM	Mg-Opx + Plag	D^x	900	1	0,25	1111	800	800	6,0	1,1	0,73	
OR51NM	Mg-Opx + Plag	PS	900	1	0,25	901	-	901	0,8	1,1	1	
OR55NM	Mg-Opx + Plag	HP	900	1	0,25	-	-	-	-	1,1	1,1	
OR58NM	Mg-Opx + Plag	PS	900	1	0,25	1190	-	1190	0,7	1,1	0,96	
532NM	Fe-Opx + Plag	D	900	1	0,12	-	-	405	5,0	0,75	0,54	
533NM	Fe-Opx + Plag	D	850	1	0,12	645	683	683	3,8	0,75	0,47	
536NM	Fe-Opx + Plag	F	800	1	0,12	-	-	-	-	-	-	Jacket leak
538NM	Fe-Opx + Plag	D^x	800	1	0,12	1080	-	563	0,9	0,75	0,73	
OR27NM	Fe-Opx + Plag	F	850	2,2	0,25	-	-	-	-	-	-	σ_1 piston*
OR44NM	Fe-Opx + Plag	HP	850	1	0,12	-	-	-	-	0,45	0,37	
OR61NM	Fe-Opx + Plag	PS	850	1	0,25	885	-	897	1,7	1,1	0,73	
OR13NM	Amph	F	900	1	0,20	-	-	-	-	-	-	Sensor break
OR14NM	Amph	F	900	1	0,20	-	-	-	-	-	-	Lead leak
OR15NM	Amph	D	900	1	0,20	348	147	147	3,7	0,9	0,62	
OR18NM	Amph	D	800	1	0,20	803	370	370	5,4	0,9	0,68	
OR16NM	Amph + Plag	F	800	1	0,20	-	-	-	-	-	-	Power failure
OR22NM	Amph + Plag	F	800	1	0,20	-	-	-	-	-	-	LVDT pb*
OR23NM	Amph + Plag	D	800	1	0,20	563	435	483	5,8	0,9	0,60	

Slip at SPI*: *unexpected slip at one of the sample/forcing block interfaces.*

Min. separation*: *problem in mineral separation. Too many unexpected grains remaining in the mineral powder.*

σ_1 piston*: *the σ_1 piston was too weak at 2,2 GPa.*

LVDT pb*: *Inadequate calibration of the linear-variable-displacement-transducer (LVDT).*

Tab 2: Summary of experimental conditions. Type: HP—hot-pressing, PS: peak stress, D: deformed samples to varying amounts of shear strain. A cross marks is added to the type of deformation when the forcing blocks started to slip at the sample interface above the Goetze criterion; τpeak: differential stress at peak, τflow: steady-state differential stress, τend: differential stress at end of experiment, γ: shear strain, th0: thickness initial of the shear zone, thf: final shear zone thickness. The th0 is approximately known, as it is initially determined from hot-pressing samples without deformation and then it is assumed that this thickness is similar for the other samples before deformation insofar as the quantity of powder is identical.

When deformation was stopped, samples were quenched to 200 °C within minutes (temperature drop of ~150 to 300 °C/min) to preserve the deformation microstructures. Subsequently, the force and confining pressure were decreased simultaneously to room pressure and temperature conditions (Marti's thesis, 2017). During initial stages of the decompression, the differential stress is kept above the confining pressure (~ 100 to 200 MPa) to prevent the formation of unloading cracks. When pressure and temperature have slowly decreased to room pressure and cooling water conditions, the cooling system and furnace can be stopped before to remove the sample assembly from the pressure vessel. Finally, the sample assembly is pressed out of the pressure vessel, carefully dismantled and the position of the thermocouples with respect to the orientation of the sample is checked (Fig. 9). The samples were then cut along the piston axis in the plane of maximum displacement and vacuum-impregnated with low viscosity epoxy to prepare thin sections for microstructural analysis.

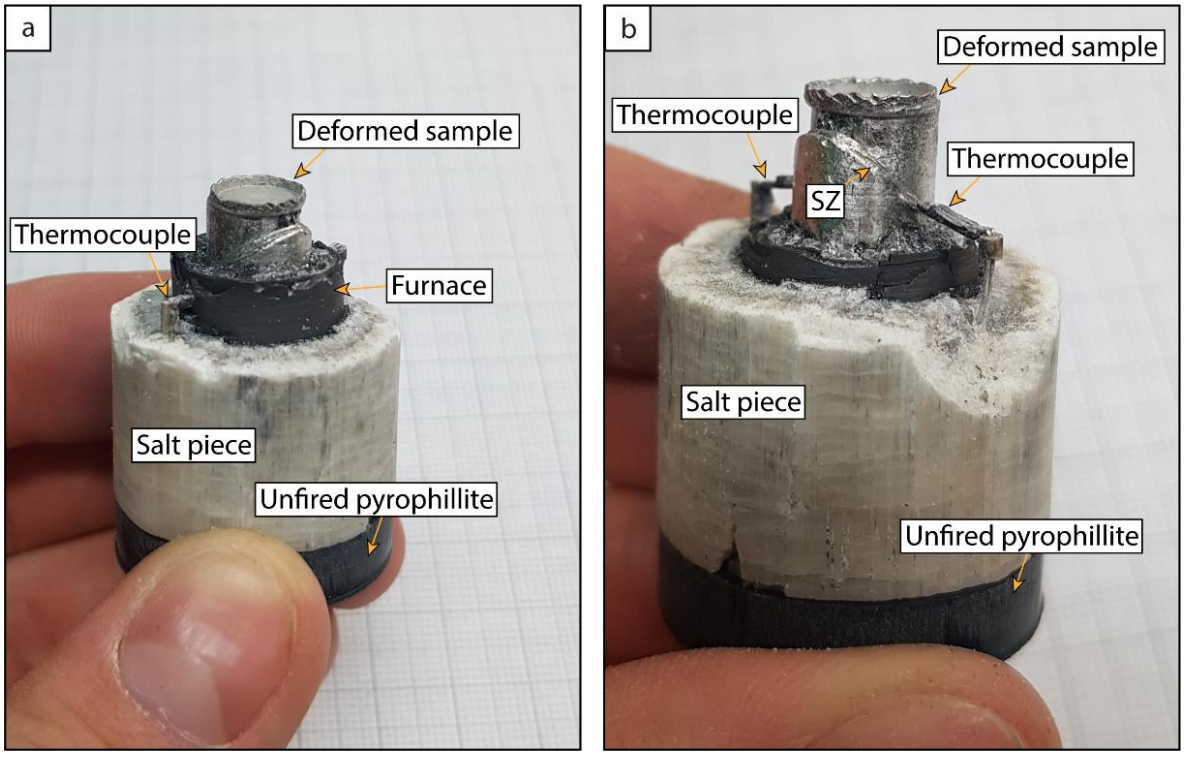

Fig 9: (**a-b**) Sample assembly extracted after the experiment containing a sample deformed in simple shear. SZ – shear zone.

2.4.3 Mechanical data processing

Experimental data were digitally recorded using Catman® Easy and processed using a MATLAB-based program inspired from the "rig" program of Matej Pec (Pec et al., 2016). The source code for the rig program is given in appendix A and can be found at https://sites.google.com/site/jacquesprecigout/telechargements-downloads.

At the onset of deformation, the load curve shows a steep-to-gentle increase of differential stress ("run-in" slope), which is due to friction in the load and sample column (Précigout et al., 2018). Then, the load curve shows an abrupt increase in differential stress ("elastic" slope) when the contact between the σ_1 piston and the top alumina piston is reached (hit point). The hit point was defined by curve fitting, through the intersection of the tangent to the "run-in" curve and the "elastic curve" (Fig. 10). The stress-strain curves of the deformed samples were then generated by applying a set of corrections on the raw data. This includes corrections on the displacement and force curves considering the elastic distortion of the apparatus (rig stiffness) (Fig. 11a). The rig stiffness, which is pressure dependent, is 13.24 µm/kN at 5 kb and 15.17 µm/kN at 10 kb. Then, the sample compaction was corrected to the shear displacement over the whole period of sample deformation (Fig. 11b) and the sample surface change is corrected with the displacement (area correction) (Fig. 11c). The following equation is used for shear experiments:

$$Shear\ surface = 2.R^2.cos^{-1}\left(\frac{d}{2 \times R}\right) - d.\sqrt{R^2} - (\frac{d}{2})^2$$

Finally, the force is corrected considering the friction of the sample assembly (Fig. 2.11d). The following equation is used to apply the correction (a value of 1.3 is applied, according to Matej Pec and Renée Heilbronner):

$$Force\ (corrected) = Force\ (uncorrected) - Displacement\ from\ hit\ point\ \times Friction$$

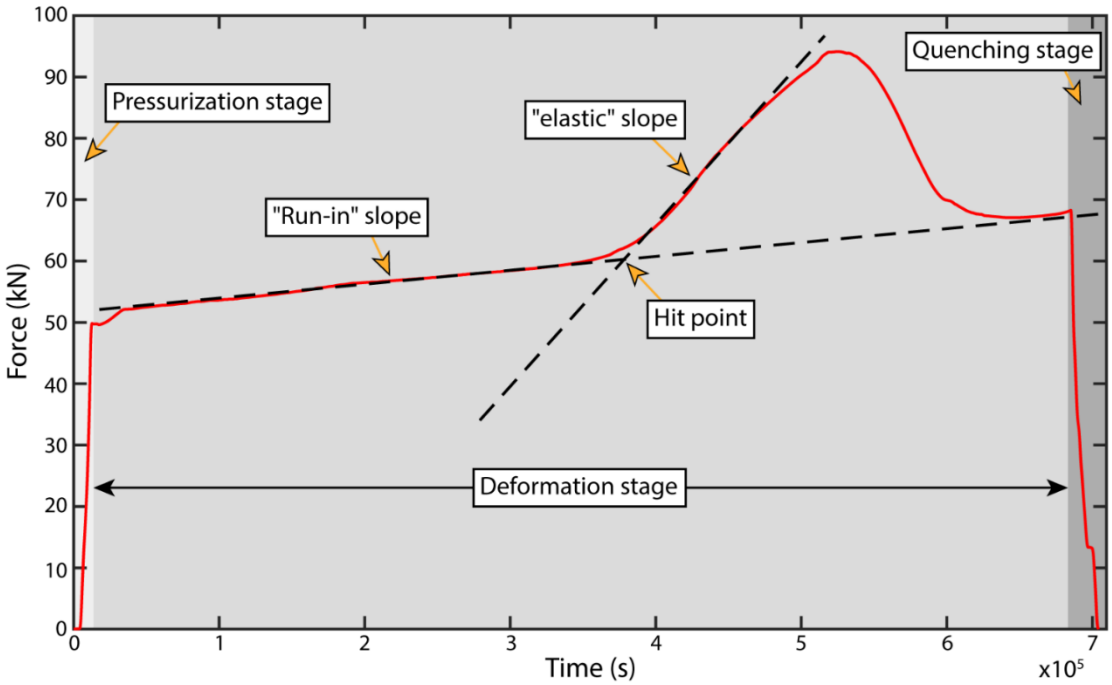

Fig 10: Example of a force-time curve during the successive steps of a deformation experiment and procedure of hit-point determination.

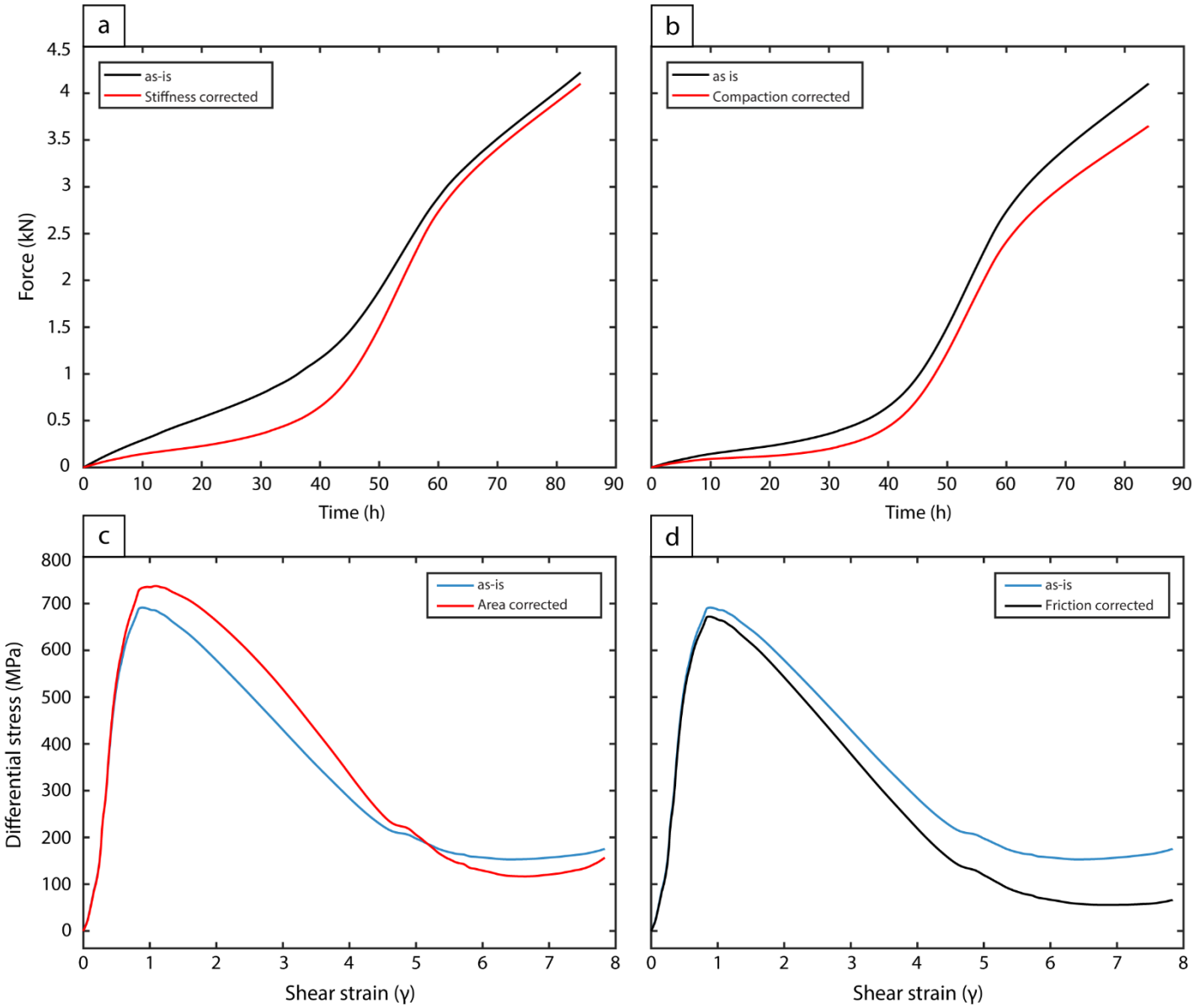

Fig 11: Corrections of the raw data. (**a**) Correction of the stiffness and (**b**) the compaction of the apparatus. (**c**) Correction of the sample surface change and (**d**) the friction.

3. Analytical procedure

3.1 Microprobe

The samples were mainly analyzed using light and scanning electron microscopy (SEM – TESCAN MIRA 3 XMU) of ISTO-BRGM (Orléans, France). Mineral compositions were determined using electron microprobe CAMECA SX Five (EPMA) at the ISTO-BRGM (Orléans, France) on carbon-coated thin sections (20 nm thickness). The analyzes were carried out with an accelerating voltage of 15 kV, a beam current of ~6 nA and a beam size of ca. 1 µm.

3.2 Electron backscatter diffraction (EBSD)

EBSD analyzes was carried out with an EDAX PEGASUS EDS/EBSD system and OIM DC 6.4 software (manufacturer EDAX, Mahwah—USA) at the BRGM (Orléans, France). The polishing procedure of thin sections includes a mechanical polishing with decreasing granulometry of diamond paste from 3 to 0.25 µm, and then a physico-chemical polishing using colloidal silica within a vibrating bath for about 1 hour. The operating conditions were set to an accelerating voltage of 20 kV, a working distance of 15 or 18 mm, and a probe current of ~6 nA. The EBSD data were processed to produce orientation maps and lattice preferred orientation (LPO) within equal-area lower-hemisphere pole figures. In these latter, we considered "one-point-per-grain" (mean orientation) in order to give the same weight to all grains independently of their size. The grains are defined so that their boundaries involve a minimum misorientation angle of 10°. Lower hemisphere pole figures of amphibole lattice preferred orientation (LPO) were calculated using MTEX softwares from the raw EBSD output. The source code for EBSD data treatment can be found at https://sites.google.com/site/jacquesprecigout/telechargements-downloads.

Texture strength is expressed through the J-index and the M-index parameters (Bunge, 1982; Skemer et al., 2005). To avoid the effect of grain size on LPO strength determination, pole figures are plotted as "one point per grain". Pole figures and J-index were collected considering a Gaussian half-width angle of 10°.

3.3 Cathodoluminescence analysis

To perform a CL analysis, the sections were placed in a vacuum chamber at Argon pressure of ~ $60x10^{-3}$ mbar. They were irradiated by a cold cathode source electron gun provided by OPEA (France). Standard tension-current beam conditions were maintained at ~13–15 kV and 90–110 µA, respectively. The angle between the gun axis and thin section plane was set to 18°. The chamber was placed on a simplified optical mount designed to minimize light absorption on the beam pathway. The optical stage was equipped with a Retiga 2000R 1394a cooled camera (captor size 1 inch, resolution 1600 x1200 pixel2, square pixel size 7.4 µm). Acquisition time was fixed to ca. 10 s for quartz and mica and ca. 2 s for feldspar.

3.4 Quantitative microstructural study

3.4.1 Grain size

Scanning electron microscope/backscattered electron (SEM/BSE) images were used to produce manually digitized grain maps, which allowed the analysis of grain size. The grain size was defined as the equivalent circular area diameter ($d_{equ} = 2 \times \sqrt{\frac{area}{\pi}}$), and measured using the software ImageSXM® (http://www.ImageSXM.org.uk) and the public domain software ImageJ (http://rsb.info.nih.gov/ij/).

In the natural study, two types of source images were used to quantify the grain size: transmitted light microscope images when grains were easily distinguishable and SEM/BSE images when the grain size was too small, including zones of mixed phases in mylonites and ultramylonites. To ensure statistical representation of data, about 22,000 grains were processed.

3.4.2 Grain contact frequency (GCF)

The grain contact frequency (GCF) between quartz-quartz (Q-Q), feldspar-feldspar (F-F) and quartz-feldspar (Q-F) was evaluated using the method described by Heilbronner and Barrett (2014). In this method, GCF between grains is expressed as deviation from a random phase distribution. Results of GCF allowed us to define spatial distributions of grains as clustered or ordered, corresponding to an increasing degree of phase mixing. For a two-phase mixing where grains are randomly distributed,

Heilbronner and Barrett (2014) define pQQ, pFF, and pQF as the predicted amount of quartz/quartz, feldspar/feldspar and quartz/feldspar boundaries, respectively. For a two-phase mixing, pQ and pF are defined as phase proportion where pQ + pF = 1. The random phase distribution that separates clustered and ordered domains is described by the following equations as a function of phase proportions:

$$pQQ = pQ \,.\, pQ = pQ^2$$

$$pFF = pF \,.\, pF = (1— pQ)^2$$

$$pQF = pQ \,.\, pF + pF \,.\, pQ = 2\, pQ\, (1 - pQ)$$

The fraction of Q-F contacts is higher than a random distribution for the “ordered” case, and the relationship is opposite for the “clustered” case. Accordingly, the fractions of Q-Q and F-F contacts are lower and higher than a random distribution for ordered and clustered cases, respectively (Heilbronner and Barrett, 2014). In other words, ordered/clustered distribution implies a higher/smaller mixing degree of phases and a larger/smaller fraction of interphase boundaries than random distribution.

3.4.3 Shape preferred orientation (SPO) and Autocorrelation function (ACF)

Grain shape preferred orientations (SPO) were analyzed using the PAROR method (Panozzo, 1983), when it is possible to distinguish individual grains. Since individual grain boundaries are difficult to distinguish, the SPO were analyzed from manually produced bitmaps using the autocorrelation function (ACF; Panozzo, 1983; Heilbronner and Tullis, 2002). The ACF method does not require segmentation of the individual grains, and consequently avoids errors and biases caused by the identification of individual grains. For further details on including equations related to the ACF, the reader is invited to consult the original study of Heilbronner, 1992. For both methods, the preferred orientation of each grain shape was plotted in a rose diagram. The aspect ratio b/a (where a and b are the long and short axis of best-fit ellipses approximating the grain shape) was also determined to document the bulk grain shape anisotropy.

Le troisième chapitre de cette thèse présente l'étude de la zone de cisaillement sud Armoricaine (CSA), qui correspond à une zone de cisaillement crustale déformant des roches granitiques dans les conditions de la croûte moyenne à inférieure. Le cisaillement sud Armoricain (CSA) enregistre et expose à l'affleurement la transition du protolithe à l'ultramylonite, ce qui traduit l'augmentation de la déformation ductile cisaillante. Afin d'étudier l'évolution de la localisation de la déformation, les différents stades de déformation ont été explorés en combinant l'analyse des microstructures, des textures et des compositions chimiques des minéraux. Cette étude révèle que l'augmentation de la contrainte du protolithe à l'ultramylonite a conduit à une succession de processus affaiblissants le volume rocheux, à commencer par la nucléation d'une phase faible, le mica, comme premier matériau affaiblissant, puis par le développement de zones de mélange à grains très fins.

N.B. : Ce chapitre fait l'objet d'un article publié dans la revue Tectonophysics. Celui-ci est néanmoins adapté afin d'éviter les répétitions avec le chapitre précédent.

CHAPTER III

Large-scale strain localization induced by phase nucleation in mid-crustal granitoids of the south Armorican massif

CONTENTS

1. Introduction

Strain localization in ductile shear zones is commonly characterized by the development of protomylonite, mylonite and fine-grained ultramylonite with increasing strain (e.g. Kilian et al., 2011; Linckens et al., 2011). As accommodating a large part of strain in large-scale structures, they play a crucial role for the dynamics of mountain belts, subduction zones or rifting. However, their occurrences have been considered as resulting from one or several processes of rheological weakening, the origins of which remain today very elusive (e.g. Stünitz and Fitz Gerald, 1993; Fliervoet et al., 1997; Fossen and Cavalcante, 2017). Investigating the processes responsible for large-scale strain localization is essential to understanding the behavior of the lithosphere-scale structures over geological timescale.

Several processes have been proposed and first introduced in Poirier (1980) and White et al. (1980) to account for a local weakening during deformation. They include the occurrence of (1) metamorphic reactions (2) geometric softening (3) chemical softening (4) a change in deformation mechanism owing to grain size reduction (5) shear heating and/or (6) pore fluid pressure effects. In polyphase rocks, the presence of different phases with various strengths may also be an important cause of ductile strain localization, as they produce a framework of interconnected weak layers (e.g. Jordan, 1988; Handy, 1990; Shea and Kronenberg, 1993; Dell'Angelo and Tullis, 1996; Lonka et al., 1998; Stewart et al., 2000; Holyoke and Tullis, 2006). Of further interest is the mechanism related to grain size reduction as it systematically occurs in ductile shear zones (e.g. White et al., 1980; Rutter and Brodie, 1988; Herwegh et al., 2011; Kilian et al., 2011; Montési and Hirth, 2003; Platt, 2015). The role of grain size reduction in strain localization thus deserves a special attention. Moreover, grain size reduction may give rise to substantial weakening when the mean grain size is small enough for grain size-sensitive (GSS) creep to control the bulk rock rheology (e.g. Boullier and Gueguen, 1975; Etheridge and Wilkie, 1979; Rutter and Brodie, 1988; Stünitz and Fitz Gerald, 1993; Fliervoet et al., 1997; De Bresser et al., 1998; Kruse and Stünitz, 1999; Kenkmann and Dresen, 2002; Précigout et al., 2007; Raimbourg et al., 2008; Linckens et al., 2011; Kilian et al. 2011; Viegas et al., 2016). Nevertheless, the sources of grain size reduction still remain poorly constrained and require further detailed studies of shear zones, particularly for polyphase rocks through large-scale structure.

In this contribution, we investigate the microstructural features of a granitoid mylonitized within a major crustal shear zone of South Brittany, Western France. This shear zone corresponds to the historical place of first recognition of S-C and S-C' fabrics (Berthé et al., 1979). Here, we focus on the strain gradient outlined by a gradual grain size reduction from undeformed protolith to ultramylonite. Using light microscope, cathodoluminescence (CL), backscattered electron (BSE) imaging along with electron backscatter diffraction (EBSD) analyzes, we describe the progressive evolution of the microstructure and associated changes in active deformation processes.

2. Geological setting

The French Armorican massif corresponds to one of the largest pieces of the Paleozoic Variscan orogenic belt, which extends throughout western and central Europe (e.g. Matte, 1991, 2001). The Variscan belt resulted from the collision between two major continental domains, the Gondwana continent to the south and the Laurussia continent to the north.

The structural pattern of the Armorican massif is dominated by late-Carboniferous W-E to NW-SE striking, dextral strike-slip shear zones, namely the North Armorican shear zone (NASZ) and South Armorican shear zone (SASZ) (e.g. Watts and Williams, 1979; Jégouzo, 1980; Matte, 1986; Tartèse et al., 2011). In the Armorican massif, the formation of crustal-scale shear zones is associated with widespread extension and magmatism during the collapse of the Variscan orogenic belt (e.g. Berthé et al., 1979; Jégouzo, 1980; Vigneresse and Brun, 1983; Ballèvre et al., 2009). Macrostructural studies demonstrated that deformation localized over time towards the contact between syntectonic plutons and host rocks (e.g. Berthé et al., 1979). From a paleogeographic point of view, the Armorican massif is divided into three main distinct parts, namely the Léon, North-Central and South-Armorican domains, all bound by major tectonic contacts including suture zones such as the Nort-sur-Erdre deformed zone (Fig. 1a, e.g. Cartier and Faure, 2004; Faure et al., 2005, Ballèvre et al., 2009). These domains drastically differ from each other by their metamorphic grade and structural style (e.g. Gumiaux et al., 2004; Faure et al., 2008; Ballèvre et al., 2009; Turrillot et al., 2011; Augier et al., 2015). The SASZ extends over hundreds of kilometers and represents a major structural zone that separates the North-Central and South Armorican domains (Fig. 1a). The SASZ

is divided into two main branches roughly oriented WNW-ESE for the northern branch and NW-SE for the southern branch (Fig. 1a; e.g. Cogne, 1960; Jégouzo, 1980). The southern branch separates the South Armorican domain in two parts: 1) the Ligerian Domain to the North characterized by Early Paleozoic ophiolites, high-pressure mafic and felsic rocks (Ballèvre et al., 1994; Bosse et al., 2000), and 2) the coastal South Armorican domain, which exhibits metamorphic and granitic rocks (Brown and Dallmeyer, 1996; Turrillot et al., 2009, 2011; Augier et al., 2015).

The present study focuses on the southernmost parts of the Ligerian Domain along the Southern branch of the SASZ, where Neoproterozoic to Lower Paleozoic metasediments are intruded by Carboniferous granitoids traditionally described as synkinematic intrusion (Fig. 1b; e.g. Berthé et al., 1979; Tartèse and Boulvais, 2012). These granitoids are affected by a variable strain intensities, giving rise to local mylonites and ultramylonites (e.g. Berthé et al., 1979). This is notably the case for the Questembert granite, where strain increases southward and reaches a maximum in the core of the Southern branch of the SASZ (Fig. 1b; e.g. Augier et al., 2011; Tartèse et al., 2012).

The studied samples were collected along a section through a satellite body of the Questembert granite massif (Fig. 1b-c). This section represents a strain gradient from undeformed or slightly deformed host rocks of the SASZ (domain 1) towards the most deformed, ultramylonitic sample in the core of the SASZ (domain 5). Accordingly, the grain size decreases and the foliation progressively transposes into the shear plane from domain 1 to domain 5 (Fig. 1c). This section has been also completed by another sample collected in the Lescastel quarry to allow comparison with very recent results of Bukovská et al. (2016) (Fig. 1b).

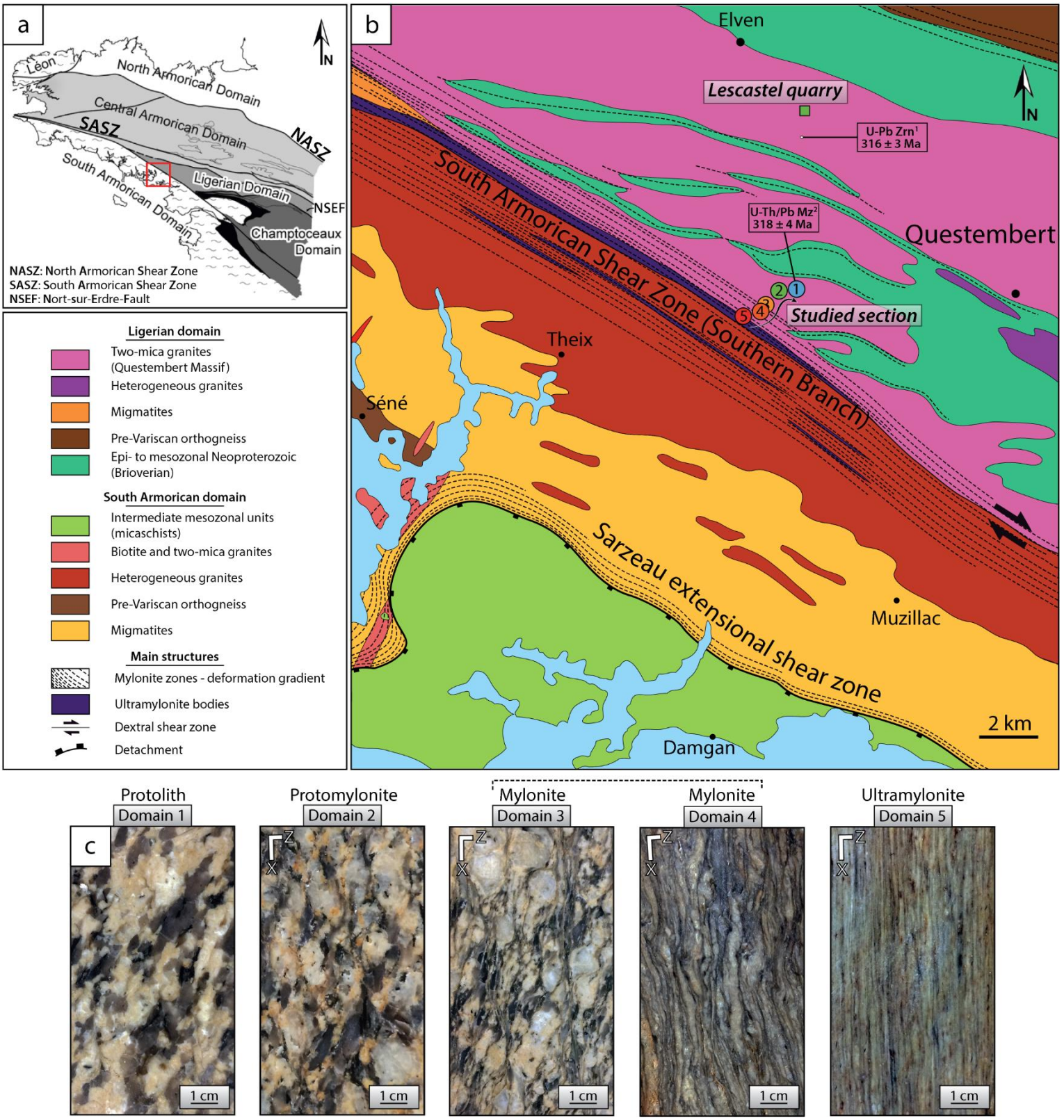

Fig 1: (**a**) Schematic map of the main domains forming the Armorican Massif, modified from Gumiaux et al., 2004. The studied area is delineated by the red rectangle. (**b**) Simplified geological map of the studied area modified from Augier et al., 2011. The location of the samples used is highlighted with colored dots. (**c**) Pictures of the samples used in this study, showing the different stages of deformation, from weakly deformed sample (domain 1) to the most deformed one (domain 5). Geochronological data are [1]Zircon U-Pb data (Tartèse et al., 2011) and [2]Monazite U-Th/Pb data (Augier et al., 2011).

3. Results

3.1 Microstructural evolution—qualitative approach

3.1.1 Strain facies across the strain gradient

The Questembert granite is traditionally described as a large-scale synkenimatic intrusion (e.g. Berthé et al., 1979; Tartèse and Boulvais, 2010). However, microscopic-scale observations showed no evidence for the presence of melts during deformation even in low-strain domains (Bouchez et al., 1992). It is mainly composed of quartz (qtz), K-feldspar (kf), plagioclase (pl) and white mica (wm) with minor amounts of biotite (bt), apatite (ap), chlorite and kaolinite. Solid-state deformation is characterized by a strain gradient from a quasi-undeformed protolith to a km-scale ultramylonite where grain size is strongly reduced (Fig. 1c). This aspect is considered in terms of strain gradients based on microstructural observations, including grain size and evolution of porphyroclast/matrix proportions as major parameters. We thus use changes in grain size and proportion of porphyroclast/matrix with respect to the protolith as proxy to define several domains of strain intensity, such as described in the following sections. In order to avoid ambiguity when considering quartz aggregates and their possible polymineralic character, the term "quartz-rich aggregates/layers" will be used in this text when referring to the domains of quartz with a volumetrically minor amount of second phases. In addition, the term "nucleation" will also be used to denote the processes involving changes in chemical composition, unlike dynamic recrystallization.

3.1.1.1 Low-strain protolith

The protolith contains abundant porphyroclasts of K-feldspar, plagioclase, mica and quartz, without discernible shape-preferred orientation. Quartz grain boundaries have variable geometries, from slightly curved to serrated (Fig. 2a). These quartz grains show weak deformation features such as sweeping or patchy undulatory extinction (Fig. 2b). In this low-strain protolith, both biotite and white micas are present in a comparable amount. These micas are either undeformed or slightly kinked and bent. Quartz-rich aggregates are associated with cracks along grain boundaries filled with biotite and white mica that form essentially at the edges of porphyroclasts (Fig. 2c). Small grains of white mica are also distributed in plagioclase as rod-like cross-sections (Fig. 2d). Plagioclase grains form large porphyroclasts locally twinned, rarely bent, and affected by fractures (Fig. 2b). K—

feldspar porphyroclasts are also frequently fractured. Some of the fractures that crosscut feldspar porphyroclasts are filled by quartz, plagioclase, white mica and biotite (Fig. 2b). K-feldspar porphyroclasts are strongly perthitic, with plagioclase exsolution lamellae (Fig. 2e). Commonly, plagioclase nucleates in many different places within and at the rim of K-feldspar grains (Fig. 2d-e). Both types of feldspar are almost undeformed, such as shown by smooth undulatory extinction and limited chemically-driven nucleation at grain boundaries.

3.1.1.2 Medium-strain protomylonite

The protomylonite samples are microstructurally and geographically close (Fig. 1b) to the one collected by Bukovská et al. (2016). Three main different types of mica microstructures are identified in the protomylonite: (1) small aligned white mica grains form disconnected trails along the grain boundaries in quartz-rich layers (Fig. 3a-b), (2) some thin and short monophase layers of mica form an anastomosing network connected by trails of very fine-grained recrystallized grains inherited from mica porphyroclasts (Fig. 3c-d), and (3) a few fine-grained polyphase layers mainly composed of mica and quartz (Fig. 3e). These mica-quartz-rich polyphase layers are subparallel to the foliation, cross-cut quartz-rich layers and wrap around feldspar porphyroclasts (Fig. 3e). The polyphase layers increase the proportion of matrix compared with the protolith. With respect to the overall size of recrystallized quartz grains, the quartz grain size is considerably smaller in these high-strain narrow zones, where elongated white micas are present in large amounts (Fig. 3e). Very few chlorite grains in the layers are also observed.

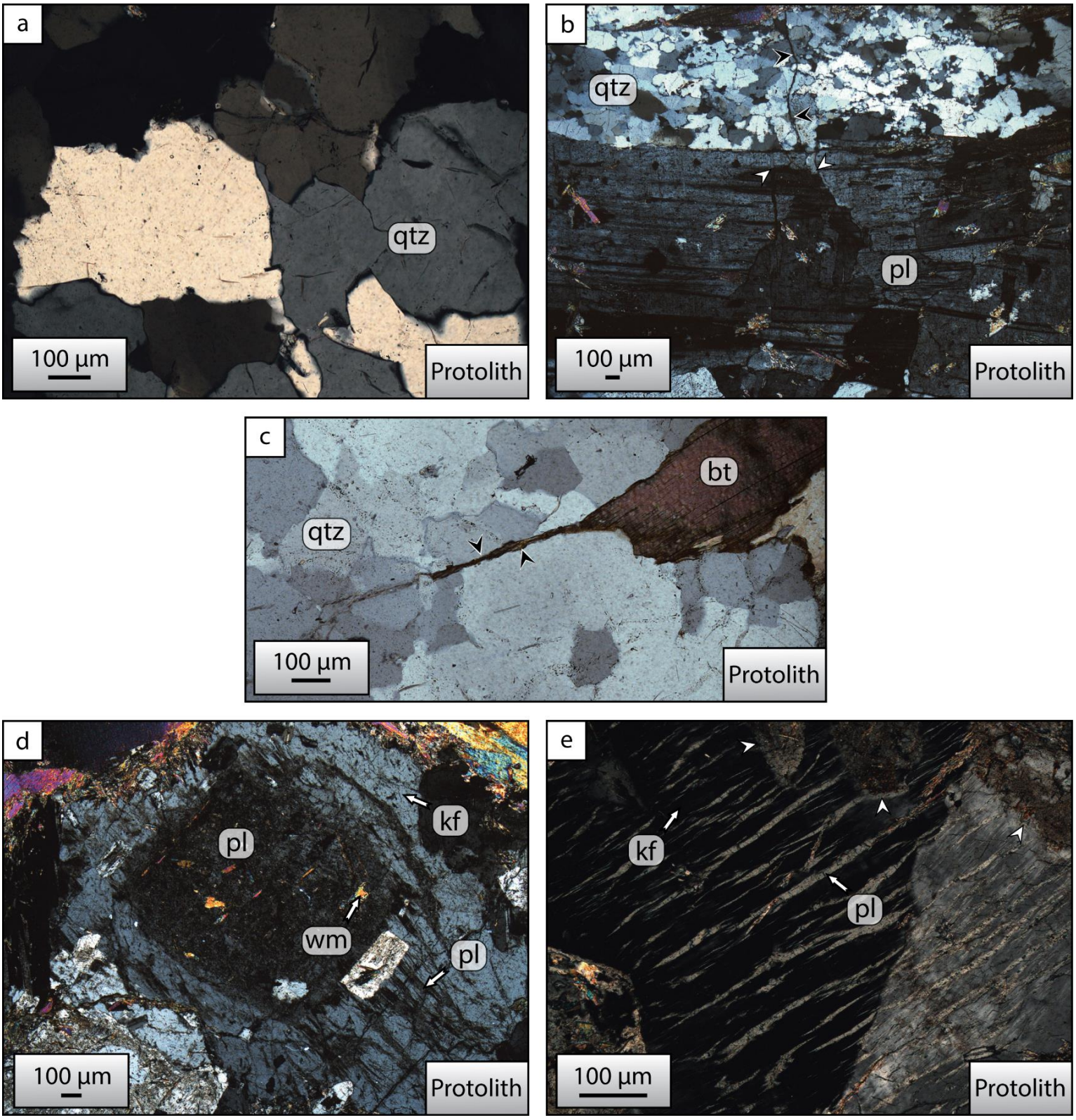

Fig 2: (**a**) Quartz grains with polygonal to lobate grain boundaries. (**b**) Plagioclase porphyroclast with mechanical twinning and fractures filled by plagioclase (white arrows), and quartz aggregate crosscut by cracks filled with biotite (black arrows). (**c**) Crack filled with biotite crosscutting quartz-rich layer (black arrows). (**d**) Rod-like cross-sections of white mica in the plagioclase. Also note that the plagioclase grain replaces that of the K-feldspar. (**e**) Large porphyroclast of K-feldspar showing the presence of oriented plagioclase exsolution. K-feldspar is progressively replaced by plagioclase grains (white arrows). All cross-polarized light micrographs. qtz: quartz, pl: plagioclase, kf: K-feldspar, wm: white mica, bt: biotite.

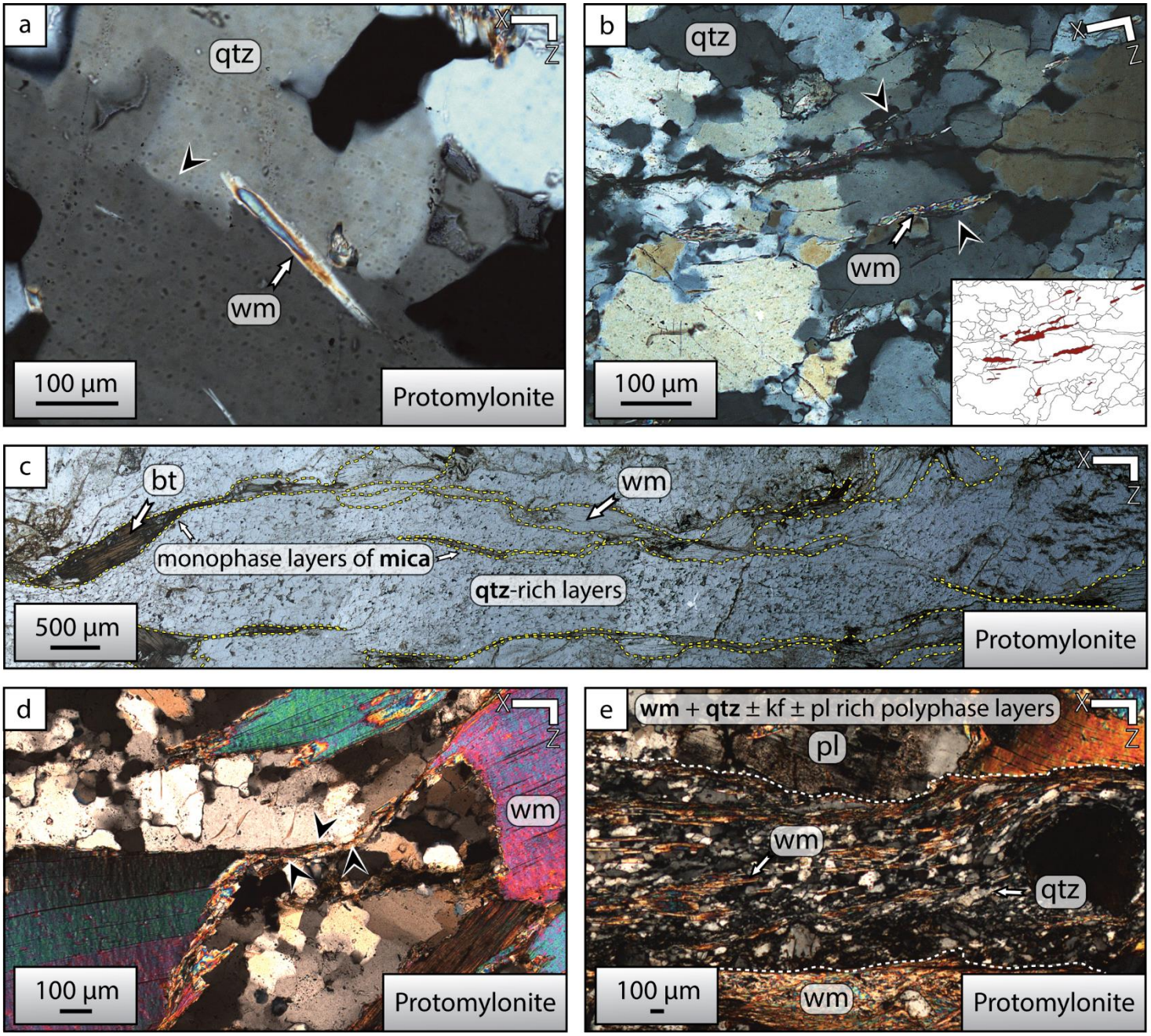

Fig 3: Cross-polarized light pictures showing the microstructures observed in protomylonite. (**a**) Small rod-like cross-sections of recrystallized white mica located at joints of two quartz grains. Note also the restricted growth of quartz by this white mica. Black arrow indicates the direction of growth. (**b**) Arrangement of small and oriented crystals of white mica (black arrows) in the quartz-rich layer, which define the foliation. (**c**) Thin monophase layers of mica crosscut quartz-rich layers and start to connect. (**d**) Connection of white micas through trails of very fine-grained white micas (black arrows). (**e**) Narrow zone of recrystallized grains forming polyphase layer composed principally of quartz and white mica. The latter are elongated preferentially parallel to the recrystallized zone margins. qtz: quartz, pl: plagioclase, kf: K-feldspar, wm: white mica, bt: biotite.

3.1.1.3 High-strain mylonite

The mylonite is composed of a network of polyphase layers wrapping up isolated relic domains (i.e., microlithons) in which inherited large porphyroclasts are still visible (Fig. 4a). Some feldspar porphyroclasts are fragments resulting from fracturing of initially larger grains. While the feldspar porphyroclasts are smaller in size and in volume fraction than those in the protomylonite, biotite and monophase layers of mica are no longer present. With respect to the protomylonite, the amount of mica-quartz-rich polyphase layers increases (Fig. 4a-b-c). Within these polyphase layers, white mica grains are strongly aligned and become interconnected (Fig. 4b-c). A large amount of apatite is also documented in these deformed zones (Fig. 4b). The pervasively recrystallized quartz grains exhibit a shape-preferred orientation nearly parallel to the mylonitic foliation (Fig. 4c). The clasts of plagioclase and K-feldspar locally occur in these zones in small quantities (Fig. 4b-c).

The mylonite is also distinguished from the protomylonite by the incipient development of other fine-grained polyphase layers enriched in quartz and K-feldspar (Fig. 4d-e). While micas are scarce in these layers, isolated grains of K-feldspar exist at triple junctions of quartz grains (Fig. 4f). Within these polyphase layers, plagioclase grains occur as clasts. Fracturing is dominant in plagioclase although a marginal nucleation of plagioclase promotes the formation of fine grains at the boundaries of the old grains. In some places, the remaining K-feldspar porphyroclasts are completely rimmed and replaced by plagioclase (Fig. 4g).

These types of fine-grained polyphase layers isolate domains where the grain size is much larger and where less deformed porphyroclasts can still be recognized. Outside of the fine-grained polyphase layers, the quartz-rich layers are highly elongated subparallel to the foliation and their grains reveal patchy or sweeping undulose extinction patterns and the presence of subgrains (Fig. 4h). Locally, new small grains of quartz recrystallize within older, larger grains of quartz (Fig. 4i).

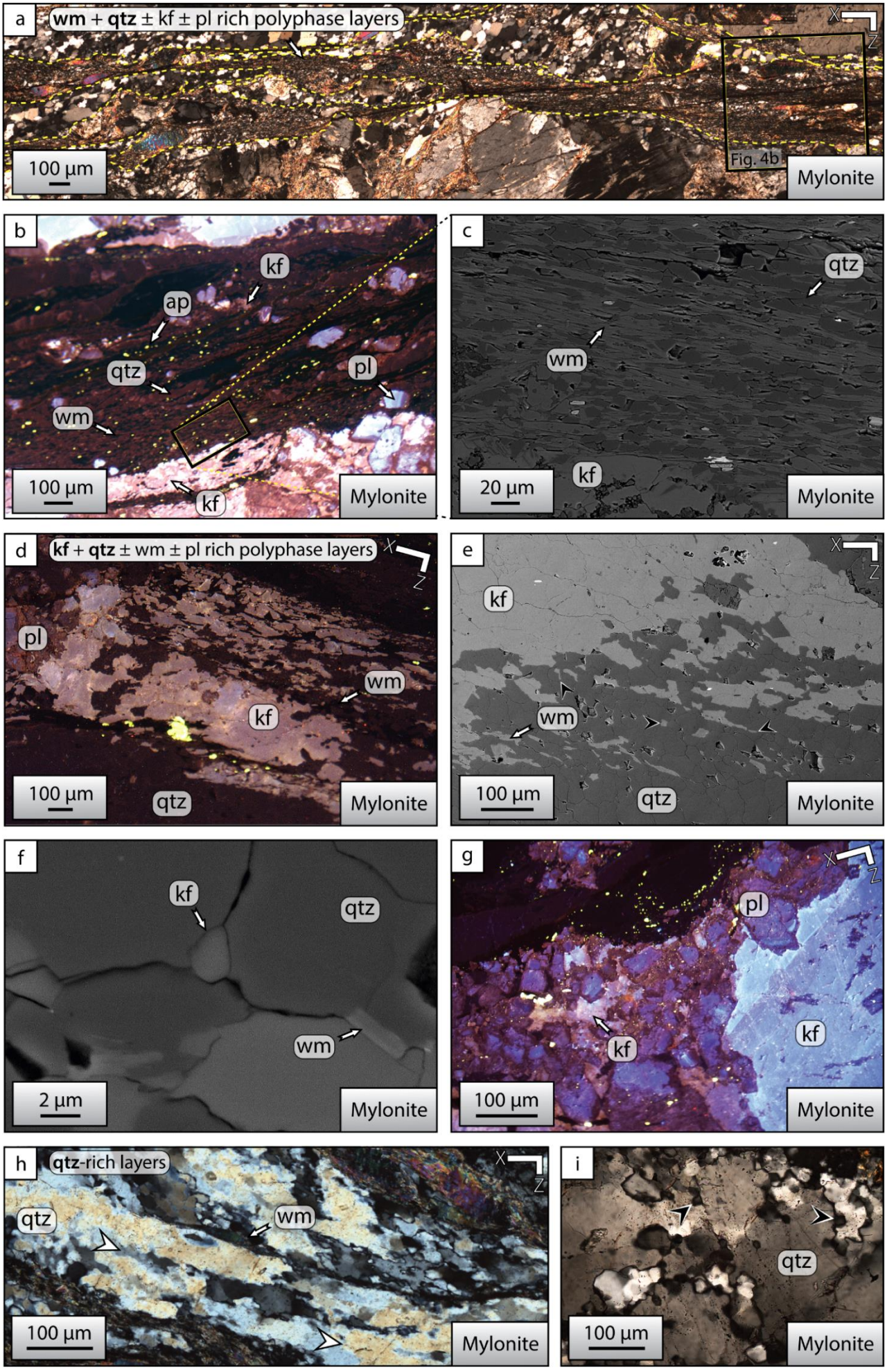
a
wm + qtz ± kf ± pl rich polyphase layers
X
Z
100 µm
Fig. 4b
Mylonite
b
kf
ap
qtz
pl
wm
100 µm
kf
Mylonite
c
qtz
wm
kf
20 µm
Mylonite
d
kf + qtz ± wm ± pl rich polyphase layers
X
Z
pl
wm
kf
100 µm
qtz
Mylonite
e
X
Z
kf
wm
100 µm
qtz
Mylonite
f
kf
qtz
wm
2 µm
Mylonite
g
X
Z
pl
kf
kf
100 µm
Mylonite
h
qtz-rich layers
X
Z
qtz
wm
100 µm
Mylonite
i
qtz
100 µm
Mylonite

Fig 4: (**a-to-h**) Coupled cross-polarized light micrographs, cathodoluminescence (CL) and SEM-BSE images representative of microstructures observed in mylonites. (**a**) Fine-grained polyphase layers (yellow dotted outline) rich in quartz and white mica, with locally few K-feldspar and plagioclase. (**b**) Close-up of the mixed-phase zone showing the partial interconnection of white micas intimately mixed with very fine-grained quartz grains. (**c**) Details of (**b**) showing the very fine-grained mixing composed at grain scale of quartz and white mica. (**d**) Polyphase layers rich in K-feldspar and quartz, with small quantities of white micas and plagioclase. (**e**) Grain size reduction of K-feldspar by precipitation in quartz essentially along grain boundaries and at triple junctions (black arrows). (**f**) K-feldspar located in triple junction of quartz grains. (**g**) Irregular plagioclase rim around a K-feldspar porphyroclast. (**h**) Quartz-rich layers strongly oriented, which show the development of subgrains (white arrows). (i) Small new quartz grains appearing along grain boundaries and within old grains (black arrows). qtz: quartz, pl: plagioclase, kf: K-feldspar, wm: white mica, ap: apatite.

3.1.1.4 Very high-strain ultramylonite

The ultramylonite is largely composed of a succession of foliation-forming parallel layers of fine grains that embed few small clasts, forming a clast-in-matrix microstructure. These latter are plagioclase grains (Fig. 5a-b), and more rarely K-feldspar and white mica grains (Fig. 5a-c). Tails around K-feldspar clasts are composed of fine-grained quartz and K-feldspar (Fig. 5c). The fine-grained parallel layers are either composed of quartz-rich layers, or of polyphase layers of quartz, K-feldspar and white mica (Fig. 5d). The vast majority of the ultramylonite consist of these polyphase layers, while quartz-rich layers occur sparsely in the form of elongated domains parallel to the foliation.

3.1.2 Microstructural evolution across the strain gradient

The prominent microstructural features of the investigated strain gradient are the grain size reduction, the formation of monophase layers of mica and polyphase layers. With increasing strain, coarse-grained mineral phases like feldspar, quartz and mica are replaced by fine-grained layers (Fig. 4-5-6). The grain size reduction of coarse-grained feldspar occurs predominantly by fracturing and nucleation of new grains with a different mineralogical composition than the protolith (Fig. 6). New grains are mostly distributed along the margins of old magmatic feldspar porphyroclasts, or within the tails of porphyroclasts (Fig. 6). The pink K-feldspar that composes the fine-grained mixed zones in the most strongly deformed domains is the same as the one that composes the rims of the coarse-grained light blue K-feldspar present in the protolith and the protomylonite (Fig. 6).

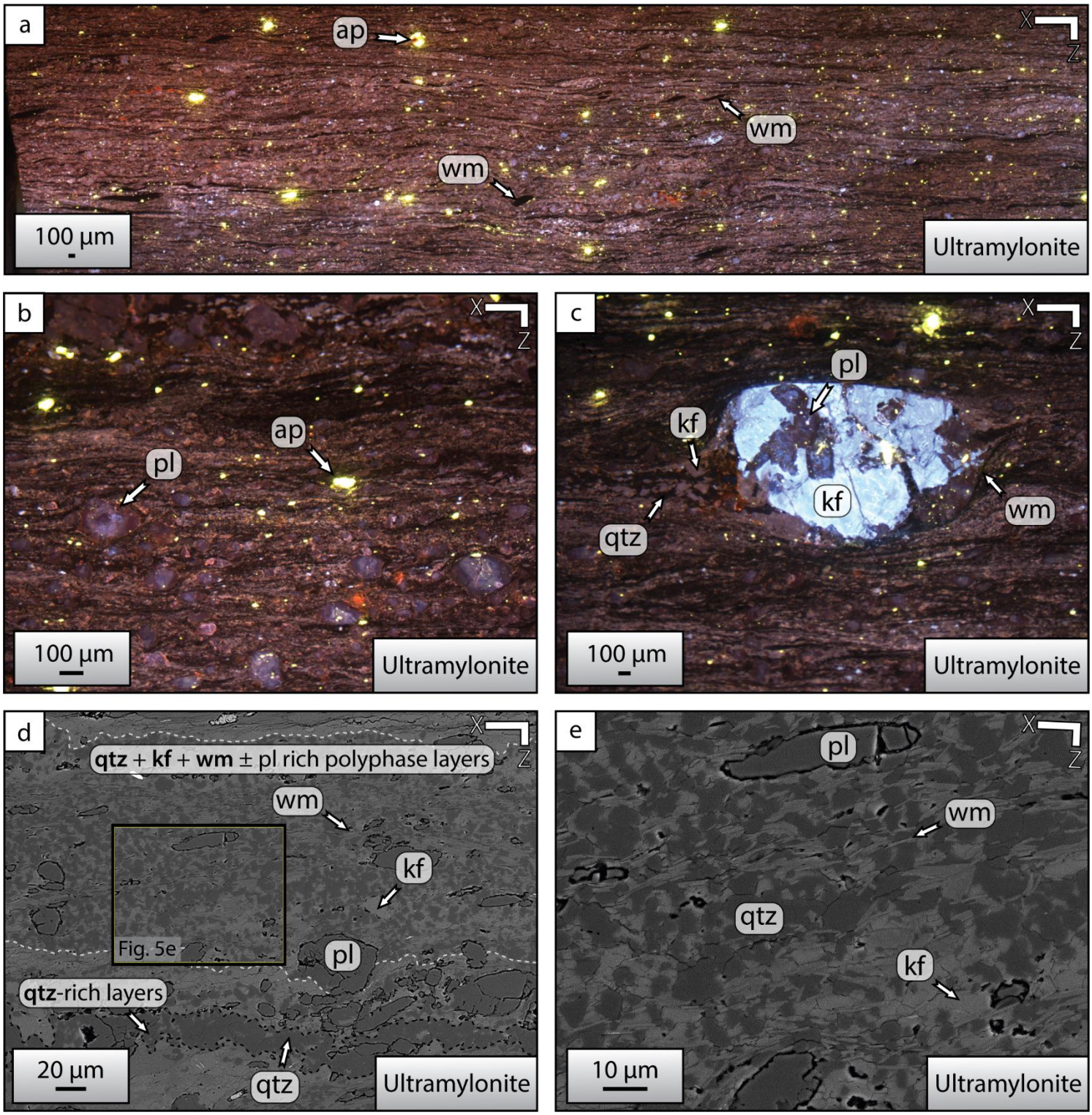

Fig 5: (**a-to-e**) Coupled cathodoluminescence (CL) and SEM-BSE images representative of microstructures documented in ultramylonite. (**a-b**) Ultramylonite textures made of intercalated bands of fine-grained polymineralic layers. Clasts are white mica (black), albite (purple) and apatite (yellow), while the pink, dark brown and black colors are due to K-feldspar, quartz and white mica, respectively. (**c**) The tails of a K-feldspar clast are filled by K-feldspar and quartz. (**d**) Layers of variable composition with quartz-rich layers and fine-grained polyphase layers rich in quartz, K-feldspar and white mica. Bigger plagioclase grains remain strong in form of clasts. (**e**) Close-up of the polyphase layers showing the thin white mica grains elongated subparallel to the lineation. qtz: quartz, pl: plagioclase, kf: K-feldspar, wm: white mica, ap: apatite.

Similarly, the plagioclase grains present in the ultramylonite are also observed as reaction products of the coarse-grained plagioclase of the protolith. These CL properties of K-feldspar and plagioclase support the connection of the microstructures throughout the strain gradient: high-strain domains (ultramylonite and mylonite) are therefore interpreted as the evolution, with increasing strain, of low strain domains (protolith and protomylonites).

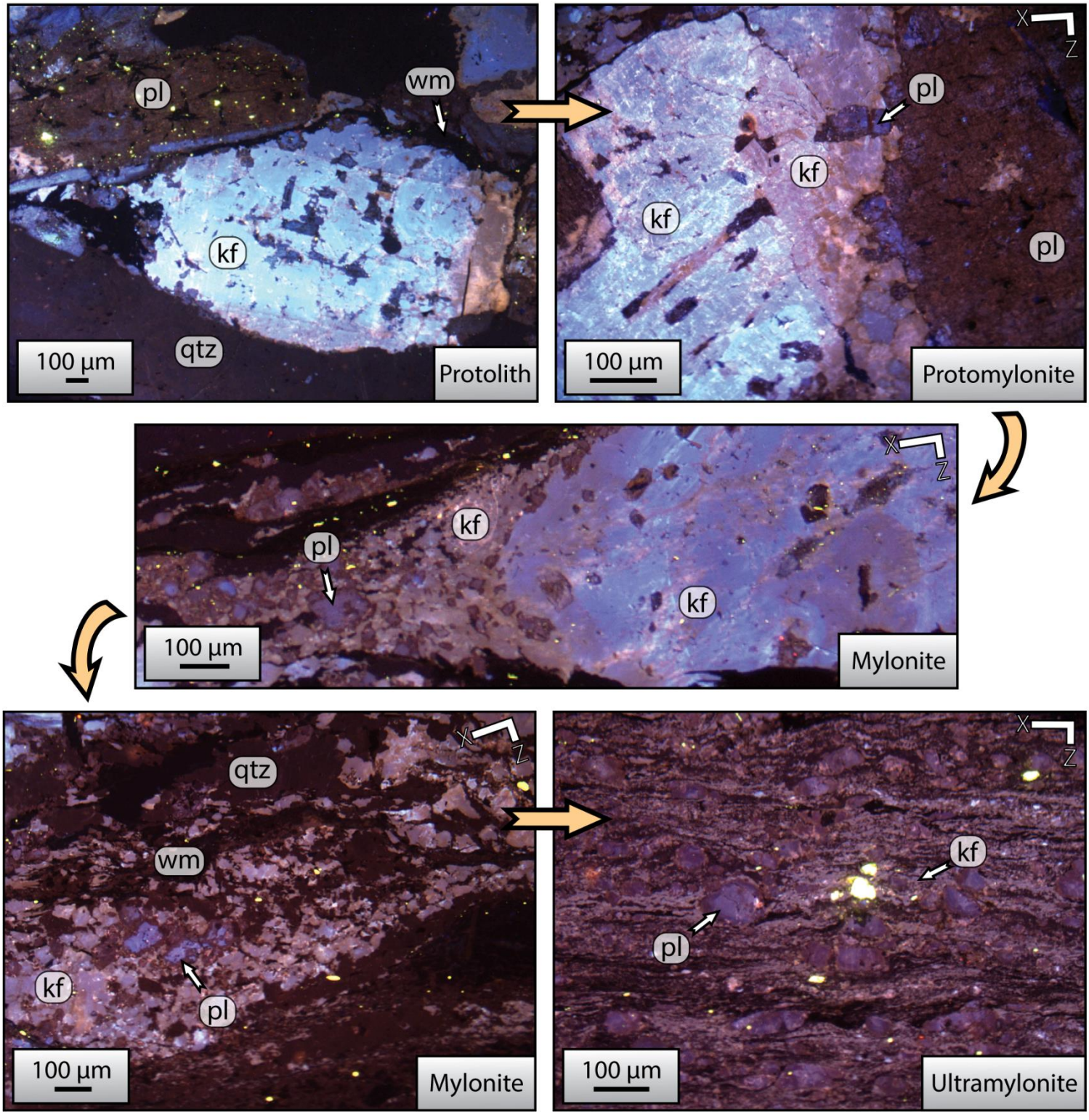

Fig. 6: Cathodoluminescence (CL) images showing the evolution of feldspar microstructures with increasing strain. On CL images, quartz is dark blue-brown, initial K-feldspar is bright blue, new K-feldspar is pink, white mica is black, initial plagioclase is brown and new plagioclase is purple. qtz: quartz, pl: plagioclase, kf: K-feldspar, wm: white mica.

3.1.3 Layers of mixed phases

The transition from protolith to ultramylonite is characterized by the development of fine-grained polyphase layers, i.e. fine-grained mixed-phase zones (Fig. 7), which include three different types depending on their phase content (Fig. 7a-c-e). The mixed-phase zones also contain plagioclase, but only locally and in very small amounts (hence not shown in images of Fig. 7). The first type (type I) involves the presence of white mica and quartz in equal proportion with minor K-feldspar (Fig. 7a-b). While scarce in the protomylonite, this mixed-phase assemblage is abundant in the anastomosing network of the mylonite polyphase layers. The two other mixed-phase zones (types II and III) are composed of quartz + feldspar and contain smaller amounts of white mica. They are very similar and simply differ by the nature of the major phase, either represented by K-feldspar (Fig. 7c-d) or quartz (Fig. 7e-f). Types II and III mixed-phase zones are observed in high-strained zones of the mylonites (domain 4), and most of the polyphase layers in ultramylonite. The micas form a partially interconnected network in type I mixtures (Fig. 7b), but they form isolated grains in types II and III (Fig. 7c-f). All fine-grained mixed-phase zones may also contain few very small clasts of mica, plagioclase, or K-feldspar.

In all of these zones, the grains of white mica show a SPO with a mean long axis subparallel to the foliation and an aspect ratio of ~ 0.32 (Fig. 7b-d-f). The quartz grains are preferentially elongated parallel to the foliation in type I mixture (aspect ratio of ~ 0.46; Fig. 7b), but they have a much more equant shape in type II and III mixtures (aspect ratio of ~ 0.72; Fig. 7d-f). The small grains of K-feldspar only present in type II and III mixtures also have more equant shape with aspect ratios of ~ 0.72 and ~ 0.60, respectively (Fig. 7d-6f).

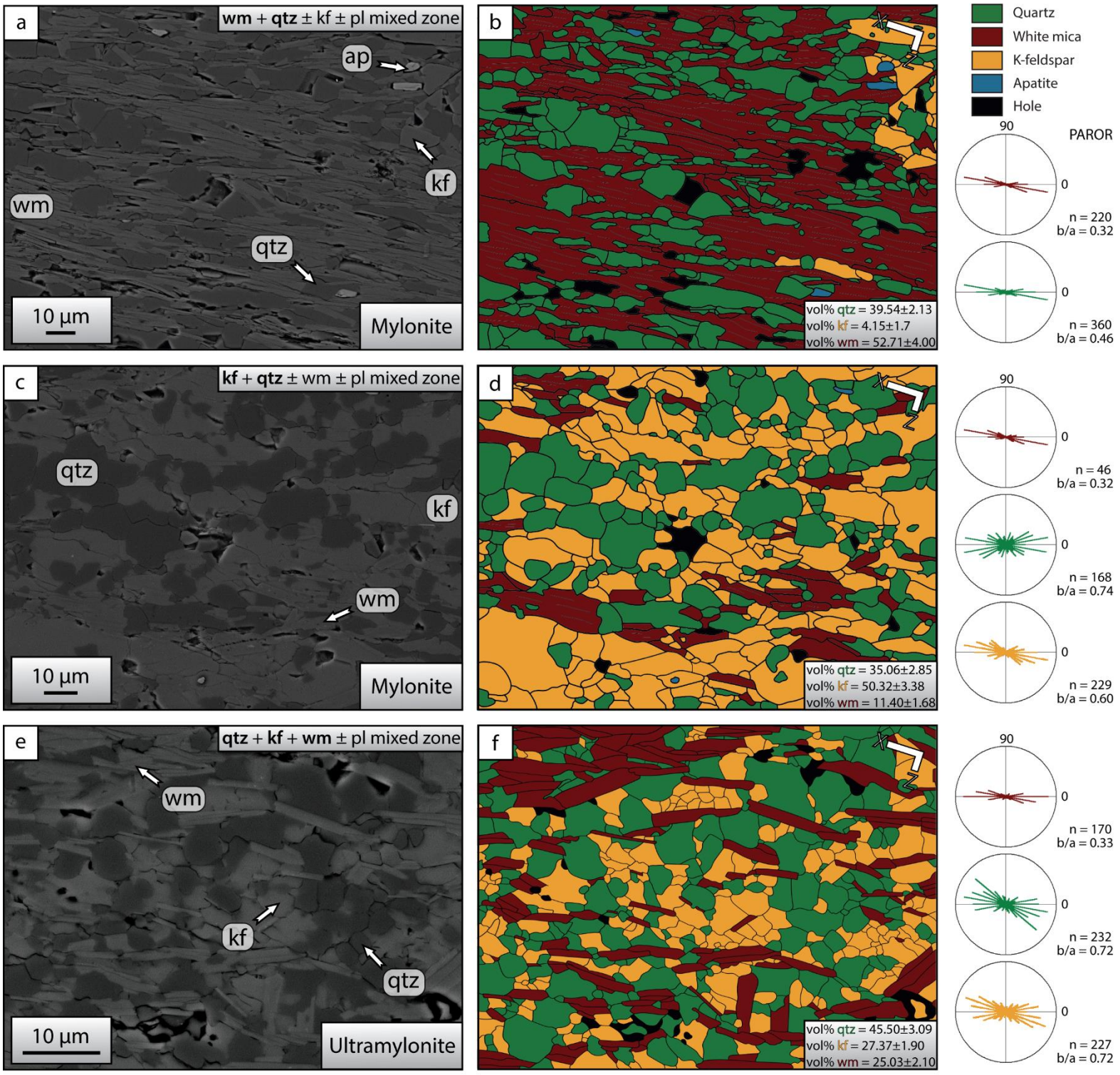

Fig. 7: (**a-c-e**) SEM-BSE images representative of the different type of mixed-phase zones and their respective manually digitized maps (**b-d-f**). Particle (PAROR) orientation of each phase is presented in a polar plot. (**a**) Mixed-phase zone rich in white mica and quartz, locally associated with K-feldspar and plagioclase. (**c**) Mixed-phase zone rich in K-feldspar, quartz, white mica, and minor plagioclase. (**e**) Mixed-phase zone similar to (**c**) with a higher proportion of white mica and where the quartz is the dominant phase. qtz: quartz, kf: K-feldspar, wm: white mica, ap: apatite.

3.2 Microstructural evolution—quantitative approach

The micro-textural study detailed below is based on digitized maps of each strain domain (Fig. 8), particularly in quartz-rich areas. Figure 8 shows the main microstructural evolution with increasing strain, including the development of quartz-rich layers and monophase layers of mica in low-strain domains (Fig. 8b) and mixed-phase zones in higher strain domains (Fig. 8c-d-e).

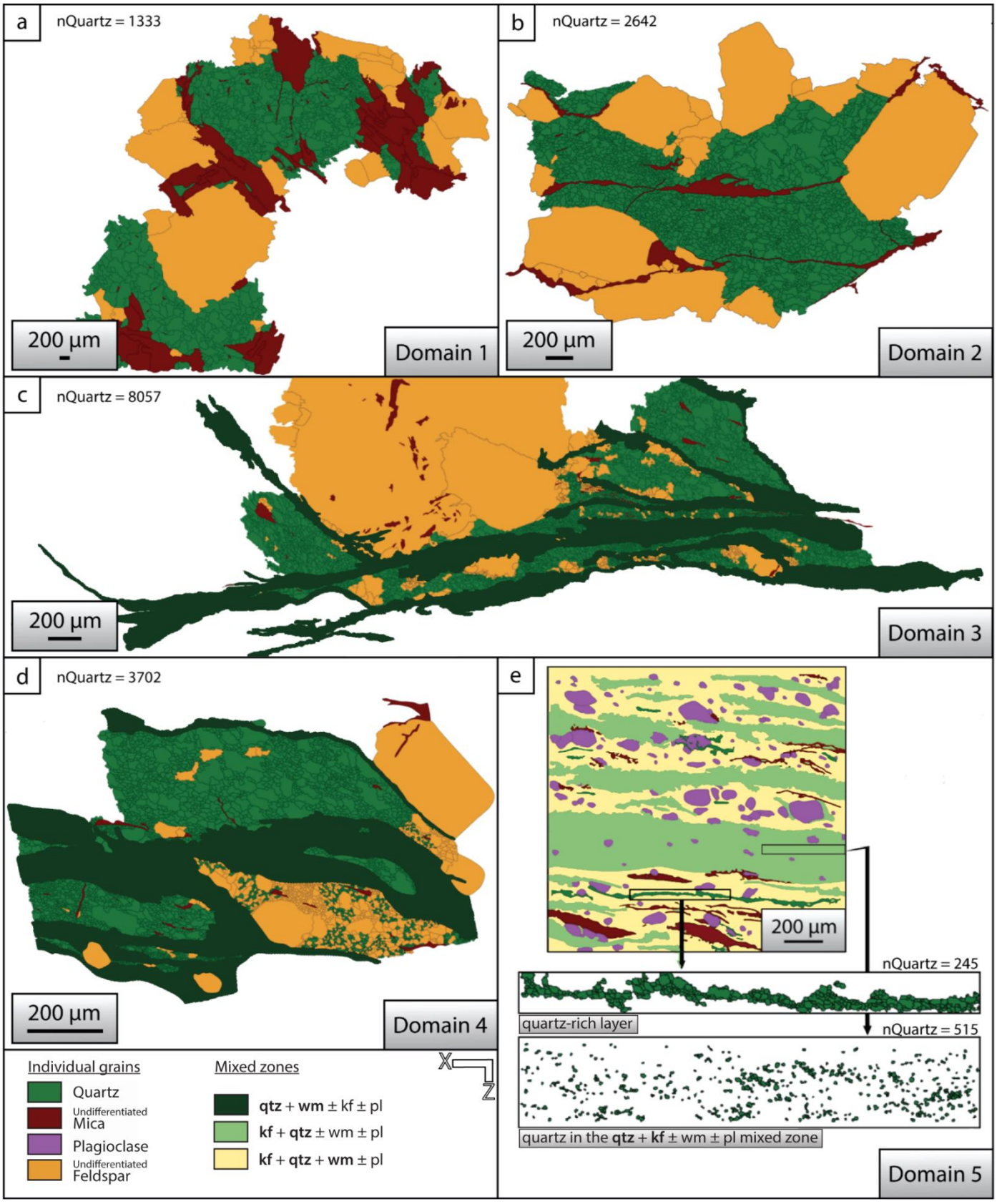

Fig. 8: (**a-to-e**) Manually digitized maps of individual grains and phase mixing of each domain of studies are used as a basis for the quantitative microtextural analyzes. Mixed-phase zones develop in the mylonite and ultramylonite stage (domains 3 to 5), as an anastomosing network of fine-grained polyphase layers (in the mylonites) or as foliation-forming layers of fine-grained mixing (in the ultramylonite). Note that no distinction is made between K-feldspar and plagioclase for the first four domains; the yellow color refers to all types of feldspar. qtz: quartz, pl: plagioclase, kf: K-feldspar, wm: white mica.

3.2.1 Grain size

Overall, there is a significant decrease in quartz grain size (equivalent diameter) with increasing strain (Fig. 9a). While the median of quartz grain size is 170 μm in domain 1 (protolith) and 120 μm in domain 2 (protomylonite), it decreases in domains 3 and 4 (mylonites) with respective median sizes of 114 μm and 38-29 μm. A gradual narrowing of the grain size distribution is observed with a wide range of size in the weakly deformed domains (1 and 2) and a rather narrow distribution for the mylonitic domains (3 and 4). In mylonites, these grain sizes correspond to the quartz-rich layers in low-strain domains where no phase mixing occurs. In contrast, where mixed-phase zones are abundant in high-strain domains, the median equivalent diameter of quartz grains is strongly reduced to 5.4 in the mylonite and 2.3 μm in ultramylonite (Fig. 9b). In these latter, a bimodal distribution of quartz grain size is observed (Fig. 9b). This is caused by the variable grain size distribution between polyphase mixed zones and preserved monophase aggregates in these high-strain domains. It is also worth to note that the recrystallized grain size of quartz in mixed-phase zones is similar and stable in mylonite and ultramylonite. The proportion of mixed-phase zones is more important in ultramylonite than in mylonite.

3.2.2 Grain Contact Frequencies (GCF)

The GCF between Q-Q, F-F and Q-F are shown in figure 9 as a function of the amount of boundary surface by these phases (Heilbronner and Barrett, 2014). Quartz grains are distributed in a clustered fashion for all domains (Fig. 10a). The GCF of quartz grains in the strongly deformed samples (strain domains 3 to 5) are closer to a random distribution than the ones in the weakly deformed samples (strain domains 1–2). With increasing strain, this implies an increase of the degree of mixing of quartz grains with other phases.

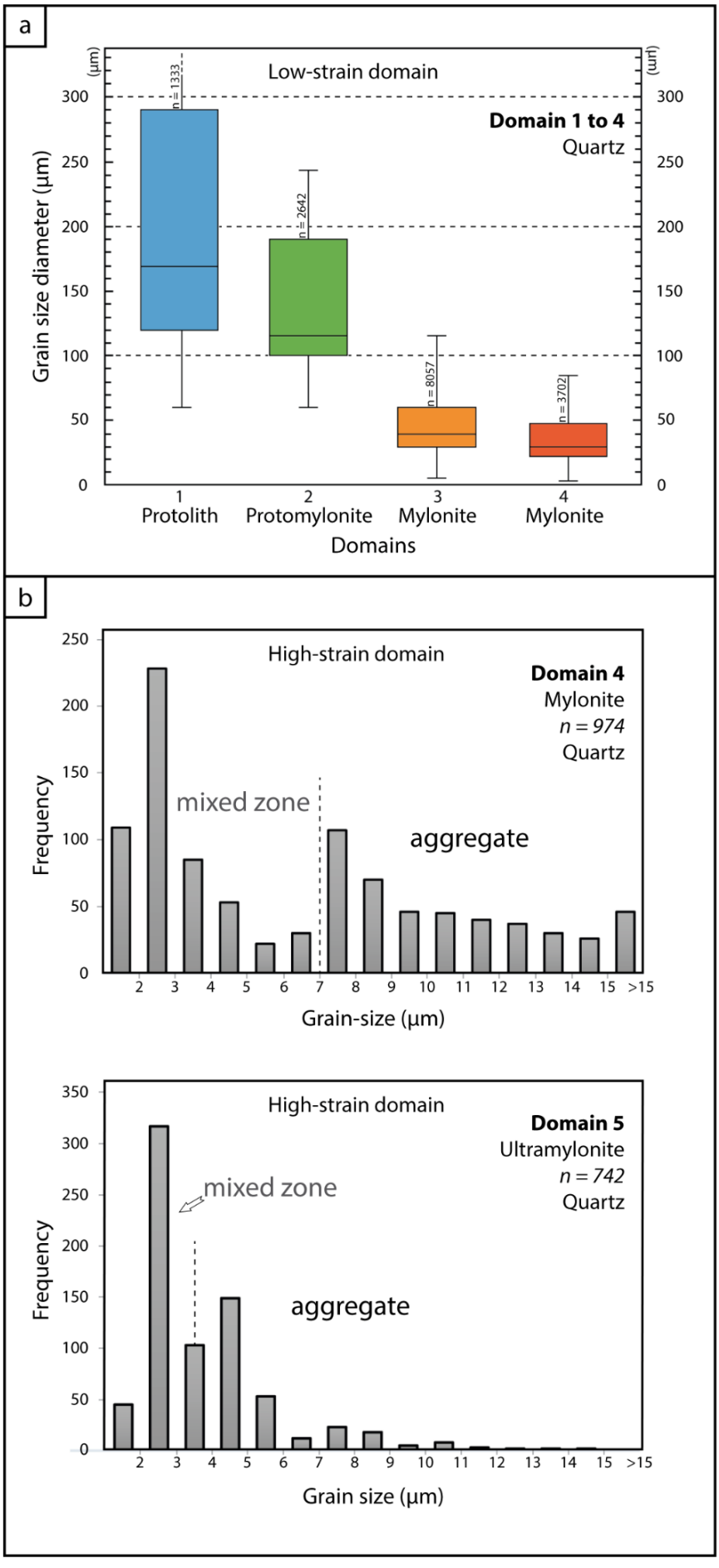
a
Low-strain domain
Domain 1 to 4
Quartz
Grain size diameter (µm)
n = 1333
n = 2642
n = 8057
n = 3702
1 Protolith
2 Protomylonite
3 Mylonite
4 Mylonite
Domains
b
High-strain domain
Domain 4
Mylonite
n = 974
Quartz
mixed zone
aggregate
Frequency
Grain-size (µm)
High-strain domain
Domain 5
Ultramylonite
n = 742
Quartz
mixed zone
aggregate
Frequency
Grain size (µm)

Fig. 9: Quartz grain size evolution. (**a**) The results are shown in box-and-whisker diagram. Individual boxes were limited by upper and lower quartiles, and within it the median was defined. This grain size evolution is obtained from cross-polarized light images, as the grain size is sufficiently large. (**b**) Evolution of quartz grain size between quartz rich aggregates and mixed-phase zones for mylonite and ultramylonite. While mylonitic quartz grain size was determined using SEM-BSE images, we used the EBSD to document the grain size in the ultramylonitic domain.

Accordingly, the feldspar grains are organized in the ordered field for all domains (Fig. 10b), but once again, there is an evolution with strain. In the weakly deformed sample (strain domain 1), the GCF between feldspar grains are closer to the random distribution curve. Thus, with increasing strain (strain domains 2 to 5), the GCF between feldspar grains move away from the random distribution curve, suggesting an increase in the mixing degree of feldspar grains with the other phases. Regarding the GCF between quartz and feldspar grains, the weakly deformed samples (strain domains 1–2) are localized in the clustered domain, while the more strongly deformed samples (strain domains 3 to 5) are located in the ordered domain, notifying again an increase in the mixing degree of quartz and feldspar grains with increasing strain.

3.2.3 Quartz Lattice Preferred Orientation (LPO)

Using equal-area lower-hemisphere pole figures, we show in Fig. 11 the quartz LPO of mylonitic (Fig. 11a-b) and ultramylonitic layers (Fig. 11c-d). In the mylonite, the quartz-rich layer exhibits a moderate LPO (Fig. 11a). The pole figure of quartz c-axes [0001] shows an incomplete crossed girdle (Fig. 11a). In the ultramylonite, a moderate quartz c-axes [0001] single girdle is developed at a large angle to the foliation and follows the sense of shear (Fig. 11c). The a-axes [11–20] of these quartz-rich layers are scattered and show locally a minor maximum close to the lineation. All of these distributions are strongly dispersed first in fine-grained quartz located at the rim of the layers (Fig. 11a-c), and in fine-grained polyphase mixed zones of both the mylonite and ultramylonite (Fig. 11b-d). The decrease of fabric strength is outlined by the evolution of the J-index and M-index from quartz-rich layers (J = 3.59 and 2.51; M = 0.13 and 0.11) to polyphase mixed zones (J = 1.63 and 1.56; M = 0.05 and 0.02) of the mylonite and ultramylonite, respectively (Fig. 11).

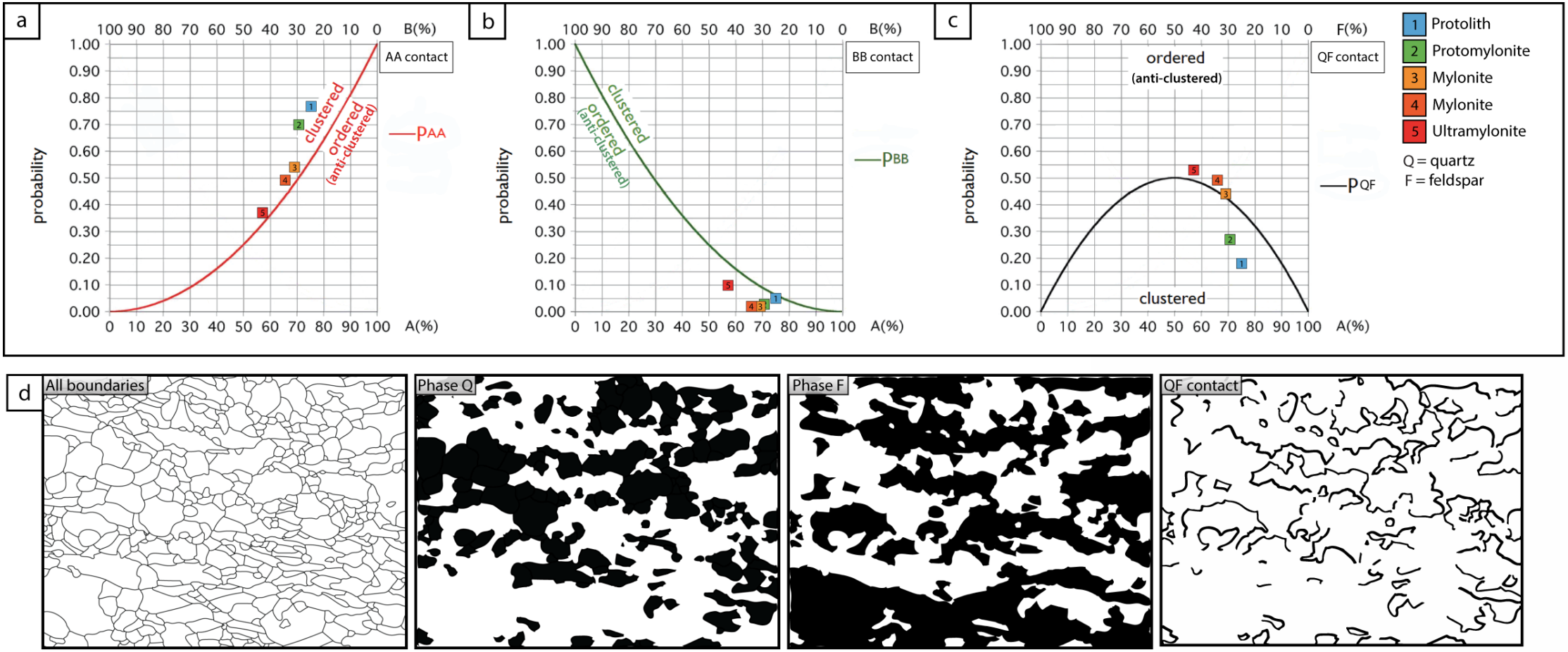

Fig. 10: (**a-to-c**) Graphs showing the probability of contact between two phases, Q=quartz and F=feldspar, for varying surface contact percentages of Q and F. The results can be compared to the curves showing the theoretical values for random distribution pQQ (**a**), pFF (**b**) and pQF (**c**). (**d**) Example of maps used for the GCF analysis. The maps of all boundaries, phase Q, phase F and contact surfaces between Q and F are successively represented.

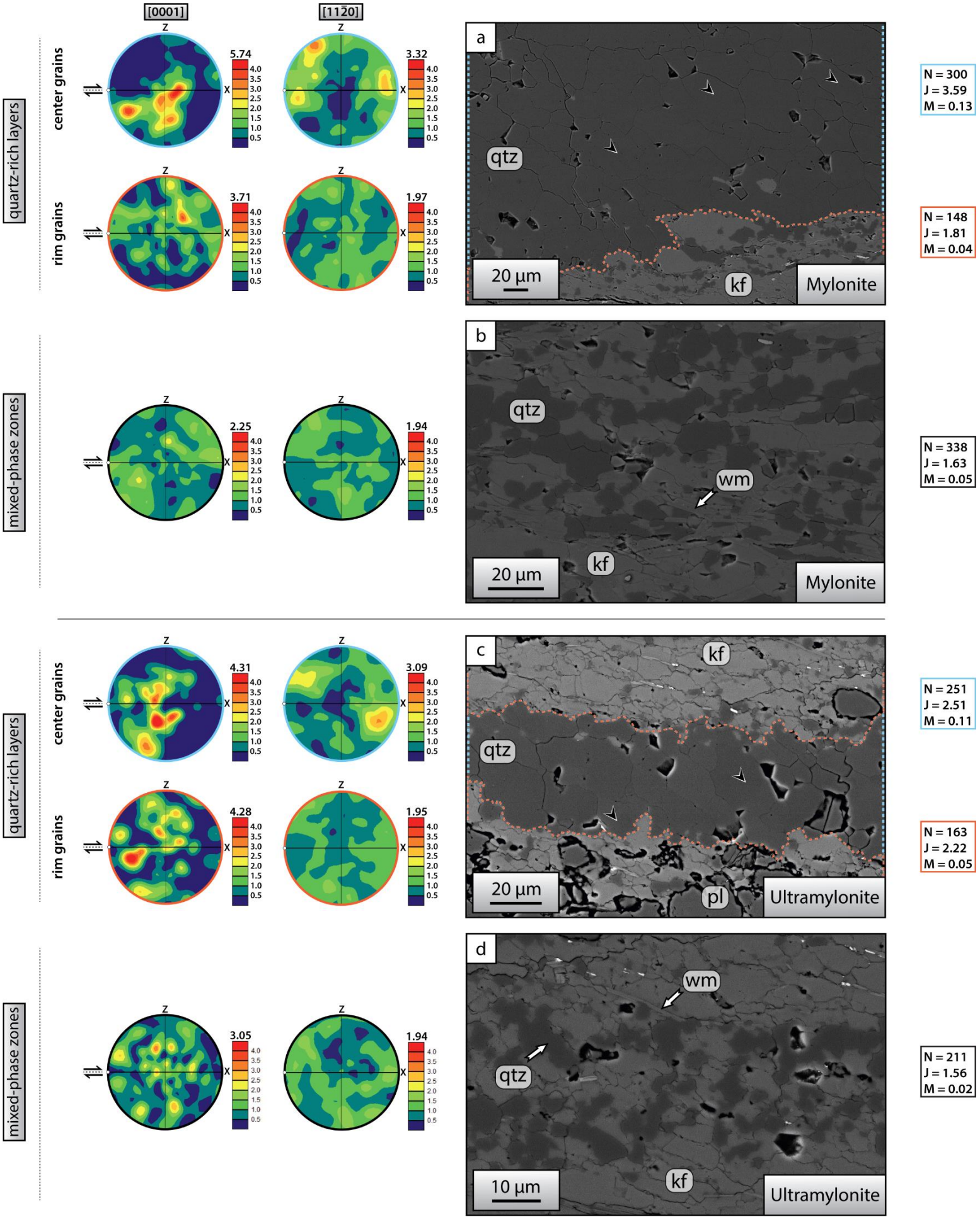
[0001]
[11$\bar{2}$0]
quartz-rich layers
mixed-phase zones
center grains
rim grains
5.74
3.32
3.71
1.97
2.25
1.94
4.31
3.09
4.28
1.95
3.05
1.94
a
b
c
d
qtz
kf
wm
pl
20 µm
10 µm
Mylonite
Ultramylonite
N = 300
J = 3.59
M = 0.13
N = 148
J = 1.81
M = 0.04
N = 338
J = 1.63
M = 0.05
N = 251
J = 2.51
M = 0.11
N = 163
J = 2.22
M = 0.05
N = 211
J = 1.56
M = 0.02

Fig. 11: (**a-to-d**) Comparison of quartz c-axis [0001] and a-axis [11–20] preferred orientation, for both aggregates and mixed-phase zones, in mylonite (**a-b**) and ultramylonite (**c-d**). There is a systematic decrease in fabric strength (J-index and M-index) between the monomineralic quartz aggregates and the fine-grained mixed-phase zones in both mylonite and ultramylonite. Related microstructures to these pole figures are also presented. The quartz aggregates in both mylonite and ultramylonite show a preferred orientation of grains (**a-c**; black arrows). All images: BSE pictures. All pole figures in the upper hemisphere and equal area. qtz: quartz, pl: plagioclase, kf: K-feldspar, phg: phengite.

4. Mineral chemistry

The bulk-rock chemical analyzes of the samples investigated and used in pseudosection calculations are given in Table 1. Analyzes were carried out in the *Centre de Recherches Pétrographiques et Géochimiques* (CRPG-Nancy) by the *Service d'Analyse des Roches et des Minéraux* (SARM). The mineral chemical compositions are summarized in Table 2. and in the isocon diagram of Fig. 12 (Grant, 1986). The average concentration of an element in the protomylonite, mylonite and ultramylonite (C^a) has been compared to the average concentration of this element in the protolith (C^0). All major element concentrations plot close to the line of constant concentration ($C^a = C^0$), or close to the lines of 10% gain ($C^a = 1.1C^0$) and 10% loss ($C^a = 0.9C^0$). Thus, the comparison between the strain domains studied indicates the lack of major chemical variations during progressive mylonitization. Nevertheless, a slight enrichment in K_2O-P_2O_5-MgO and depletion in Na_2O in the mylonite/ultramylonite compared to the protolith is reported (Fig. 12).

The chemical composition of white mica shows that the recrystallized grains are richer in celadonite component than the large magmatic white micas (Fig. 13a). Thus, the large magmatic white mica grains correspond to muscovite, whereas the fine recrystallized grains of white mica (especially abundant in mixed-phase zones) are phengites. The feldspar grains have a narrower compositional range (Fig. 13b-c), but within this narrow range we can observe a tendency of the recrystallized grains to be slightly richer in An-component for plagioclase (Fig. 13b). The K-feldspar in mixed-phase zones is richer in Or-component (Fig. 13c). The plagioclase grains also appear to have zoning patterns with a blue core and a brown rim in terms of cathodoluminescence colors (Fig. 5c), but no chemical variation is identified with the EPMA (Table 2).

Sample type	Protolith	Protomylonite	Mylonite	Ultramylonite
Wt% oxide				
SiO_2	75.57	73.88	72.95	74.37
TiO_2	0.11	0.08	0.18	0.13
Al_2O_3	14.29	14.94	15.39	14.96
Fe_2O_3	0.81	0.89	0.79	0.78
MnO	0.02	0.03	0.01	0.01
MgO	0.18	0.19	0.20	0.21
CaO	0.53	0.61	0.47	0.53
Na_2O	3.37	3.65	2.96	2.69
K_2O	4.43	4.40	5.08	5.30
P_2O_5	0.39	0.37	0.48	0.50
Total	99.70	99.04	98.51	99.48
Molar content				
SiO_2	1.2577	1.2296	1.2141	1.2378
TiO_2	0.0014	0.0011	0.0023	0.0016
Al_2O_3	0.1402	0.1465	0.1509	0.1467
Fe_2O_3	0.0051	0.0056	0.0049	0.0049
MnO	0.0002	0.0004	0.0001	0.0001
MgO	0.0045	0.0047	0.0050	0.0052
CaO	0.0095	0.0109	0.0084	0.0095
Na_2O	0.0544	0.0589	0.0478	0.0434
K_2O	0.0470	0.0467	0.0539	0.0563
P_2O_5	0.0014	0.0013	0.0017	0.0018
Total	1.5212	1.5056	1.4891	1.5072

Tab 1: Bulk rock chemical compositions of the four studied grades of deformation.

Type	K-feldspar			Plagioclase			White mica	
	Porphyroclast	New grain	Grain in mixed zones	Clast core	Clast rim	Grain in mixed zones	Porphyroclast	Grain in mixed zones
Wt% oxide								
SiO_2	66.24	64.86	64.66	67.62	68.76	66.27	45.72	46.63
TiO_2	0.06	0.00	0.03	0.00	0.00	0.00	0.52	0.35
Al_2O_3	18.12	18.13	17.79	19.74	19.87	19.77	33.42	30.27
FeO	0.00	0.00	0.12	0.08	0.00	0.00	31.37	3.17
MnO	0.00	0.01	0.00	0.03	0.03	0.00	0.00	0.08
MgO	0.02	0.00	0.00	0.00	0.03	0.00	0.81	1.55
CaO	0.00	0.00	0.00	0.96	0.69	1.49	0.00	0.00
Na_2O	0.55	0.54	0.43	10.97	11.30	10.66	0.75	0.16
K_2O	15.91	16.16	16.22	0.16	0.08	0.18	10.44	11.05
Total	100.90	99.70	99.25	99.56	100.75	98.37	93.03	93.26
Formula								
Si	3.04	3.01	3.01	2.98	2.99	2.96	3.12	3.21
Ti	0.00	0.00	0.00	0.00	0.00	0.00	0.03	0.02
Cr	0.00	0.00	0.00	0.00	0.00	0.00	0.00	0.00
Al	0.98	0.99	0.98	1.03	1.08	1.04	2.69	2.46
Fe	0.00	0.00	0.01	0.00	0.00	0.00	0.08	0.25
Mn	0.00	0.00	0.00	0.00	0.00	0.00	0.00	0.00
Mg	0.00	0.00	0.00	0.00	0.00	0.00	0.08	0.16
Ca	0.00	0.00	0.00	0.05	0.03	0.07	0.00	0.00
Na	0.05	0.05	0.04	0.94	0.95	0.92	0.10	0.02
K	0.93	0.96	0.96	0.01	0.00	0.01	0.91	0.97
Total	5.00	5.00	5.00	5.00	5.00	5.00	7.00	7.00
XMg molar							0.51	0.39

Note. XMg molar = Mg/(Mg + Fe).

Tab 2: Representative chemical composition of K-feldspar, plagioclase and white mica between porphyroclast and grain in mixed zones.

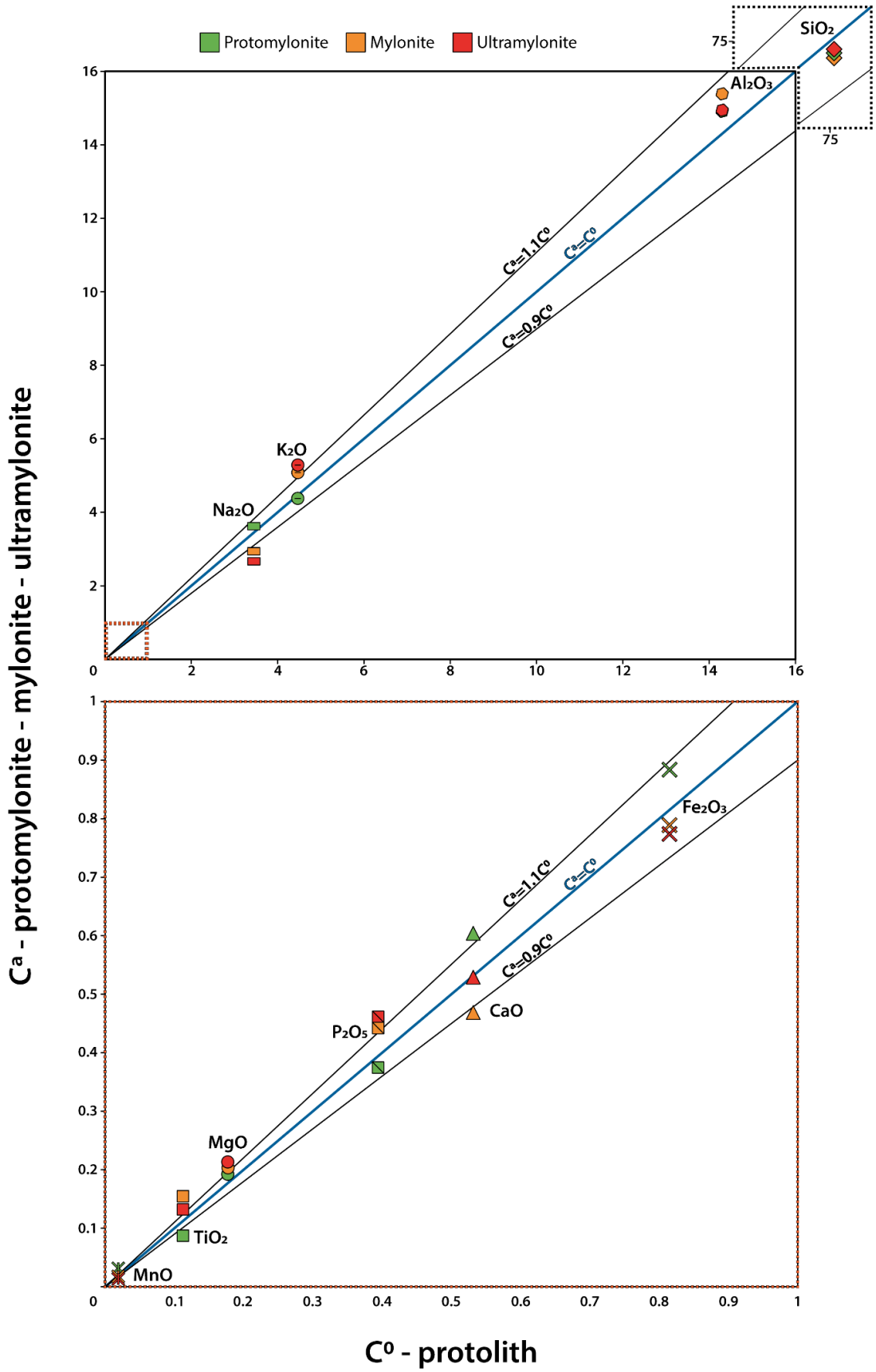

Fig. 12: Isocon diagram comparing the chemical composition of the protolith (C0) with those of protomylonite, mylonite and ultramylonite (Ca). The blue line (Ca=C0) represents the constant concentration, while the black lines represent 10% gains and 10% losses of components in Ca compared to C0.

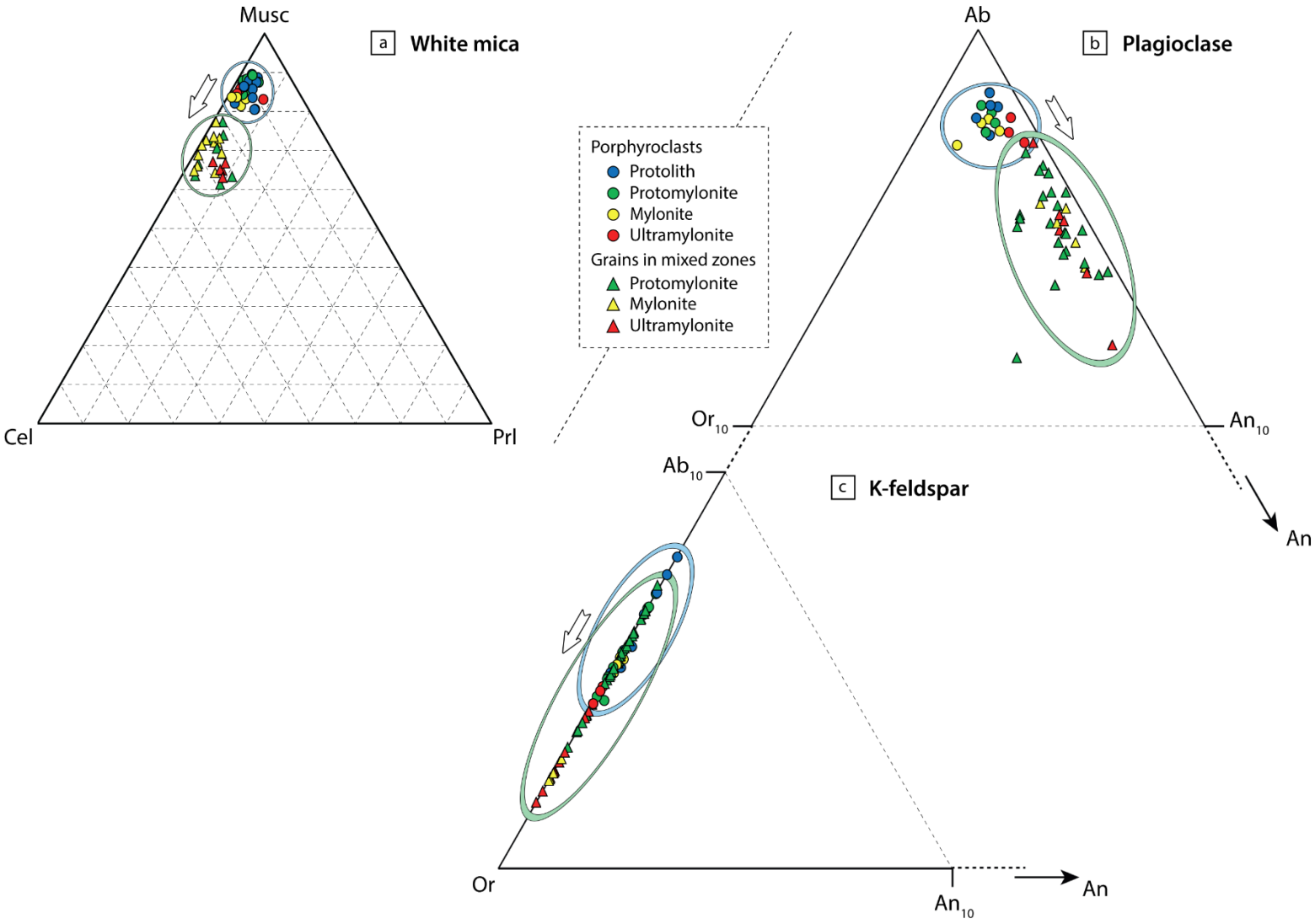

Fig. 13: (**a-b-c**) Chemical composition of white mica, plagioclase and K-feldspar. (**a**) Celadonite-Muscovite-Pyrophyllite ternary diagram shows composition of white mica grains from different stages of deformation. (**b-c**) Albite-Orthoclase-Anorthite combined ternary diagram for both plagioclase and K-feldspar composition is also presented for different stages of deformation.

To better characterize the P-T conditions based on mineral compositions, we further show two pseudosections in Fig. 14. Over a large range of pressures, temperatures and parageneses, K-feldspar, quartz, white mica, and plagioclase are all stable, i.e., the assemblage observed in high-strain domains. Nevertheless, in all of the predicted parageneses, additional accessory minerals are present in particular to incorporate Fe and Mg. Above 320–350°C, biotite is stable, whereas below this temperature range, chlorite is the stable phase. The predicted amount of these accessory minerals is very low (below 1% for chlorite and 2% for biotite; Fig. 14a), reflecting the very low concentration in Fe and Mg in the bulk-rock. The parageneses observed do not include any of the accessory

minerals predicted by the pseudosection (clinozoisite, chlorite and biotite). On the other hand, we observed the destabilization of biotite in the evolution from the protolith to mylonite/ultramylonite, suggesting that deformation occurred at temperature lower than the biotite-out reaction. The plagioclase in fine-grained polyphase layers shows compositional range between 3 and 8% of anorthite component. The molar isopleths in white mica (phengite) show that Si content of phengite is dependent on both, pressure and temperature and evolves from 3.06 per formula unit (p.f.u) in the high temperature/low-pressure side to 3.26 (p.f.u) in the low temperature/high-pressure side (Fig 14b). In addition, the X_{Mg} ratio ranges between 0.36 and 0.43 (Fig. 14b). Phengite compositions do not show considerable variation in Si content between the strain domains. Nevertheless, there is an important range of composition (Si p.f.u) from 3.16 to 3.23 and X_{Mg} molar ratio from 0.37 to 0.41 (Fig. 14b).

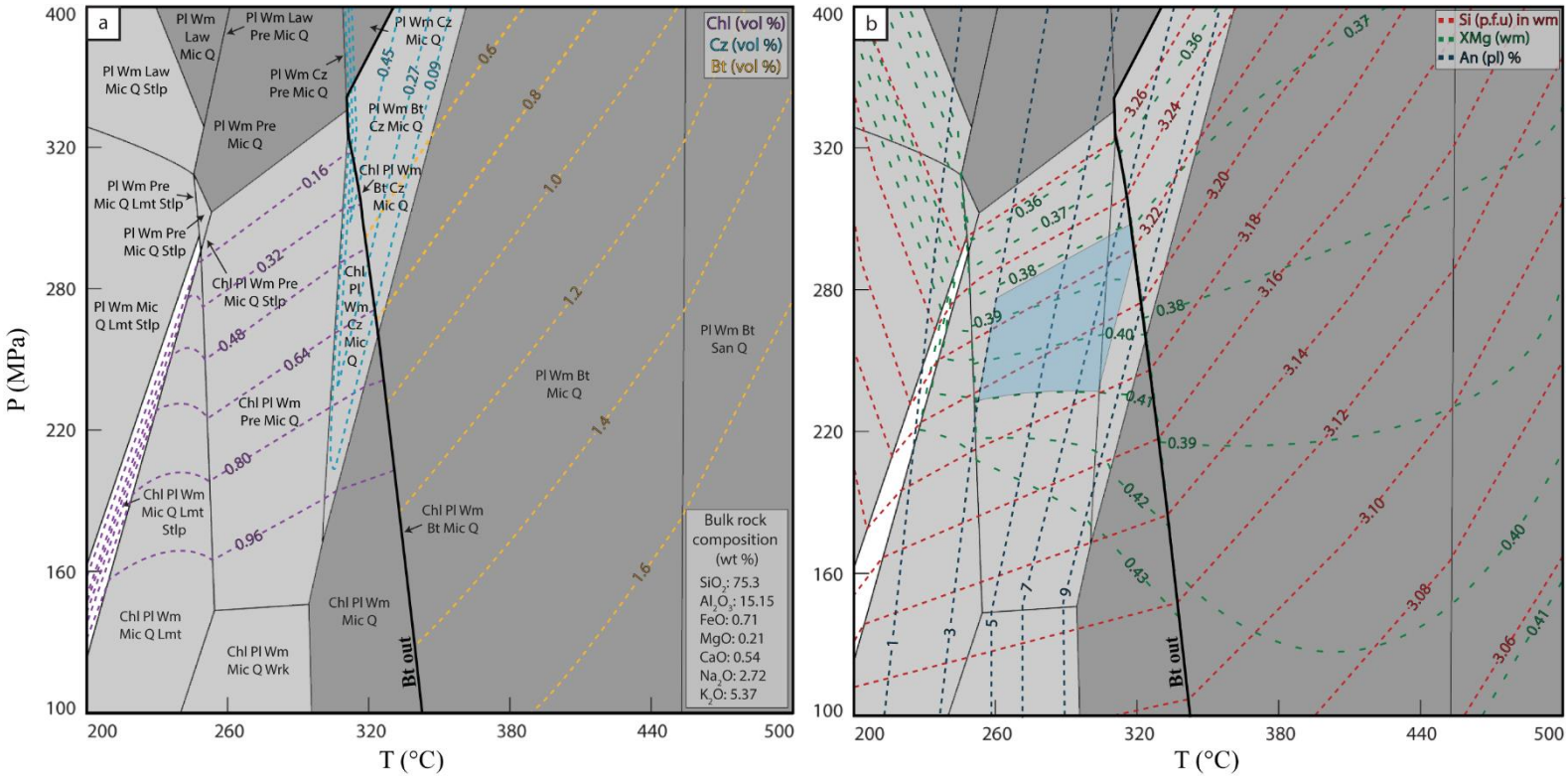

Fig. 14: (**a**) P-T pseudosection calculated in the CNKFMASH system with water in excess and the following solution models: Ti-Fe-Mg-Mn-biotite with compound formation (Powell and Holland, 1999), white mica (Coggon and Holland, 2002; Auzanneau et al., 2010), feldspar (Holland and Powell, 2003), and chlorite (Holland et al., 1998). Isopleth plots of the amount of chlorite, clinozoisite and biotite are also superimposed. (**b**) Representation of Si and XMg content in white mica isopleth plots and the compositional isopleths of anorthite component in plagioclase. The blue area represents the intersection of the compositional isopleths of Si and XMg in white mica and anorthite component in plagioclase. Phase relationships were determined using the Perple_X thermodynamic software (Connolly, 2005), version 6.7.9 with the thermodynamic database of Holland and Powell, (2004).

5. Discussion

5.1 P-T conditions of deformation

Across the South Armorican Shear Zone, previous petrological studies have shown that deformation occurred under greenschist to lower amphibolite facies metamorphic conditions, and strain localization took place below the low temperature biotite isograd (300–350°C; e.g. Gapais and White, 1982; Bukovská et al., 2016). Our analyzes show a constant composition of the phengite in mixed zones across the strain gradient (Fig. 13a), which suggest constant P-T conditions during deformation, as the rock composition is also relatively constant.

Given the rock chemical composition, the P-T conditions of deformation are also constrained by the Fe/Mg-bearing phases (Fig. 14). Nevertheless, their predicted abundance is very small (clinozoisite/chlorite: below 1%, biotite: below 2%) (Fig. 14a). Based on their observation of chlorite in layers, Bukovská et al. (2016) defined the stability field for deformation as associated with the parageneses of chlorite, plagioclase, white mica, clinozoisite, microcline and quartz. The absence of clinozoisite in their microstructural study is explained by the substitution of the latter by another Ca-bearing phase such as apatite (Bukovská et al., 2016). Considering our microstructural observations, this is consistent with the large amount of apatite documented in the deformed zones (e.g. Fig. 4b). In the actual parageneses of our deformed samples, biotite is absent, while large biotite grains were present in the magmatic assemblage. On the other hand, chlorite is also in most cases absent in our high-strain samples and all Fe and Mg are completely taken up by the phengite, as can be approximately inferred from its modal abundance and composition (Table 1–2). When chlorite is present, its textural relationship with the mylonitic assemblage is rather unclear, casting some doubt on the stability of chlorite during deformation. There is therefore much uncertainty on the P-T conditions of deformation, even if the destabilization of biotite from the magmatic paragenesis and the intersection of compositional isopleths suggest that deformation occurred at temperatures below the biotite-out reaction curve, i.e., below ~ 320–350°C, similar to the conclusions of Gapais and White (1982) and Bukovská et al. (2016) (Fig. 14).

5.2 Mechanisms of grain size reduction from protolith to ultramylonite

Dynamic recrystallization is a major process for grain size reduction during plastic flow (e.g. Etheridge and Wilkie, 1979; Behrmann, 1985; Fliervoet and White, 1995; Kruse and Stünitz, 1999; De Bresser et al., 2001; Kenkmann and Dresen, 2002; Stipp et al., 2002), provided that the conditions of deformation in terms of grain size, temperature, pressure and differential stress are so that the rock deform in the dislocation creep regime (Hirth and Tullis, 1992; Passchier and Trouw, 2005). The pervasive occurrence of dynamic recrystallization is demonstrated in quartz microstructures (e.g. Fig. 4h), and results in strong grain size reduction (Fig. 9). The recrystallization microstructures are characterized by plastically elongated quartz-rich layers subparallel to the foliation (Fig. 4h). Their grains reveal patchy or sweeping undulose extinction patterns and the presence of numerous subgrains. More rarely, small bulges and new grains of quartz are developed along grain boundaries of old quartz grains (Fig. 4i). These observations involve subgrains rotation recrystallization (SGR) as the dominant dynamic recrystallization process of quartz, with a minor and local contribution to bulging recrystallization (BLG; e.g. Drury and Urai, 1990).

Grain size reduction can also result from (1) the nucleation of new grains of different composition (e.g. Kruse and Stünitz, 1999; Kenkmann and Dresen, 2002; Kilian et al., 2011; Herwegh et al., 2011; Platt, 2015; Précigout and Stünitz, 2016), (2) melt-rock reactions (Dijkstra et al., 2002), and/or (3) cataclasis/fracturing (e.g. Hippler and Knipe, 1990; Stünitz et al., 2003; Kruhl et al., 2007; Viegas et al., 2016). Owing to the lack of melt-rock reactions in shear zones formed under greenschist facies conditions, melting cannot be considered for grain size reduction. In these conditions, feldspar is generally expected to be mechanically strong, and grain size reduction is usually associated with nucleation, fracturing and reaction (e.g. Simpson and Wintsch, 1989; Hippertt, 1998; Tsurumi et al., 2003; Ree et al., 2005; Menegon et al., 2006).

The effect of nucleation of new grains to reduce the grain size is twofold. First, in itself, the nucleation of small grains is achieved at the expense of larger grains, which are affected by dissolution (Kilian et al., 2011), e.g. K-feldspar formed at triple junction in quartz aggregates (Fig. 4f). Second, nucleation of phase A within a cluster of grains of phase B result in pinning phase B grain boundaries (Fig. 3a-b; e.g. Kruse and Stünitz, 1999; Herwegh and Jenni, 2001; Herwegh and Berger, 2004; Song and Ree, 2007; Brodhag and Herwegh, 2010; Linckens et al., 2015; Hunter et al., 2016; Cross and

Skemer, 2017; Gilgannon et al., 2017). In the early stages of deformation, quartz-rich layers reveal the presence of tiny white mica grains located along quartz grain boundaries (Fig. 3a-b). The small micas formed at grain boundaries inhibit the motion of quartz grain boundaries (Fig. 3a-b; e.g. Herwegh and Jenni, 2001; Linckens et al., 2015; Gilgannon et al., 2017). Such pinning acts against grain growth and maintains a small grain size (e.g. De Ronde et al., 2005; Linckens et al., 2015). This combined effect of nucleation to decrease the grain size is apparent in mylonites and ultramylonites, where the grain size of quartz is significantly larger in domains essentially composed of quartz compared to domains composed of quartz and feldspar (Fig. 9).

Feldspar grain size reduction is mainly induced by a combination of fracturing and nucleation, such as replacement reaction of K-feldspar by plagioclase (Fig. 4g). This combination leads to the breakdown of the large porphyroclasts into smaller fragments (Fig. 6). Fracturing of feldspar and nucleation microstructures were described in natural shear zones deformed under greenschist facies conditions (e.g. Fitz Gerald and Stünitz, 1993; Ree et al., 2005) similar to the ones in this study (Fig. 2b). In addition to its role of reducing the grain size, fracturing also enables fluid access and transport of elements required for nucleation to reduce the grain size (Fitz Gerald and Stünitz, 1993). Consequently, the dominant grain size controlling processes are dynamic recrystallization (quartz), nucleation of new grains with a different composition (feldspar and mica) and fracturing (feldspar).

5.3 Formation of a weak mica network

Mica is typically viewed as the weakest phase in granitoid rocks (e.g. Tullis and Wenk, 1994). The micas in the protolith are present as undeformed or only slightly bent magmatic phases. Locally, cracks filled with mica crosscut quartz-rich layers and typically occur at the tip of large magmatic micas (Fig. 2c). With increasing strain, the protomylonite exhibits newly formed micas that tend to organize into proto-layers, defined as an alignment of several micas parallel to each other and cutting across quartz-rich layers or precipitate along quartz grain boundaries (Fig. 3a-b). When located at quartz grain boundaries, these micas locally induce pinning of grain boundaries (e.g. Fig. 3a). With further evolution, an anastomosing interconnected network of monophase layers composed of mica starts to form (Fig. 3c). The onset of interconnection occurred where trails of very fine-grained phengites connect the large inherited grains of micas (Fig. 3c-d).

The formation of an interconnected weak layer microstructure requires the coalescence of the weak phases. The experiments of Dell'Angelo and Tullis (1996) investigated weak phase interconnection of quartz, while that of Holyoke and Tullis (2006) was more focused on mica interconnection. The latter proposes that stress concentration and brittle deformation in strong phases such as feldspar may induce weaker grains to become interconnected. Although the brittle deformation is mostly localized in feldspar porphyroclasts with a large number of fractures (Fig. 2b), cracks filled with mica are also observed in quartz-rich layers (e.g. Fig. 2c). These cracks occurred essentially at the tips of large mica grains where a phase strength contrast between quartz and mica is present. According to Holyoke and Tullis (2006), the stress concentration adjacent to weak phases may induce local brittle deformation, and could explain the formation of mica cracks crosscutting the quartz-rich layers. These cracks which are best preserved in low-strain domains, with limited ductile overprint, may enhance fluid access and then nucleation of grains that act as shear band precursors (e.g. Bukovská et al., 2016; Wehrens et al., 2016). Brittle deformation as evidenced by fractures and cracks is thus considered here as an initial important mechanism for localization of deformation, although its importance later decreases with a switch in dominant plasticity (e.g. Fusseis and Handy, 2008). The nucleation of micas in cracks and along quartz grain boundaries combined with the initial plasticity of old grains could lead to the interconnection of these weak phases. The low-temperature conditions of the SASZ deformation are in agreement with such an interplay between brittle and plastic deformation active at greenschist conditions (e.g. Passchier, 1984; Fusseis and Handy, 2008; Wehrens et al., 2016).

5.4 Phase mixing with increasing strain

5.4.1 Evidence for nucleation of new grains

The transition from weakly deformed samples to highly deformed ones is accompanied by grain size reduction and a gradual dispersion of quartz grains from aggregates to mixed-phase zones (Fig. 9). In the protolith, the protomylonite, and in some low-strain domains in mylonite, the quartz is arranged in quartz-rich layers (Fig. 3c-4h), while in high-strain domains in mylonite and ultramylonite the quartz is intimately mixed with other phases (Fig. 7c-e). Indeed, there is an increase in mixing concomitant with an

increase of strain (Fig. 10). There is no or limited evolution between the mylonite and ultramylonite, neither between the protolith and protomylonite. The sharp increase towards mixing corresponds micro-structurally to the increase in polyphase mixed zones within mylonites (e.g. Fig. 4a-c-d). It is more than likely that between quartz-rich layers with small amounts of white mica and the first documented polyphase layers, i.e. fine-grained mixed zone rich in white mica and quartz, there must be transitions (Fig. 3b-e). The appearance of monophase layers of white mica may point towards such transitional microstructures (Fig. 3c).

Dynamic recrystallization during plastic deformation, as a result of either SGR or grain boundary bulging, may reduce the grain size, but it is not expected to induce alone phase separation (Kilian et al., 2011). An additional process is required such as e.g. nucleation of new grains in dilatant sites to induce a spatial rearrangement of mineral phases, giving rise to phase mixing. Evidence of nucleation are first observed in the weakly deformed domains where fine-grained white micas occur along quartz grain boundaries (Fig. 3a-b), and in the form of small oriented particles in feldspar (Fig. 2d). Micas also filled fractures in feldspar clasts and quartz aggregates (Fig. 2b). Evidence of phase nucleation also includes the occurrence of isolated K-feldspar grains located at triple junctions in quartz-rich layers and in newly formed fine-grained mixed-phase zones (Fig. 4e-f-g; e.g. Kilian et al. 2011), and the local formation of tails of fine-grained quartz and K-feldspar, which nucleate around K-feldspar clasts in the ultramylonite (Fig. 5c). Thus, quartz aggregates are progressively disintegrated by dispersed feldspar with increasing strain. In addition, the formation of mixed-phase zones within clasts tails may be due to the nucleation of new phases (Fig. 5c; e.g. Kruse and Stünitz, 1999). These microstructures are in agreement with the increasing amount of grain contact between quartz and feldspar grains with increasing strain (Fig. 10). Phase nucleation is also consistent with the contrasted quartz LPO observed between quartz-rich layers and mixed-phase zones (Fig. 11). In these mixed phase zones, the quartz LPO is dispersed with respect to adjacent quartz-rich layers, which could be the result of enhanced nucleation in mixed-phase zones (Fig. 11). A similar process has been already documented in several experimental and natural studies to cause grain size reduction, loss of LPO and phases mixing (e.g. Kilian et al., 2011; Précigout and Stünitz, 2016; Cross and Skemer, 2017).

5.4.2 Driving force for nucleation

The formation of fine-grained polyphase assemblage by nucleation of new grains may be enhanced by chemical reactions (e.g. Stünitz and Tullis, 2001) and/or grain-boundary sliding (GBS; e.g. Linckens et al., 2014; Linckens et al., 2015). The nucleation of new grains with a different composition such as e.g. small and scattered white mica in dilatant sites may attest for intergranular fluid circulation (Fig. 3a-b; Fig. 4f; e.g. Oliot et al., 2014). The fluid circulation allows the transport of dissolved elements required for nucleation. In the case studied here, chemical variations—even small—are systematically observed between the porphyroclasts and newly formed grains (Fig. 13)**.** Thus, a purely mechanical phase mixing is considered as very unlikely because of these chemical variations, implying instead mass transfer via fluids. Element transport is manifested by the slight enrichment of K_2O-P_2O_5-MgO and depletion of Na_2O with increasing strain (Fig. 12). All domains of the strain gradient from protolith to ultramylonite contain white mica. White mica porphyroclasts show quite homogeneous muscovite-rich composition, whereas fine-grained white mica is enriched in the Mg-celadonite-component (phengite; Fig. 13). This gradient of reaction appears coeval with the investigated strain gradient and may explain the slight enrichment in MgO in the bulk composition. The enrichment of K2O and depletion of Na2O may be a result of the nucleation of new Or-rich, K-feldspar and An-rich plagioclase with increasing strain. However, the variations in composition are too small to be interpreted with any level of confidence. Therefore, we suggest that the scale of mass transport is limited in order to maintain a quite homogeneous bulk composition, but it allows the local transport of elements required for chemically-driven nucleation.

To achieve the progressive breakdown of quartz aggregates with increasing strain by nucleation of new phases, GBS is an additional process that may be invoked. GBS is one important deformation mechanism that commonly combines with other mechanisms to deform any fine-grained mixed-phase zones (e.g. Raj and Ashby, 1971; Ashby and Verrall, 1973; Passchier and Trouw, 2005; Langdon, 2006; Warren and Hirth, 2006; Svahnberg and Piazolo, 2010; Miranda et al., 2016). When the displacement along grains is not fully accommodated, this may induce the opening of cavities into which the material can diffuse (e.g. Fliervoet et al., 1997; Fusseis et al., 2009; Kilian et al. 2011; Platt, 2015; Précigout and Stünitz, 2016; Précigout et al., 2017; Gilgannon et al., 2017). Nucleation of new grains in cavities inhibits grain growth and may promote the activity of grain size

sensitive creep (e.g. Herwegh et al., 2011; Menegon et al., 2015; Gilgannon et al., 2017). In our case, several observations are consistent with a component of GBS during deformation and following nucleation in cavities, such as (1) the dispersion and weakening of pre-existing moderate LPO (Fig. 3.11; Jiang et al., 2000; Bestmann and Prior, 2003), (2) the relatively equant grain shape of quartz and K-feldspar (Fig. 7d-f; Passchier and Trouw, 2005), (3) the increase in mixing degree of quartz and feldspar grains with increasing strain due to e.g. phase nucleation (Fig. 10c; Kruse and Stünitz, 1999), and (4) the homogeneous mixing in the alternating fine-grained polymineralic layers of ultramylonite (Fig. 5a; Fliervoet et al., 1997) From the above, it is concluded that the main driving forces for nucleation are due to the combination of chemical reactions and grain-boundary sliding under the presence of fluids.

5.5 Succession of deformation mechanisms and weakening processes

5.5.1 Evolution from protolith to protomylonite

Increasing strain from protolith to protomylonite resulted in the development of interconnected monophase layers of mica (Fig. 3c). The initial deformation of old magmatic mica grains by kinking, bending and recrystallization along the edges suggests a process of crystal plastic deformation (Holyoke and Tullis, 2006). This process combined with the nucleation of micas in cracks and along quartz grain boundaries may have promoted the interconnection of these weak phases in the protomylonite. The formation of a network of mica-bearing monophase layers have also been described in several granitic rocks deformed under greenschist to amphibolite facies conditions (Berthé et al., 1979; Gapais, 1989; Vernon et al., 2004; Johnson and Brown, 2004; Bukovská et al., 2016; Hunter et al., 2016, Wehrens et al., 2016, 2017) and is a major process for the weakening of the rock and the localization of deformation (e.g. Holyoke and Tullis, 2006; Menegon et al., 2008; Montési, 2013; Gardner et al., 2017). In addition, the reaction progress forming weak material as phengite in high-strain polyphase layers and ultramylonite is also expected to promote the localization of shear deformation, particularly when local grain size reduction in involved (Fig. 4a; e.g. Keller et al., 2004; Fossen and Cavalcante, 2017).

A recent study characterized initiation and early evolution of shear bands in the

Questembert granite (Bukovská et al., 2016). The most deformed domain of the strain gradient cover in their study showed similar features to the so-called low-strain protomylonite or even low-strain mylonite in the present study (Fig. 8b-c). Indeed, they also pointed out the presence of coarse-grained quartz-rich layers and large porphyroclasts alternating with fine-grained polyphase layers comprising quartz, white mica and K-feldspar (Fig. 3). Unlike their study, we presented additional stages of evolution characterized by significant decrease in grain size and increase in mixing zones (Fig. 4–5).

5.5.2 Evolution from protomylonite to ultramylonite

5.5.2.1 General features

Increasing strain led to the formation of high-strain mylonite and ultramylonite characterized by the disintegration of most of large feldspar porphyroclasts and coarse-grained quartz-rich layers (Fig. 8e). This evolution results in the development of well-mixed fine-grained zones with a few preserved quartz-rich layers, forming alternating layers in the ultramylonite (Fig. 5–7). This is consistent with studies showing that in quartzo-feldspathic rocks deformed under greenschist facies conditions, mylonites and ultramylonites are composed largely of fine-grained mixed-phase zones (e.g. Stünitz and Fitz Gerald, 1993; Fliervoet et al., 1997). The fine-grained mixed-phase zones are commonly observed in the form of homogeneous mixing of all phases (e.g. Fitz Gerald and Stünitz, 1993; Fliervoet et al., 1997; Tsurumi et al., 2003), or in the form of alternating layers of fine-grained mixed-phase zones (e.g. Ree et al., 2005; Ishii et al., 2007). The geometrical organization of these zones in our study is close to the latter observations. Nevertheless, their compositions differ from published studies (Behrmann and Mainprice, 1987; Fitz Gerald and Stünitz, 1993; Fliervoet et al., 1997; Tsurumi et al., 2003; Ree et al., 2005; Ishii et al., 2007), where mixed zones are principally composed of plagioclase + K-feldspar with less proportion of quartz ± mica ± other minerals.

5.5.2.2 Temporal sequence of protolith-protomylonite-mylonite-ultramylonite

According to Augier et al. (2011), the most deformed ultramylonitic domain in the core of the shear zone presents locally less deformed rock portions that correspond to

lower-strained domains. Identifying these relics of less deformed rocks suggests that the ultramylonite domains are the evolution, with increasing strain, of low-strain domains. An additional evidence in favor of this evolution with strain is revealed by CL-colors and textures. The pink feldspar grains and the light blue plagioclase porphyroclasts present in the ultramylonite are already observed as reaction rim products, in the protolith and protomylonite (Fig. 6). Furthermore, the homogeneous bulk rock composition (Table. 1; Fig. 12) and the constant composition of the new nucleated phengites throughout the strain gradient (Fig. 13a) suggest that the protolith is identical in all strain facies. Consequently, high-strain domains (ultramylonite and mylonite) are interpreted as the evolution, with increasing strain, of low strain domains (protolith and protomylonites).

5.5.2.3 Preserved quartz-rich layers and fine-grained mixed zones in high-strain mylonite and ultramylonite

The well-developed SPO in the preserved quartz-rich layers in mylonite and ultramylonite, combined with the typical SGR recrystallization microstructures and the dominance of prism-<a> and rhomb—<a> active slip systems suggest dislocation creep as the dominant deformation mechanism (Fig. 11a-c; Passchier and Trouw, 2005). As indicated by the nearly random LPO of fine quartz grains at the rim of the layers, the quartz-rich layers are locally dismembered and incorporated in the polyphase mixed zones (Fig. 11a-c). Since we consider the ultramylonite and its fine-grained polyphase layers as the most evolved domains of the studied strain facies, the remaining quartz-rich layers in this domain must be considered as relics of an original mylonitic fabric before total disaggregation (e.g. Gilgannon et al., 2017). Although the quartz LPO in quartz-rich layers near the mixed zones is initially moderate, the evolution of the LPO fabric between these two domains suggests that during the disaggregation the quartz LPO dispersed (Fig. 11).

The polyphase mixed zones are characterized by a very small grain size (Fig. 9b), a weaker LPO relative to quartz-rich layers (Fig. 11), a higher degree of phase mixing (Fig. 7–9), and an equant shape of quartz grains (Fig. 7). Based on these observations, we argue that deformation in the fine-grained mixed-phase zones is dominated by grain size-sensitive (GSS) mechanisms, including a contribution of GBS (e.g. Behrmann and Mainprice, 1987; Rutter and Brodie, 1988; Olgaard, 1990; Linckens et al., 2011). GBS contributes to the dispersion of phases, reflected in their anticlustered distribution (Fig.

10c), the homogeneous mixing in the alternating layers (Fig. 5a), and to the weakening of the LPO in mixed-phase zones (Fig. 11; e.g. Behrmann and Mainprice, 1987; Stünitz and Fitz Gerald, 1993; Kilian et al., 2011). Some plagioclase clasts are also preserved and scattered throughout the microstructure in the ultramylonite (Fig. 5a-b). These plagioclases are characterized by a grain shape mostly rounded with convex grain boundaries, which is one evidence for a mechanically strong phase (e.g. Naziri et al., 1975; Stünitz and Fitz Gerald, 1993). Such microstructures are observed in the study of Lonka et al. (1998) and may reflect the progressive rotation of plagioclase clasts as rigid body in a ductile fine-grained zone during diffusion-accommodated GBS. The increase in GSS contribution to overall strain is in turn a weakening process (e.g. Boullier and Gueguen, 1975, Kerrich et al., 1980; De Bresser et al., 2001; Stünitz and Tullis, 2001; Menegon et al., 2015; Précigout and Stünitz, 2016) resulting in further strain localization in the deforming domain.

6. Conclusion

An evolution in microstructures and deformation mechanisms occurred across the different finite strain domains developed across the South Armorican Shear Zone in the Questembert granite. The microstructural, chemical and EBSD analyzes allow us to draw the following conclusions:

1. The transition from protolith to ultramylonite is associated with grain size reduction, which occurred by dynamic recrystallization, nucleation of grains with a different composition and fracturing.

2. The transition from protolith to ultramylonite is also associated with a large increase in phase mixing. Phase mixing is mainly controlled by nucleation, whose driving force involves a combination of chemical reactions and grain-boundary sliding/dilatancy.

3. A reduced grain size may have triggered a transition in deformation mechanism with increasing strain. The quartz-rich layers, which display moderate LPO patterns, are deformed predominantly by dislocation creep, whereas the loss of LPO in polyphase fine-grained mixed zones, where strain has been strongly localized, suggests that diffusion creep and GBS became the dominant deformation mechanism. GBS is also highlighted by the occurrence of isolated K-feldspar grains located at triple junctions, and contributing to the dispersion of phases.

4. The early brittle deformation in low-strain domains, such as cracks in quartz aggregates, enhances fluid access and chemical reactions/nucleation to reduce grain size. A consequence of the formation of cracks and fluid-assisted nucleation is the interconnection of weak mica monophase layers in protomylonite.

5. With increasing strain, the mica-bearing layers evolve first into an interconnected network of fine-grained polyphase layers enriched in quartz and phengite in protomylonite and mylonite, and then by layers of fine-grained polyphase mixing composed of K-feldspar, quartz and phengite homogeneously mixed in mylonite and ultramylonite.

6. The strain weakening of the rock is a two-step process and the nature of the weak material, mica then fine-grained polyphase mixed zones that can deform by

7. diffusion-accommodated grain boundary sliding, changes along with strain.

Although the pressure-temperature path of the shear zone is poorly constrained, the constant composition of the mica throughout the strain gradient suggests that the succession in weakening processes is not related to changing P-T conditions but to the accumulation of strain itself.

Afin de mieux appréhender les mécanismes liés au développement des zones de cisaillement et l'effet lié à l'interaction entre la déformation et les réactions minérales sur la rhéologie des roches, nous avons effectué des expériences de déformation en cisaillement à l'aide d'un dispositif de déformation de type Griggs. Ces expériences ont été réalisées sur des assemblages biphasiques représentatifs de la croûte inférieure et, pour comparaison, sur des assemblages monophasés. Les expériences de déformation présentent l'avantage de pouvoir contrôler certaines variables, telles que la vitesse et la quantité de déformation. De telles expériences offrent ainsi l'occasion d'étudier l'évolution de la résistance mécanique, qui est fonction des processus actifs responsables du développement des zones de cisaillement. Le chapitre IV expose idéalement la capacité dont la déformation fait preuve pour faciliter les réactions minérales, la nucléation, la formation de mélange de phases à grains fins et, inversement, comment une telle évolution des microstructures aboutit à la localisation de la déformation et à l'affaiblissement des assemblages. Cette interaction entre la déformation et les réactions minérales est susceptible d'avoir de fortes répercussions sur le développement et la durabilité des zones de cisaillement de la croûte terrestre.

N.B. : Ce chapitre fait l'objet d'un article soumis dans la revue Journal of Structural Geology. Similairement au chapitre précédemment, le chapitre IV est adapté afin d'éviter les redondances.

CHAPTER IV

Strain localization and weakening induced by interplay between deformation and mineral reactions: Insights from experimentally deformed plagioclase-pyroxene assemblages

CONTENTS

1. Introduction

Strain localization and resulting shear zones are considered to be fundamental features of plate tectonics on Earth (e.g. Tackley, 1998; Bercovici and Ricard, 2012). They accommodate a large amount of strain and have a direct control on rock rheology, so their development is critical to be addressed to understanding the dynamics of the lithosphere. The formation of viscous shear zones has been considered as resulting from one or several processes of strain-induced weakening, which expresses as a stress drop at constant strain rate or an increase of strain rate at constant stress (e.g. Paterson, 2013). Possible weakening mechanisms include: (1) Geometric and/or (2) fabric softening, (3) a change in deformation mechanism (e.g., due to grain size reduction), (4) fracturing, (5) metamorphic mineral reactions, (6) shear heating (7) water- or (8) melt-induced weakening (e.g. Poirier, 1980; White et al. 1980; Burlini and Bruhn, 2005). While some of these mechanisms apply to monophase rocks, others are more typical of polyphase materials.

As a starting point, laboratory-derived flow laws have been determined for the deformation of monophase materials to understand the rheology of important rock-forming minerals in the viscous regime of the lithosphere, including olivine (e.g., Chopra and Paterson, 1981), quartz (Paterson and Luan, 1990), plagioclase (Rybacki and Dresen, 2000; Dimanov et al., 1999) and pyroxene (Bystricky and Mackwell, 2001). For instance, the experiments of, e.g., Rybacki and Dresen, (2000) and Chen et al., (2006), have shown that water may considerably reduce the strength of aggregates of feldspar and pyroxene. Flow laws and grain size reduction by dynamic recrystallization are also best described in deformation experiments of monophase materials (e.g. White et al. 1980, Schmid 1982, Rutter and Brodie, 1988). These experiments gave rise to a potential source of weakening induced by a transition from grain-size-insensitive to grain-size sensitive creep, but this transition is not expected to occur in monophase aggregates because grain growth is extensive enough at elevated temperature to counteracts the weakening effect of grain size reduction (e.g. De Bresser et al., 2001).

Except for very minor cases, the lithosphere consists of polyphase rocks. Thus, a growing body of literature has also addressed the rheology of polyphase material, given the fact that such a rheology is likely to be different from that of monophase ones (e.g. Bürgmann and Dresen, 2008). The presence of additional phases in polyphase aggregates inhibits grain growth and controls microstructures through pinning (e.g. Olgaard and

Evans, 1986; Herwegh et al., 2011). Hence, the dominant deformation mechanism can be expected to differ as a consequence of phase interactions. Of particular interest, the rheology of polyphase aggregates for gabbroic composition has a fundamental importance for understanding the mechanical behavior of the oceanic and lower crusts; mafics are the most abundant rock types in these crustal layers (e.g. Weaver and Tarney, 1984; Christensen and Mooney, 1995). However, experimental studies of high-temperature deformation of gabbroic composition are still comparatively rare (e.g. Dimanov et al., 2003, 2007; Dimanov and Dresen, 2005), and none of these studies have considered mineral reactions. They only focused on the role of secondary phases, grain size, water content, stress and spatial distribution of grains to account for changing flow stress and dominant deformation mechanism in polyphase feldspar-pyroxene aggregates. Other studies suggest nevertheless that the occurrence of mineral reactions during viscous flow may have the potential to weaken rocks and consequently localize strain (e.g. Stünitz and Tullis, 2001; De Ronde et al., 2004, 2005; Getsinger and Hirth, 2014; Marti et al., 2017, 2018).

Strain localization and weakening in viscous shear zones as a result of mineral reactions are mostly achieved through changes in P-T conditions (e.g. Gapais, 1989; Newman et al., 1999) or through fluid-rock interactions (e.g. Austrheim, 1987; Menegon et al., 2015). Changes in P-T conditions commonly occur during oceanic and continental subduction and exhumation along crustal-scale shear zones, where the thermodynamic disequilibrium promotes the growth of new stable minerals (e.g. Gerya et al., 2002; Jamtveit et al., 2016). In addition, shear zones represent permeable pathways for fluids that enhance diffusion and strongly catalyze mineral reactions under both, low (e.g. Fitz Gerald and Stünitz, 1993; Newman and Mitra, 1993; Mansard et al., 2018) and high metamorphic grades (e.g. Brodie, 1980; Boundy et al., 1992; Glodny et al., 2003). The importance of mineral reaction lies in the possible grain size reduction and change in deformation mechanism leading to a switch to grain-size sensitive creep, giving rise to substantial weakening (e.g. Etheridge and Wilkie, 1979; Olgaard, 1990; Stünitz and Fitz Gerald, 1993; Fliervoet et al., 1997; De Bresser et al., 1998; Kruse and Stünitz, 1999; De Bresser et al., 2001; Kenkmann and Dresen, 2002; Precigout et al., 2007; Raimbourg et al., 2008; Linckens et al., 2011; Kilian et al., 2011; Viegas et al., 2016). Mineral reactions also contribute to form mixing zones that play an important role of weakening because the pinning of grain boundaries impedes grain growth and keep the grain size small (e.g. Etheridge and Wilkie, 1979; Herwegh et al., 2011). In this contribution, we investigate

the evolution of microstructures in two-phase plagioclase-pyroxene shear experiments, which provide important insights on weakening mechanisms and localization of deformation during shear zone development. This study is an ideal example of how deformation can facilitate metamorphic reactions, heterogeneous nucleation, formation of fine-grained phase mixtures, and how conversely such an evolution in microstructures eventually results in strain localization and weakening of polyphase aggregates. This also shows the importance of taking into account the behavior of polyphase assemblages when dealing with the behavior of the lithosphere.

2. Results

2.1 Mechanical data

The terminology used to describe stress-strain curves is explained in Fig. 1a. The same color code is used for different temperatures, and a cross indicates when the forcing blocks started to slip at the sample interface.

2.1.1 Pure plagioclase and pyroxene samples

The pure plagioclase experiments at 800 °C and 900 °C show similar types of stress-strain curves. At 800 °C the sample shows more than 200 MPa higher flow stress than the sample deformed at 900 °C (Fig. 1b), and both samples deform at stresses below the Goetze criterion. The Goetze criterion ($\Delta\sigma \leq P_{conf}$) is used as an empirical criterion to delineate stress conditions where rocks deform plastically (Kohlstedt et al., 1995). In both experiments, the differential stress slightly decreases after reaching a peak stress at $\gamma < 1$ (Fig. 1b). The pure pyroxene experiment with a larger initial grain size fraction (powder sieved to extract a grain fraction $\leq$40 μm) is very strong at 900 °C, reaching a peak stress of ~1600 MPa at γ ~0.6, well above the Goetze criterion (Fig. 1b). The experiment was stopped during the stress drop as only brittle deformation was expected to occur at these high differential stresses.

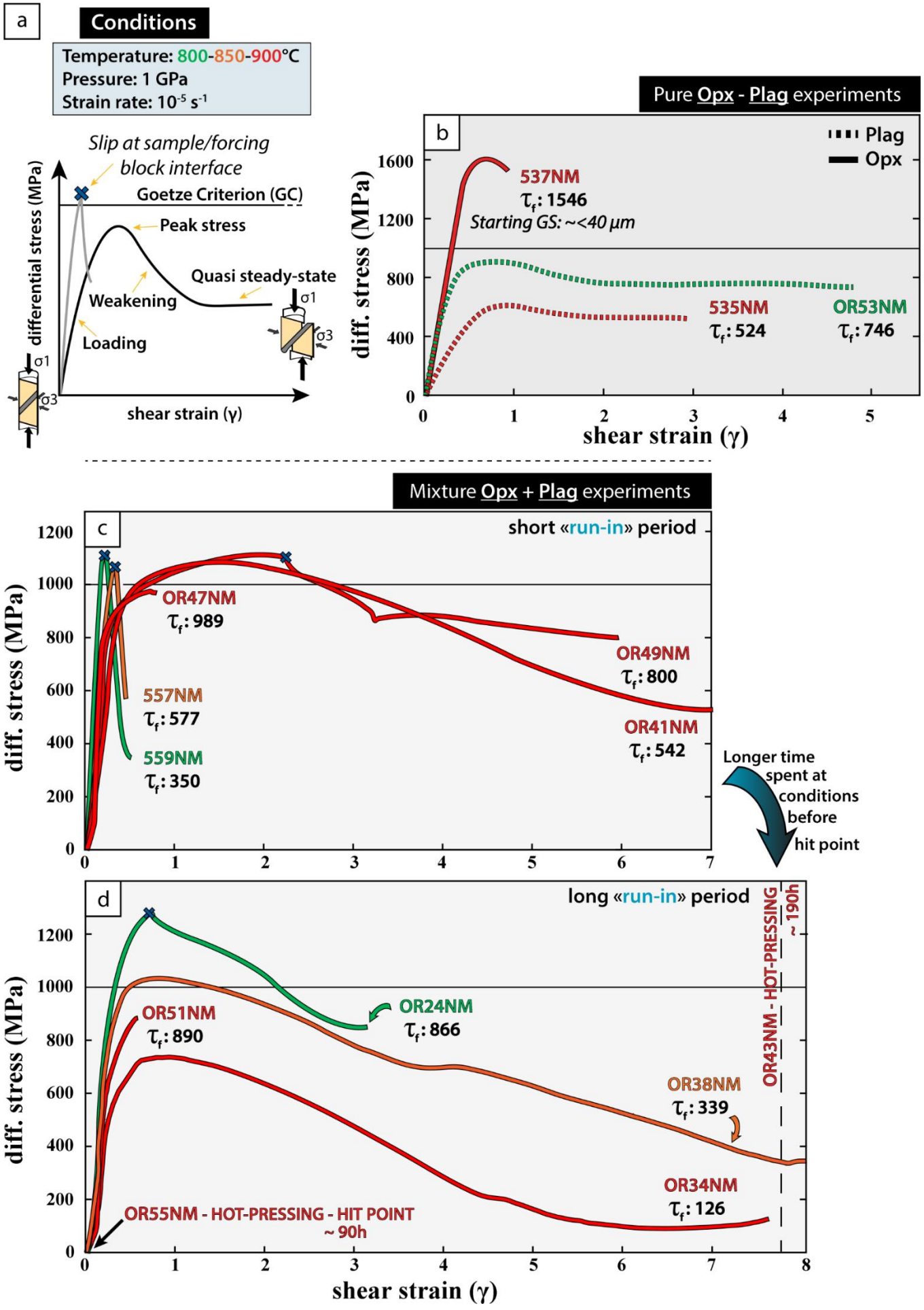
a
Conditions
Temperature: 800-850-900°C
Pressure: 1 GPa
Strain rate: 10-5 s-1
Slip at sample/forcing block interface
Goetze Criterion (GC)
Peak stress
Quasi steady-state
Weakening
Loading
differential stress (MPa)
shear strain (γ)
σ1
σ3
Pure Opx - Plag experiments
b
Plag
Opx
537NM
τf: 1546
Starting GS: ~<40 µm
535NM
τf: 524
OR53NM
τf: 746
diff. stress (MPa)
shear strain (γ)
Mixture Opx + Plag experiments
c
short «run-in» period
OR47NM
τf: 989
OR49NM
τf: 800
557NM
τf: 577
OR41NM
τf: 542
559NM
τf: 350
Longer time spent at conditions before hit point
d
long «run-in» period
OR43NM - HOT-PRESSING ~ 190h
OR51NM
τf: 890
OR24NM
τf: 866
OR38NM
τf: 339
OR34NM
τf: 126
OR55NM - HOT-PRESSING - HIT POINT ~ 90h
diff. stress (MPa)
shear strain (γ)

Fig 1: Differential stress (MPa) versus shear strain (γ) curves. (**a**) Set of terms used to describe the mechanical data. (**b**) Stress-strain curves showing the mechanical behavior of two pure plagioclase samples deformed at 800 and 900 °C. The mechanical curve of a pure pyroxene sample deformed at 900 °C with an initial coarser grain size (<40 μm) is also plotted. (**c-d**) Set of experiments deforming an Opx + Plag mixture at different temperatures (800, 850 and 900 °C), and at constant confining pressure, strain rate and water content. These experiments are separated in two graphs according to the different duration of the "run-in" section. The color coding refers to the temperature of the experiments.

2.1.2 Plagioclase—pyroxene mixtures

The experiments on phase mixtures can be divided into two different series depending on the time spent at P-T conditions before the contact between the σ_1 piston and top alumina piston (hit point). After a short "run-in" period (<65h at temperature and pressure conditions before hit point), the pyroxene + plagioclase (Opx + Plag) mixtures are very strong at 800 °C (559NM) and 850 °C (557NM), reaching a peak stress of ~ 1100 MPa at $\gamma \sim 0.3$ (Fig. 1c). Then, $\Delta\sigma$ drops suddenly far below the Goetze criterion due to slip at one of the sample/forcing block interfaces. The samples deformed at 900 °C show peak stress values close to those at 800 and 850 °C, but for higher shear strain (γ ~1.5). At 900 °C, there is a gradual and pronounced weakening after peak stress. In one case, slip occurs at the forcing block interface, and the differential stress decreases below the Goetze criterion before stabilizing around 800 MPa (OR49NM). In the other case, the sample weakens continuously with a reduction of ~50% in differential stress, until reaching a quasi-steady-state shear stress around 550 MPa near $\gamma \sim 6.5$ (OR41NM).

After a longer "run-in" period (> 70h at temperature and pressure conditions before the hit point), the Opx + Plag mixtures show a less steep loading curve compared to shorter run-in period experiments (Fig. 1d), indicating a lower strength of the samples (the loading curve in the solid-medium apparatus at high temperatures is not a purely elastic, but involves a component of permanent sample strain; Richter et al., (2018). At 800 °C, a stress drop occurs at a peak stress value near γ ~0.7 (above the Goetze criterion at ~ 1250 MPa), probably caused by slip at one sample-forcing block interface (OR24NM). In contrast, the other samples at 850 °C (OR38NM) and 900 °C (OR34NM) weaken continuously after peak stress, and then approach a quasi-steady-state shear stress at $\gamma \sim 7.8$ and $\gamma \sim 6$, respectively (Fig. 1d). In these last 2 experiments, the weakening is very pronounced with ~64% of weakening for the 850 °C sample and ~78% for the 900 °C sample compared to peak stress values.

These sets of experiments (Fig. 1) demonstrate that pure phase samples are either very strong and deform only in the brittle field (Opx), or relatively weak and deform plastically (Plag) at a moderate to low flow stress without significant weakening after peak stress. The initial strength of mixed phase samples (peak stress) lies between the two extreme values of the pure phase samples, but the mixed phase samples weaken after peak stress and give rise to a final strength far weaker than the weakest of our mono-phase samples (i.e., pure plagioclase).

2.2 Microfabrics and composition

2.2.1 Pure end-members experiments

The pure Plag samples deformed at 800 °C and 900 °C are microstructurally similar to one another and show homogeneous deformation. Although it is difficult to distinguish all individual plagioclase grains in BSE images, there is clear plagioclase grain size refinement locally (Fig. 2a). Recrystallized grains do not show different chemical composition with respect to the relict grains. While our experiments are stronger than those carried out by Stünitz and Tullis (2001), the microstructures are similar and no reaction products are formed at the P-T conditions imposed.

The pure Opx sample with larger initial grain size ($\leq$40 μm) deformed at 900 °C shows extensive fracturing, indicative of brittle deformation (Fig. 2b). The pervasive fractures result in a locally dramatically reduced pyroxene grain size (down to <1 μm; Fig. 2c). No indication for plastic deformation was detected.

2.2.2 Mixed phase samples

2.2.2.1 High shear strain samples

2.2.2.1.1 General features

At 850 °C, the high-strain sample is characterized by a single high strain zone that traverses the sample through the center from one interface of the forcing block to the other (Fig. 3). The reaction products appear pervasively in the whole sample, but the high-strain zone contains considerably more reaction products (~80%) than the low-strain one

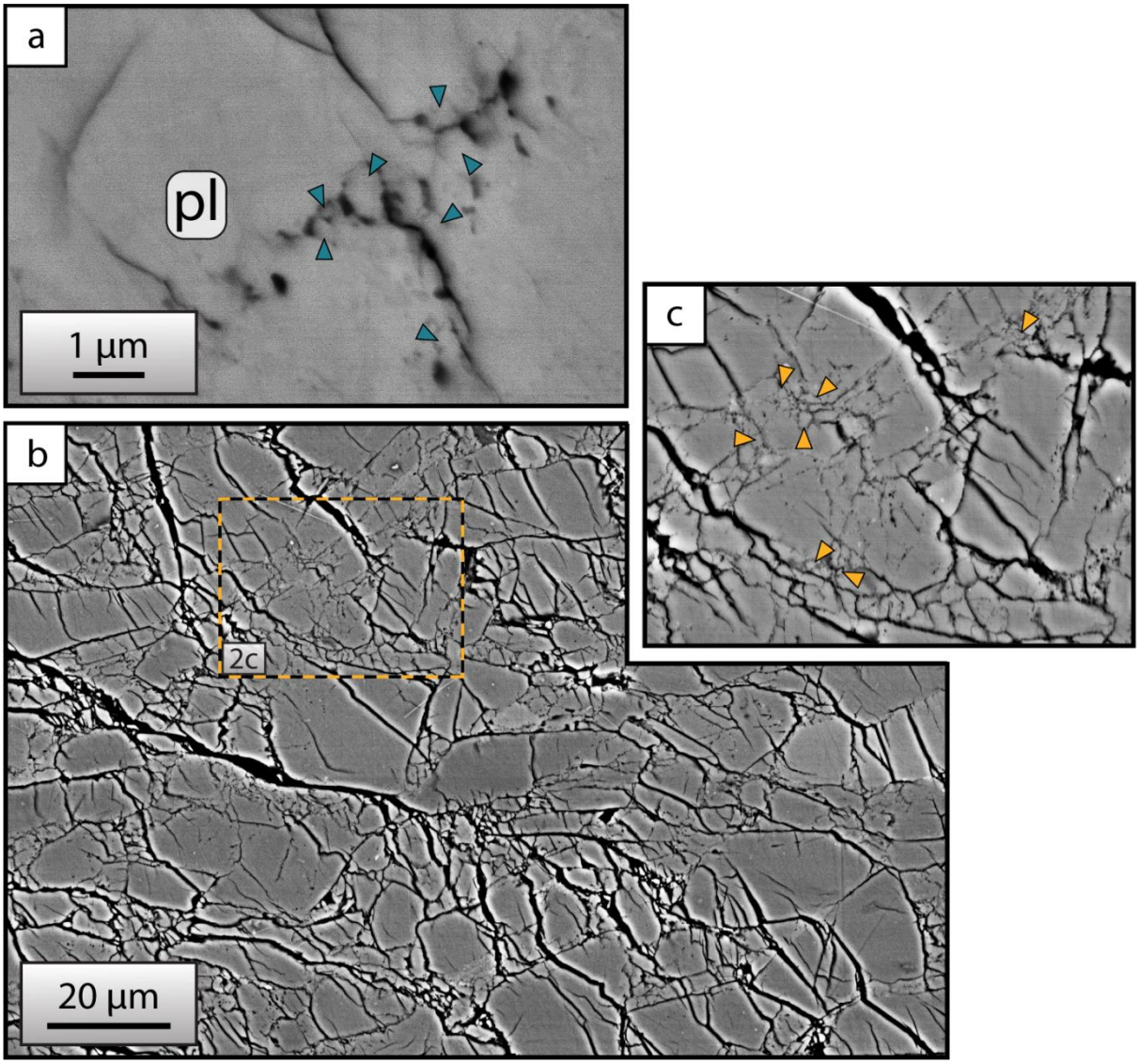

Fig 2: SEM-BSE images representative of microstructures documented in pure plagioclase (**a**) and pyroxene (**b-c**) experiments. (**a**) Plagioclase grain size refinement (blue arrows). (**b**) Extensive fracturing of pyroxene. (**c**) Close-up of the pyroxene grains showing extensive grain size refinement (orange arrows). pl = plagioclase.

(~28%). The grain size of the reaction product also substantially reduces in the high-strain zone with respect to the low-strain regions. In this latter, the reaction product develops as coronas at the Opx_1-$Plag_1$ boundaries, or as monophase aggregates without the development of mixed phase zones (Fig. 4a). This reaction product is identified as newly-formed pyroxene (Opx_2), plagioclase ($Plag_2$) and amphibole (Amph); all of which were absent from the starting material. The original Opx_1 clasts are locally cut by brittle fractures, reducing slightly the grain size (Fig. 4b) and the fractures are filled with Opx_2 reaction products.

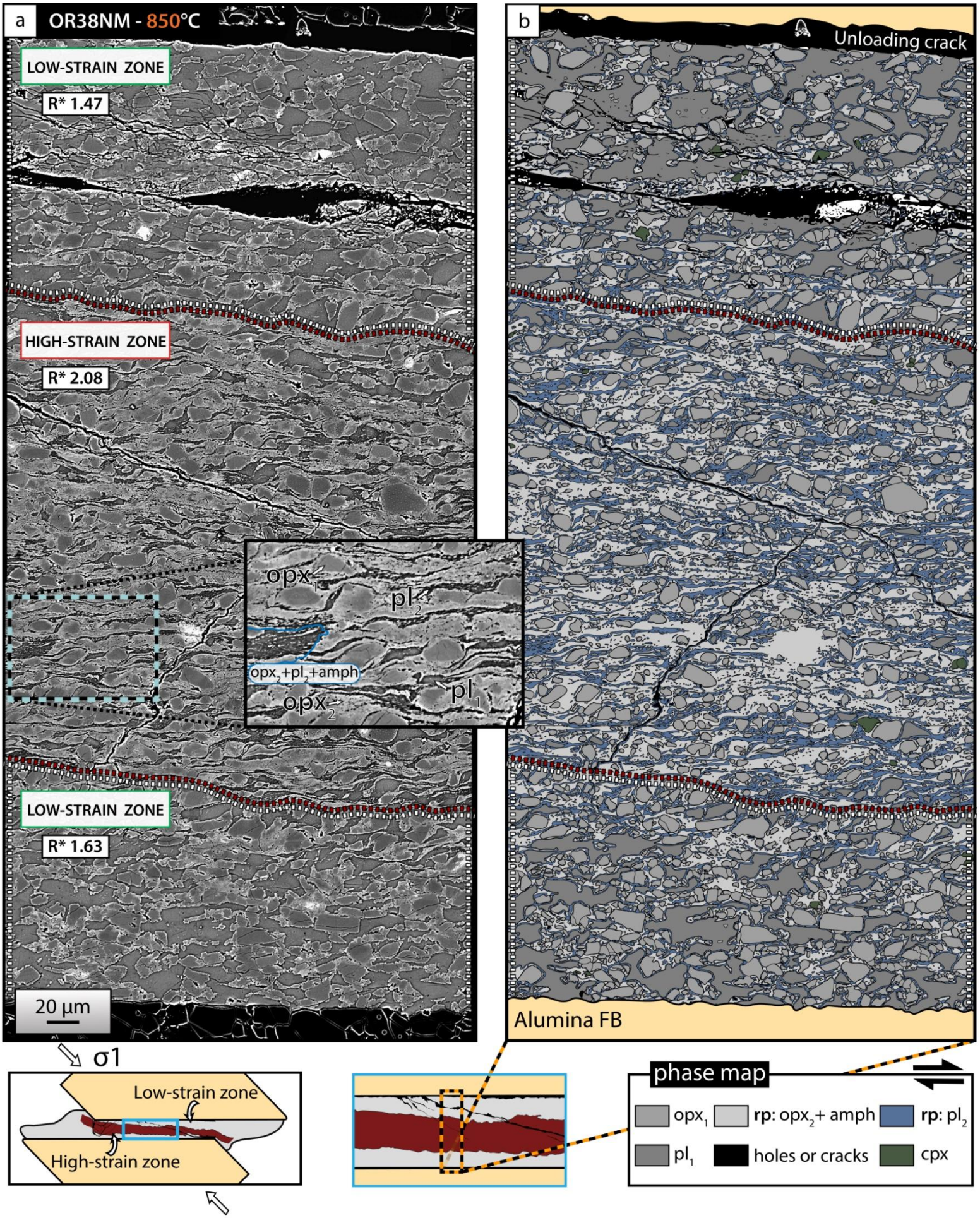
a
OR38NM - 850°C
LOW-STRAIN ZONE
R* 1.47
HIGH-STRAIN ZONE
R* 2.08
LOW-STRAIN ZONE
R* 1.63
20 µm
opx1
pl2
opx2+pl2+amph
opx2
pl1
b
Unloading crack
Alumina FB
σ1
Low-strain zone
High-strain zone
phase map
opx1
rp: opx2+ amph
rp: pl2
pl1
holes or cracks
cpx

Fig 3: SEM-BSE transect of a part of high shear strain sample (**a**) and the related manually digitized phase map (**b**) showing the overall strain gradient in the shear zone from top to bottom. This transect is characterized by a heterogeneity in the amount of reaction and deformation. rp = reaction products, opx = orthopyroxene, cpx = clinopyroxene, pl = plagioclase, amph = amphibole, alumina FB = alumina forcing block.

The transition between low-and high-strain zones can locally be gradual and shows the incipient mixing of phases at the edges of original Opx_1 (Fig. 4c-d). The reaction progressively consumes the pre-existing Opx_1 and induces the development of σ-tails parallel to the shear direction. These tails locally coalesce and form interconnected shear bands of fine-grained reaction products composed of Opx_2, $Plag_2$ and locally Amph, which usually have rounded grain shapes (Fig. 4c-d).

2.2.2.1.2 High-strain zones

Reactions in high-strain zones result in intense grain size reduction and in coalescence of foliation-forming layers of fine grains parallel to each other into mixed phase shear bands, usually laterally connected and subparallel to the shear direction (Fig. 4e-f, 5). Some of the shear bands have a synthetic orientation with respect to the bulk shear zone (C'-type orientation in the sense of Berthé et al., 1979), others are parallel to the shear direction (C-type orientation). At 850 °C, the majority of shear bands are organized within high-strain zones of ~250–300 µm thick (Fig. 5a-b). Similar features are shared at 900 °C, although deformation is more distributed (Fig. 5c-d-e).

The modal proportion of reaction products reaches locally 80% in the high-strain zones, as these products replace most of the pre-existing large grains, including the original $Plag_1$ (Fig. 6a). Thus, most of the fine-grained mixed phase shear bands are composed of reaction product (Opx_2, $Plag_2$ and Amph). The high-strain zones still comprise some original Opx_1 clasts that are embedded in the fine-grained reaction product (Fig. 4e), but these clasts are reduced in size (from reaction) and appear less elongated and more disoriented compared to those of the low-strain zones (Fig. 6b). The Opx_1 appears therefore as a mechanically rigid clast within weaker mixing zones composed of reaction product, the grain size of which is typically below one micron.

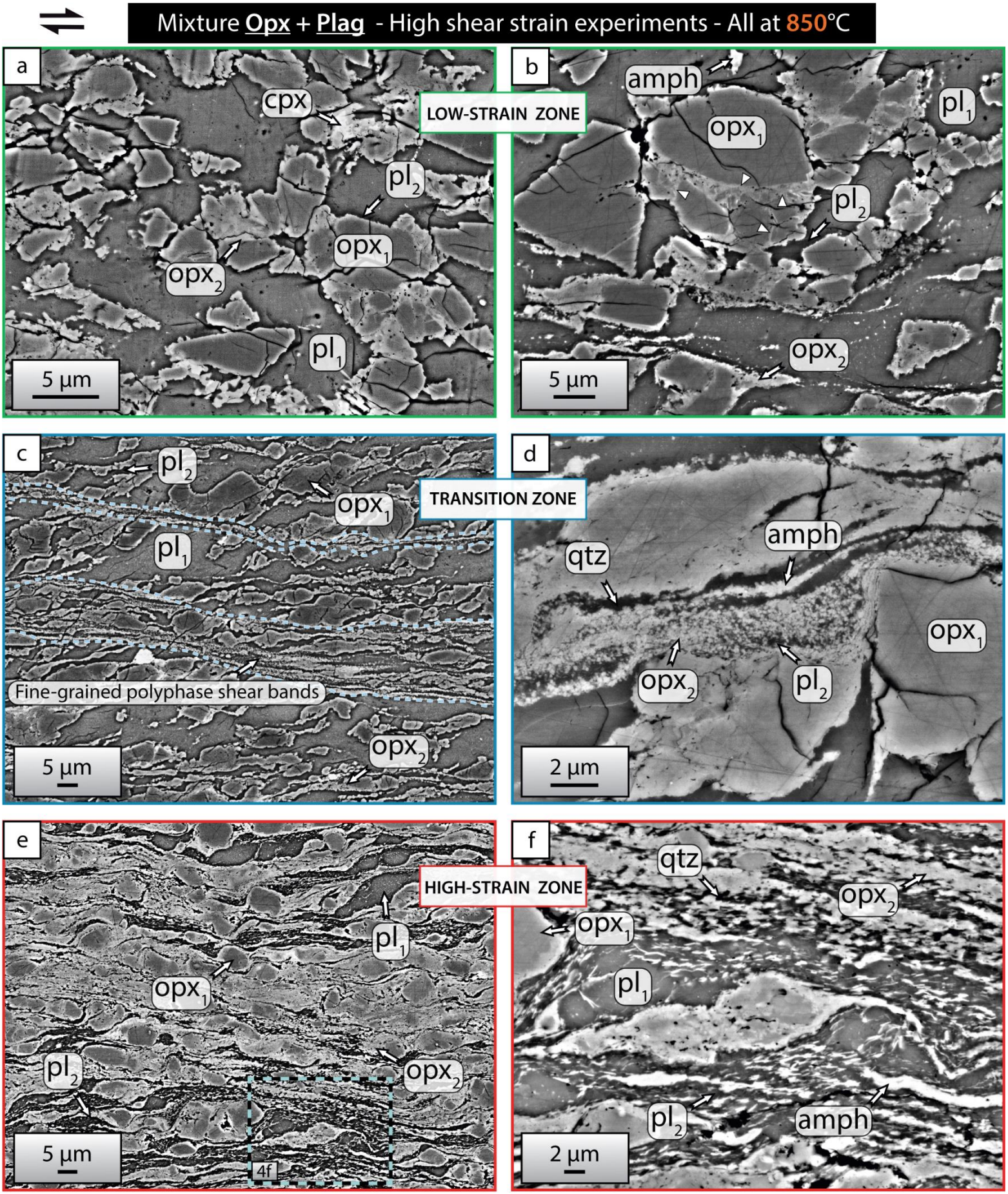

Fig 4: SEM-BSE images representative of microstructures observed in high shear strain experiments. (**a-b**) The reaction product appears as coronas around the original Opx_1 and as aggregates in low-strain zones. Pyroxene is locally fractured and filled with reaction product (white arrows). (**c-d**) The transition zone shows the development of fine-grained tails and shear bands extending at the edges of Opx_1. These tails form fine-grained mixed zones rich in Opx_2, Pl_2

and Amph. (**e-f**) High-strain zones textures are made of intercalated fine-grained polyphase shear bands. In these zones, there is an extensive phase mixing between Opx_2, Pl_2 and Amph.

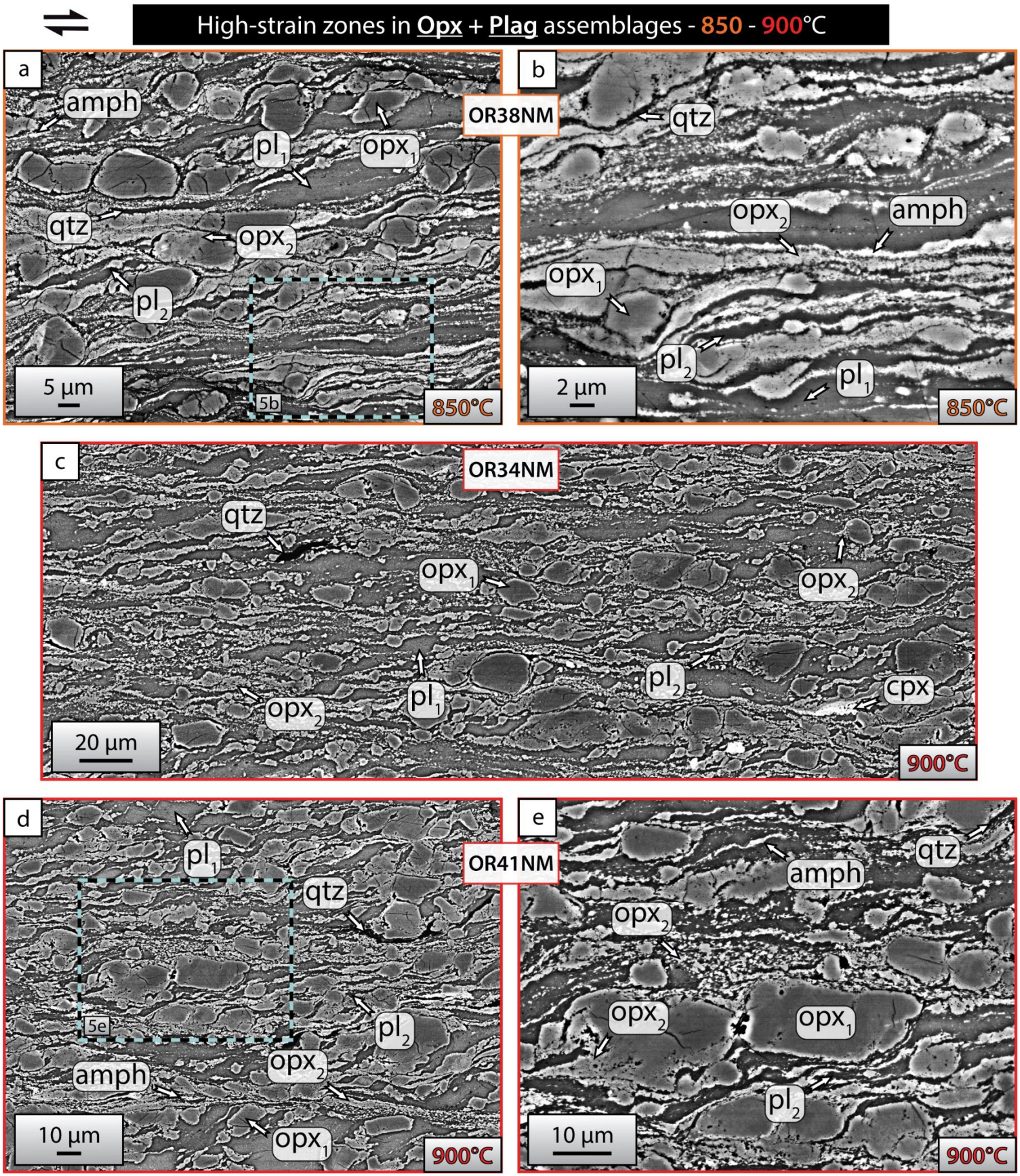

Fig 5: SEM-BSE images representative of microstructures observed in high-strain zones. Three samples deformed to high-shear strain are documented: one deformed at 850 °C (**a-b**) and two others deformed at 900 °C (**c-d-e**). In each case, the high-strain zones are made of fine-grained polyphase shear bands, mainly composed of Opx_2, Pl_2 and Amph. However, the volume fraction of reaction product is larger at 850 °C and the deformation is more localized compared to samples deformed at 900 °C, which show more distributed deformation and lower amounts of amphiboles at shear zone scale. Opx = orthopyroxene, cpx = clinopyroxene, pl = plagioclase, amph = amphibole, qtz = quartz.

There is a gradient in the aspect ratio and the orientation of reaction product between low- and high-strain zones. The bulk aspect ratio is higher in the high-strain zones, where the amount of reaction product is the most abundant (Fig. 6). Moreover, the bulk aspect ratio is around one and a half times higher in the high-strain zones compared to the low-strain ones. The reaction product in the high strain zones is also strongly oriented subparallel to the shear plane (piston interface (Fig. 6d; α between ~ 3° and 5°). In the low strain zones, the reaction product is less oriented (Fig. 6d; α ~ 9°). By applying the equation that relates the preferred orientation of passive lines with respect to the shear plane ($\gamma = 2/\tan 2\theta$; Ramsay, 1980), we can estimate that local shear strain reaches γ ~11 to 16 in the high-strain zones and γ ~ 6 in the low-strain ones.

2.2.2.1.3 Mineral chemistry

Overall, major compositional changes in plagioclase and pyroxene are coeval with grain size reduction in sample shear zones (Fig. 7a-b). The chemical composition of new grains of plagioclase and pyroxene distinctly differs from that of relict clasts. While the chemical composition of clasts is mostly An59, the new reaction rim ($Plag_2$) is more albitic (An52; Fig. 7a). The reaction also results in almost complete disappearance of $Plag_1$ in the high-strain zones (Fig. 6a), and within mixed phase zones and shear bands, the anorthite component of fine-grained $Plag_2$ is slightly lower than that of new rims (An49).

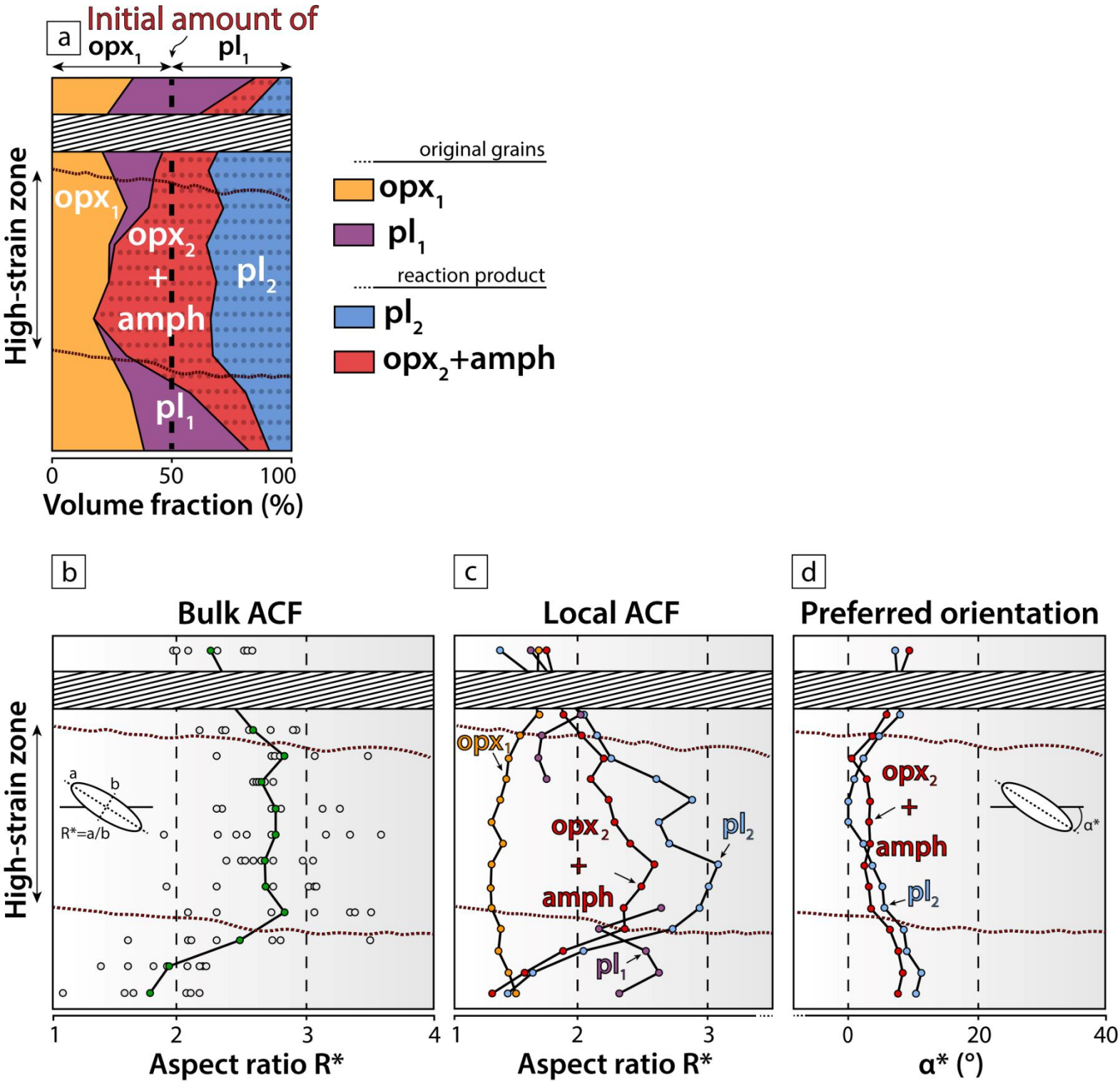

Fig 6: Analysis of the transect of high shear strain sample (Fig. 4). (**a**) The amount of reaction product is higher in the high-strain zone compared to low-strain ones. (**b-c-d**) The ACF analysis reveal a higher aspect ratio in the high-strain zones, essentially related to the reaction product, which are preferentially oriented subparallel to the piston interfaces. For reference, panel (**a**) shows the evolution of phases volume fraction through the transect. To avoid errors, Opx2 and Amph are grouped together. Panel (**b**) displays the bulk aspect ratio R*, while the panel (**c**) displays the individual aspect ratio R*. Panel (**d**) shows the preferred orientation α* with respect to the piston interfaces. Opx = orthopyroxene, cpx = clinopyroxene, pl = plagioclase, amph = amphibole.

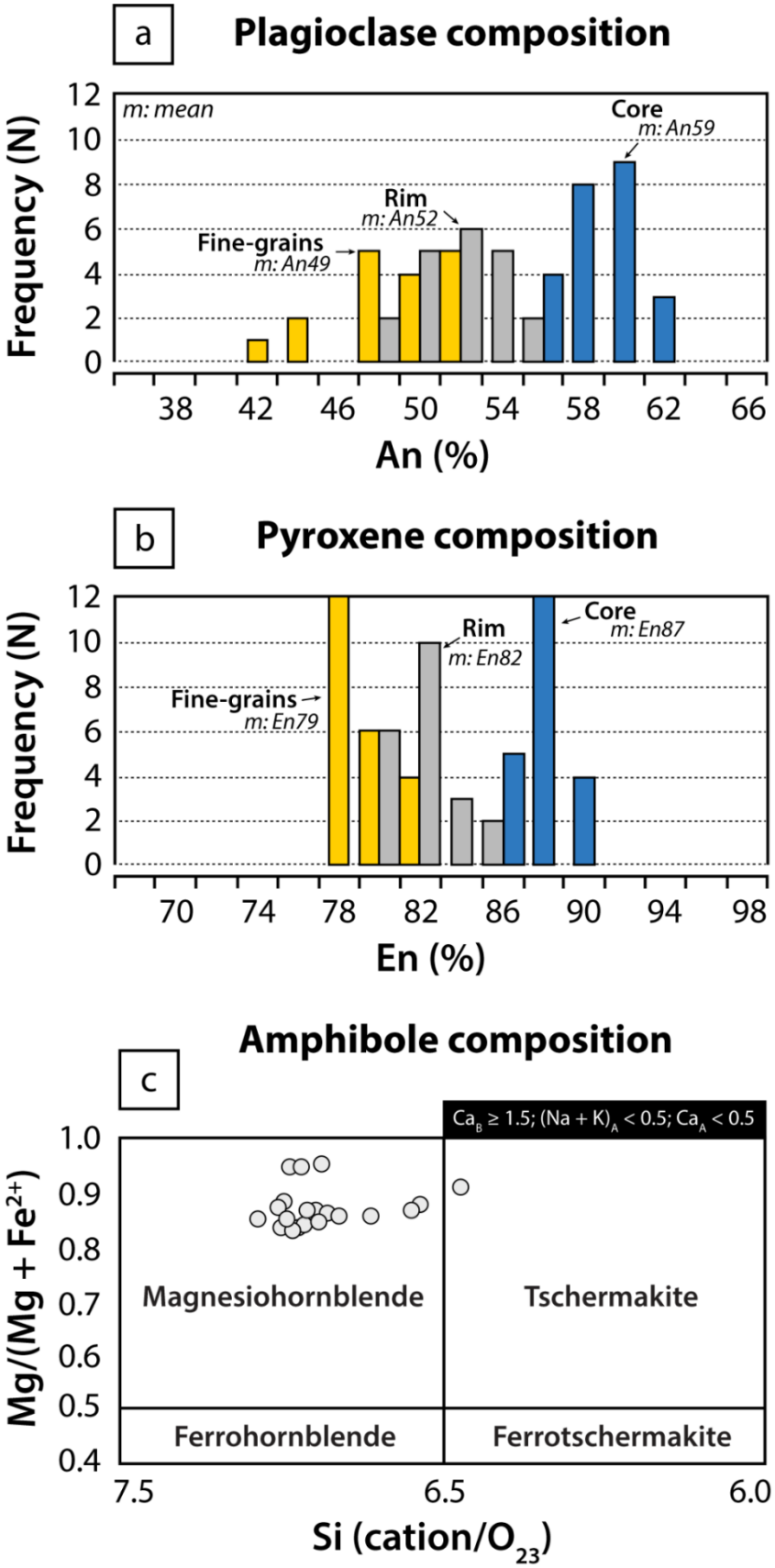

Fig 7: Chemical composition of plagioclase (**a**), pyroxene (**b**), and amphibole (**c**). The chemical compositions of plagioclase and pyroxene are divided into three subsets: clast-core, clast-rim and fine grains.

Pyroxene has the same chemical evolution relationship between relict clasts and new rims (Fig. 7b). The chemical composition of clasts (Opx_1) varies from En(86) to En(90), while the rim composition (Opx_2) shows a decreasing enstatite content down to En(82). The composition of fine-grained new Opx2 in the high-strain zone decreases even more to En(79). The reaction product thus characterizes by an enrichment in iron content, together with the formation of new amphibole grains enriched in Mg and depleted in Fe. These syn-kinematic amphibole appears in both, more and less deformed zones, but they are more abundant in fine-grained shear bands and in the sample deformed at 850 °C. Based on large grains composition in the low-strain zones—the grain size is too fine in shear bands of the high-strain zones to distinguish individual grains and measure the composition—, amphiboles are essentially classified as magnesio-hornblende and tschermakite (Fig. 7c).

2.2.3 Hot-pressing and peak stress experiments

Some samples were hot-pressed (without deformation) for the same duration as the high shear strain samples for comparison of microstructure and reaction progress. Hot-pressing samples of Opx + Plag at 900 °C show the development of reaction product (Fig. 8a-b), which have the same composition of Opx_2, $Plag_2$ and Amph in the deformed samples. The reaction product only occurs as thin coronas at the Opx_1-$Plag_1$ phase boundaries. The volume of reaction product reaches about 3% in the sample held for 100h and about 10% in the one held at the same pressure and temperature for 193h. Except from this increase in reaction product, there is no difference between the two hot-pressing samples.

In samples where the deformation was stopped at peak stress, the microstructures differ slightly in the amount of reaction product and their arrangement with respect to the microstructures of the hot-pressing experiments (Fig. 8c-d). Indeed, the amount of reaction product slightly increases in peak stress experiments compared to the hot-pressing ones. The reaction product is relatively homogeneously distributed in the samples, although it starts to coalesce locally and forms partially connected layers (Fig. 8d). The original Opx_1 and $Plag_1$ grains are also slightly elongated in the flow direction. When these experiments reach relatively high conditions of differential stress, close to the Goetze criterion, fractures locally affect the pyroxene and cause a slight reduction in grain size.

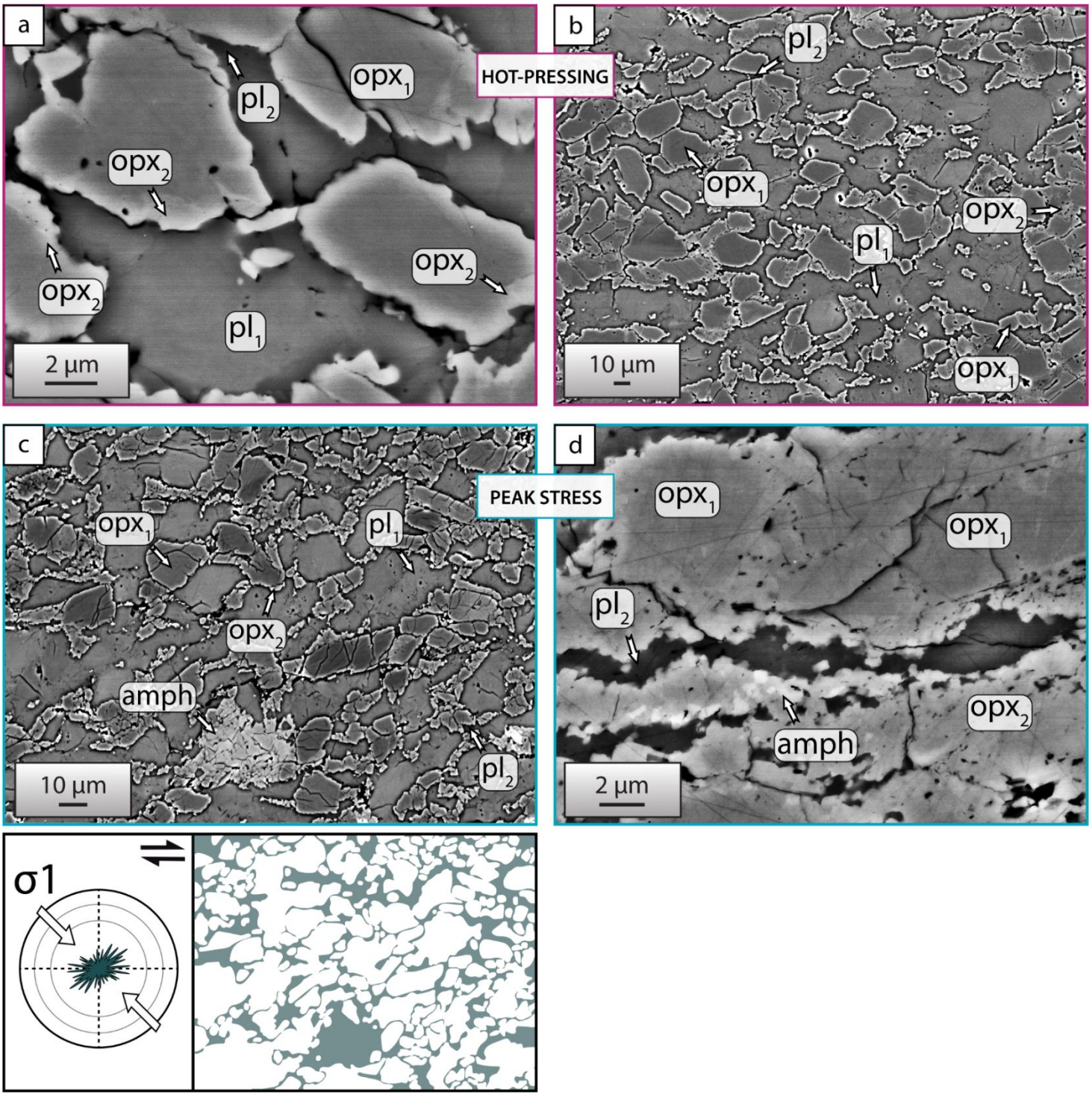

Fig 8: SEM-BSE images representative of microstructures observed in the hot-pressing experiments (**a-b**) and peak stress experiments (**c-d**). (**a-b**) Thin reaction coronas that start forming at the Opx_1-Pl_1 interphase boundaries. This consists essentially of Opx_2 and $Plag_2$. (**c**) Representative microstructures observed at peak stress where the reaction product starts to form aggregates that are partially connected in the direction of extension. (**d**) Irregular grain boundaries composed of small grains of newly formed reaction product. Opx = orthopyroxene, cpx = clinopyroxene, pl = plagioclase, amph = amphibole.

2.2.4 Intermediate shear strain experiment

In our set of experiments, one sample was taken to a more or less intermediate strain and is considered as a transient sample between peak stress and high shear strain experiments (Fig. 1c; OR49NM). This sample is characterized by the development of subparallel fine-grained polyphase layers or shear bands (Fig. 9a), both composed of an intimate mixture of extremely fine-grained Opx_2, $Plag_2$ and Amph (Fig. 9b). The layers and shear bands originate from tails that extend from the edges of original Opx_1 (Fig. 9c), and progressively coalesce to form an interconnected network (Fig. 9a).

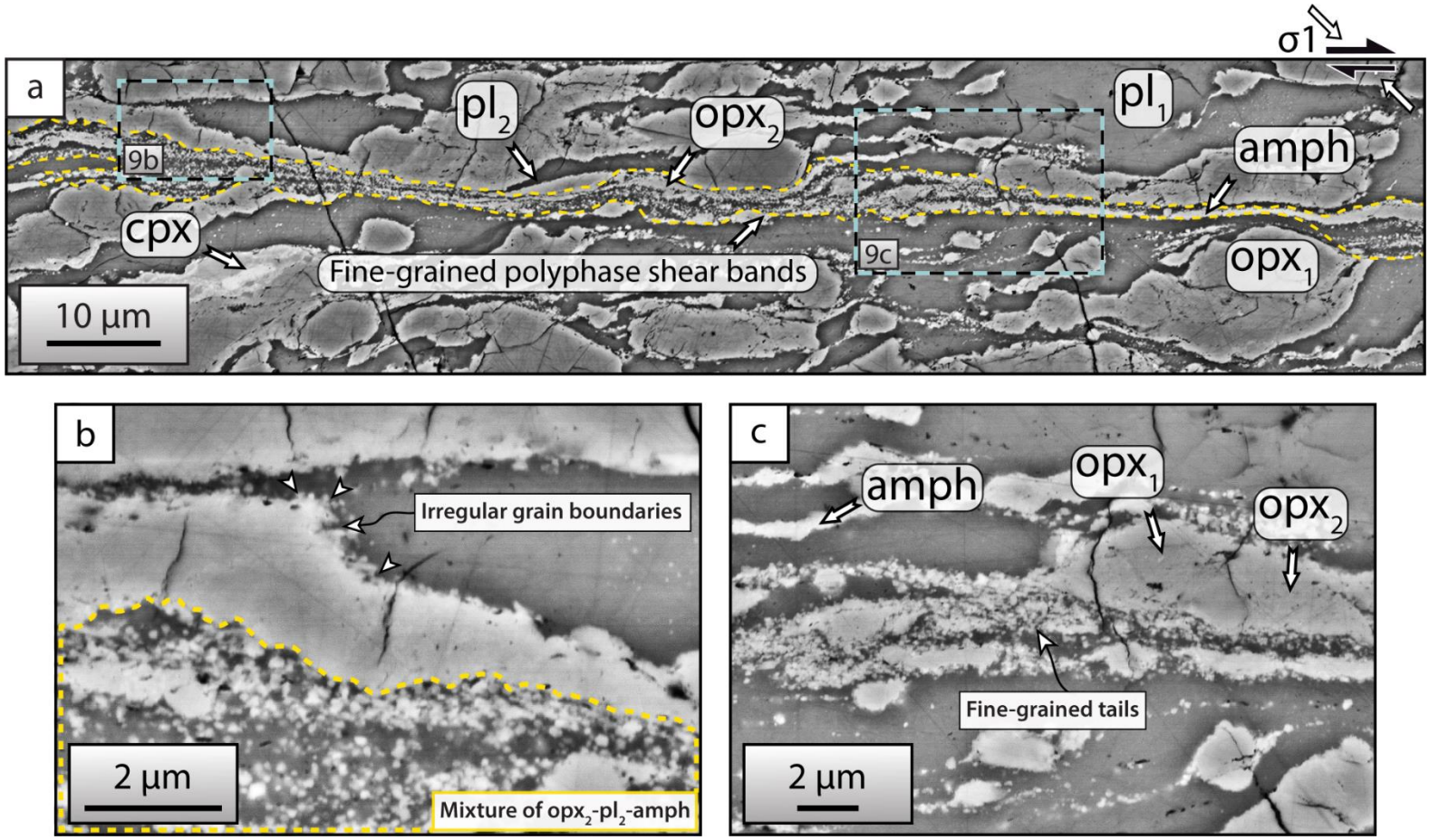

Fig 9: SEM-BSE images showing characteristic microstructures of the nascent mixing of phases. (**a**) Incipient interconnection of thin fine-grained polyphase layers (yellow dotted outline) subparallel to the shear plane (horizontal direction). (**b**) Close-up of layers showing fine-grained mixture of Opx2, Pl2 and Amph. (**c**) Close-up of incipient mixing forming tails at the edges of original Opx1. Opx = orthopyroxene, cpx = clinopyroxene, pl = plagioclase, amph = amphibole.

2.3 Grain size

The overall grain size for both plagioclase and pyroxene grains is strongly reduced with increasing strain. Most of the pyroxene grain size reduction occurs after the peak stress, and hence, during the weakening and development of fine-grained mixed phase zones (Fig. 10). While the pyroxene grain size remains almost unchanged at peak stress with respect to the starting material (only cracking refines the grain size to a mode of 15.6 μm), it strongly decreases in mixed phase zones at high shear strain (mode of distribution = 0.2 μm). To ensure accurate grain size determination, we have excluded plagioclase from the measurements because of the difficulty to distinguish individual grains in plagioclase aggregates. Despite this issue, visual inspection suggests that the plagioclase grain size in stable fine-grained mixtures is similar to that of pyroxene.

2.4 Reaction progress

The set of experiments performed at different durations and 900 °C is used to illustrate the relation between the volume fraction of reaction product with time and the effect of deformation on reaction (Fig. 11). The volume fraction of reaction product increases from ~3% for 100h to ~10% at 193h if deformation is not applied (OR55NM and OR43NM) (Fig. 11a). In contrast, even after a short period of deformation to small strain at peak stress, the volume fraction of reaction product increases to ~11% (OR51NM) and ~18% (OR47NM) (Fig. 11a). This amount of reaction product is higher than the amount documented for the hot-pressing experiment with equivalent duration. Thus, the influence of deformation on the amount of reaction product is higher than the influence of time. This influence has an effect on the strength of the deformed assemblages, as the more reaction product they contain, the weaker they are (Fig. 11b). The deformed and undeformed samples therefore significantly differ in terms of Avrami relationship, i.e., in terms of reaction progress without incubation time before the hit point (Fig. 11b).

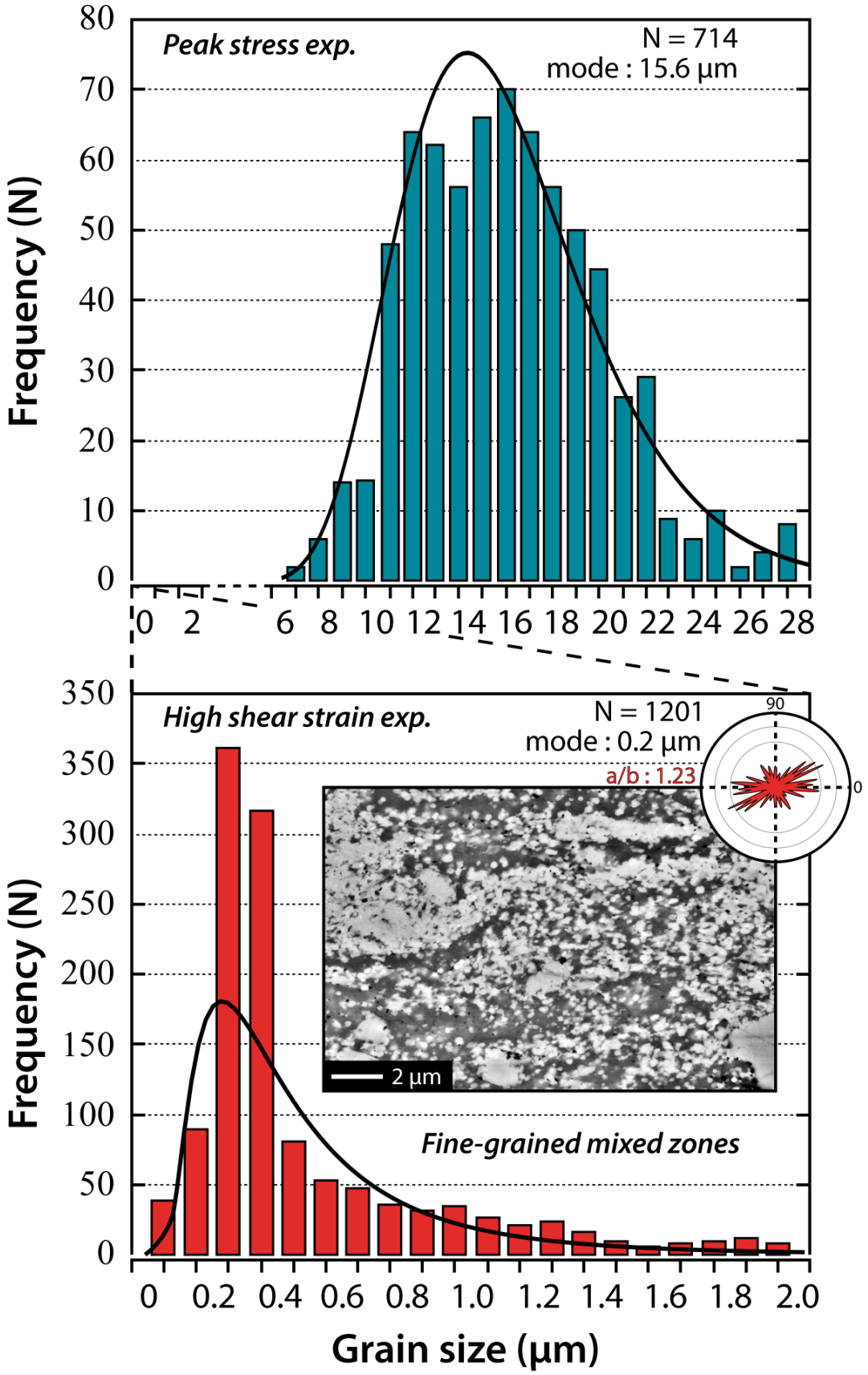

Fig 10: Grain size evolution of pyroxene between peak stress experiment (mode: 15.6 µm) and the newly formed Opx2 in fine-grained mixed zones in high shear strain experiments (mode: 0.2 µm). The black curve represents a best-fit to the log-normal distribution. The average value for the aspect ratio of new Opx grains is a/b = 1.23.

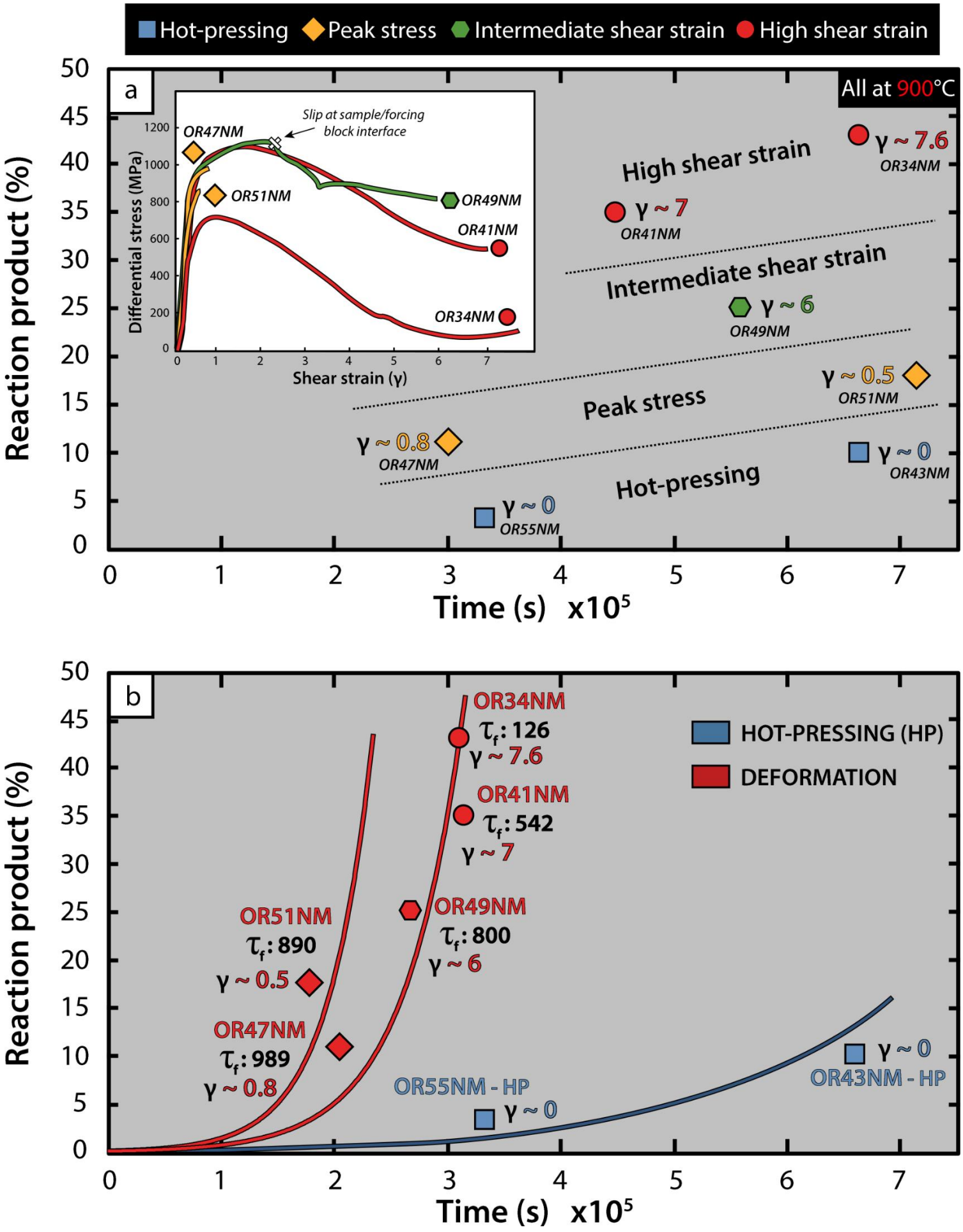
Hot-pressing
Peak stress
Intermediate shear strain
High shear strain
a
All at 900°C
Slip at sample/forcing block interface
OR47NM
OR51NM
OR49NM
OR41NM
OR34NM
Differential stress (MPa)
Shear strain (γ)
High shear strain
γ ~ 7.6
OR34NM
γ ~ 7
OR41NM
Intermediate shear strain
γ ~ 6
OR49NM
Peak stress
γ ~ 0.5
OR51NM
γ ~ 0.8
OR47NM
Hot-pressing
γ ~ 0
OR43NM
γ ~ 0
OR55NM
Reaction product (%)
Time (s) x10⁵
b
HOT-PRESSING (HP)
DEFORMATION
OR34NM
τf: 126
γ ~ 7.6
OR41NM
τf: 542
γ ~ 7
OR49NM
τf: 800
γ ~ 6
OR51NM
τf: 890
γ ~ 0.5
OR47NM
τf: 989
γ ~ 0.8
OR55NM - HP
γ ~ 0
γ ~ 0
OR43NM - HP
Reaction product (%)
Time (s) x10⁵

Fig 11: Evolution of the amount of reaction product as a function of time in plagioclase—pyroxene experiments at 900 °C. Symbols denote types of experiments performed, which include hot-pressing, peak stress, intermediate and high shear strain experiments. The graph (**a**) shows the different types of experiments, strain rate and associated mechanical data in stress-strain graph. (**b**) Evolution of the volume fraction of reaction product (RP) with time, and effect of deformation on reaction and sample strength. Exponential curve fitting for hot-pressed or deformed samples are color coded. One exponential curve for deformed samples is fitted for peak stress samples, while the other is fitted for higher shear strain samples. The duration of the deformed experiments is taken from the hit-point.

3. Discussion

3.1 Mechanical data

The mechanical data of our experiments show a systematic difference in the rheological evolution between monomineralic samples (opx or plag) and phase mixtures (Fig. 1): The monomineralic samples either deform by brittle mechanisms only (opx; the experiment was stopped before failing completely), or they deform viscously at steady state stresses following a weakening of less than 150 MPa (plag). The deformation of pure Opx also gives rise to high differential stress at 900 °C ($\Delta\sigma$ ~1600 MPa; Fig. 1b). Advances in rock deformation studies provided detailed documentations about the creep behavior of pyroxene (e.g. Bystricky and Mackwell, 2001; Dimanov et al., 2003, Dimanov and Dresen, 2005; Chen et al., 2006), but mostly for CPx; the mechanical behavior of Opx remains very limited (Bruijn and Skemer, 2014; Bystricky et al., 2016). The comparison of Opx mechanical results and estimated strain rates for wet Cpx, by applying the flow law of Dimanov and Dresen (2005), suggest that the Opx strength is higher compared to that of the Cpx (Fig. 12a). For pure Plag, our flow stresses at the given strain rate for $\gamma > 2$ (= steady state conditions) are in good agreement (Fig. 12b) with the flow law by Rybacki and Dresen (2000) using the conversion between simple shear and coaxial strain rates of $\dot{\varepsilon} = \dot{\gamma} / \sqrt{3}$ (Tokle et al., 2019). Our results for pure phase Plag and Opx are thus quite consistent with previous results found in the literature.

The mixture samples deform under continuous weakening after attaining a peak stress that is intermediate between the end-member strengths of Opx and Plag, strength of which is consistent with a Reuss-Voigt- or Taylor-Sachs models (e.g., Dimanov and Dresen, 2005). However, the Opx in our case appears to be stronger than Cpx and deforms only by brittle processes, so that the peak strength of the 2-phase composite sample is between the two end-members and near the Goetze criterion (Fig. 1).

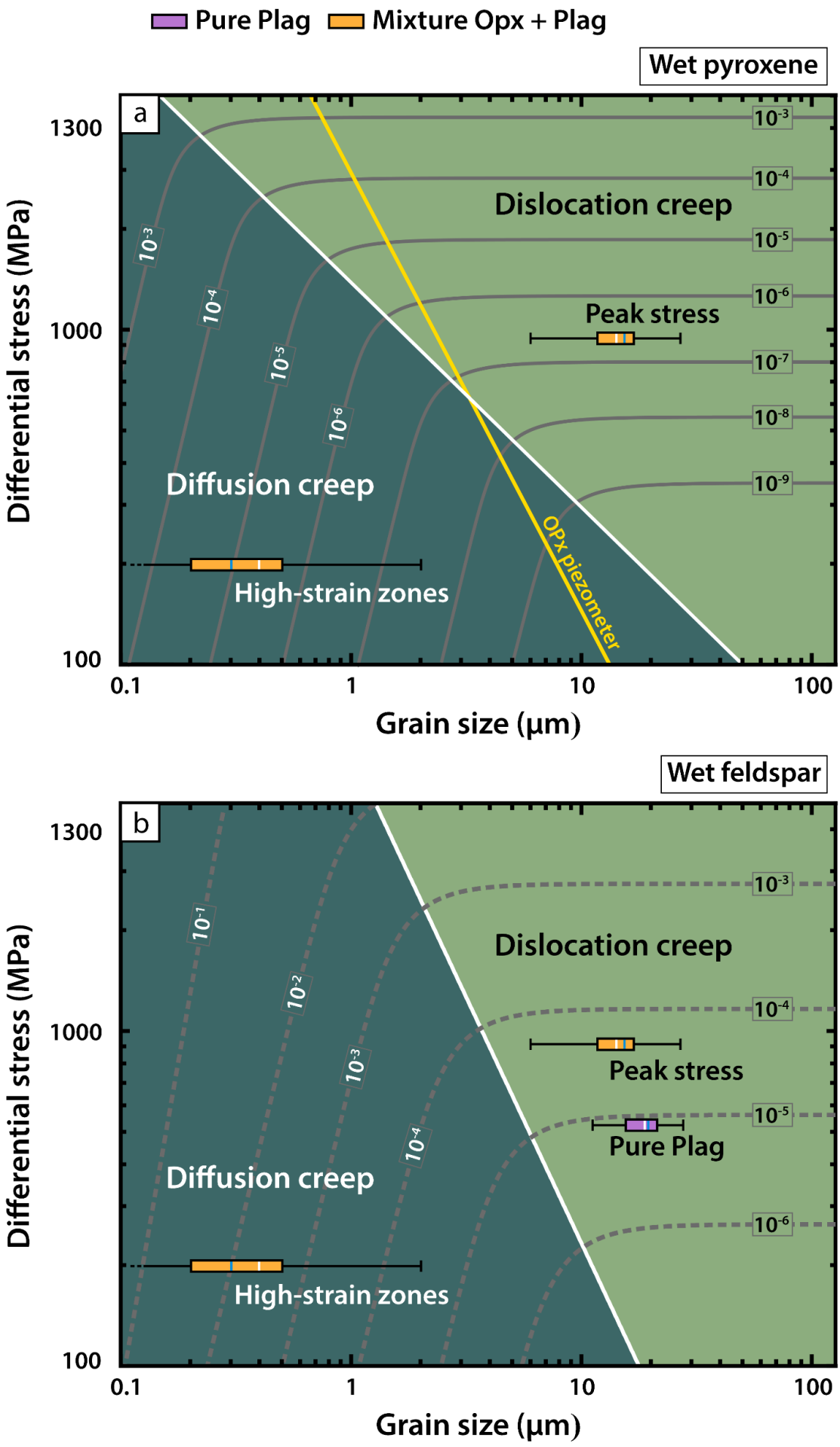
Pure Plag
Mixture Opx + Plag
Wet pyroxene
a
Dislocation creep
Peak stress
Diffusion creep
High-strain zones
OPx piezometer
Differential stress (MPa)
Grain size (µm)
1300
1000
100
0.1
1
10
100
Wet feldspar
b
Dislocation creep
Peak stress
Pure Plag
Diffusion creep
High-strain zones
Differential stress (MPa)
Grain size (µm)

Fig 12: Deformation mechanism map for wet pyroxene (**a**) and wet feldspar (**b**) at 900 °C and 1 GPa as a function of differential stress and grain size. On this map, we plot the differential stress and grain size of Opx at peak stress and in mixed zones of high shear strain experiments in both cases, as we consider that the grain size of these phases is similar. The deformation conditions of the pure Plag sample is also plotted. The grain size is represented in box-and-whisker diagram. Individual boxes were limited by upper and lower quartiles, and within it the median (white lines) and the mode (blue lines) was defined. The flow laws for wet pyroxene are from Dimanov and Dresen (2005), while those for wet feldspar are from Rybacki and Dresen (2000). The grain size piezometer for Opx (yellow line) is taken from the study of Linckens et al. (2014).

In addition, the pronounced weakening after peak stress produces final flow stresses that are far below (up to 800 MPa) the Goetze criterion($\Delta\sigma \leq P_{conf}$) nearby the strength of the weaker end-member phase. This suggests that the deformation mechanism of the phase mixture differs from those of the end-members. Otherwise, the strength of the composite would lie between the end-member strengths of a Reuss-Voigt or Taylor-Sachs-model. As discussed below, such a different rheological evolution may be explained by the progressive modification of the phase assemblage and microstructure through chemical interactions, i.e., mineral reactions.

3.2 Nucleation and grain size reduction

From figures 3 to 6, the local zones of reaction product accommodate far more strain than the relict phases Opx and Plag, so that the reaction product is responsible for the mechanical weakening of the samples. In addition, the microstructures at peak stress conditions mainly consist of coronas with only incipient mixed phase zones (Fig. 8c-d), and hence, most of the phase mixing starts after the peak stress. Reaction product also has a very small grain size (Fig. 10). As the intense grain size reduction and phase mixing start to appear both after peak stress (Fig. 13), strain weakening and partitioning into high-strain zones (Fig. 5) likely commence as a consequence of these processes.

Although there is no flow law for Plag + Opx mixtures and composite flow laws only exist for Cpx + Plag (Dimanov and Dresen, 2005), we plotted the measured grain size modes of the fine-grained reaction product (Opx + Plag) into the existing Cpx and Plag deformation mechanisms maps for a semi-quantitative comparison. The observed grain sizes of Opx at the final strength of the composite phase mixtures plot into the diffusion creep field at the nominal applied strain rates of the samples (Fig. 12), whereas the Plag at the same grain size yields an order of magnitude of higher strain rates.

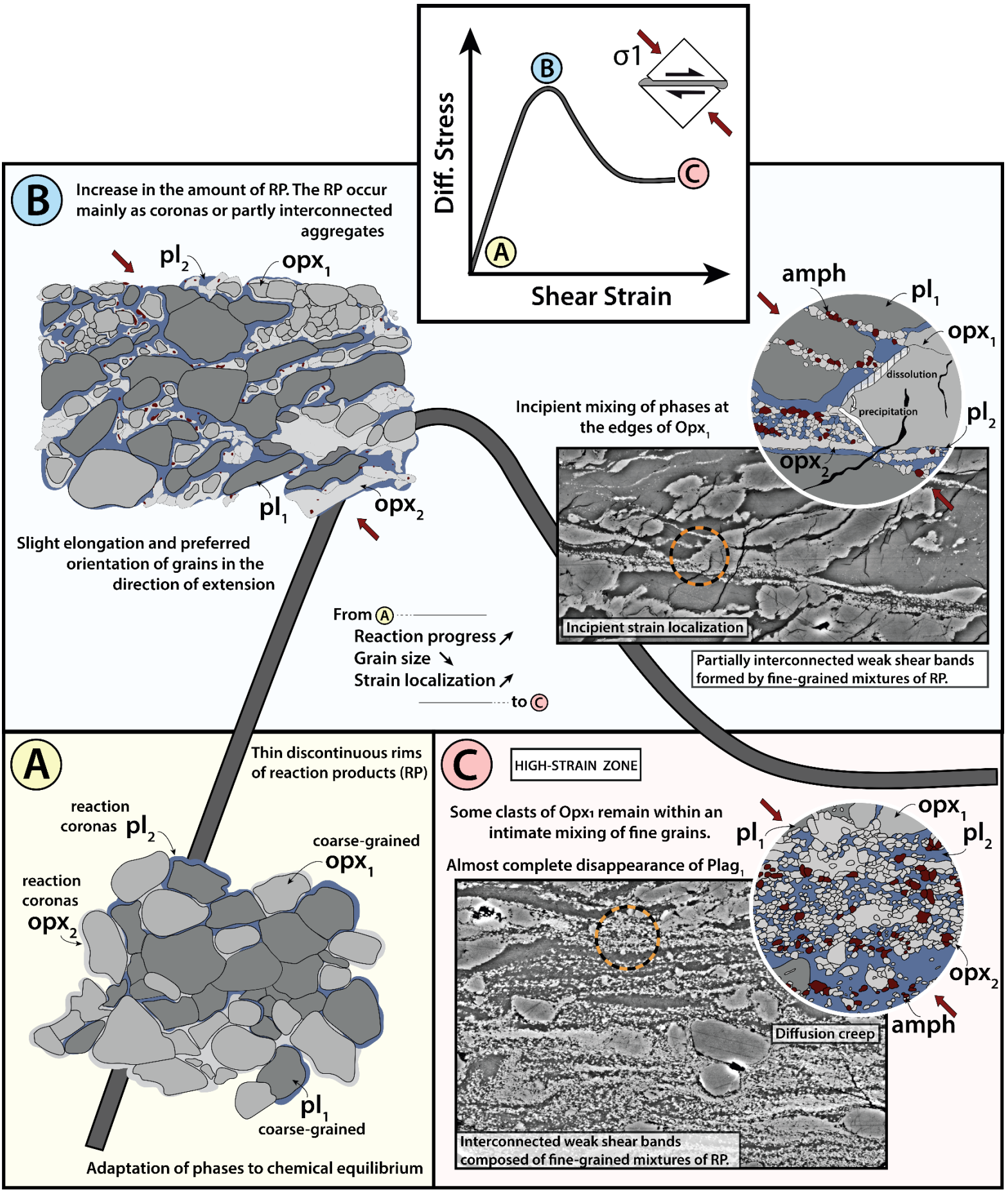
Diff. Stress
Shear Strain
σ1
A
B
C
B
Increase in the amount of RP. The RP occur mainly as coronas or partly interconnected aggregates
pl2
opx1
pl1
opx2
Slight elongation and preferred orientation of grains in the direction of extension
amph
pl1
opx1
dissolution
precipitation
pl2
opx2
Incipient mixing of phases at the edges of Opx1
Incipient strain localization
Partially interconnected weak shear bands formed by fine-grained mixtures of RP.
From A
Reaction progress ↗
Grain size ↘
Strain localization ↗
to C
A
Thin discontinuous rims of reaction products (RP)
reaction coronas pl2
coarse-grained opx1
reaction coronas opx2
pl1
coarse-grained
Adaptation of phases to chemical equilibrium
C
HIGH-STRAIN ZONE
Some clasts of Opx1 remain within an intimate mixing of fine grains.
Almost complete disappearance of Plag1
pl1
opx1
pl2
opx2
amph
Diffusion creep
Interconnected weak shear bands composed of fine-grained mixtures of RP.

Fig 13: Schematic textural and microstructural evolution of plagioclase-pyroxene mixture from hot-pressing conditions (**A**) to strongly deformed shear zones (**C**), illustrating the different stages of strain localization and weakening during deformation.

Because of strain partitioning, the expected strain rates in the high-strain zones are higher than the bulk ones by a factor of 2 to 3. Thus, the strain rates of the Plag—Opx mixtures are in the range of the Cpx strain rates and slower than the predicted ones for Plag in the diffusion creep field (Fig. 12).

Several processes are generally invoked to account for phase transformations that may reduce grain size and promote phase mixing, influencing the rock strength. Some workers proposed that melt reactions may strongly influence the mechanical behavior of rocks of the lower crust by inducing phase mixing and introducing a low viscosity melt in the system (e.g. Rosenberg and Handy, 2005). In our case, the P-T conditions imposed to the Opx + Plag system are definitely outside of the melt-forming field, in agreement with the lack of melt in our samples. Another weakening process may involve dynamic recrystallization in the regime 1 of Hirth and Tullis (1992), i.e., if recrystallization mostly occurs by bulging, but dynamic recrystallization does not produce phase mixing, and the pyroxene grain size in zones of mixed phase reaction products falls far below the orthopyroxene piezometer (Fig. 4.12; Linckens et al., 2014). The new Opx_2-grains also have a different chemical composition compared to the starting material (Fig. 7), which excludes fracturing as a source of extensive grain size comminution (e.g. Ree et al., 2005; Park et al., 2006; Pec et al., 2012, 2016). In low-strain zones of samples that reach high differential stress conditions, discrete fractures affect Opx_1 clasts, inducing their breakdown into smaller fragments but not to extensive size comminution. In contrast, phase nucleation and a switch to grain size sensitive dissolution-precipitation creep has been described in previous studies (e.g. Kilian et al., 2011; Herwegh et al., 2011; Wassmann and Stöckhert, 2013; Hidas et al., 2016; Précigout and Stünitz, 2016; Marti et al., 2018; Prigent et al., 2018). As typically associated with metamorphic reactions (e.g. De Ronde et al., 2004, 2005), such a phase nucleation may account for changing chemistry and phase mixing during extensive grain size reduction in our experiments.

3.3 Mineral reaction and dissolution-precipitation creep

While the development of reaction coronas induces limited grain size reduction and no phase mixing in low-strain zones (Fig. 4a-b, 13), the grain size reduction is much more intense in high-strain zones, combined with phase mixing (Fig. 4e-f, 5, 13). At the margin of high-strain zones, the early stages of phase mixing are preserved (Fig. 4c-d, 13). Fine-grained layers composed of Opx_2, $Plag_2$ and Amph extend at the edges of Opx_1 clasts and progressively replace the original $Plag_1$ (Fig. 4c-d). The mixing starts at the edges of the original Opx_1 that is gradually dissolved as evidenced by irregular grain boundaries, where new grains nucleate in some localities along low-stress sites of Opx_1 grain boundaries (Fig. 4c). These microstructures suggest that diffusion mass transport takes place and facilitates dissolution—precipitation creep. Previous studies also showed that phase nucleation forming tails at the expense of clasts may increase the degree of mixing in natural shear zones (e.g. Kruse and Stünitz, 1999; De Ronde et al., 2004, 2005, Holyoke and Tullis, 2006a, b, Kilian et al., 2011, Mansard et al., 2018).

In our experiments, the nucleation of small phases causes an irreversible effect on the deformation processes because no grain growth is observed with increasing strain or larger duration of the experiments. The mixing of phases causes pinning of grain boundaries and impedes grain growth, so the fine grain size of the mixed phase zones is preserved (e.g. Fliervoet et al., 1997; Herwegh et al., 2011; Kilian et al., 2011, Platt, 2015). Therefore, the nucleation of fine-grained mixed phase layers is an efficient mechanism to maintain deformation of weak material.

One important accommodation process in diffusion creep is grain boundary sliding (e.g, Langdon, 2006). In a reacting and simultaneously deforming mineral assemblage, it has a two-fold effect: it creates new contact surfaces for reaction and it produces potential cavitation sites, where new phases can nucleate (e.g., Kilian et al., 2011, Menegon et al., 2015, Précigout and Stünitz, 2016; Précigout et al., 2017). In this way, phase mixing is promoted, in agreement with 1) the heterogeneous nucleation of fine grains (Fig. 10), 2) the relatively well-mixed phases in high-strain zones (Fig. 4e-f, 5), and 3) the fact that pyroxene and plagioclase grain size in these zones falls within the diffusion creep field (Fig. 11). The significant weakening and strain localization during deformation is consistent with the increase in strain rate (e.g. Schmid et al., 1980, Rutter and Brodie, 1988; Montési, 2007; Precigout et al., 2007; Raimbourg et al., 2008; Gueydan et al., 2014). Due in particular to the dominance of diffusion creep and the occurrence of weakening resulting in strain localization, the fine-grained high-strain zones constitute

the parts of the sample that weaken the most.

3.5 Influence of deformation on reactions

A common response to the effect of deformation on solid-state chemical reactions is that the deformation may enhance the kinetics of mineral reactions (e.g. Yund and Tullis, 1991; Wintsch et al., 1995; Baxter and De Paolo, 2004; Imon et al., 2002; Yonkee et al., 2003; Holyoke and Tullis, 2006; De Ronde and Stunitz, 2007, Richter et al., 2016). In our high-strain samples, we document a strong localization of deformation into high-strain zones (Fig. 3). The fact that the reaction product constitutes much of the high-strain zones at 850 and 900 °C (Fig. 6a) strongly argues in favor of reaction kinetics enhanced by deformation. This deformation-reaction feedback is more pronounced at 850 °C, as the amount of syn-kinematic amphiboles formed in high-strain zones is higher. A similar feedback was found in sheared plagioclase-olivine experiments at 900 °C (De Ronde and Stünitz, 2007), and they showed that the local strain is highly correlated with reaction progress. Recently, Marti et al., (2018) also described the positive feedback between deformation and reaction progress in experimentally deformed plagioclase-pyroxene mixtures, but with less reaction product. The greater reaction progress and larger amount of fine-grained mixed phase zones in our samples may be attributed to the small grain size of our starting material in otherwise very similar experimental procedures as Marti et al., (2018). The partially smaller grain size in our samples provides a greater surface area of phase boundaries as sites of potential reactions.

The evidence that deformation affects reaction kinetics comes from the comparison of hydrostatic hot-pressing samples, the deformed samples to peak stress, and to higher shear strain (Fig. 11a). The main difference between these samples is the bulk amount of reaction product. The comparison of hot-pressing samples held at 900 °C and 1 GPa for a different period of time (~100h and 193h) reveals a slight increase in the amount of reaction product with time (Fig. 11b). Similarly, the comparison of two deformed samples to peak stress that reached similar shear strain for a different period of time (~85h and 200h) only shows a slight increase of reaction product (Fig. 11b). This difference in incubation time before deformation, however, is potentially important in terms of rheological behavior. The longer the incubation time before the hit point, the greater the volume of reaction product, and the weaker is the sample at peak stress (Fig. 1, 11a-b). Nonetheless, the comparison of hot-pressing and peak stress samples with a

similar period of time reveals that the influence of time on the amount of reaction product is minor compared to the effect of deformation (Fig. 11b).

Although 2 data points for hot-pressing samples are not sufficient to establish an accurate Avrami relationship, an Avrami curve is fitted for comparison with other samples (Fig. 11). The initial slow reaction progress in hydrostatic samples compared to deformed samples (without the incubation time) is obvious (Fig. 11c). With increasing strain, there clearly is a greater volume of reaction product. Similar results have been documented in experimentally deformed fine-grained gneiss (Holyoke and Tullis, 2006 a, b) and plagioclase + olivine samples (De Ronde and Stunitz, 2007). The main reason for the faster reaction progress in deformed samples is probably the introduction of defects into the reactants, i.e. the increase of the activation energy for the reaction at otherwise identical pressure and/or temperature overstepping conditions (De Ronde and Stunitz, 2007).

3.6 Geological application—shear localization in nature

In our deformation experiments the starting material Opx + Plag was deliberately chosen to be out of equilibrium at the experimental pressure and temperature conditions. In nature, P-T conditions change occur at lower rates, potentially inducing progressive changes in mineral assemblages (e.g. Herwegh et al., 2011). However, cases of preserved metastable mineral assemblages in undeformed rocks are well documented, while deformed equivalents of the same rock body have reacted (e.g. Austrheim and Griffin, 1985, Koons et al., 1987, Früh-Green, 1994). Thus, mineral reaction and its interplay with deformation is of great importance in nature (e.g. Kerrich et al., 1980; Brodie and Rutter, 1985; Handy and Stünitz, 2002; Keller et al., 2004; Mansard et al., 2018). Indeed, it has been shown by the study of, e.g., Keller et al., 2004 that the extent of metamorphic reactions is greater in shear zones, as reaction may cause strain localization by producing a mechanically weak aggregate. This shares similarities with natural studies showing that strain and mineral reactions are intimately linked and influence each other (e.g. Mitra, 1978; Brodie and Rutter, 1985; Whitmeyer and Wintsch, 2005). Thus, the investigated polyphase mixture is a good analogue to natural shear zones involving strain-enhanced chemical reactions and reaction-enhanced strain weakening, although large overstepping of reaction boundary may occur in our experiments.

It is now well established that the lower crust is lithologically heterogeneous, mainly consisting of mafic rocks dominated by feldspar and pyroxene (e.g. Kirby and Kronenberg, 1987; Christensen and Mooney, 1995; Rudnick and Fountain, 1995). Experimental investigations on the rheology of feldspar (e.g. Rybacki and Dresen, 2000; Dimanov et al., 2003), pyroxene (e.g. Bystricky and Mackwell, 2001), and polyphase assemblages of feldspar and pyroxene (Dimanov and Dresen, 2005) reveal that these two phases are mechanically strong, although pyroxene is 1–2 orders of magnitude stronger than feldspar under dry conditions (e.g. Dimanov and Dresen, 2005). Our study also demonstrates that Opx + Plag assemblages are strong, but as soon as these assemblages react, the sample is viscously deformed and the strength weaken. Indeed, the deformation of Opx + Plag assemblages promotes diffusion-controlled chemical reactions which induce the nucleation of new intrinsically strong phases, i.e., plagioclase and pyroxene (Fig. 1a). However, these strong phases nucleate as fine grains within weak mixed phase zones (Fig. 5, 10), causing a switch in deformation mechanism, and thereby extending the range of conditions where the fine-grained mixed zones are weaker than the unreacted assemblages. Several workers pointed out that such localization of strain in weak layers may control the degree of weakening in polyphase rocks (e.g. White et al., 1980; Handy, 1989). This is of great importance in the comprehension of the rheological behavior of the lower crust, because a large amount of fine-grained weak zones allows to preserve the weak long-term behavior of a shear zone in the lower crust. Thus, the rheology of polyphase assemblages is controlled by many factors, including mineral reactions, grain size reduction and strain partitioning. The effect of these processes related to the complex interaction between plagioclase and pyroxene on lower crust rheology are however not taken into account in the current lithospheric models. These models should consider mechanical polyphase layers to describe the lower crust, as it has been shown in natural lower-crustal shear zones (e.g. Kanagawa et al., 2008; Kruse and Stünitz, 1999).

4. Conclusion

In this study, we have performed rock deformation experiments on plagioclase + pyroxene and pure end-member assemblages in Griggs-type deformation apparatus at 1 GPa, and temperatures ranging from 800 to 900 °C. The analysis of pure end-member assemblages reveals that in the absence of reaction, only initial strain weakening due to recrystallization occurs in Plag, which then deforms at steady-state stress. And Opx deforms only by brittle mechanisms. In contrast, plagioclase + pyroxene assemblages show extensive strain weakening caused by mineral reactions. These deformed assemblages show the importance of the interaction between deformation and reaction on grain size reduction and phase mixing, leading to strain partitioning and weakening in fine-grained shear zones. This study represents a good analogue to natural shear zones involving mechanical weakening caused by mineral reactions, particularly in mafic rocks. At the onset of deformation, new phases nucleate in aggregates as mixed phase tails and layers at the expense of original pyroxene and progressively replace the original plagioclase. The change of phase composition together with phase mixing indicates that grain size reduction originates from dissolution-precipitation. This suggests that pressure-solution creep may have significantly contributed to weaken the mixture samples. As deformation and reaction progress, thin weak layers coalesce to form simply connected material in high-strain zones. The intense grain size reduction occurring in mixed high-strain zones considerably changes the rheology of the assemblage, and it increases the strength contrast between the weak high-strain zones, able to deform by grain-size sensitive diffusion creep, and the mechanically strong low-strain ones. The interplay between deformation and reaction is responsible for strain partitioning and localization in high-strain zones. The degree of connectivity of the reacted material controls the bulk rheology of the shear zone.

Le chapitre 5 vise à approfondir notre étude expérimentale sur la localisation de la déformation en comparant l'évolution rhéologique d'assemblages biphasiques dont la composition initiale est proche. Ce chapitre révèle que les réactions minérales précoces peuvent avoir un impact considérable sur la résistance des assemblages, car ces réactions conditionnent leurs résistances dans les premiers stades de la déformation. Les assemblages se déforment à contrainte plus faible lorsqu'ils réagissent plus rapidement. La capacité des minéraux à réagir détermine ainsi les portions de roches qui se déforment. Soumis à des contraintes plus importantes, ces assemblages présentent des comportements très différents selon le degré de rétroaction de la déformation sur les réactions, la nature des produits de réaction, leurs proportions et le degré d'interconnectivité des phases faibles. Les expériences illustrent notamment que des zones de mélange à grains fins fortement connectées sont significativement plus faibles que des domaines monophasés dont l'interconnexion est limitée. Globalement, la résistance des assemblages au pic de contrainte et l'affaiblissement de la résistance suite au développement de domaines faibles et interconnectés, semblent être largement contrôlés par les réactions minérales. Ainsi, la composition des phases minérales, dans la mesure où elles régissent la réactivité, participe grandement à l'initiation de l'affaiblissement et à l'évolution à long terme de la résistance des zones de cisaillement.

CHAPTER V

Experimental evidence of weakening and strain localization induced by minor metastability of mafic rocks

CONTENTS

1. Introduction

Mafic rocks constitute a large part of the oceanic crust and may be one of the main components of the lower continental crust (Rudnick and Fountain, 1995). The major constituents of mafic rocks, i.e., pyroxene and plagioclase, are typically strong minerals that show crystal plastic deformation only at high temperatures in natural systems (e.g., Rutter and Brodie, 1985, 1992; Brodie and Rutter, 1985). However, there are abundant examples of strongly deformed mafic rocks, and many of these are deformed at relatively low temperatures, at which they show metamorphic retrogression (Rutter and Brodie, 1985). For instance, concomitant deformation and metamorphism is observed along oceanic detachments, where deep levels of the oceanic mafic crust are exhumed (Harigane et al., 2008; Schroeder and John, 2004). Strongly sheared meta-gabbros are also present in exhumed subduction belts (Imon et al., 2004; Shelley, 1994) or in large-scale transcurrent shear zones (Jolivet and Miyashita, 1985; Shelley, 1994) In most of these cases, the decreasing temperature conditions during deformation results in coeval mineral reactions, often with a large grain size decrease. The coupling between strain and reactions is therefore essential to understand the process of strain localization, as observed in mafic mylonites (Rutter and Brodie 1992).

Data from high-temperature deformation experiments of mafic rocks are relatively scarce (e.g. Dimanov et al., 2003, 2007; Dimanov and Dresen, 2005; Marti et al., 2018). The study of mylonitic deformation of these rocks provides insights, at small-scale, into the deformation mechanisms and strain localization processes and, at large-scale, into the strength of the lower crust (e.g. Rutter and Brodie, 1992; Kanagawa et al., 2008). There are two main mechanisms of rock deformation in the viscous deformation regime: (1) Dislocation creep (crystal plasticity; e.g. Paterson 2013), and (2) Diffusion creep (including grain scale diffusion creep, dissolution precipitation creep (DPC), and diffusion accommodated grain boundary sliding (GBS) (e.g. Ashby and Verrall, 1973; Langdon, 2006; and references therein). The pyroxenes typically deform by crystal plasticity only at high temperatures and high stresses (e.g. Coe and Kirby, 1975), while GBS and diffusion creep (i.e., grain-size sensitive (GSS) processes) typically operate at low temperature and low stresses (e.g., Paterson, 1995). In addition to temperature and stress, the transition from crystal plasticity to GSS creep is controlled by grain size.

Many workers have pointed out the close concomitance between grain size reduction and the activation of GSS creep in a variety of mafic assemblages (e.g. Stünitz, 1993; Kruse and Stünitz, 1999; Kenkman and Dresen, 2002; Baratoux et al., 2005; Kanagawa et al., 2008; Mehl and Hirth, 2008; Menegon et al., 2015; Okudaira et al., 2015). For this reason, grain size reduction is recognized as one of the most significant mechanisms that control rheological properties (e.g. Schmid 1982; Brodie and Rutter, 1987; Bercovici and Ricard, 2012; Montési, 2013, Platt, 2015), and the dominant grain-size-controlling processes usually include dynamic recrystallization (e.g., Schmid 1982; Brodie and Rutter, 1987; Behrmann, 1985; Fliervoet and White, 1995; Vissers et al., 1997), and/or metamorphic reactions (e.g. Rubie, 1983; Fitz Gerald and Stünitz, 1993; Stünitz and Fitz Gerald, 1993; Newman et al., 1999). While dynamic recrystallization is considered to have only a transient mechanical effects (Rutter and Brodie, 1988), a small grain size can be stabilized in phase mixtures where grain growth is inhibited by the pinning of grain boundaries (e.g., Olgaard and Evans, 1986, 1988; Fliervoet et al., 1997; Herwegh et al., 2011; Herwegh and Berger, 2004). Furthermore, while phase separation and compositional layering commonly arise during plastic flow of mineral aggregates, the mineral phases are rearranged during metamorphic reactions and nucleation, so that fine-grained mixed-phase zones and polyphase shear bands develop (e.g., Stünitz and Tullis, 2001; De Ronde 2004, 2005; Kilian et al., 2011; Platt, 2015; Mansard et al., 2018). Such a spatial rearrangement controls the bulk strength of the rock, particularly when these phases have a large mechanical contrast. In particular, the interconnection of weak materials is necessary to induce a significant drop of bulk strength (e.g. Jordan, 1988; Handy, 1994; Dell'Angelo and Tullis, 1996; Holyoke and Tullis, 2006a, b).

The principal objective of this contribution is to study the effect of initial rock composition on the feedback processes between reaction and deformation. To do so, we have performed rock deformation experiments on "wet" assemblages of plagioclase-pyroxene assemblages in a Griggs-type solid-medium deformation apparatus. As representative of the lower crust, the starting material was composed of plagioclase (labradorite) and either Mg-rich Opx (from peridotite) or Fe-rich Opx (from a granulite-facies anorthosite) to investigate on the effect of different phase compositions. We also performed deformation experiments on Amph + Plag and pure Amph assemblages at similar conditions to complete the study. All these assemblages were deformed to varying amount of strain, including at the early stages of deformation, which can be challenging

to access when studying natural cases because of successive overprints. In this contribution, we suggest that viscous strain localization is primarily dependent on the ability of minerals to react, and that even small initial differences in composition can lead to large differences in mechanical strength and deformation processes.

2. Results

2.1 Mechanical data

Depending on the starting material, the mechanical data significantly differ with respect to each other (Fig. 1). At 850 and 900 °C, the Mg-rich samples (Fig. 1b-c) are characterized by a pronounced peak stress at shear strains of less than $\gamma \sim 1$, whereas the Fe-rich ones do not show any peak stress, but only a steady-state flow or strain hardening behavior (Fig. 1d). At 800 °C, the peak stresses of all Opx + Plag samples are above the Goetze criterion ($\Delta\sigma \leq P_{conf}$), which provides an empirical upper limit for viscous creep. Above this limit, samples tend to deform by brittle mechanisms (Kohlstedt et al., 1995) and a slip may occur at the interface between the sample and one forcing block. For a short run-in periods (< 65 hrs), the high stresses caused such a slip and a sudden drop of $\Delta\sigma$ occurred (557NM, and 559NM; Fig. 1b) for 800 °C and 850 °C. In contrast, two samples at 900 °C show a pronounced strain weakening after peak stress. In one case, the sample fall substantially below the Goetze criterion as a result of slip along the forcing block interface and stabilizes around 800 MPa (OR49NM). In the other case, the sample weakens continuously after peak stress and reach a quasi-steady-state for $\gamma \sim 6.5$ (OR41NM). In the experiments with longer run-in periods, the Mg-rich assemblages weaken systematically after peak stress. They reach stresses lower than 400MPa at 850 °C and 900 °C, corresponding to ~64% (OR38NM) and ~78% (OR34NM) of the peak stress before reaching a quasi-steady-state shear stress near $\gamma \sim 6.5$ (OR34NM) and $\gamma \sim 7.7$ (OR38NM), respectively (Fig. 1c).

The Fe-rich assemblage deformed at 800 °C also reaches a high peak stress (~1080 MPa) followed by a sudden strength drop, again indicating that the piston slipped at the sample-forcing-block-interfaces (Fig. 1d). At 850 °C, sample behavior is no longer comparable to those of the mixed Mg-rich assemblages, as no weakening occurs after peak stress and a quasi-steady-state shear stress is reached at low shear strain ($\gamma \sim 2$). At 900 °C, the sample remains weak, but hardens continuously until $\gamma \sim 5$, unlike the other experiments (Fig. 1d).

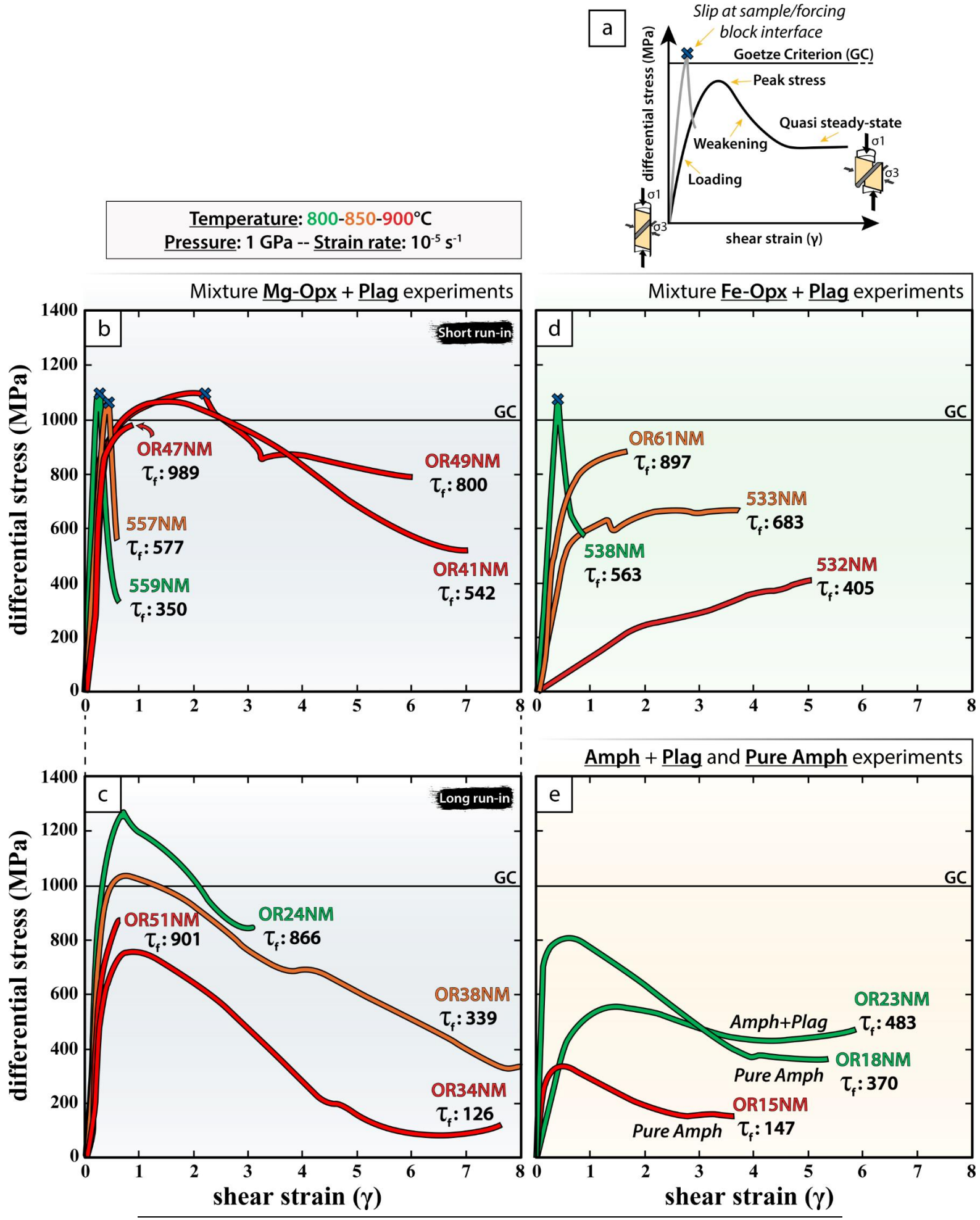
a
Slip at sample/forcing block interface
Goetze Criterion (GC)
Peak stress
Quasi steady-state
Weakening
Loading
differential stress (MPa)
shear strain (γ)
σ1
σ3
Temperature: 800-850-900°C
Pressure: 1 GPa -- Strain rate: 10-5 s-1
Mixture Mg-Opx + Plag experiments
Mixture Fe-Opx + Plag experiments
Amph + Plag and Pure Amph experiments
b
Short run-in
d
c
Long run-in
e
GC
OR47NM τf: 989
OR49NM τf: 800
557NM τf: 577
559NM τf: 350
OR41NM τf: 542
OR61NM τf: 897
533NM τf: 683
538NM τf: 563
532NM τf: 405
OR51NM τf: 901
OR24NM τf: 866
OR38NM τf: 339
OR34NM τf: 126
Amph+Plag
OR23NM τf: 483
Pure Amph
OR18NM τf: 370
OR15NM
Pure Amph τf: 147
differential stress (MPa)
shear strain (γ)

Fig 1: Mechanical data. (**a**) Terms used to describe the different stages of an experiment. (**b-c**) Differential stress (MPa) versus shear strain (γ) showing the mechanical behavior of the Mg-Opx + Plag (Mg-rich) assemblages deformed at temperatures ranging from 800 to 900 °C, at constant confining pressure of 1 GPa and strain rate of 10^{-5} s^{-1}. The difference between (**b**) and (**c**) is related to the different duration of the "run-in" section, i.e. time spent at P-T conditions before the hit point. Mechanical data for Fe-Opx + Plag (Fe-rich) (**d**), Amph + Plag and Pure Amph (**e**) assemblages are also plotted in stress-strain graphs. Opx = orthopyroxene, cpx = clinopyroxene, pl = plagioclase, amph = amphibole.

With respect to the Opx + Plag assemblages, the Amph + Plag and pure Amph assemblages do not reach the same strength, regardless of the deformation temperature (Fig. 1e). At 800 °C, the Amph + Plag assemblage reaches a peak stress of ~563 MPa, and then slightly weakens to ~483 MPa at γ ~5.8. The pure Amph assemblages deformed at 800 and 900 °C show stress-strain curves with a significant weakening after peak stress at γ ~0.5. However, at 800 °C the sample documents a peak stress of ~450 MPa higher than the sample deformed at 900 °C, and it records a flow stress of more than 200 MPa.

Our set of experiments reveals two distinct types of mechanical behavior: one that show a pronounced weakening after high peak stress (Mg-rich and pure Amph assemblages) and a second one without weakening (Fe-rich and Amph + Plag assemblages) or describes some hardening (Fe-rich assemblage at 900 °C, 532NM), but deform at considerably lower stresses (Fig. 1d).

2.2 Mineral reactions and microstructures

Mineral reactions occur pervasively in our deformed assemblages. The pervasive occurrence of mineral reactions induces substantial changes in grain sizes and spatial distribution of phases. This is reflected in the development of shear bands in the deformed assemblages. For the sake of clarity, the term "bulk shear zone" refers to the whole assemblage deformed between the two alumina forcing blocks, while the term "shear bands" refers to a zone of variable thickness of high shear strain accommodation. In addition, the term "high-strain zone" is also used to refer to domains of intense coalescence of fine-grained shear bands connected through the bulk shear zone.

The Mg-rich assemblages deformed to high shear strain are characterized by the development of low-strain zones and high-strain zones (Fig. 2a). Mineral reactions are mainly localized within a single broad through-going high-strain zone that traverses the sample from one interface of the forcing block to the other (at 850 °C; Fig. 2a).

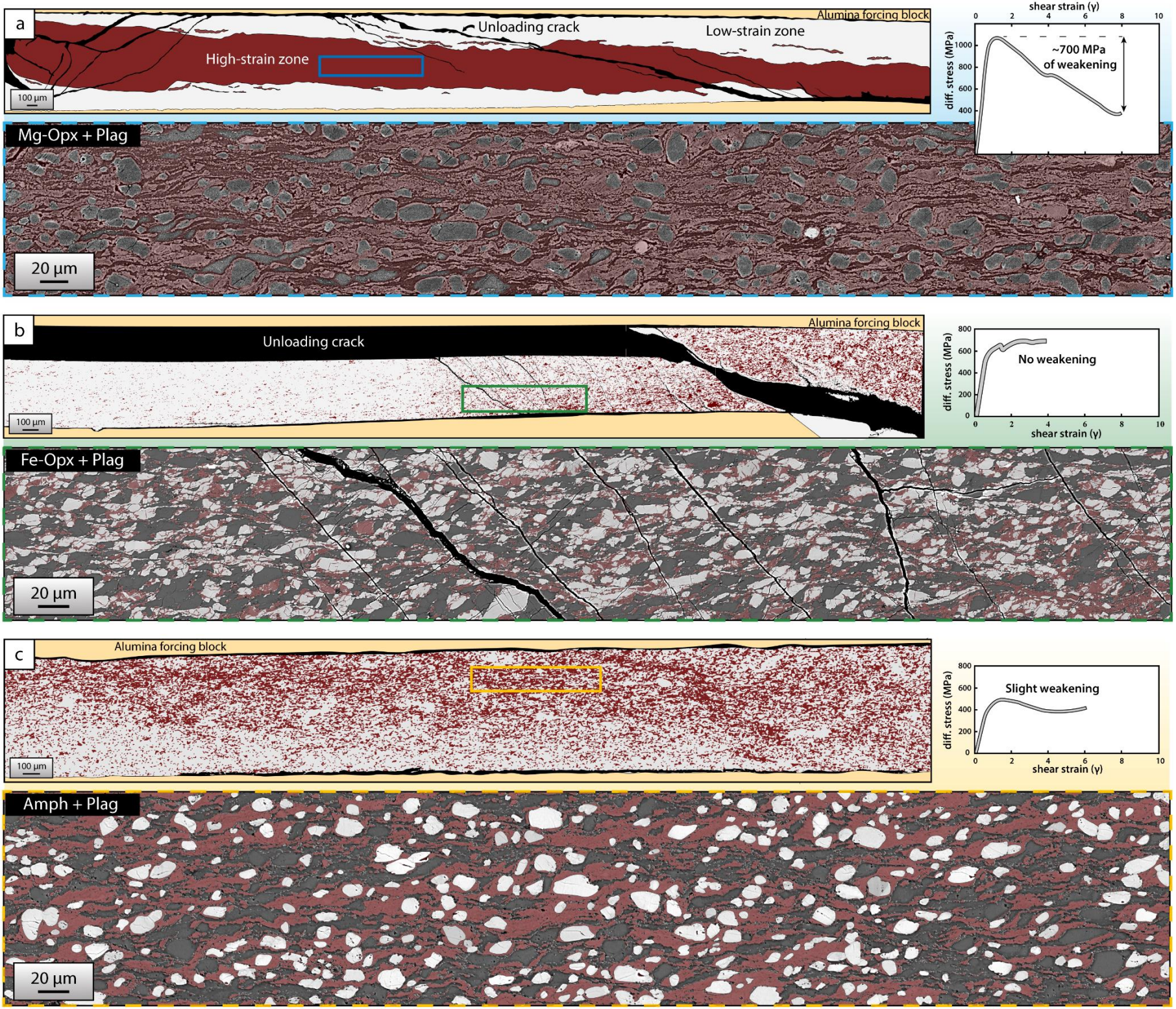
a
Alumina forcing block
Unloading crack
Low-strain zone
High-strain zone
100 µm
shear strain (γ)
diff. stress (MPa)
~700 MPa
of weakening
Mg-Opx + Plag
20 µm
b
Alumina forcing block
Unloading crack
100 µm
No weakening
Fe-Opx + Plag
20 µm
c
Alumina forcing block
100 µm
Slight weakening
Amph + Plag
20 µm

Fig 2: Distribution of reaction products after deformation in the Mg-rich (**a**), Fe-rich (**b**), and Amph + Plag (**c**) assemblages. For each assemblage, a manually digitized overview of the shear zone is associated with a zoomed part of it. The mechanical data associated to these assemblages are also represented in stress-strain graphs.

Within the high-strain zone, mineral reactions are localized as fine-grained mixed zones and C-geometry shear bands subparallel to the shear plane (or forcing block interface) (Fig. 3a-to-c, 4a-to-f). The C-type shear bands are mainly composed of fine Opx_2, $Plag_2$ and Amph that show equant grains when their identification is possible on SEM images (Fig. 3, 8a). The original large grains of $Plag_1$ and Opx_1 form clasts embedded into a mixture of reaction products (Fig. 2a). In contrast, the reaction products in the low-strain zones occur essentially as coronas or as aggregates surrounding Opx_1 clasts (Fig. 3d-e). The main difference between the assemblages deformed at 850 °C and 900 °C is the degree of strain localization. At 850 °C, strain is highly localized in a ~250–300 μm-wide single zone, while at 900 °C, strain is more distributed in the sample (and therefore local strain is lower), but all microstructural features are similar (Fig. 3f-g).

At the scale of the bulk shear zone, both the Fe-rich and Amph + Plag assemblages are banded and show a sub-horizontal mylonitic foliation characterized by the development of Amph-rich shear bands (Fig. 2b-c). These bands wrap the original and larger Opx (Fe-rich assemblages; Fig. 2b) and Amph (Amph + Plag assemblages; Fig. 2c) grains, and alternate with aggregates of original grains. The mylonitic foliation is better defined in the Amph + Plag assemblage because of more pervasive deformation and strain localization (Fig. 2c). Indeed, the shear bands are more heterogeneously distributed in the Fe-rich assemblage deformed at 850 °C (Fig. 2b). This results in the development of an anastomosing network of Amph-rich shear bands more or less connected depending on the initial assemblage (Fig. 2c), but without forming any through-going high-strain zone (Fig. 2a).

In more details, the reaction products in the Fe-rich assemblages are similar to those observed in the Mg-rich assemblages, but there is less Opx_2 and Amph-$Plag_2$ is the main reaction product (Fig. 5, 4g-to-j). From site to site in the sample deformed at 850 °C, a variable proportion of Opx and Plag have reacted. Mineral reactions preferentially occur in strongly deformed areas as partly interconnected monophase aggregates and shear bands (Amph) (Fig. 5a-b), while in less deformed areas, the reaction products occur mainly as thick seams at grain boundaries of extensional sites of Opx_1 and $Plag_1$ clasts (Fig. 5c). At 900 °C, the sample is more homogeneously deformed with a similar

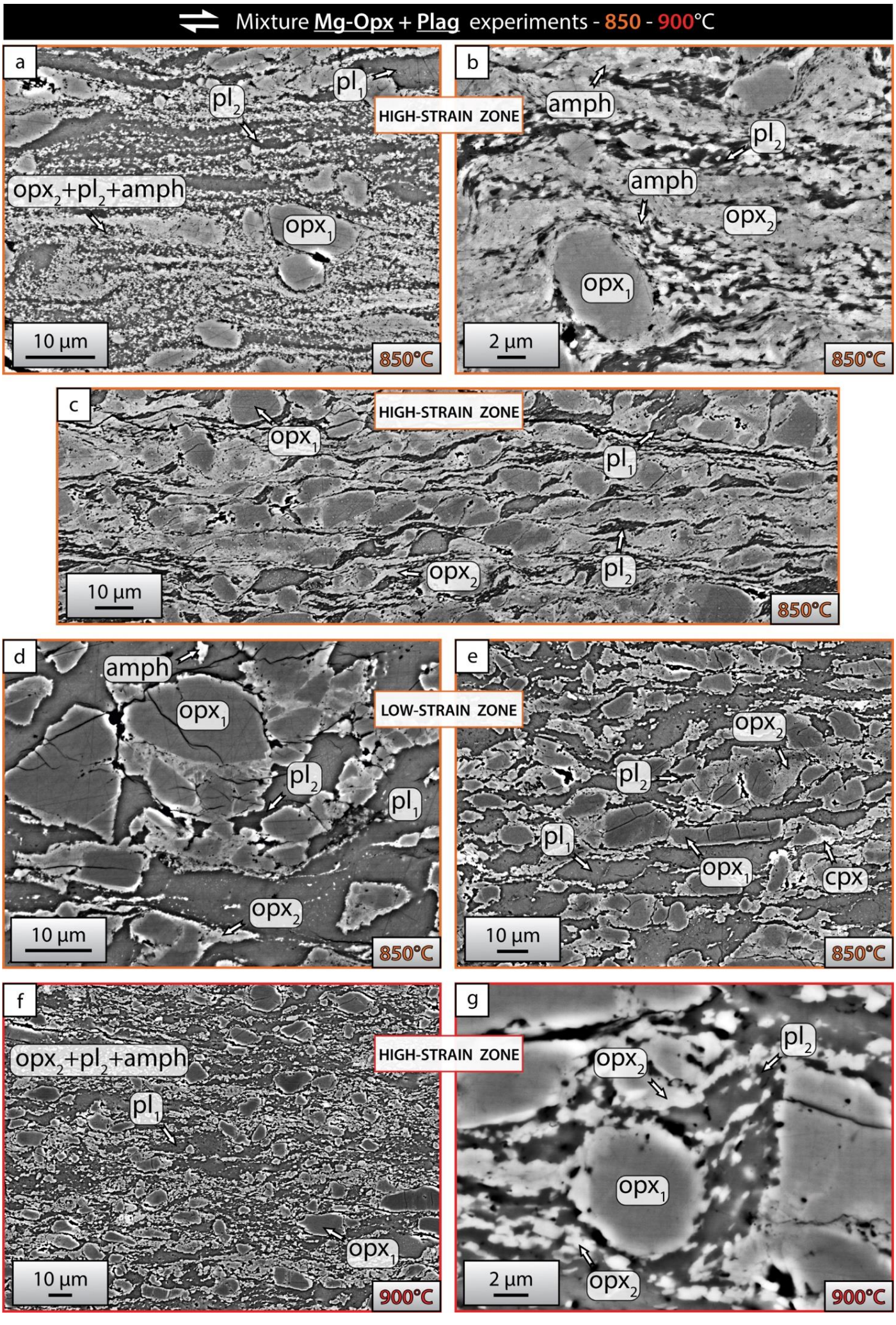
Mixture Mg-Opx + Plag experiments - 850 - 900°C
a
pl2
pl1
HIGH-STRAIN ZONE
opx2+pl2+amph
opx1
10 µm
850°C
b
amph
pl2
amph
opx2
opx1
2 µm
850°C
c
HIGH-STRAIN ZONE
opx1
pl1
opx2
pl2
10 µm
850°C
d
amph
opx1
LOW-STRAIN ZONE
pl2
pl1
opx2
10 µm
850°C
e
opx2
pl2
pl1
opx1
cpx
10 µm
850°C
f
opx2+pl2+amph
HIGH-STRAIN ZONE
pl1
opx1
10 µm
900°C
g
pl2
opx2
opx1
2 µm
opx2
900°C

Fig 3: SEM-BSE images representative of microstructures observed in deformed Mg-rich assemblages. Opx_2 and $Plag_2$ are the main reaction products. (**a-b**) At 850 °C, mineral reactions are mainly localized in the high-strain zones in the form of fine-grained mixed zones. (**c**) The original $Plag_1$ almost completely disappears. (**d**) In low-strain zones, the reaction products appear as coronas around the original Opx1 and as aggregates. (**e**) Opx_1 is locally fractured and filled with reaction products. (**f-g**) Similar microstructures are observed at 900 °C, although deformation is less localized compared to the assemblage deformed at 850 °C. opx = orthopyroxene, pl = plagioclase, amph = amphibole.

distribution of reaction products as observed at 850 °C (Fig. 5d-e). The Amph + Plag assemblage (Fig. 6a-to-c, 4k-l) deformed at 800 °C produced a large amount of reaction products composed of $Amph_2$, $Plag_2$, Cpx, and minor zoisite (Zo). There is a spatial relationship between Amph and Cpx as the latter occurs in small grains, predominantly around Amph clasts ($Amph_1$) mixed with small grains of $Amph_2$ (Fig. 6a-b). Unlike Fe-rich assemblages, the shear bands involve several phases (Amph and Cpx) in the Amph + Plag assemblages (Fig. 6, 9). Regarding the pure Amph assemblages deformed at 800 and 900 °C (Fig. 6d-e), mineral reactions are homogeneously distributed with the formation of $Amph_2$, Cpx and minor Zo, Qtz and garnet (Grt). Reaction induces the development of mixed phase zones of $Amph_2$ and Cpx and unmixed zones of Grt, Zo and Qtz (Fig. 4m-n).

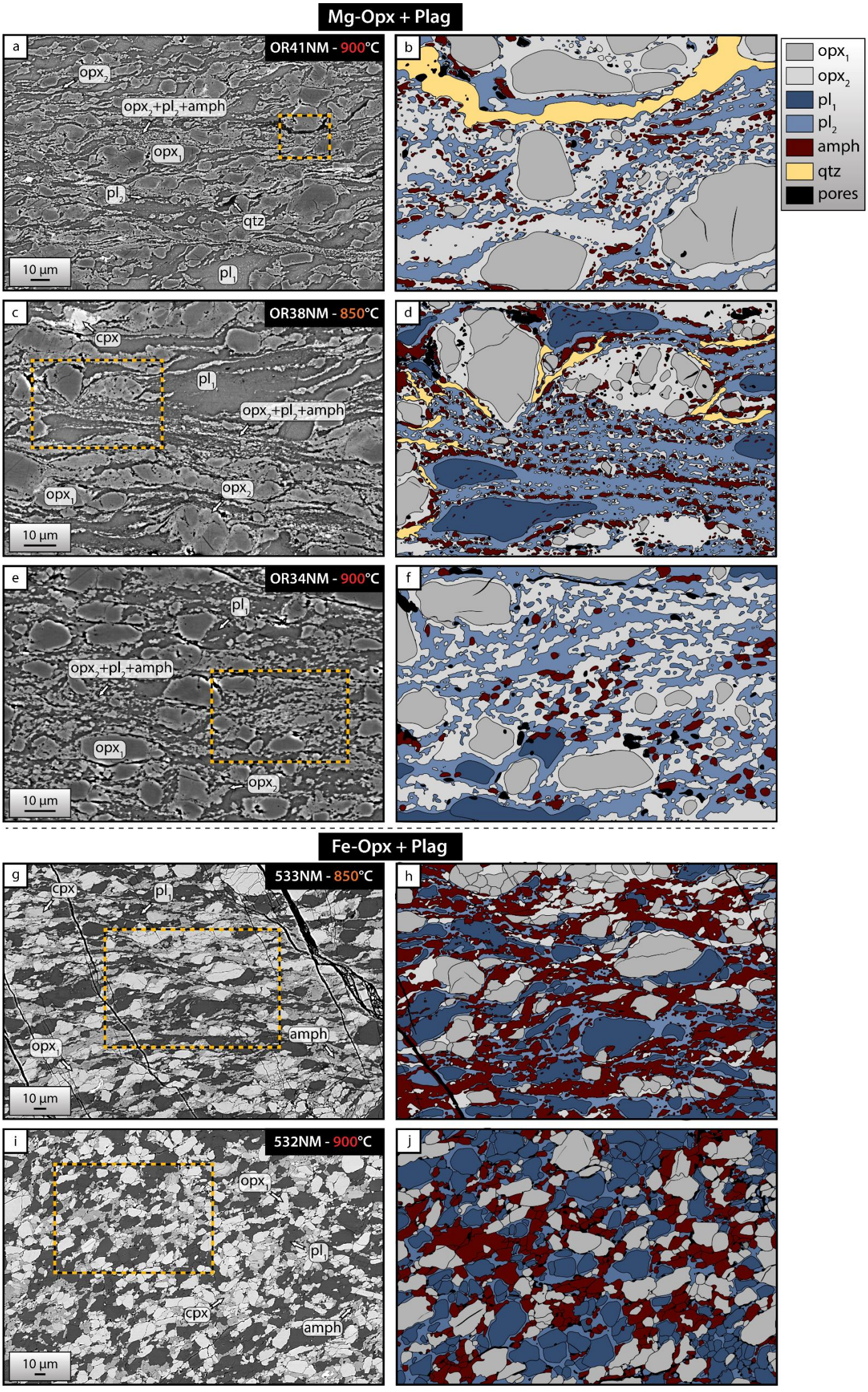
Mg-Opx + Plag
a
OR41NM - 900°C
opx2
opx2+pl2+amph
opx1
pl2
qtz
pl1
10 µm
b
opx1
opx2
pl1
pl2
amph
qtz
pores
c
OR38NM - 850°C
cpx
pl1
opx2+pl2+amph
opx1
opx2
10 µm
d
e
OR34NM - 900°C
pl1
opx2+pl2+amph
opx1
opx2
10 µm
f
Fe-Opx + Plag
g
533NM - 850°C
cpx
pl1
amph
opx1
10 µm
h
i
532NM - 900°C
opx1
pl1
cpx
amph
10 µm
j

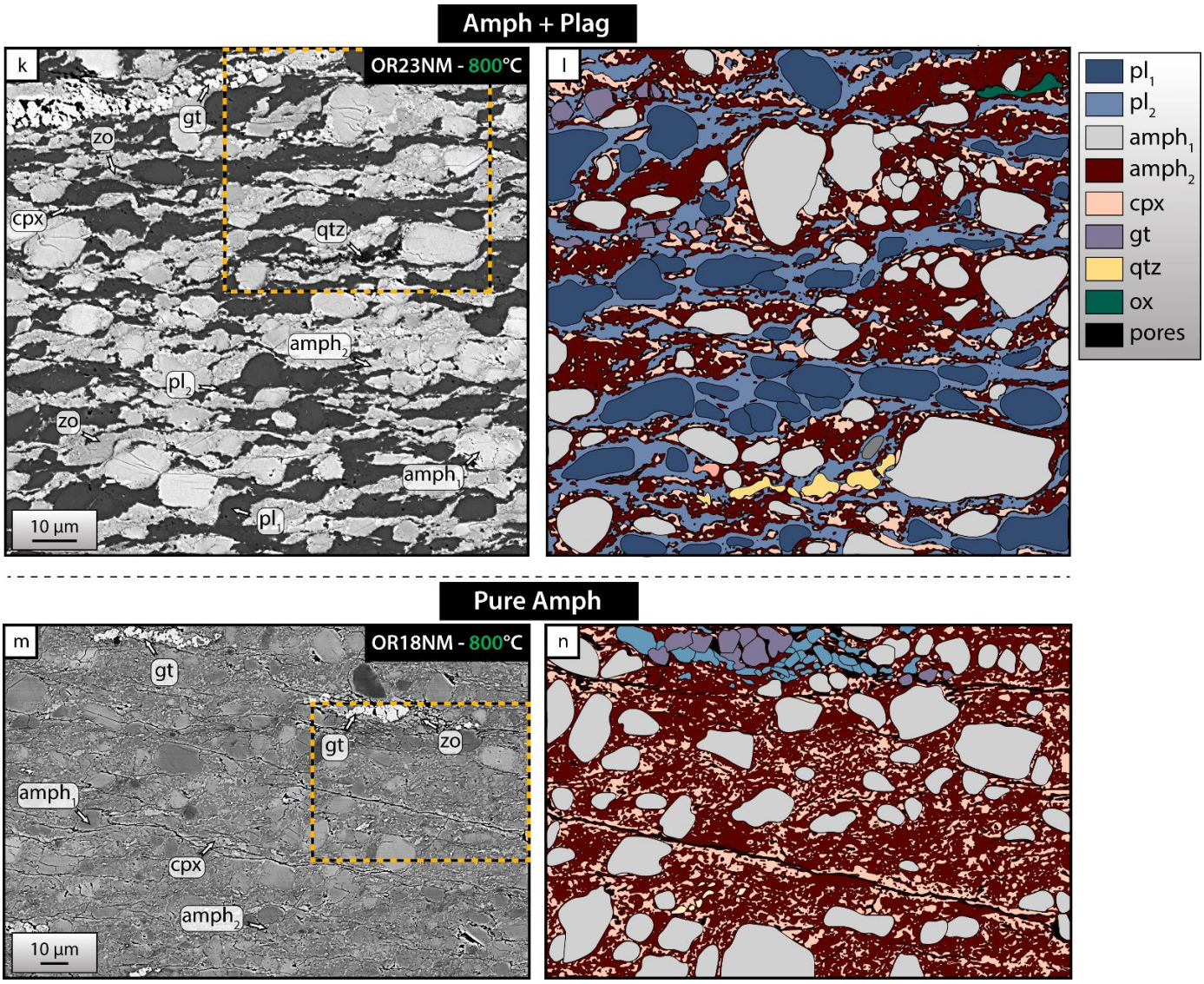

Fig 4: SEM-BSE images representative of the different small-scale microstructures encountered in the assemblages and their respective manually digitized phase maps. Please note that the resolution is too low to resolve the full extent of phase mixing. Opx = orthopyroxene, cpx = clinopyroxene, pl = plagioclase, amph = amphibole, qtz = quartz, gt = garnet, zo = zoisite.

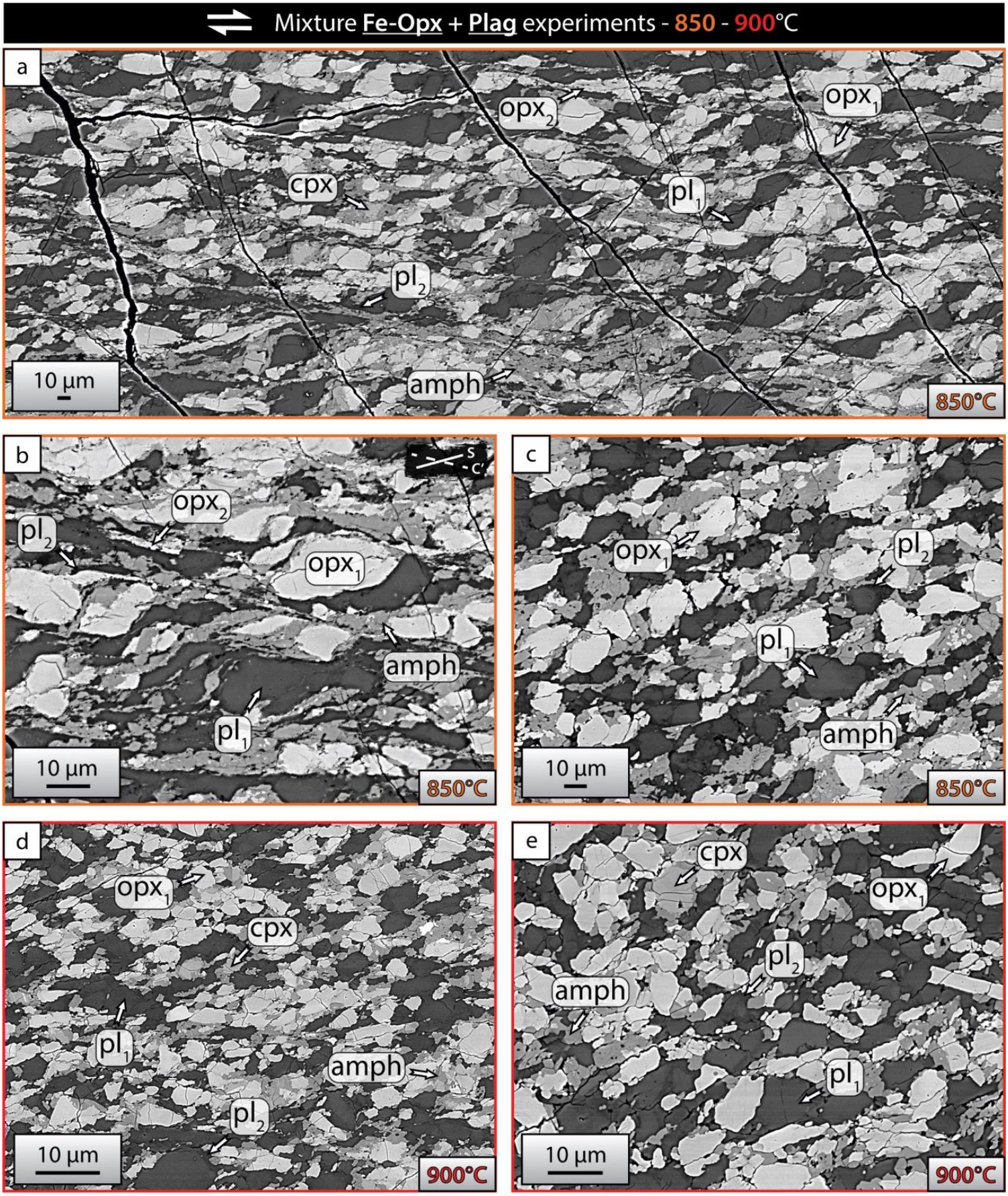

Fig 5: SEM-BSE images representative of microstructures documented in deformed Fe-rich assemblages. Amph and Plag2 are the main reaction products. At 850 °C, the deformation is heterogeneously distributed and a strain gradient is clearly apparent at sample scale. (**a-b**) In strongly deformed parts, the Amph appears as partially connected shear bands, while in the other parts (**c**) it appears as thick coronas around the Opx1 and Plag1 clasts. (**e-f**) At 900 °C, the deformation is more homogeneously distributed and the reaction products appear as reaction coronas. Opx = orthopyroxene, cpx = clinopyroxene, pl = plagioclase, amph = amphibole.

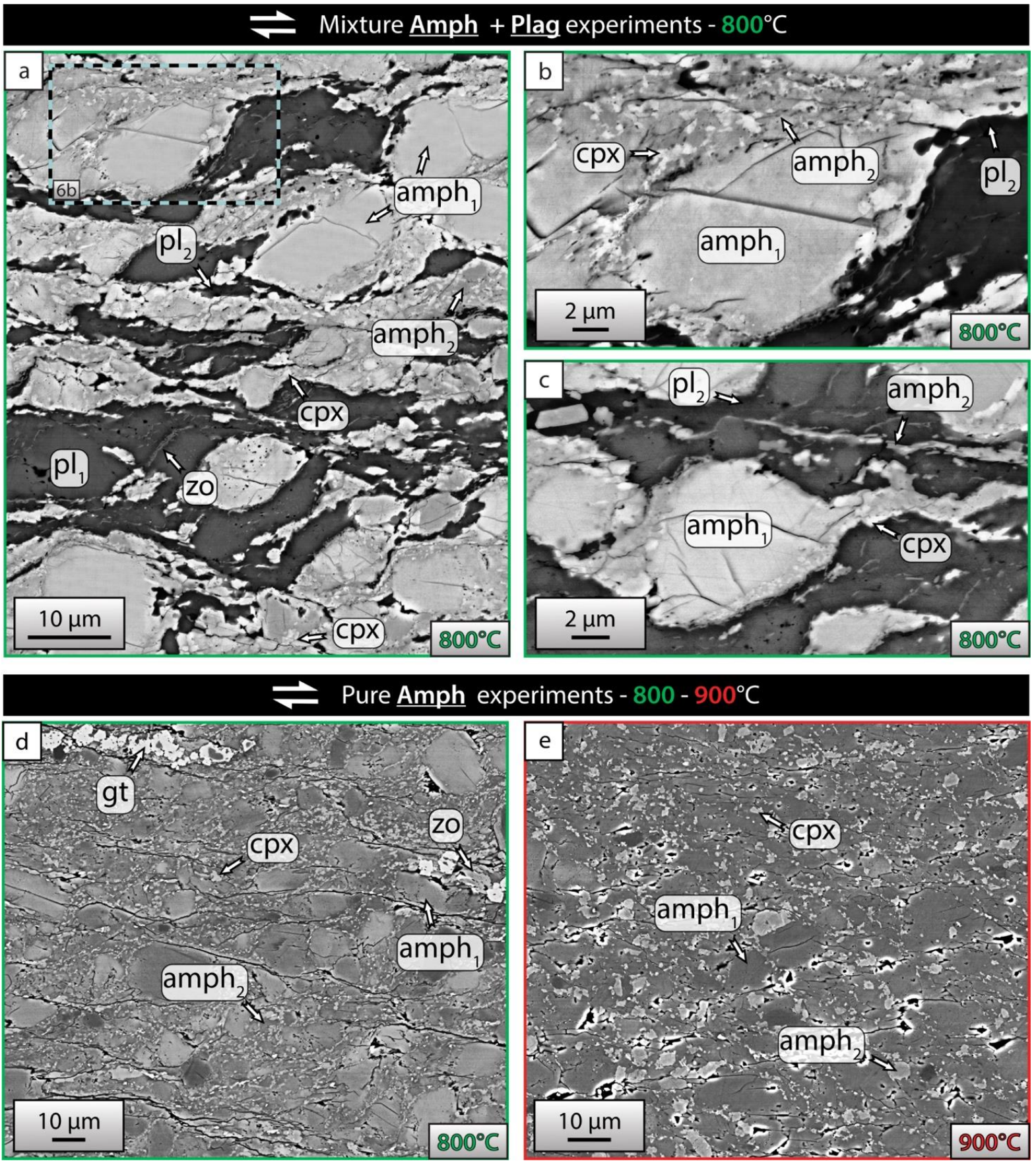

Fig 6: SEM-BSE images representative of microstructures shown in deformed Amph + Plag and pure Amph assemblages. (**a-b-c**) Nucleation of Amph-rich layers in the Amph + Plag assemblage deformed at 800 °C. (**d-e**) The pure Amph assemblages deformed at 800 °C and 900 °C show the development of fine-grained mixed phase zones of $Amph_2$ and Cpx. Opx = orthopyroxene, cpx = clinopyroxene, pl = plagioclase, amph = amphibole, gt = garnet, zo = zoisite

2.3 Chemical composition

The chemical composition of new grains is systematically different compared to the original ones. In each assemblage, the original plagioclase is labradorite that exhibits rims of more albitic $Plag_2$ (Fig. 7a-a'). The fine grains within mixed zones are also more albitic (Fig. 7a-a'). For the Opx_2, the ferrosilite content increases with respect to the original Opx_1, regardless of the original Opx_1 composition (Fig. 7b). The newly formed Cpx in the Amph + Plag and pure Amph assemblages are classified as augite (Fig. 7b). It is worth mentioning that the composition of the main reaction products (pyroxene and plagioclase) in the Fe-rich assemblages are farther away from the starting composition, compared to the main products composition in the Mg-rich assemblages. Moreover, the overstepping of reaction for the Fe-rich and Mg-rich assemblages was calculated by Alexis Plunder using the Perple_X thermodynamic software. The overstepping of reaction is larger in the Fe-rich assemblages (Tab. 1).

The composition of the original Amph used in both Amph + Plag and pure Amph experiments is not constant and varies in the magnesio-hornblende field (Fig. 7c). Regarding the newly formed Amph for all assemblages, they are classified mainly as magnesio-hornblende and tschermakite (Fig. 7c). There are nonetheless four chemically distinct populations of new Amph, depending on the composition of the starting mixture, as shown in the plot of Si vs. $Mg/(Mg+Fe^{2+})$ (Fig. 7c).

2.4 Initial shear localization

In the Mg-rich assemblages, shear is initially localized at the edges of original Opx_1 where the nucleation of fine-grained tails of mixed phases that define the general shear foliation (Fig. 8a). The new grains of Opx_2 are locally isolated by the presence of $Plag_2$ and Amph grains. In contrast, the initial strain localization in the Fe-rich assemblages forms nearly single-phase amphibole shear bands by nucleation of Amph extending from boundaries between Opx_1 and Plag (Fig. 8b). In the Amph + Plag assemblages, the reaction products nucleate at the edges of original $Amph_1$ clasts and tend to organize into an anastomosing network of thin amphibole and zoisite tails mainly parallel to the shear plane (Fig. 8c). In other cases, Opx_2 and Amph tails form at the extensional sites of Opx_1 clasts (Fig. 5b) and remain in contact with these clasts to define σ-type tails extending from the Opx_1 clasts. These grains are often found in contact with the surrounding albitic rim of Plag grains.

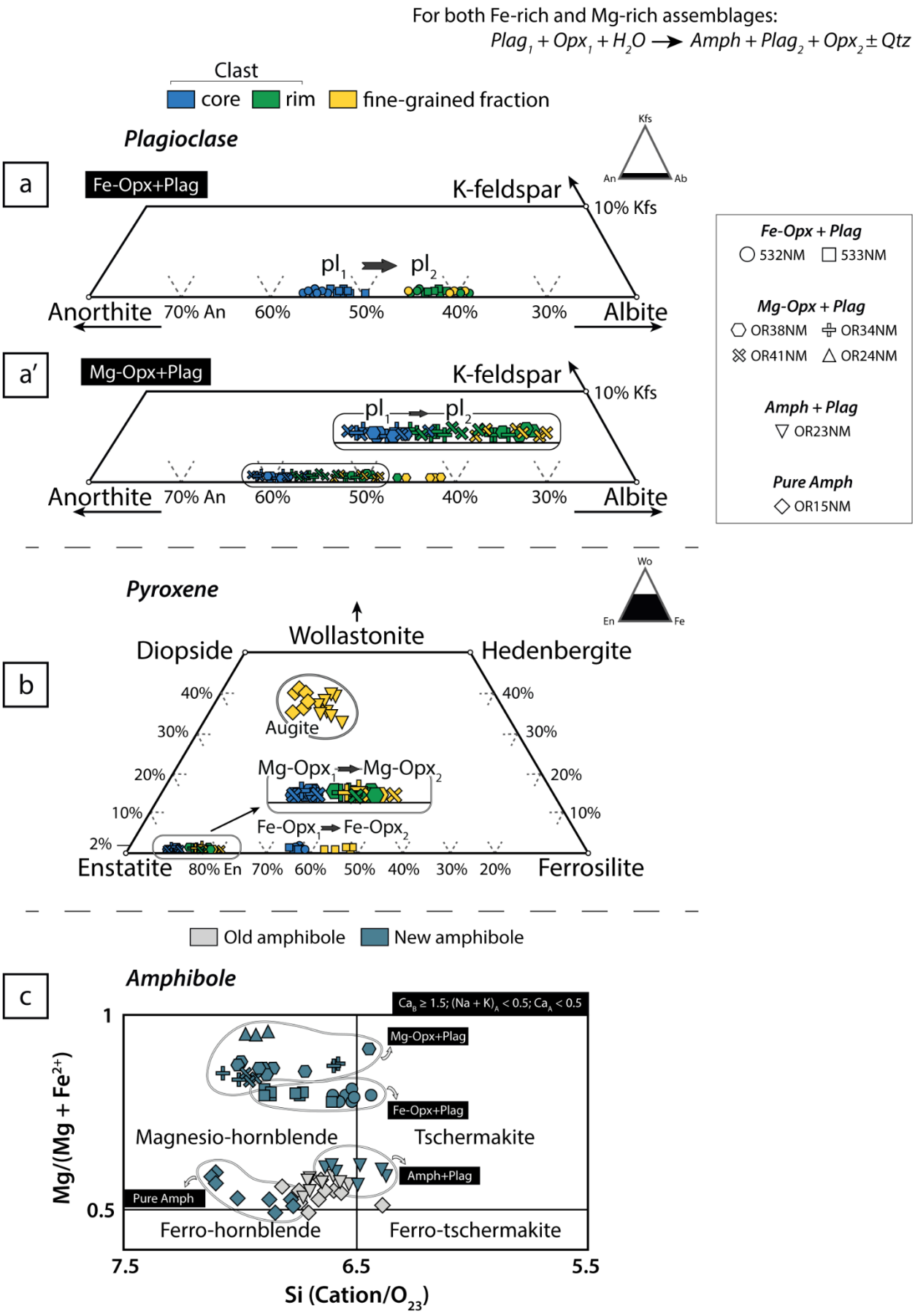

Fig 7: Mineral composition plots. Plagioclase compositions in the Fe-rich (**a**) and Mg-rich (**b**) assemblages plotted on the ternary diagram of orthoclase ($KAlSi_3O_8$), albite ($NaAlSi_3O_8$) and

anorthite ($CaAlSi_3O_8$). (**c**) Pyroxene compositions plotted on the ternary diagram of wollastonite ($Ca_2Si_2O_6$), enstatite ($Mg_2Si_2O_6$) and ferrosilite ($Fe_2Si_2O_6$). Chemical composition of plagioclase and pyroxene are divided into three subsets: clast-core, clast-rim and fine grains. (**d**) Classification of amphiboles in a $Mg/(Mg + Fe^{2+})$ versus Si content graph, for the case of $Ca \geq 1.5$; $(Na + K)_A < 0.5$; $Ca_A < 0.5$.

Mg-Opx + Plag	Enthalpy (H)	Entropy (S)	T (°C)	P (GPa)	Gibbs free energy (G) (J/kg)	ΔG (Prod. – React.)
Reactant	-12634000	2050.75	800	1	-14834454,8	**-2796.66**
Reactant	-12572400	2106.58	850	1	-14938089,3	**-3265.79**
Reactant	-12511000	2160.34	900	1	-15045078,8	**-3060.35**
Product	-12634200	2053.17	800	1	-14837251,4	
Product	-12572600	2103.31	850	1	-14941355,1	
Product	-12510600	2163.29	900	1	-15048139,2	
Fe-Opx + Plag						
Reactant	-11597600	2021.98	800	1	-13767184,5	**-3979.07**
Reactant	-11537800	2076.50	850	1	-13869709,5	**-3995.20**
Reactant	-11478000	2128.54	900	1	-13974777,4	**-4161.53**
Product	-11598800	2024.57	800	1	-13771163,6	
Product	-11539100	2078.90	850	1	-13873704,7	
Product	-11479100	2131.15	900	1	-13978939	

Tab 1: Overstepping of reaction for the Mg-rich and Fe-rich assemblages calculated with Perple_X.

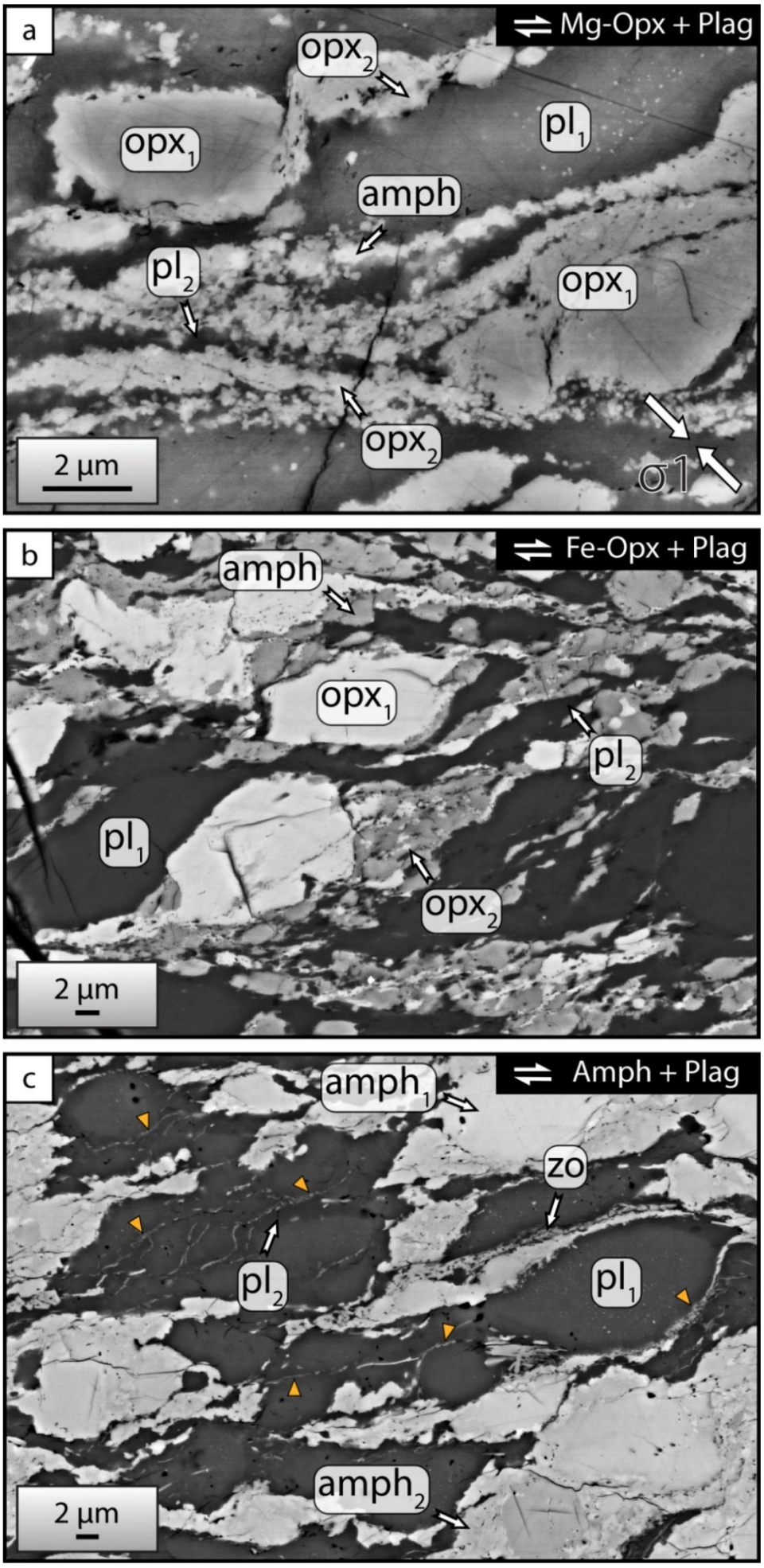
a
⇌ Mg-Opx + Plag
opx2
pl1
opx1
amph
pl2
opx1
opx2
σ1
2 µm
b
⇌ Fe-Opx + Plag
amph
opx1
pl2
pl1
opx2
2 µm
c
⇌ Amph + Plag
amph1
zo
pl2
pl1
amph2
2 µm

Fig 8: SEM-BSE images of incipient nucleation and shear localization. (**a**) In the Mg-rich assemblages, fine-grained tails of mixed phases nucleate at the edges of original grains. In the Fe-rich (**b**) and Amph + Plag (**c**) assemblages, the nucleation is fairly monophase. The new grains tend to organize into anastomosing network of thin amphibole and zoisite (orange triangle). Opx = orthopyroxene, pl = plagioclase, amph = amphibole, zo = zoisite.

To summarize, two types of reaction products and related microstructures form in the three different starting material assemblages: (1) In the Mg-rich samples, fine-grained phase mixtures are produced and localize into contiguous bands approximately parallel to the forcing block interface, i.e., the shear plane. (2) In the Fe-rich and Amph + Plag materials, either nearly mono-mineralic Amph shear bands or coarse-grained mixed tails of Amph + $Plag_2$ develop from clast rims. While fine-grained reaction products in case (1) arise with C-type shear bands, the sample fabrics of case (2) develop S-C' shear band geometry, the C' bands of which are filled by Amph.

2.5 Abundance and grain size of reaction products

The transition from low-strain to high-strain zones in the Mg-rich assemblages is accompanied by a significant grain size reduction from ~ 15 μm to ~0.2 μm (Fig. 9a). The high-strain zones concentrate most of the reaction products with roughly ~65% and locally more than ~ 80% of material replaced. This proportion is substantially higher compared to that in the low-strain zones (~ 28%), where no mixed phase layers develop. Similarly, in the mixed zones of pure Amph assemblages, the new grains are very small (~ 0.6 μm) and they represent nearly ~61% of the assemblage (Fig. 9b). The Amph grain size is also reduced in Fe-rich assemblages compared to the starting material (Fig. 9c), but the reaction products are less mixed and show a grain size that is approximately one order of magnitude larger (1.9 μm) than in the Mg-rich samples (0.2 μm). At 850 °C the reaction products are heterogeneously distributed and their proportion increases with increasing proximity to higher-strained portions of the shear zone. In contrast, at 900 °C the amount of reaction products remains roughly constant as there is no strain gradient, and reach approximately ~32%. Finally, in the Amph + Plag assemblages, the nucleation of Amph-rich shear bands is extensive (~ 36%) and the grain size decreases to ~1.3 μm (Fig. 9d).

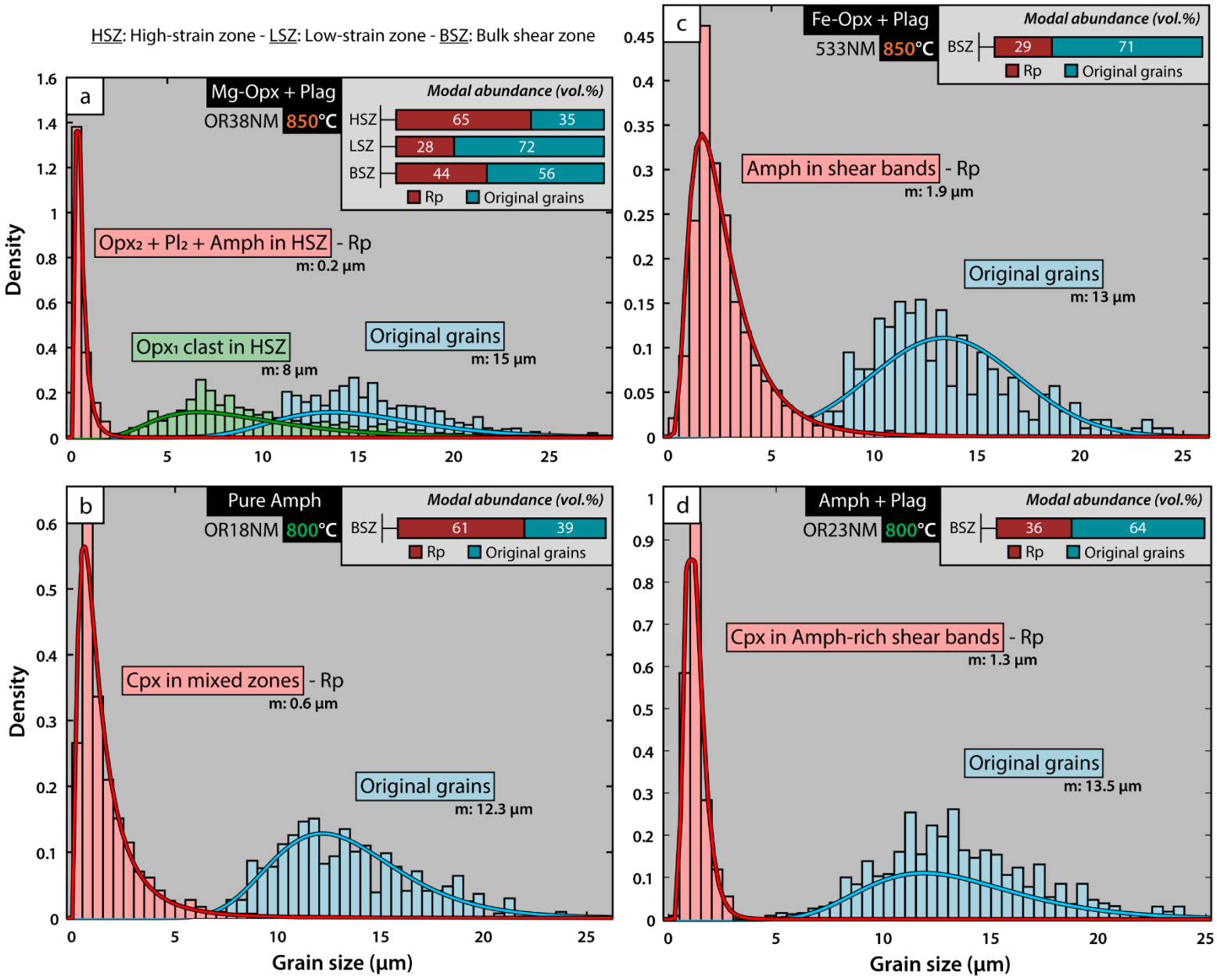

Fig 9: Grain size distribution reported as histogram of grain size versus density for different category of grains in the Mg-Opx + Plag (**a**), pure Amph (**b**), Fe-Opx + Plag (**c**), and Amph + Plag (**d**) assemblages. Overall, there is a significant and systematic reduction in grain size between the original grains and the reaction products. The log normal distribution curves are fit for each grain size distribution. The modal proportion (vol.%) of reaction products and original grains of each assemblage are also reported.

2.6 Analysis of SPO and amphibole LPO

Amph formed during deformation of Fe-rich assemblages exhibits a distinct SPO oriented at ~30° to the shear direction (Fig. 10a-b). These Amph occur as reaction coronas around original Opx_1 grains, and form partly interconnected aggregates that define the foliation. $Plag_2$ and Opx_2 also reveal a well-defined SPO similarly oriented to Amph. It should be

noted that the preferred orientation of Amph is sub-parallel to the minimum principal stress direction (Fig. 10a-b). In addition, the Amph reaction seams in high-stress sites of Opx grain boundaries is significantly thinner compared to that in low-stress or extensional sites, indicating that Amph grows preferentially in pressure shadows. In the higher strained portions of the shear zone deformed at 850 °C, the foliation defined by Amph layers rotates and is now well oriented sub-parallel to the boundaries of the shear bands (Fig. 10c). Within these shear bands, Amph grains show a moderate LPO with [001] axes aligned subparallel to the boundaries of C' shear bands and poles (100) normal to the shear plane (Fig. 10c). In the mixed zones of Mg-rich assemblages, the fine grains are characterized by an equant grain shapes (axial ratio a/b: 1.23; Fig. 11), and a weak preferred orientation parallel to the shear foliation and 45° to it (Fig. 11).

3. Discussion

3.1 Nucleation, grain size reduction and phase mixing

In this study, the deformation of two-phase assemblages is accompanied by the development of new grains with 1) systematic changes in composition (Fig. 7), 2) significant grain size reduction (Fig. 10) and 3) a new spatial arrangement of reaction products into fine-grained mixed phase or mainly monomineralic zones (Fig. 4). Based on these observations, we infer that grain size reduction and phase mixing result from the nucleation of new phases (e.g. Kruse and Stünitz, 1999; Kenkmann and Dresen, 2002; Kilian et al., 2011; Platt, 2015; Précigout and Stünitz, 2016). Despite common features, our samples have developed two sets of microstructures, distinguished mainly by the size and spatial arrangement of reaction products and the degree of phase mixing. We discuss these differences below.

In the Mg-rich assemblages, a strain gradient is clearly observed and expressed by the development of low- and high-strain zones (Fig. 3, 9a). This is particularly notable in the sample deformed at 850 °C. The transition from low- to high-strain zone is accompanied by drastic grain size reduction and increase in reaction products within localized mixed zones (Fig. 10a). Indeed, the grain size of reaction products in the mixed high-strain zones (~0.2 μm) is two orders of magnitude smaller than the grain size in low-strain zones, where most grains of the starting material are preserved (~10–20 μm; Fig. 10a).

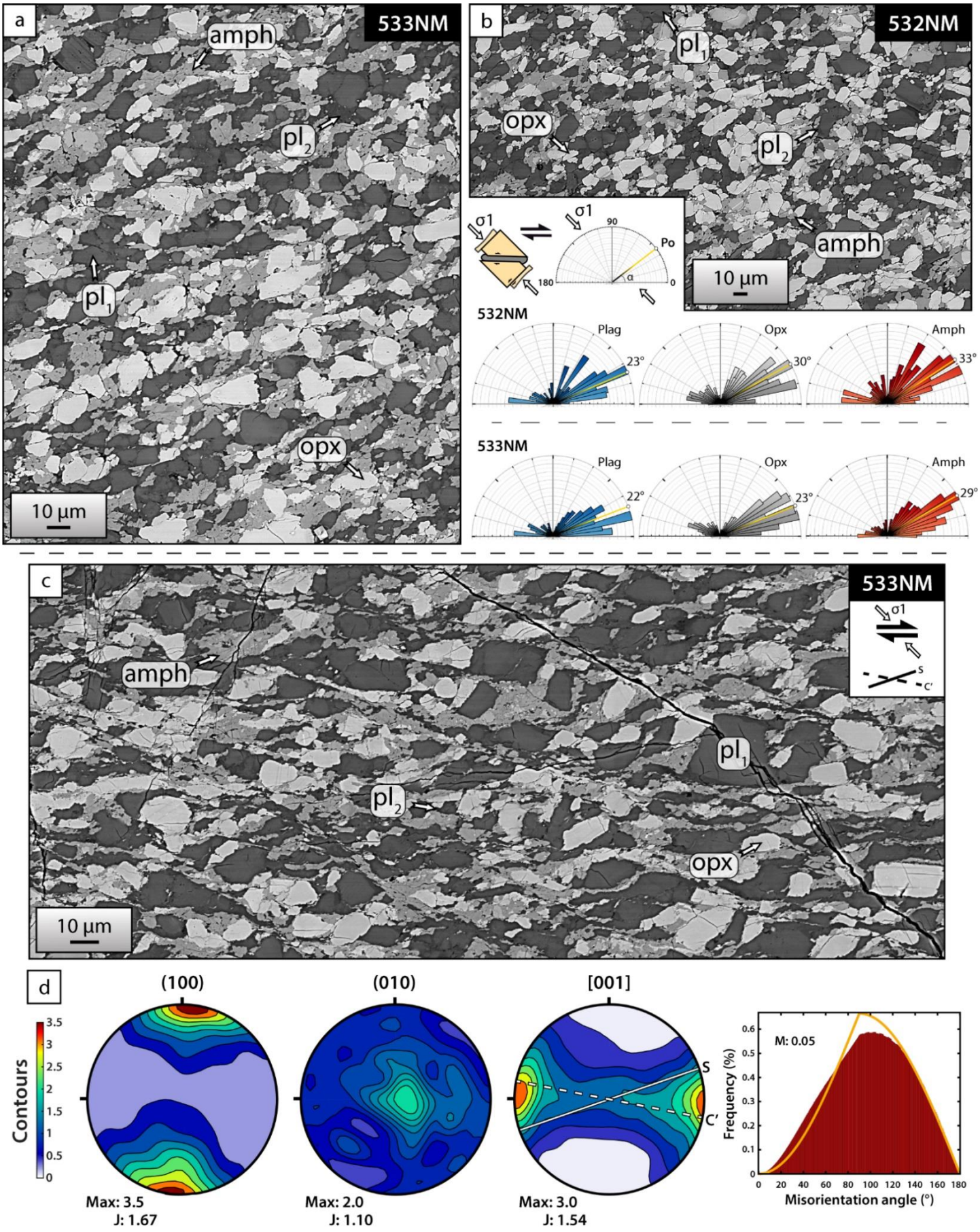

Fig 10: SPO and Amph LPOs. (**a-b**) Rose diagrams of the SPO of $Plag_1$, Opx_1 and Amph in the Fe-Opx + Plag assemblages (**a**: 533NM—850 °C and **b**: 532NM—900 °C). (**c**) Strongly deformed part of the Fe-Opx + Plag assemblage deformed at 850 °C. (**d**) Amph LPOs are shown for the (100) plane, (010) plane and [001] axis with respect to the shear direction, considering one point per grain. Opx = orthopyroxene, pl = plagioclase, amph = amphibole.

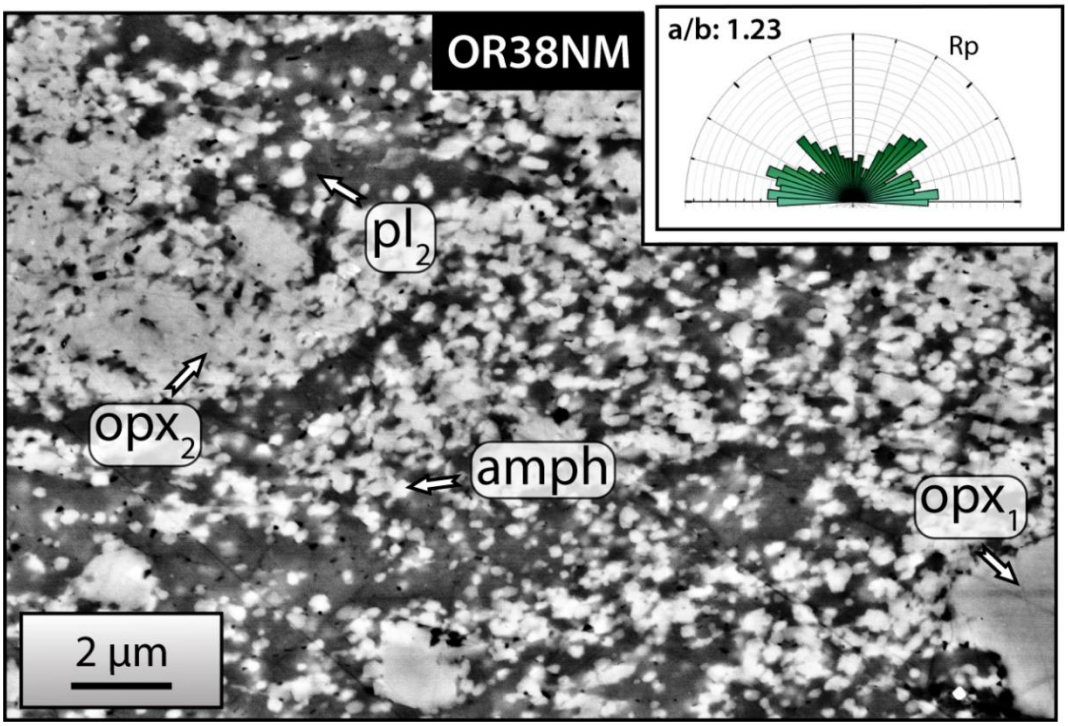

Fig 11: Rose diagram of the SPO of undifferentiated reaction products in fine-grained mixed zones in the Mg-Opx + Plag assemblages. Opx = orthopyroxene, pl = plagioclase, amph = amphibole.

Similarly, an extensive nucleation of reaction products within mixed-phase zones is documented in the pure Amph assemblages (Fig. 6d-e). The reaction products are also very small, far below the micron (~0.6 µm; Fig. 10b). Such a correlation between deformation, mineral reactions and related grain size reduction in Mg-rich assemblages has been documented in Mansard et al., (submitted). This feature has also been observed in experimentally deformed fine-grained gneiss (Holyoke and Tullis, 2006a, b), plagioclase + olivine samples (De Ronde et al., 2004; De Ronde and Stünitz, 2007), and plagioclase + pyroxene samples (Marti et al., 2018).

In the Fe-rich assemblages, the Amph is significantly more abundant and there is less phase mixing (Fig. 4g-j). The reaction products occur mainly as thick coronas around the Opx_1 (Fig. 5c) or as Amph monophase tails and shear bands (Fig. 5a-b). The abundance of reaction products increases with increasing proximity to strongly deformed portions of the shear zone. The reaction products have a smaller grain size (~1.9 µm) than the starting material, but this grain size is one order of magnitude larger than the mixed reaction products in the Mg-rich assemblages (Fig. 10c). Similarly to the Fe-rich assemblages, Amph-rich shear bands developed in the Amph + Plag assemblages

(Fig. 6a-c), and the grain size, although significantly reduced compared to the original grains, is not as small as that documented in the mixed zones in the Mg-rich assemblages (Fig. 10d). However, compared to the Fe-rich assemblages, there is an extensive nucleation of fine-grained Cpx within Amph-rich shear bands that increases the degree of phase mixing (Fig. 4k-i).

In a general way, we can distinguish two types of major microstructures: (1) in one case we observe intense grain size reduction via the nucleation of reaction products that are intensely mixed (Mg-rich and pure Amph assemblages). (2) In the other case, the reaction products are far less intensely mixed (Fe-rich) with the development of monophase—or moderately mixed (Amph + Plag)—shear bands that form tails or bands of larger reaction products connected to old clasts.

3.2 Deformation processes

As the reaction products in Mg-rich samples occur in pervasively mixed high-strain zones with an average grain size well below one micron and the production of equant grains, the dominant deformation mechanism is inferred to be grain size sensitive creep. The absence of well-developed layering of separate phases and absence of strong elongation of individual grains during GSS creep suggests that grain boundary sliding makes the dominant kinematic contribution to the finite strain (Rachinger sliding; e.g. Langdon, 2006). Such a deformation mechanism should probably be termed “diffusion accommodated grain boundary sliding” (GBS) or, more general, as a fluid has been present and solution precipitation is the probable transfer mechanism, “dissolution precipitation creep” (DPC). The pronounced weakening of the samples made strain rate stepping problematic in our experiments, so that the deformation mechanism is primarily identified based on microstructures. At first, the microstructures are similar to other cases where such deformation mechanisms have been identified (e.g. Marti et al., 2017, 2018; De Ronde et al. 2005; Stünitz and Tullis, 2001; Holyoke and Tullis 2006a, b; Tasaka et al., 2016, 2017; Getsinger and Hirth, 2014). The transition from low- to high-strain zones in the Mg-rich assemblages marks the transition from a two-phase aggregate with strong phases potentially deforming by dislocation creep to a grain size sensitive rheology, including DPC and/or GBS (e.g., Boullier and Gueguen, 1975; Kerrich et al., 1980; Schmid 1982; Brodie and Rutter, 1987; Kilian et al., 2011), where samples deform by low stresses (Fig. 2). The spatial arrangement of mineral phases in mixed aggregates

impedes grain growth (e.g. Olgaard and Evans, 1986, 1988, Herwegh et al., 2011). As documented by Mansard et al. (submitted), the mixing of mineral phases is homogeneous and starts from peak stress, in favor of GBS accommodated by DPC (e.g. Fliervoet et al., 1997; Kilian et al., 2011; Linckens et al., 2011). The original $Plag_1$ almost completely disappeared in the high-strain zones of Mg-rich samples, while the original Opx_1 remain as small clasts embedded in fine-grained mixed zones (Figs. 3a-to-c, 9a). Although the Opx_1 are still present, their proportion, aspect ratio and size decrease compared to the ones in the low-strain zones (Fig. 3). This suggests that Opx_1 grains act as rigid particles affected by dissolution and together with $Plag_1$, represent a source of elements required for the development of the ductile fine-grained zone deformed by diffusion-accommodated GBS.

In the Fe-rich samples, the deformation mechanism is also assumed to be DPC, demonstrated by the fact that (1) the samples deform at lower stresses well below the Goetze criterion, and (2) the microstructures that consist of elongate mineral aggregates of reaction products dominantly grow in the extension direction, shear bands, or in dilatant sites (Figs. 2, 5, 10). The nucleation of reaction products and local dilatancy could also require the operation of GBS (Lifshitz sliding; Langdon, 2006). The grain sizes of the reaction products in the Fe-rich samples are larger, resulting in higher flow stresses compared to the final stresses, after weakening, of the Mg-rich samples (Fig. 2, 10c; e.g. Mansard et al., submitted).

In addition, Amph fabric measurements display a fairly moderate, but consistent LPO with [001] axes aligned sub-parallel to the boundaries of C' shear bands (Fig. 11). This type of LPO is typical for naturally deformed amphibole (e.g. Jung, 2017; Berger and Stünitz, 1996). It is traditionally believed that significant LPO of minerals is attributed to viscous deformation dominated by dislocation creep (e.g. Nicolas and Christensen, 1987; Knipe, 1989; Wenk and Christie, 1991). However, an increasing number of studies have found that LPOs can develop without the dominance of dislocation creep, as shown in olivine (e.g. Sundberg and Cooper, 2008; Miyazaki et al., 2013, Précigout and Hirth, 2014), plagioclase (e.g. Barreiro et al., 2007) and amphibole (e.g. Getsinger and Hirth, 2014). The Amph LPOs presented here are similar to the ones documented in experimentally deformed amphibolite by Getsinger and Hirth, (2014), and to natural samples deformed at lower crustal conditions (e.g. Berger and Stünitz, 1996; Getsinger et al., 2013; Menegon et al., 2015; Okudaira et al., 2015). These studies have

demonstrated that oriented grain growth of pyroxenes and amphibole can lead to consistent amphibole/pyroxene LPO, even though diffusion creep is the dominant deformation mechanism. We thus interpret the presence of amphibole LPO in our samples as resulting from an oriented growth with the fastest growth direction (c-axis) in the flow direction. This supports an important contribution of metamorphic re-equilibration, chemical transport, and hence, DPC in the development of Amph mylonitic foliation in the Fe-rich and Amph + Plag assemblages (e.g. Bons and Den Brok, 2000; Berger and Stünitz, 1996).

3.3 Formation of polyphase vs. monophase shear bands and implications for the degree of rheological weakening

3.3.1 Polyphase shear bands

In the Mg-rich assemblages, the mixed-phase zones are strongly connected and form at 850 °C a single high-strain zone that traverses the sample through the center from one interface of the forcing block to the other (Fig. 9a). The deformation microstructures at early stages of our experiments suggest that phase mixing occurs at grain boundaries with the nucleation of fine grains in polyphase tails (Figs. 8a). These polyphase tails, into which strain is partitioned, are composed of Opx_2, $Plag_2$ and Amph. It has been documented by e.g., Kruse and Stünitz, (1999), Kenkmann and Dresen, (2002), Linckens et al. (2015) that phase mixing can be enhanced by the nucleation of phases within clast tails. The effect of mixing on the grain size is significant as grain growth is impeded by the nucleation of the second phase and preserves a small grain size in the mixed phase zones (Fig. 10a), forming a stable microstructure (e.g. Olgaard and Evans, 1986; 1988; Olgaard, 1990; Stünitz and Fitz Gerald, 1993; Herwegh and Berger, 2004; Warren and Hirth, 2006 Farla et al., 2013). The opening of cavities in which material can nucleate (e.g. Fusseis et al., 2009; Platt, 2015; Menegon et al., 2015; Précigout and Stünitz, 2016; Précigout et al., 2017; Gilgannon et al., 2017) may be an additional factor to promote mixing and to stabilize small grain sizes.

3.3.2 Monophase shear bands

The majority of reaction products occurs in strongly deformed portions of the shear zones, indicating a close relationship between deformation and mineral reactions in

the Fe-rich assemblages (Fig. 9b). However, these portions are not characterized by the development of intensely mixed phase zones, as in the Mg-rich assemblages. Indeed, progressive increasing strain and reaction progress induce the formation of either monophase shear bands of Amph or less intensely mixed Opx_2 + Amph zones (Fig. 4, 5). Similarly, the Amph + Plag assemblage is banded and shows a sub-horizontal mylonitic foliation characterized by the development of Amph-rich shear bands. These shear bands cannot be considered strictly as monophase bands, but they are relatively similar to Amph shear bands documented in the Fe-rich assemblages.

3.3.3 Effects of shear bands interconnection on the degree of rheological weakening

There is a significant difference in shear band connectivity depending on the pair of minerals studied. The Mg-rich mixture tends to produce mixed fine-grained C-geometry bands in high-strain zones (Figs. 3, 4, 8, 9a). The development of a single through-going high-strain zone is associated with a significant weakening after peak stress (Fig. 9a). It is considered that in Mg-rich sample, the low final shear stress more or less represents the flow stress of the fine-grained aggregate. In contrast, the Fe-rich and Amph + Plag mixtures tend to form clusters and partially connected Amph-rich tails of clasts (S-geometries) or C'-type shear bands (Figs. 4, 5, 8, 9b-c). When the shear bands and tails of clasts are only partially connected, there is no peak stress and no weakening observed in the experiments (Fig. 9b; Fe-rich assemblages). This lack of major weakening can be caused by two aspects: either by (1) The absence of highly connected aggregates of reaction products or by (2) the fact that grains are too large and less intensely mixed, so that GSS creep is less. In addition, the connectivity of the reaction products appears to be also affected by their geometry: The fine-grained C-type bands are parallel to the shear plane and seem to connect much more easily than the local S- and C'-type tails and shear bands.

The fact that the connectivity of weak zones has a major weakening effect on the bulk sample strength has been documented by, e.g., Pec et al. (2012, 2016), Palazzin et al., (2018), Richter et al., (2018) and certainly is a major rheological factor in these mafic samples, too. However, in addition to the connectivity, different microstructures are documented in the weak parts of each sample, pointing to a difference in GBS/DPC mechanisms. The less intensely mixed layers, tails and shear bands in the Fe-rich

assemblages display higher aspect ratios of the reaction products, i.e., more fiber-like grains (Fig. 5c; 11a-b). These microstructures constitute a type of DPC that is tending more towards grain-scale DPC, where ideally (in the end-member case) the grain shapes would reflect the finite strain. The Fe-rich samples are far from the end-member case, but they approach this situation more than the fine-grained well mixed bands of equant grains in Mg-rich samples (Fig. 3a-b; 12), where DPC is probably dominated by GBS. The difference in strain rate between the end-member cases at the same stress is less than one order of magnitude, so that it will be difficult to determine in most geological environments. In our case, the grain size will play a major role, indicating that it is the combination of faster strain rates in the finer grained layers and connectivity of the reaction product zones that causes the pronounced weakening in the Mg-rich samples.

3.4 The role of reaction kinetics on material strength

In the Fe-rich samples, the higher iron content of Opx_1 favors the formation of Amph with only a minor amount of Opx_2, whereas in the Mg-rich samples, the nucleation of a new Opx_2 is promoted. The composition of the reaction products (pyroxene and plagioclase) in the Fe-rich assemblages is farther away from the starting material composition at the imposed P-T conditions, compared to the same reaction product compositions in the Mg-rich assemblages (Fig. 7a-a'-b). Because the starting material composition in the Fe-rich is far from the equilibrium, it is inferred that its total free energy is higher compared to that of the final reaction products. This is consistent with the overstepping of reaction which is larger in the Fe-rich assemblages (Table. 1). Consequently, the Fe-rich assemblages react faster than the Mg-rich assemblages. It is observed that the formation of product phases commences earlier in the Fe-rich assemblage (Mansard et al.; submitted). Considering that the rheological behavior is controlled by the reaction products, it is inferred that the Fe-rich assemblages do not develop a peak stress behavior and deform at lower stresses than the Mg-rich assemblages (Fig. 2b-d, 13). However, although in the Fe-rich assemblages product phases nucleate faster than in the Mg-rich assemblages at early stages of the experiment, the proportion of reacted material is higher in Mg-rich assemblages at high-shear strain and the grains that nucleate are smaller in size (Fig. 10, 13).

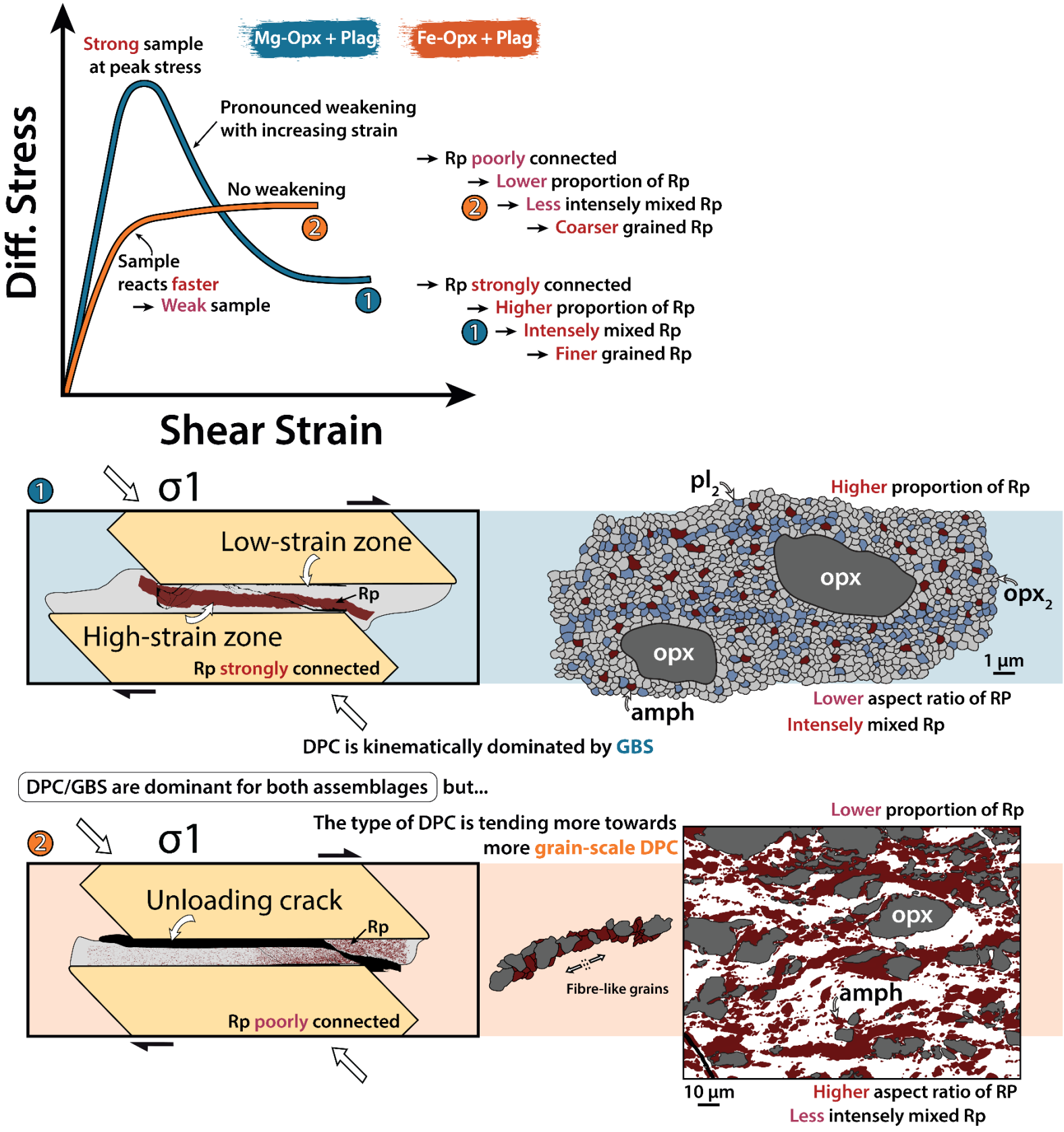

Fig 12: Schematic mechanical and microstructural evolution of the deformed Mg-rich and Fe-rich assemblages. Rp = reaction product, opx = orthopyroxene, pl = plagioclase, amph = amphibole.

In addition, the weakening with increasing strain is far more pronounced in the Mg-rich assemblages (Fig. 2, 13). The reason for the difference in mechanical behavior and in reaction kinetics is two-fold: (1) The Mg-rich samples have experienced a longer incubation period before the hit point, so that the reaction products could nucleate at an early stage with respect to the onset of deformation, and hence, lower the peak strength (Mansard et al., submitted), and (2) the mixing and finer grain sizes of the reaction products in Mg-rich samples cause greater strain partitioning and would indicate a faster nucleation rate after peak stress, although the Fe-rich samples react faster at early stages of experiment because of greater difference in composition between all products and reactant phases (Fig. 9, 13). Deformation and reaction products are strongly localized and connected in high-strain zones of the Mg-rich assemblages (Fig. 10a), while in Fe-rich samples reaction products are localized and poorly connected (Fig. 10b). In the case where the viscosity of the reaction products is very low (fine-grained mixed zones in the Mg-rich) compared to the starting material, the reacted domains tend to connect much better during the deformation (Fig. 10a, 13). The interconnection of the dispersed fine-grained reaction products caused subsequent strain to be significantly partitioned. Considering that deformation enhances the kinetics of reactions (De Ronde and Stünitz, 2007; Mansard et al., submitted), this feature suggests more advanced reaction progress in the Mg-rich samples. On the contrary, if the reaction products are more viscous (in Fe-rich samples; amphibole appears to be one of the strongest silicates; Brodie and Rutter, 1985; Berger and Stünitz, 1996), or even if there is hardening during the reaction (Fe-rich at 900 °C; Fig. 2d), the feedback effect of enhancing reaction kinetics appears more difficult and there is no weakening observed during the deformation—samples are considerably weaker than without reaction, though. Therefore, the viscosity of the Fe-rich and Amph + Plag assemblages is related to their ability to transform and connect.

The reason why the reaction products in Mg-rich samples are finer grained and do not stay attached to the original Opx_1 clasts is yet unknown. The difference in phase distribution between the two different starting materials forms one of the major reasons for their later strength development during connectivity and reaction progress. This situation illustrates that substantially more work is needed to understand the relationship between mineral reaction and mechanical behavior.

3.5 Geological application

In this study, the rheological behavior of two-phase mixtures of mafic composition is dependent on mineral reactions and particularly sensitive to compositional differences, as small chemical variations can trigger strain localization and weakening, even at low shear strain. In both starting materials, the reactions combined with the operation of GSS creep allow the deformation of the mafic assemblage. Without mineral reactions, the mafic assemblage of pyroxene and plagioclase would be too strong to be deformed by dislocation creep at the applied strain rates (Mansard et al., submitted). This situation is the same in naturally deformed rocks: Below ~ 700 °C, pyroxene and plagioclase assemblages do not show significant crystal plastic deformation (e.g. Rutter and Brodie, 1985, 1992). The partly extensive deformation of mafic rocks at lower metamorphic grades appears to be dependent upon mineral reactions, which can induce the development of rheologically weaker phases, or in the formation of fine-grained aggregates deforming by GSS creep, or in both (e.g. Rutter and Brodie, 1992; Stünitz, 1993; Handy and Stünitz, 2002; Brander et al., 2012; Okudaira et al., 2017).

At low shear strain and identical P-T conditions, the small difference in composition between the Fe-rich and Mg-rich assemblages induces clear differences in mechanical strength at peak stress and weakening behavior. These observations are crucial as it is known that shear zones represent preferential regions for mineral reactions to occur, either owing to deformation (e.g. Brodie, 1980) or to the presence of fluids (e.g. Etheridge et al., 1983) during protracted shearing (e.g. Brodie, 1980; Philippot and Kienast, 1989; Newman et al., 1999). Thus, local spatial variations in chemical composition can induce gradients in deformation due to sufficient differences in the mechanical behavior to localize strain (e.g. Holyoke et al., 2006a, b). In addition, our observations suggest that the mechanical strength at peak stress is controlled by the ability of the material to react and to connect weak material, and not necessarily by the strength of the reaction products. In fact, the Fe-rich assemblages produce intrinsically stronger reaction products (amphibole) than the fine-grained mixed aggregates and layers in the Mg-rich assemblages, and yet Fe-rich assemblages are weaker at low shear strain because they react faster. Our results suggest that small initial differences in composition of the minerals in natural materials can trigger strain localization and lead to large differences in mechanical strength, regardless of the intrinsic strength of the reaction products. These observations mainly apply to the initiation and early stages of shear zone formation, as

once the incipient stages of strain localization and weakening are initiated, additional mechanisms are involved and control the development of the shear zones in space and time.

The development of natural shear zones commonly arises into distinctive monophase layers (e.g. Berthé et al., 1979; Gapais, 1989) and/or polyphase mixtures (e.g. Fliervoet et al., 1997; Keller et al., 2004; Warren and Hirth, 2006; Kanagawa et al., 2008; Raimbourg et al., 2008; Okudaira et al., 2015) that may be found in the same shear zone as alternating layers (e.g. Kenkman et al., 2002; Kilian et al., 2011; Oliot et al., 2014; Mansard et al., 2018). In our case, the progressive deformation of two-phase assemblages also shows the development of (1) strongly localized polyphase high-strain zone associated with a significant weakening after peak stress (Mg-rich assemblages), and (2) partially connected, locally monophase and localized shear bands that do not induce major weakening (Fe-rich and Amph + Plag assemblages). Strain localization into reaction-derived fine-grained mixture is also well documented in nature with the dominance of diffusion-accommodated GBS and/or DPC mechanisms (e.g. Stünitz, 1993; Newman et al., 1999; Handy and Stünitz, 2002; Kanagawa et al., 2008; Okudaira et al., 2015) and is expected to promote major rheological weakening (e.g. Fliervoet et al., 1997; Svahnberg and Piazolo, 2013; Warren and Hirth, 2006; Platt, 2015). The development of Amph-rich aggregates and layers, notably through dissolution and precipitation processes, is also commonly documented in mid- to lower-crustal banded mylonites (e.g. Berger and Stünitz, 1996; Imon et al., 2002; Imon et al., 2004; Baratoux et al., 2005; Getsinger et al., 2013; Elyaszadeh et al., 2018).

When applied to natural shear zones, our results suggest that (1) The ability of minerals to react controls the portions of rocks that deform, and (2) minor chemical and mineralogical variations can considerably modify the strength of deformed assemblages. Then, significant strain localization and partitioning at high shear strain, expressed by the development of interconnected high-strain zones (Mg-rich), illustrates that fine-grained polyphase mixed zones can be weaker than coarse-grained, poorly-connected ones (Fe-rich and Amph + Plag). These results emphasize the importance of strain partitioning, grain size reduction and interconnectivity of weak material as a primary control of lithospheric strength. This also suggests that the rheology of mafic rocks, which constitute a large part of the oceanic crust and may be one of the main components of the lower continental crust, cannot be summarized as being rheologically controlled by monophase materials.

4. Conclusion

Shear deformation experiments of monophase and polyphase assemblages show a clear relationship between deformation and mineral reactions. A greater volume of reaction products is documented with increasing strain. This study shows that the premise of mineral reaction and strain localization has a major impact on sample strength because it conditions the resistance of the assemblage at low shear strain. Indeed, the Fe-rich assemblages deform at lower stresses than the Mg-rich assemblages because they react faster at early stages of experiment. Thus, chemically close assemblages may have significantly different strength depending on the ability of these minerals to react. With increasing strain, this work also illustrates two very contrasted pathways in the material evolution, controlled by the properties of the reaction: In one case (Fe-rich and Amph + Plag assemblages), the reaction products (mostly monophase amphibole) have a relatively large grain size and do not induce significant weakening. In such a case, the reaction products are only partially connected, the bulk strength is stable and the feedback effect of deformation on reaction is limited. In the other case (Mg-rich and pure Amph assemblages), the fine-grained, mixed-phase reaction products are much weaker than the initial material. There, mechanically weak zone of reaction product tends to form an interconnected zone that leads to a large macroscopic weakening, and the drastic increase in proportion of reaction products with strain suggests a large feedback effect. Overall, the value of the initial peak stress (that is responsible for determining where strain will start localizing) or the large weakening associated with the formation of fine-grained products (that determine whether shear bands thicken or not), seem to be largely controlled by the chemical reactions.

CHAPTER VI

Syntheses and general discussion

CONTENTS

Over the past decades, an increasing number of studies aimed at understanding the rheological behavior of the lithosphere has highlighted that shear zones are key rheological structures influencing the strength of the lithosphere, since these represent zones of weakness where strain localizes during geodynamic processes (e.g. Jolivet, 1995; Rutter et al., 2001; Vauchez et al., 2012; Snyder and Kjarsgaard, 2013; Fossen and Cavalcante, 2017). Major ductile shear zones are generally established at depth, from mid to lower crust and deeper. Moreover, there is a major debate concerning the true rigidity of this portion of the lithosphere as its composition and structure are still subject to discussion (e.g. Christensen and Mooney, 1995; Rudnick and Gao, 2003; Bürgmann and Dresen, 2008; Petit et al., 2008; Hacker et al., 2015). Thus, the understanding of the behavior of shear zones that localized strain and deformed rocks at mid-lower crustal conditions is one of the missing pieces of a sophisticated puzzle that will improve our comprehension of the rheology of the lithosphere.

In this manuscript, we have proposed a short "Journey to the Center of the Earth", whose vision is significantly different from that of Jules Verne, and aims at studying the structure and evolution in space and time of shear zones. We opted for a multi-scale approach, starting with the study of a crustal-scale strike-slip fault that deformed granitoids at mid-crustal conditions (SASZ), and then with the study of experimentally deformed polyphase assemblages representative of the lower crust at high P-T conditions.

1. Development of shear zones through the succession of weakening processes that localized strain

Our natural case study investigates the South Armorican Shear Zone (SASZ) in the South Armorican Massif in France. The SASZ corresponds to a crustal-scale shear zone that deforms granitoid rocks at mid-crustal conditions. With increasing strain from weakly deformed (protolith) to highly deformed (ultramylonite) rocks, this shear zone is characterized by (1) a significant grain size reduction, (2) the development of monophase layers of mica in moderately (protomylonite) and further deformed (mylonite) rocks, and (3) their subsequent replacement by fine-grained mixed-phase zones in ultramylonite. Thus, there is an increase of mixing and a decrease of grain size concomitant with an increase of strain. The strain gradient from protolith to ultramylonite is also accompanied by the increase and subsequent decrease of quartz LPO. We proposed that the causes for interconnection of mica are the formation of cracks in the protolith combined with fluid—

assisted nucleation. The latter process also plays a major role in phase mixing, as attested by the precipitation of a secondary phase at triple junctions in quartz-rich layers and in fine-grained tails of inherited K-feldspar porphyroclasts in ultramylonite. We suggest that phase nucleation is the major process behind phase mixing, and possibly together with grain-boundary sliding (GBS) to open cavities during deformation. Indeed, microstructural features also indicate that grain size has triggered a transition from grain size insensitive (GSI) to grain size sensitive (GSS) creep, including grain boundary sliding (GBS).

- Instead of a single process, this natural case study highlights a succession of weakening processes in the evolution of the SASZ, starting with the nucleation of mica as a first weakening material (typically viewed as the weakest phase in granitoid rocks, e.g. Tullis and Wenk, 1994), and then evolving with the formation of very fine-grained mixed-phase zones with increasing strain.

- A reduced grain size has triggered a transition in dominant deformation mechanism with increasing strain. While the quartz-rich layers are deformed predominantly by dislocation creep, the fine-grained mixed zones, which display a reduction in quartz LPO, are predominantly deformed by GBS.

- The fine-grained polyphase mixtures that develop in replacement of the interconnected network of mica are considered to be the weakest end member shear zone geometry. The reduction of grain size is consequently believed to play a critical role in strain localization to form the shear zone.

In order to study how shear zones develop and how the interplay between deformation and mineral reactions influence rock rheology, we then performed shear experiments on fine-grained two-phase assemblages representative of the lower crust and, for comparison, pure phase material experiments in a Griggs-type solid-medium deformation apparatus. Experiments were performed at a constant shear strain rate of 10^{-5} s^{-1}, a confining pressure of 1 GPa and temperatures between 800 and 900 °C. One of the major advantages of laboratory deformation experiments is the ability to control some variables, such as the strain rate and the amount of strain. This kind of experiment provides an opportunity to study the early stages of deformation, which is often complex

as natural shear zones provide access only to the final stage of deformation and many early-stage features have been obliterated by late-stage deformation. It also provides information about the mechanical strength evolution, which depends on the active processes responsible for the development of shear zones.

2. Influence of mineral composition on strain localization and weakening at low shear strain

Experimental results from the deformation of two-phase assemblages (pyroxene-plagioclase) show a strong relationship between the ability of minerals to react, the amount of reaction products and the strength of materials. With regards to the quantity of reaction products, it has been found that two starting assemblages, with the same mineralogical mixture (plagioclase—pyroxene), can reach significantly different peak stress depending on the proportion of reaction products. The more reaction products an assemblage contains, the weaker it is. Consequently, mineral reaction has a direct control on rock rheology.

Starting with the same mineralogical mixture (plagioclase—pyroxene), we used two types of orthopyroxene, the composition which is enriched in either Magnesium (Mg) or Iron (Fe). At a first order, we find that: (i) the nature of the reaction products, (ii) the strain partitioning, and (iii) the reaction kinetics are significantly different. In the case (1) (Fe-rich assemblages), the higher iron content of Opx_1 favors the formation of Amph with only a minor amount of Opx_2, while in the case (2) (Mg-rich assemblages), the nucleation of a new Opx_2 is favored. In the case (1), the initial deformation zones are either nearly monomineralic Amph shear bands or coarser grained mixed tails of Amph + $Plag_2$ from clast rims, while in the case (2), shear directly localized at the edges of original Opx_1 by the nucleation of fine-grained tails of mixed phases that define the general shear foliation. The composition of the reaction products (pyroxene and plagioclase) in the case (1) is farther away from the starting material composition at the imposed P-T conditions, compared to the same reaction product compositions in the case (2). As the starting material composition in the case (1) is farther away from the equilibrium, its total free energy is higher compared to that of the final reaction products, and it reacts faster than the case (2). This is consistent with the overstepping of reaction which is larger in the case (1). As the rheological behavior is controlled by the reaction products, it is inferred that the case (1) deforms at lower stresses than the case (2). Overall, each sample reacts differently in terms of strain localization and resistance, depending on the degree of

metastability and reaction progress is a first-order control on strength.

- These observations reveal that the rheological behavior of two-phase assemblages (plagioclase-pyroxene) is extremely sensitive to their mineralogical composition and that small chemical variations can initiate strain localization and induce large differences in resistance. Thus, the documented variations in resistance at low shear strain are dependent on the ability of the two-phase mixtures to react (due to the degree of metastability) and on the variable proportion of weak and secondary phases generated by this reaction.

3. Effect of the mutual interplay between deformation and mineral reactions on the rheology of shear zones

Whereas the peak stress of plagioclase + pyroxene assemblages is documented between the ones of the end-member phases, the strength of polymineralic materials strongly differs according to the deformed assemblages. Once strain is initiated, a succession of synkinematic processes occurs and induce a large variety of behavior based notably on rock type and the way strain partitions. Mg-rich assemblages strongly weaken after peak stress and reaches flow stresses that stabilize far below those of the weaker phase (plagioclase). Such a weakening is coeval with the development of highly connected shear bands of polyphase, fine-grained material. The dominant deformation mechanism in fine-grained material is inferred to be grain size sensitive with DPC and/or GBS, facilitated by grain size reduction, which is driven by nucleation of reaction products. Experiments on pure Amph assemblages show a similar concomitance between the presence of fine-grained mixed phase zones and a pronounced weakening after initial peak stress. In contrast, the Fe-rich samples only produce partially connected, coarse-grained aggregates of monophase material, which may account for the absence of significant weakening. Similar microstructures have been documented in the mixed Amph + Plag assemblage that hardly weaken. The lack of major weakening in Fe-rich and Amph + Plag samples can be caused by two aspects: (1) the absence of highly connected aggregates of reaction products, and (2) the considerably larger grain size of the less intensely mixed reaction products. Although the dominant deformation mechanism is also DPC with the operation of GBS in the Fe-rich assemblages, the microstructures in the weak parts of the different types of samples are different, pointing to a difference in GBS/DPC mechanisms. Indeed, in the Fe-rich assemblages, the reaction

products display a larger aspect ratios, i.e., more like fibre-like grains, in the Amph-rich tails and shear bands. These microstructures constitute a type of DPC that is tending more towards more grain-scale DPC, where ideally (in the end-member case) the grain shapes would reflect the finite strain. The Fe-rich samples are far from the end-member case, but they approach this situation clearly more than the fine grained well mixed bands of equant grains in Mg-rich samples, where DPC is kinematically probably dominated by GBS.

As previously mentioned, the reaction product in the Fe-rich assemblages nucleate faster than in the Mg-rich assemblages in the early stages of deformation. However, at high-shear strain, the proportion of reacted material is higher in Mg-rich assemblages. We consider that this difference is related to the viscosity of the reactions products and how strain is partitioned. In the Mg-rich assemblages, the viscosity of the reaction products is very low (fine-grained mixed zones) compared to the starting material. The reaction products tend to connect much better during the deformation. The interconnection of these weak reaction products caused subsequent strain to be significantly partitioned, and we documented that deformation has an enhancing effect on the reaction kinetics, leading to a more advanced reaction progress in the Mg-rich assemblages. In contrast, in the Fe-Opx + Plag assemblages, the reaction products are more viscous (Amph) and poorly connected. The feedback effect of deformation on enhancing reaction rates appears weaker in this case, in spite of a larger overstepping of reaction with respect to Mg-rich assemblages.

- Without synkinematic weakening processes, the strength of materials is governed by that of the minerals that compose them. Our study shows that deformed two-phase assemblages attain a peak stress that is intermediate between the two end-members strength of Opx and Plag. The strength is consistent with a Reuss-Voigt- or Taylor-Sachs models (e.g. Dimanov and Dresen, 2005). However, the complex interaction between two phases and/or between deformation and mineral reactions induces the succession and accumulation of synkinematic processes whose effect on the weakening of materials can be significant. We pointed out that deformation significantly enhances the kinetics of mineral reactions, which in turn strongly weaken the deforming samples (Mg-rich and pure Amph assemblages) through strain localization and phase nucleation, both probably driven by grain-size-sensitive dissolution-precipitation creep.

4. Geological application and conclusion

In our experimental case study, the starting material composed of pyroxene and plagioclase was deliberately chosen to be out of equilibrium at the experimental pressure and temperature conditions. The materials are brought to out-of-equilibrium conditions without sufficient time to equilibrate, which induces a significant overstepping of reaction boundaries (Marti et al., 2017). In nature, the variations of pressure and temperature occur at lower rates, potentially leading to more progressive changes in mineral assemblages (e.g. Herwegh et al., 2011). However, cases of preserved metastable mineral assemblages in undeformed rocks are well documented, while deformed equivalents of the same rock body have reacted (e.g. Austrheim and Griffin, 1985, Koons et al., 1987, Früh-Green, 1994). Thus, mineral reaction and its interplay with deformation is of great importance in nature (e.g. Kerrich et al., 1980; Brodie and Rutter, 1985; Handy and Stünitz, 2002; Keller et al., 2004). This is also what we observe in our natural case study, in the SASZ, with mineral reactions that cause strain localization by producing a mechanically weak aggregate (**Chapter III**). Thus, our deformation experiments are a good analogue to natural shear zones involving strain-enhanced chemical reactions and reaction-enhanced strain weakening.

Without mineral reactions, the starting pyroxene and plagioclase in our experiments are too strong to be deformed by dislocation creep at the applied strain rates. This is consistent with experimental studies on the rheology of feldspar (e.g. Rybacki and Dresen, 2000; Dimanov et al., 2003), pyroxene (e.g. Bystricky and Mackwell, 2001), and polyphase assemblages of feldspar and pyroxene (Dimanov and Dresen, 2005), that demonstrate that these phases are mechanically strong. It is also consistent with natural studies showing that below ~700 °C pyroxene and plagioclase do not show significant crystal plastic deformation (e.g. Rutter and Brodie, 1985, 1992). In contrast, as soon as the starting material reacts, the sample is viscously deformed and the strength weaken. Similarly, the deformation of mafic rocks also appears to be dependent upon mineral reactions (e.g. Stünitz, 1993; Kenkman and Dresen, 2002). It was found during our experimental study that the mechanical strength at low shear strain is controlled by the ability of the material to react. Moreover, the strength seems to be independent, at least initially, of the intrinsic strength of the reaction products. Indeed, although the Fe-rich assemblages favor the nucleation of an intrinsically stronger reaction product (Amph), compared to fine-grained mixed aggregates in the Mg-rich assemblages, they are weaker

at low shear strain because they react faster. These observations are valuable because they show the importance of mineral reactions during the early stages of shear zone development. With increasing strain, the study also reveals that strongly connected, fine-grained mixed zones in the Mg-rich assemblages (e.g. ultramylonite) are weaker than poorly connected, coarse-grained monophase domains in th Fe-rich assemblages (e.g. mylonite). This accounts therefore for the long-term, quasi-permanent weakness of highly deformed shear zone (i.e., ultramylonite) where fine-grained, phase mixing occurs upon mineral reactions, provided that the reaction kinetics remains limited enough. If the weakening is transient and limited to the reaction stage, the material will harden as soon as the reaction is complete (Fe-rich assemblages).

- When applied to natural shear zones, our results suggest that (1) The ability of minerals to react controls the portions of rocks that deform, and that (2) Small chemical and mineralogical variations can considerably modify the strength of deformed assemblages.

- The significant strain localization and partitioning at high shear strain, expressed by the development of interconnected high-strain zones, illustrates that fine-grained polyphase mixed zones are weaker than only locally connected and coarse-grained monophase domains. This is of great importance in the understanding of the rheological behavior of the lower crust, because a large amount of fine-grained weak zones allows to preserve the weakness of a shear zone in the lower crust over long periods of time. In other words, the weakening is not restricted to the reaction stage and is permanently acquired. These results emphasize the importance of strain partitioning, grain size reduction and interconnectivity of weak minerals as a primary control of lithospheric strength.

General conclusion

Even nowadays, the absence of directly measurable data beyond a few kilometers makes estimation of the rheology of the lithosphere very complex and there is in particular a strong debate concerning the true rigidity of the middle and lower crust. Understanding the rheology of the lithosphere has required and will continue to require extensive investigations in various disciplines of Earth Sciences. Structural geologists have documented that the deformation of the lithosphere is highly heterogeneous, with strain localization at all depths and scales—strain is particularly localized in shear zones in the middle and lower crust. This preferential accumulation of strain in shear zones serves as evidence that these structures can substantially affect the overall strength of the lithosphere. The purpose of this study was to improve the current knowledge about the rheological behavior of shear zones. In this study, we have documented a close concomitance between deformation and mineral reactions, and that small initial differences in composition can lead to very large differences in mechanical strength. Phase compositions, in as much they control the reactivity, play a first-order role on both the initiation of weakening but also on the long-term evolution and strength of shear zones. These observations are instructive insofar as they indicate that strain localization can be initiated by small chemical and mineralogical variations within, for example, an environment without brittle precursors. This is also crucial as it is known that shear zones represent preferential regions for mineral reactions to occur, either owing to deformation or to the presence of fluids during protracted shearing. From our observations, it is apparent that the rheology of polyphase rocks such as mafic rocks, which constitute a large part of the oceanic crust and may be one of the main components of the lower continental crust, can hardly be simplified as being rheologically controlled by monophase materials. In order to further use the rheological models as a predictive tool for lithospheric rheology, it seems necessary to use appropriate laws that consider the complexity of regional structures and their evolution. This includes in particular (1) the polyphase nature of the lithospheric envelopes, (2) the complex interaction between mineral phases, and (3) the heterogeneous deformation of the lithosphere, which contains areas of intense strain localization (shear zones). However, given the microstructural complexity of shear zones, the selection of rheological laws for modeling the ductile behavior of the middle and lower crust is not self-evident. The present study, however, suggests that rheological laws should take into consideration strain-weakening rheology to incorporate strain localization.

BIBLIOGRAPHY

Ashby, M.. , Verrall, R.. , 1973. Diffusion-accommodated flow and superplasticity. Acta Metallurgica 21, 149–163. https://doi.org/10.1016/0001-6160(73)90057-6

Augier, R., Choulet, F., Faure, M., Turrillot, P., 2015. A turning-point in the evolution of the Variscan orogen: the ca. 325 Ma regional partial-melting event of the coastal South Armorican domain (South Brittany and Vendée, France). Bulletin de La Société Géologique de France 186, 63–91. https://doi.org/10.2113/gssgfbull.186.2-3.63

Augier, R., Menier, D., Vliet-Lanoë, B. Van, Hallégouet, B., Chauris, L., Turrillot, P., Carn, A., Thinon, I., 2011. Notice de la carte géologique de France au 1/50000 : feuille de Vannes St GILDAS-DE-RHUIS Feuille 417.

Austrheim, H., 1987. Eclogitization of lower crustal granulites by fluid migration through shear zones. Earth and Planetary Science Letters 81, 221–232. https://doi.org/10.1016/0012-821X(87)90158-0

Austrheim, H., Griffin, W.L., 1985. Shear deformation and eclogite formation within granulite-facies anorthosites of the Bergen Arcs, western Norway. Chemical Geology 50, 267–281. https://doi.org/10.1016/0009-2541(85)90,124-X

Auzanneau, E., Schmidt, M.W., Vielzeuf, D., D Connolly, J.A., 2010. Titanium in phengite: a geobarometer for high temperature eclogites. Contributions to Mineralogy and Petrology 159, 1–24. https://doi.org/10.1007/s00410-009-0412-7

Ballèvre, M., Bosse, V., Ducassou, C., Pitra, P., 2009. Palaeozoic history of the Armorican Massif: Models for the tectonic evolution of the suture zones. Comptes Rendus - Geoscience 341, 174–201. https://doi.org/10.1016/j.crte.2008.11.009

Ballèvre, M., Marchand, J., Godard, G., Goujou, J.-C., Christian, J., Wyns, R., 1994. Eo-Hercynian Events in the Armorican Massif. Pre-Mesozoic Geology in France and Related Areas. Springer Berlin Heidelberg, Berlin, Heidelberg, 183–194. https://doi.org/10.1007/978-3-642-84915-2_19

Baratoux, L., Schulmann, K., Ulrich, S., Lexa, O., 2005. Contrasting microstructures and deformation mechanisms in metagabbro mylonites contemporaneously deformed under different temperatures (c. 650 C and c. 750 C). Geological Society, London, Special Publications 243, 97–125. https://doi.org/10.1144/GSL.SP.2005.243.01.09

Barreiro, J.G., Lonardelli, I., Wenk, H.R., Dresen, G., Rybacki, E., Ren, Y., Tomé, C.N., 2007. Preferred orientation of anorthite deformed experimentally in Newtonian creep. Earth and Planetary Science Letters 264, 188–207. https://doi.org/10.1016/J.EPSL.2007.09.018

Baxter, E.F., Depaolo, Æ.D.J., 2004. Can metamorphic reactions proceed faster than bulk strain ? 657–670. https://doi.org/10.1007/s00410-003-0525-3

Behrmann, J.H., 1985. Crystal plasticity and superplasticity in quartzite; A natural example. Tectonophysics 115, 101–129. https://doi.org/10.1016/0040-1951(85)90102-7

Behrmann, J.H., Mainprice, D., 1987. Deformation mechanisms in a high-temperature quartz-feldspar mylonite: evidence for superplastic flow in the lower continental crust. Tectonophysics 140, 297–305. https://doi.org/10.1016/0040-1951(87)90236-8

Benson, D.J., Fu, H.H., Meyers, M.A., 2001. On the effect of grain size on yield stress: Extension into nanocrystalline domain. Materials Science and Engineering A 319–321, 854–861. https://doi.org/10.1016/S0921-5093(00)02029-3

Bercovici, D., Ricard, Y., 2012. Mechanisms for the generation of plate tectonics by two-phase grain-damage and pinning. Physics of the Earth and Planetary Interiors 202–203, 27–55. https://doi.org/10.1016/J.PEPI.2012.05.003

Berger, A., Stünitz, H., 1996. Deformation mechanisms and reaction of hornblende: examples from the Bergell tonalite (Central Alps). Tectonophysics 257, 149–174. https://doi.org/10.1016/0040-1951(95)00125-5

Berthé, D., Choukroune, P., Jegouzo, P., 1979. Orthogneiss, mylonite and non coaxial deformation of granites: the example of the South Armorican Shear Zone. Journal of Structural Geology 1, 31–42. https://doi.org/10.1016/0191-8141(79)90019-1

Bestmann, M., Prior, D.J., 2003. Intragranular dynamic recrystallization in naturally deformed calcite marble: Diffusion accommodated grain boundary sliding as a result of subgrain rotation recrystallization. Journal of Structural Geology 25, 1597–1613. https://doi.org/10.1016/S0191-8141(03)00006-3

Bons, P.D., Den Brok, B., 2000. Crystallographic preferred orientation development by dissolution-precipitation creep. Journal of Structural Geology. 1713–1722. https://doi.org/10.1016/S0191-8141(00)00075-4

Bosse, V., Feraud, G., Ruffet, G., Ballèvre, M., Peucat, J.-J., De Jong, K., 2000. Late Devonian subduction and early-orogenic exhumation of eclogite-facies rocks from the Champtoceaux Complex (Variscan belt, France). Geological Journal 35, 297–325. https://doi.org/10.1002/gj.864

Bouchez, J.L., Delas, C., Gleizes, G., Nédélec, A., Cuney, M., 1992. Submagmatic microfractures in granites. Geology 20, 35. https://doi.org/10.1130/0091-7613(1992)020<0035:SMIG>2.3.CO; 2

Boullier, A.M., Gueguen, Y., 1975. SP-Mylonites : Origin of some mylonites by superplastic flow. Contributions to Mineralogy and Petrology 50, 93–104. https://doi.org/10.1007/BF00373329

Boundy, T.M., Fountain, D.M., Austrheim, H., 1992. Structural development and petrofabrics of eclogite facies shear zones, Bergen Arcs, western Norway: implications for deep crustal deformational processes. Journal of Metamorphic Geology 10, 127–146. https://doi.org/10.1111/j.1525-1314.1992.tb00075.x

Bozkurt, E., 2001. Neotectonics of turkey—a synthesis. Geodinamica Acta 14, 3–30. https://doi.org/10.1080/09853111.2001.11432432

Brace, W.F., Kohlstedt, D.L., 1980. Limits on lithospheric stress imposed by laboratory experiments. Journal of Geophysical Research: Solid Earth 85, 6248–6252. https://doi.org/10.1029/JB085IB11P06248@10.1002/(ISSN)2169–9356.STRESLITH1

Brander, L., Svahnberg, H., Piazolo, S., 2012. Brittle-plastic deformation in initially dry rocks at fluid-present conditions: Transient behaviour of feldspar at mid-crustal levels. Contributions to Mineralogy and Petrology 163, 403–425. https://doi.org/10.1007/s00410-011-0677-5

Brodhag, S.H., Herwegh, M., 2010. The effect of different second-phase particle regimes on grain growth in two-phase aggregates: Insights from in situ rock analogue experiments. Contributions to Mineralogy and Petrology 160, 219–238. https://doi.org/10.1007/s00410-009-0474-6

Brodie, K.H., 1980. Variations in mineral chemistry across a shear zone in phlogopite peridotite. Journal of Structural Geology 2, 265–272. https://doi.org/10.1016/0191-8141(80)90059-0

Brodie, K.H., Rutter, E.H., 1987. The role of transiently fine-grained reaction products in syntectonic metamorphism: natural and experimental examples. Canadian Journal of Earth Sciences 24, 556–564. https://doi.org/10.1139/e87-054

Brodie, K.H., Rutter, E.H., 1985. On the Relationship between Deformation and Metamorphism, with Special Reference to the Behavior of Basic Rocks. Springer, New York, NY, 138–179. https://doi.org/10.1007/978-1-4612-5066-1_6

Brown, M., Dallmeyer, R.D., 1996. Rapid Variscan exhumation and the role of magma in core complex formation: southern Brittany metamorphic belt, France. Journal of Metamorphic Geology 14, 361–379. https://doi.org/10.1111/j.1525-1314.1996.00361.x

Bruijn, R.H.C., Skemer, P., 2014. Grain-size sensitive rheology of orthopyroxene. Geophysical Research Letters 41, 4894–4903. https://doi.org/10.1002/2014GL060607

Bukovská, Z., Jeřábek, P., Morales, L.F.G., 2016. Major softening at brittle-ductile transition due to interplay between chemical and deformation processes: An insight from evolution of shear bands in the South Armorican Shear Zone. Journal of Geophysical Research: Solid Earth 121, 1158–1182. https://doi.org/10.1002/2015JB012319

Bunge, H.-J., 1982. Texture analysis in materials science : mathematical methods. Butterworths, London.

Bürgmann, R., Dresen, G., 2008. Rheology of the Lower Crust and Upper Mantle: Evidence from Rock Mechanics, Geodesy, and Field Observations. Annual Review of Earth and Planetary Sciences 36, 531–567. https://doi.org/10.1146/annurev.earth.36.031207.124326

Burlini, L., Bruhn, D., 2005. High-strain zones: laboratory perspectives on strain softening during ductile deformation. Geological Society, London, Special Publications 245, 1–24. https://doi.org/10.1144/GSL.SP.2005.245.01.01

Burov, E.B., Watts, A.B., 2006. The long-term strength of continental lithosphere: "jelly sandwich" or "crême brûlée"? GSA Today 16 (1), 4–10. https://doi.org/10.1130/1052-5173(2006)016<4:TLTSOC>2.0.CO;2

Byerlee, J., 1978. Friction of rocks. Rock Friction and Earthquake Prediction. Birkhäuser Basel, Basel, 615–626. https://doi.org/10.1007/978-3-0348-7182-2_4

Bystricky, M., Lawlis, J., Mackwell, S., Heidelbach, F., Raterron, P., 2016. High-temperature deformation of enstatite aggregates. Journal of Geophysical Research: Solid Earth 121, 6384–6400. https://doi.org/10.1002/2016JB013011

Bystricky, M., Mackwell, S., 2001. Creep of dry clinopyroxene aggregates. Journal of Geophysical Research: Solid Earth 106, 13443–13454. https://doi.org/10.1029/2001JB000333

Cartier, C., Faure, M., 2004. The Saint-Georges-sur-Loire olistostrome, a key zone to understand the Gondwana-Armorica boundary in the Variscan belt (Southern Brittany, France). International Journal of Earth Sciences 93, 945–958. https://doi.org/10.1007/s00531-004-0398-3

Chen, S., Hiraga, T., Kohlstedt, D.L., 2006. Water weakening of clinopyroxene in the dislocation creep regime. Journal of Geophysical Research 111, B08203. https://doi.org/10.1029/2005JB003885

Chopra, P.N., Paterson, M.S., 1981. The experimental deformation of dunite. Tectonophysics 78, 453–473. https://doi.org/10.1016/0040-1951(81)90,024-X

Christensen, N.I., Mooney, W.D., 1995. Seismic velocity structure and composition of the continental crust: A global view. Journal of Geophysical Research: Solid Earth 100, 9761–9788. https://doi.org/10.1029/95JB00259

Coble, R.L., 1963. A model for boundary diffusion controlled creep in polycrystalline materials. Journal of Applied Physics 34, 1679–1682. https://doi.org/10.1063/1.1702656

Coe, R.S., Kirby, S.H., 1975. The orthoenstatite to clinoenstatite transformation by shearing and

reversion by annealing: Mechanism and potential applications. Contributions to Mineralogy and Petrology 52, 29–55. https://doi.org/10.1007/BF00378000

Coggon, R., Holland, T.J.B., 2002. Mixing properties of phengitic micas and revised garnet-phengite thermobarometers. Journal of Metamorphic Geology 20, 683–696. https://doi.org/10.1046/j.1525-1314.2002.00395.x

Cogne, J., 1960. Metamorphismes et granitisations en liaison avec l'evolution orogenique en Bretagne meridionale. Bulletin de La Société Géologique de France S7-II. https://doi.org/10.2113/gssgfbull.S7-II.2.213

Connolly, J.A.D., 2005. Computation of phase equilibria by linear programming: A tool for geodynamic modeling and its application to subduction zone decarbonation. Earth and Planetary Science Letters 236, 524–541. https://doi.org/10.1016/J.EPSL.2005.04.033

Cross, A.J., Skemer, P., 2017. Ultramylonite generation via phase mixing in high-strain experiments. Journal of Geophysical Research: Solid Earth 122, 1744–1759. https://doi.org/10.1002/2016JB013801

De Bresser, J.H.P., Peach, C.J., Reijs, J.P.J., Spiers, C.J., 1998. On dynamic recrystallization during solid state flow: Effects of stress and temperature. Geophysical Research Letters 25, 3457–3460. https://doi.org/10.1029/98GL02690

De Bresser, J.H.P., Ter Heege, J.H., Spiers, C.J., 2001. Grain size reduction by dynamic recrystallization: Can it result in major rheological weakening? International Journal of Earth Sciences 90, 28–45. https://doi.org/10.1007/s005310000149

De Ronde, A.A., Heilbronner, R., Stünitz, H., Tullis, J., 2004. Spatial correlation of deformation and mineral reaction in experimentally deformed plagioclase—olivine aggregates. Tectonophysics 389, 93–109. https://doi.org/10.1016/J.TECTO.2004.07.054

De Ronde, A.A., Stünitz, H., 2007. Deformation-enhanced reaction in experimentally deformed plagioclase-olivine aggregates. Contributions to Mineralogy and Petrology 153, 699–717. https://doi.org/10.1007/s00410-006-0171-7

De Ronde, A.A., Stünitz, H., Tullis, J., Heilbronner, R., 2005. Reaction-induced weakening of plagioclase-olivine composites. Tectonophysics 409, 85–106. https://doi.org/10.1016/j.tecto.2005.08.008

Dell'Angelo, L.N., Tullis, J., 1996. Textural and mechanical evolution with progressive strain in experimentally deformed aplite. Tectonophysics 256, 57–82. https://doi.org/10.1016/0040-1951(95)00166-2

Dijkstra, A., Drury, M., Vissers, R., Newman, J., 2002. On the role of melt-rock reaction in mantle shear zone formation in the Othris Peridotite Massif (Greece). Journal of Structural Geology 24, 1431–1450. https://doi.org/10.1016/S0191-8141(01)00142-0

Dimanov, A., Dresen, G., 2005. Rheology of synthetic anorthite-diopside aggregates: Implications for ductile shear zones., Journal of Geophysical Research: Solid Earth. https://doi.org/10.1029/2004JB003431

Dimanov, A., Dresen, G., Xiao, X., Wirth, R., 1999. Grain boundary diffusion creep of synthetic anorthite aggregates: The effect of water. Journal of Geophysical Research: Solid Earth 104, 10483–10497. https://doi.org/10.1029/1998JB900113

Dimanov, A., Lavie, M.P., Dresen, G., Ingrin, J., Jaoul, O., 2003. Creep of polycrystalline anorthite and diopside. Journal of Geophysical Research: Solid Earth 108. https://doi.org/10.1029/2002JB001815

Dimanov, A., Rybacki, E., Wirth, R., Dresen, G., 2007. Creep and strain-dependent microstructures of synthetic anorthite—diopside aggregates. Journal of Structural

Geology 29, 1049–1069. https://doi.org/10.1016/J.JSG.2007.02.010

Drury, M.R., Urai, J.L., 1990. Deformation-related recrystallization processes. Tectonophysics 172, 235–253. https://doi.org/10.1016/0040-1951(90)90033-5

Elyaszadeh, R., Prior, D.J., Sarkarinejad, K., Mansouri, H., 2018. Different slip systems controlling crystallographic preferred orientation and intracrystalline deformation of amphibole in mylonites from the Neyriz mantle diapir, Iran. Journal of Structural Geology 107, 38–52. https://doi.org/10.1016/j.jsg.2017.11.020

England, P. 1986. Comment on "Brittle Failure in the Upper Mantle During Extension of Continental Lithosphere" by Dale S. Sawyer. Journal of Geophysical Research: Solid Earth 91, 10,487–10,490. https://doi.org/10.1029/JB091iB10p10487

Etheridge, M.A., Wilkie, J.C., 1979. Grainsize reduction, grain boundary sliding and the flow strength of mylonites. Tectonophysics 58, 159–178. https://doi.org/10.1016/0040-1951(79)90327-5

Evans, B., Renner, J., Hirth, G., 2001. A few remarks on the kinetics of static grain growth in rocks. International Journal of Earth Sciences 90, 88–103. https://doi.org/10.1007/s005310000150

Farkašovský, R., Bónová, K., Košuth, M., 2016. Microstructural, modal and geochemical changes as a result of granodiorite mylonitisation—a case study from the Rolovská shear zone (Čierna hora Mts, Western Carpathians, Slovakia). Geologos 22, 171–190. https://doi.org/10.1515/logos-2016-0019

Farla, R.J.M., Karato, S.-I., Cai, Z., 2013. Role of orthopyroxene in rheological weakening of the lithosphere via dynamic recrystallization. Proceedings of the National Academy of Sciences of the United States of America 110, 16,355–60. https://doi.org/10.1073/pnas.1218335110

Faure, M., Bé Mézème, E., Cocherie, A., Rossi, P., Chemenda, A., Boutelier, D., 2008. Devonian geodynamic evolution of the Variscan Belt, insights from the French Massif Central and Massif Armoricain. Tectonics 27, n/a-n/a. https://doi.org/10.1029/2007TC002115

Faure, M., Bé Mézème, E., Duguet, M., Cartier, C., Talbot, J.Y., 2005. Paleozoic tectonic evolution of medio-Europa from the example of the French Massif Central and Massif Armoricain. Journal of the Virtual Explorer 19. https://doi.org/10.3809/jvirtex.2005.00120

Fitz Gerald, J., Stünitz, H., 1993. Deformation of granitoids at low m~tamo~~ic grade. I: Reactions and grain size reduction. Elsevier Science Publishers B.V 221, 269–297. https://doi.org/10.1016/0040-1951(93)90,164-F

Fliervoet, T.F., White, S.H., 1995. Quartz deformation in a very fine grained quartzo-feldspathic mylonite: a lack of evidence for dominant grain boundary sliding deformation. Journal of Structural Geology 17, 1095–1109. https://doi.org/10.1016/0191-8141(95)00007-Z

Fliervoet, T.F., White, S.H., Drury, M.R., 1997. Evidence for dominant grain-boundary sliding deformation in greenschist- and amphibolite-grade polymineralic ultramylonites from the Redbank Deformed Zone, Central Australia. Journal of Structural Geology 19, 1495–1520. https://doi.org/10.1016/S0191-8141(97)00076-X

Fossen, H., Cavalcante, G.C.G., 2017. Shear zones—A review. Earth-Science Reviews 171, 434–455. https://doi.org/10.1016/J.EARSCIREV.2017.05.002

Früh-Green, G.L., 1994. Interdependence of deformation, fluid infiltration and reaction progress recorded in eclogitic metagranitoids (Sesia Zone, Western Alps). Journal of Metamorphic Geology 12, 327–343. https://doi.org/10.1111/j.1525-1314.1994.tb00026.x

Fusseis, F., Handy, M.R., 2008. Micromechanisms of shear zone propagation at the brittle—viscous transition. Journal of Structural Geology 30, 1242–1253.

https://doi.org/10.1016/J.JSG.2008.06.005

Fusseis, F., Handy, M.R., Schrank, C., 2006. Networking of shear zones at the brittle-to-viscous transition (Cap de Creus, NE Spain). Journal of Structural Geology 28, 1228–1243. https://doi.org/10.1016/j.jsg.2006.03.022

Fusseis, F., Regenauer-Lieb, K., Liu, J., Hough, R.M., De Carlo, F., 2009. Creep cavitation can establish a dynamic granular fluid pump in ductile shear zones. Nature 459, 974–977. https://doi.org/10.1038/nature08051

Gapais, D., 1989. Shear structures within deformed granites: mechanical and thermal indicators. Geology 17,1144–1147. https://doi.org/10.1130/0091-7613(1989)017<1144:SSWDGM>2.3. CO

Gapais, D., White, S.H., 1982. Ductile Shear Bands in a Naturally Deformed Quartzite. Textures and Microstructures 5, 1–17. https://doi.org/10.1155/TSM.5.1

Gardner, R., Piazolo, S., Evans, L., Daczko, N., 2017. Patterns of strain localization in heterogeneous, polycrystalline rocks—a numerical perspective. Earth and Planetary Science Letters 463, 253–265. https://doi.org/10.1016/j.epsl.2017.01.039

Gerbi, C., 2012. Evaluating the utility of a phase distribution parameter in calculating the bulk viscous strength of two-phase composites. Journal of Structural Geology 39, 224–236. https://doi.org/10.1016/J.JSG.2012.02.008

Gerbi, C., Johnson, S.E., Shulman, D., Klepeis, K., 2016. Influence of microscale weak zones on bulk strength. Geochemistry, Geophysics, Geosystems 17, 4064–4077. https://doi.org/10.1002/2016GC006551

Gerya, T. V., Stöckhert, B., Perchuk, A.L., 2002. Exhumation of high-pressure metamorphic rocks in a subduction channel: A numerical simulation. Tectonics 21, 6-1-6—19. https://doi.org/10.1029/2002tc001406

Getsinger, A J, Hirth, G., 2014. Amphibole fabric formation during diffusion creep and the rheology of shear zones. 535–538. https://doi.org/10.1130/G35327.1

Getsinger, A.J., Hirth, G., Stünitz, H., Goergen, E.T., 2013. Influence of water on rheology and strain localization in the lower continental crust. Geochemistry, Geophysics, Geosystems 14, 2247–2264. https://doi.org/10.1002/ggge.20148

Gilgannon, J., Fusseis, F., Menegon, L., Regenauer-Lieb, K., Buckman, J., 2017. Hierarchical creep cavity formation in an ultramylonite and implications for phase mixing. Solid Earth 85,194, 1193–1209. https://doi.org/10.5194/se-8-1193-2017

Glodny, J., Austrheim, H., Molina, J.F., Rusin, A.I., Seward, D., 2003. Rb/Sr record of fluid-rock interaction in eclogites: The Marun-Keu complex, Polar Urals, Russia. Geochimica et Cosmochimica Acta 67, 4353–4371. https://doi.org/10.1016/S0016-7037(03)00370-3

Goetze, C., Evans, B., 1979. Stress and temperature in the bending lithosphere as constrained by experimental rock mechanics. Geophysical Journal of the Royal Astronomical Society 59, 463–478. https://doi.org/10.1111/j.1365-246X.1979.tb02567.x

Grant, J.A., 1986. The isocon diagram; a simple solution to Gresens' equation for metasomatic alteration. Economic Geology 81, 1976–1982. https://doi.org/10.2113/gsecongeo.81.8.1976

Gueydan, F., Leroy, Y.M., Jolivet, L., Agard, P., 2003. Analysis of continental midcrustal strain localization induced by microfracturing and reaction-softening. Journal of Geophysical Research: Solid Earth 108. https://doi.org/10.1029/2001jb000611

Gueydan, F., Morency, C., Brun, J.P., 2008. Continental rifting as a function of lithosphere mantle strength. Tectonophysics 460, 83–93. https://doi.org/10.1016/j.tecto.2008.08.012

Gueydan, F., Précigout, J., Montési, L.G.J., 2014. Strain weakening enables continental plate tectonics. Tectonophysics 631, 189–196. https://doi.org/10.1016/J.TECTO.2014.02.005

Gumiaux, C., Gapais, D., Brun, J.P., Chantraine, J., Ruffet, G., 2004. Tectonic history of the Hercynian Armorican shear belt (Brittany, France). Geodinamica Acta 17, 289–307. https://doi.org/10.3166/ga.17.289-307

Hacker, B.R., Kelemen, P.B., Behn, M.D., 2015. Continental Lower Crust. Annual Review of Earth and Planetary Sciences 43, 167–205. https://doi.org/10.1146/annurev-earth-050212-124117

Handy, M.R., 1994. Flow laws for rocks containing two non-linear viscous phases: A phenomenological approach. Journal of Structural Geology 16, 287–301. https://doi.org/10.1016/0191-8141(94)90035-3

Handy, M.R., 1990. The solid-state flow of polymineralic rocks. Journal of Geophysical Research 95, 8647. https://doi.org/10.1029/JB095iB06p08647

Handy, M.R., 1989. Deformation regimes and the rheological evolution of fault zones in the lithosphere: the effects of pressure, temperature, grainsize and time. Tectonophysics 163, 119–152. https://doi.org/10.1016/0040-1951(89)90122-4

Handy, M.R., Brun, J.P., 2004. Seismicity, structure and strength of the continental lithosphere. Earth and Planetary Science Letters 223 (3-4), 427–441. https://doi.org/10.1016/j.epsl.2004.04.021

Handy, M.R., Stünitz, H., 2002. Strain localization by fracturing and reaction weakening—a mechanism for initiating exhumation of subcontinental mantle beneath rifted margins. Geological Society, London, Special Publications 200, 387–407. https://doi.org/10.1144/GSL.SP.2001.200.01.22

Handy, M.R., Wissing, S.B., Streit, L.E., 1999. Frictional-viscous flow in mylonite with varied bimineralic composition and its effect on lithospheric strength. Tectonophysics 303, 175–191. https://doi.org/10.1016/S0040-1951(98)00251-0

Harigane, Y., Michibayashi, K., Ohara, Y., 2008. Shearing within lower crust during progressive retrogression: Structural analysis of gabbroic rocks from the Godzilla Mullion, an oceanic core complex in the Parece Vela backarc basin. Tectonophysics 457, 183–196. https://doi.org/10.1016/j.tecto.2008.06.009

Heilbronner, R., Barrett, S., 2014. Spatial Distributions. Image Analysis in Earth Sciences. Springer Berlin Heidelberg, Berlin, Heidelberg, 351–368. https://doi.org/10.1007/978-3-642-10343-8_1

Heilbronner, R., Tullis, J., 2002. The effect of static annealing on microstructures and crystallographic preferred orientations of quartzites experimentally deformed in axial compression and shear. Geological Society, London, Special Publications 200, 191–218. https://doi.org/10.1144/GSL.SP.2001.200.01.12

Heilbronner, R.P., 1992. The autocorrelation function: an image processing tool for fabric analysis. Tectonophysics 212, 351–370. https://doi.org/10.1016/0040-1951(92)90,300-U

Herring, C., 1950. Diffusional viscosity of a polycrystalline solid. Journal of Applied Physics 21, 437–445. https://doi.org/10.1063/1.1699681

Herwegh, M., Berger, A., 2004. Deformation mechanisms in second-phase affected microstructures and their energy balance. Journal of Structural Geology 26, 1483–1498. https://doi.org/10.1016/J.JSG.2003.10.006

Herwegh, M., Jenni, A., 2001. Granular flow in polymineralic rocks bearing sheet silicates: New evidence from natural examples. Tectonophysics 332, 309–320.

https://doi.org/10.1016/S0040-1951(00)00288-2

Herwegh, M., Linckens, J., Ebert, A., Berger, A., Brodhag, S.H., 2011. The role of second phases for controlling microstructural evolution in polymineralic rocks: A review., Journal of Structural Geology. https://doi.org/10.1016/j.jsg.2011.08.011

Hidas, K., Tommasi, A., Garrido, C.J., Padrón-Navarta, J.A., Mainprice, D., Vauchez, A., Barou, F., Marchesi, C., 2016. Fluid-assisted strain localization in the shallow subcontinental lithospheric mantle. Lithos 262, 636–650. https://doi.org/10.1016/j.lithos.2016.07.038

Hippertt, J., 1998. Breakdown of feldspar, volume gain and lateral mass transfer during mylonitization of granitoid in a low metamorphic grade shear zone. Journal of Structural Geology 20, 175–193. https://doi.org/10.1016/S0191-8141(97)00083-7

Hippler, S.J., Knipe, R.J., 1990. The evolution of cataclastic fault rocks from a pre-existing mylonite. Geological Society, London, Special Publications 54, 71–79. https://doi.org/10.1144/GSL.SP.1990.054.01.08

Hirth, G., Tullis, J., 1992. Dislocation creep regimes in quartz aggregates. Journal of Structural Geology 14, 145–159. https://doi.org/10.1016/0191-8141(92)90,053-Y

Holland, T., Baker, J., Powell, R., 1998. Mixing properties and activity-composition relationships of chlorites in the system MgO-FeO-Al2O3-SiO2-H2O. European Journal of Mineralogy 10, 395–406. https://doi.org/10.1127/ejm/10/3/0395

Holland, T., Powell, R., 2003. Activity-composition relations for phases in petrological calculations: an asymmetric multicomponent formulation. Contributions to Mineralogy and Petrology 145, 492–501. https://doi.org/10.1007/s00410-003-0464-z

Holland, T.J.B., Powell, R., 2004. An internally consistent thermodynamic data set for phases of petrological interest. Journal of Metamorphic Geology 16, 309–343. https://doi.org/10.1111/j.1525-1314.1998.00140.x

Holyoke, C.W., Tullis, J., 2006a. Mechanisms of weak phase interconnection and the effects of phase strength contrast on fabric development. Journal of Structural Geology 28, 621–640. https://doi.org/10.1016/j.jsg.2006.01.008

Holyoke, C.W., Tullis, J., 2006b. Formation and maintenance of shear zones. Geology 34, 105–108. https://doi.org/10.1130/G22116.1

Hunter, N.J.R., Hasalová, P., Weinberg, R.F., Wilson, C.J.L., 2016. Fabric controls on strain accommodation in naturally deformed mylonites: The influence of interconnected micaceous layers. Journal of Structural Geology 83, 180–193. https://doi.org/10.1016/j.jsg.2015.12.005

Hutton, D.H.W., Dempster, T.J., Brown, P.E., Becker, S.D., 1990. A new mechanism of granite emplacement: Intrusion in active extensional shear zones. Nature 343, 452–455. https://doi.org/10.1038/343452a0

Imon, R., Okudaira, T., Fujimoto, A., 2002. Dissolution and precipitation processes in deformed amphibolites: an example from the ductile shear zone of the Ryoke metamorphic belt, SW Japan. Journal of Metamorphic Geology 20, 297–308. https://doi.org/10.1046/j.1525-1314.2002.00367.x

Imon, R., Okudaira, T., Kanagawa, K., 2004. Development of shape- and lattice-preferred orientations of amphibole grains during initial cataclastic deformation and subsequent deformation by dissolution-precipitation creep in amphibolites from the Ryoke metamorphic belt, SW Japan., Journal of Structural Geology. https://doi.org/10.1016/j.jsg.2003.09.004

Ishii, K., Kanagawa, K., Shigematsu, N., Okudaira, T., 2007. High ductility of K-feldspar and

development of granitic banded ultramylonite in the Ryoke metamorphic belt, SW Japan. Journal of Structural Geology 29, 1083–1098. https://doi.org/10.1016/j.jsg.2007.02.008

Jackson, J.A., 2002. Strength of the continental lithosphere: time to abandon the jelly sandwich? GSA Today 12, 4–10. https://doi.org/10.1130/1052-5173(2002)012<0004:SOTCIT>2.0.CO;2.

Jamtveit, B., Austrheim, H., Putnis, A., 2016. Disequilibrium metamorphism of stressed lithosphere., Earth-Science Reviews. https://doi.org/10.1016/j.earscirev.2015.12.002

Jégouzo, P., 1980. The South Armorican Shear Zone. Journal of Structural Geology 2, 39–47. https://doi.org/10.1016/0191-8141(80)90032-2

Jiang, Z., Prior, D.J., Wheeler, J., 2000. Albite crystallographic preferred orientation and grain misorientation distribution in a low-grade mylonite: implications for granular flow. Journal of Structural Geology 22, 1663–1674. https://doi.org/10.1016/S0191-8141(00)00079-1

Johnson, T., Brown, M., 2004. Quantitative constraints on metamorphism in the Variscides of southern Brittany—A complementary pseudosection approach. Journal of Petrology 45, 1237–1259. https://doi.org/10.1093/petrology/egh012

Jolivet, L., 1995. *La déformation des continents*. Hermann, Paris. 413 pp.

Jolivet, L., Miyashita, S., 1985. The Hidaka Shear Zone (Hokkaido, Japan): Genesis during a right-lateral strike-slip movement. Tectonics 4, 289–302. https://doi.org/10.1029/TC004i003p00289

Jordan, P., 1988. The rheology of polymineralic rocks—an approach. Geologische Rundschau 77, 285–294. https://doi.org/10.1007/BF01848690

Jung, H., 2017. Crystal preferred orientations of olivine, orthopyroxene, serpentine, chlorite, and amphibole, and implications for seismic anisotropy in subduction zones: a review., Geosciences Journal. https://doi.org/10.1007/s12303-017-0045-1

Kanagawa, K., Shimano, H., Hiroi, Y., 2008. Mylonitic deformation of gabbro in the lower crust: A case study from the Pankenushi gabbro in the Hidaka metamorphic belt of central Hokkaido, Japan. Journal of Structural Geology 30, 1150–1166. https://doi.org/10.1016/j.jsg.2008.05.007

Karato, S.-I., Paterson, M.S., FitzGerald, J.D., 1986. Rheology of synthetic olivine aggregates: Influence of grain size and water. Journal of Geophysical Research 91, 8151. https://doi.org/10.1029/jb091ib08p08151

Kelemen, P.B., Hirth, G., 2012. Reaction-driven cracking during retrograde metamorphism: Olivine hydration and carbonation. Earth and Planetary Science Letters 345–348, 81–89. https://doi.org/10.1016/j.epsl.2012.06.018

Keller, L.M., Abart, R., Stünitz, H., De Capitani, C., 2004. Deformation, mass transfer and mineral reactions in an eclogite facies shear zone in a polymetamorphic metapelite (Monte Rosa nappe, western Alps). Journal of Metamorphic Geology 22, 97–118. https://doi.org/10.1111/j.1525-1314.2004.00500.x

Kenkmann, T., Dresen, G., 2002. Dislocation microstructure and phase distribution in a lower crustal shear zone—An example from the Ivrea-Zone, Italy. International Journal of Earth Sciences 91, 445–458. https://doi.org/10.1007/s00531-001-0236-9

Kenkmann, T., Dresen, G., 1998. Stress gradients around porphyroclasts: Palaeopiezometric estimates and numerical modeling. Journal of Structural Geology 20, 163–173. https://doi.org/10.1016/S0191-8141(97)00074-6

Kerrich, R., Allison, I., Barnett, R.L., Moss, S., Starkey, J., 1980. Microstructural and chemical transformations accompanying deformation of granite in a shear zone at Miéville,

Switzerland; with implications for stress corrosion cracking and superplastic flow. Contributions to Mineralogy and Petrology 73, 221–242. https://doi.org/10.1007/BF00381442

Kilian, R., Heilbronner, R., Stünitz, H., 2011. Quartz grain size reduction in a granitoid rock and the transition from dislocation to diffusion creep. Journal of Structural Geology 33, 1265–1284. https://doi.org/10.1016/j.jsg.2011.05.004

Kirby, S.H., 1985. Rock mechanics observations pertinent to the rheology of the continental lithosphere and the localization of strain along shear zones. Tectonophysics 119, 1–27. https://doi.org/10.1016/0040-1951(85)90030-7

Kirby, S.H., 1980. Tectonic stresses in the lithosphere: Constraints provided by the experimental deformation of rocks. Journal of Geophysical Research: Solid Earth 85, 6353–6363. https://doi.org/10.1029/JB085IB11P06353@10.1002/(ISSN)2169–9356.STRESLITH1

Kirby, S.H., Kronenberg, A.K., 1987. Rheology of the lithosphere: Selected topics. Reviews of Geophysics 25, 1219. https://doi.org/10.1029/RG025i006p01219

Knipe, R.., 1989. Deformation mechanisms—recognition from natural tectonites. Journal of Structural Geology 11, 127–146. https://doi.org/10.1016/0191-8141(89)90039-4

Kohlstedt, D.L., Evans, B., Mackwell, S.J., 1995. Strength of the lithosphere: Constraints imposed by laboratory experiments. Journal of Geophysical Research: Solid Earth 100, 17587–17602. https://doi.org/10.1029/95JB01460

Koons, P.O., Rubie, D.C., Fruch-Green, G., 1987. The effects of disequilibrium and deformation on the mineralogical evolution of quartz diorite during metamorphism in the eclogite facies. Journal of Petrology 28, 679–700. https://doi.org/10.1093/petrology/28.4.679

Kronenberg, A.K. and Tullis, J., 1984. Flow strengths of quartz aggregates: Grain size and pressure effects dur to hydrolytic weakening. Journal of Geophysical Research: Solid Earth 89, 4281–4297. https://doi.org/10.1029/JB089iB06p04281

Kruhl, J., Erdmann, S., Büttner, S., 2007. Brittle-ductile microfabrics in naturally deformed cordierite: Evidence for significant short-term strain-rate variations. Journal of Structural Geology 29, 355–374. https://doi.org/10.1016/J.JSG.2006.09.002

Kruse, R., Stünitz, H., 1999. Deformation mechanisms and phase distribution in mafic high-temperature mylonites from the Jotun Nappe, southern Norway. Tectonophysics 303, 223–249. https://doi.org/10.1016/S0040-1951(98)00255-8

Langdon, T.G., 2006. Grain boundary sliding revisited: Developments in sliding over four decades. Journal of Materials Science 41, 597–609. https://doi.org/10.1007/s10853-006-6476-0

Le Pichon, X., 1968. Sea-floor spreading and continental drift. Journal of Geophysical Research 73, 3661–3697. https://doi.org/10.1029/jb073i012p03661

Linckens, J., Bruijn, R.H.C., Skemer, P., 2014. Dynamic recrystallization and phase mixing in experimentally deformed peridotite. Earth and Planetary Science Letters 388, 134–142. https://doi.org/10.1016/J.EPSL.2013.11.037

Linckens, J., Herwegh, M., Müntener, O., Mercolli, I., 2011. Evolution of a polymineralic mantle shear zone and the role of second phases in the localization of deformation. Journal of Geophysical Research: Solid Earth 116. https://doi.org/10.1029/2010JB008119

Linckens, J., Herwegh, M., Müntener, O., 2015. Small quantity but large effect—How minor phases control strain localization in upper mantle shear zones. Tectonophysics 643, 26–43. https://doi.org/10.1016/j.tecto.2014.12.008

Lockner, D.A., Beeler, N.M., 2002. 32 Rock failure and earthquakes, International Geophysics. https://doi.org/10.1016/S0074-6142(02)80235-2

Lonka, H., Schulmann, K., Venera, Z., 1998. Ductile deformation of tonalite in the Suomusjärvi shear zone,south-western Finland. Journal of Structural Geology 20, 783–798. https://doi.org/10.1016/s0191-8141(98)00003-0

Maggi, A., Jackson, J.A., McKenzie, D., Priestley, K., 2000. Earthquake focal depths, effective elastic thickness, and the strength of the continental lithosphere. Geology 28, 495–498. https://doi.org/10.1130/0091-7613(2000)28<495:EFDEET>2.0.CO;2

Mainprice, D., Paterson, M.S., 1984. Experimental studies on the role of water in the plasticity of quartzite. Journal of Geophysical Research 89, 4257–4269. https://doi.org/10.1029/JB089iB06p04257

Mansard, N., Raimbourg, H., Augier, R., Précigout, J., Le Breton, N., 2018. Large-scale strain localization induced by phase nucleation in mid-crustal granitoids of the south Armorican massif. Tectonophysics 745, 46–65. https://doi.org/10.1016/j.tecto.2018.07.022

Marti, S., 2017. Rheology of Fault Rocks - an experimental Study on the Brittle-Viscous Transition in Mafic Rocks. Thesis, University of Basel.

Marti, S., Stünitz, H., Heilbronner, R., Plümper, O., Drury, M., 2017. Experimental investigation of the brittle-viscous transition in mafic rocks—Interplay between fracturing, reaction, and viscous deformation. Journal of Structural Geology 105, 62–79. https://doi.org/10.1016/j.jsg.2017.10.011

Marti, S., Stünitz, H., Heilbronner, R., Plümper, O., Kilian, R., 2018. Syn-kinematic hydration reactions, grain size reduction, and dissolution-precipitation creep in experimentally deformed plagioclase-pyroxene mixtures. Solid Earth 9, 985–1009. https://doi.org/10.5194/se-9-985-2018

Matte, P., 2001. The Variscan collage and orogeny (480-290 Ma) and the tectonic definition of the Armorica microplate: a review. Terra Nova 13, 122–128. https://doi.org/10.1046/j.1365-3121.2001.00327.x

Matte, P., 1991. Accretionary history and crustal evolution of the Variscan belt in Western Europe. Tectonophysics 196, 309–337. https://doi.org/10.1016/0040-1951(91)90,328-P

Matte, P., 1986. Tectonics and plate tectonics model for the Variscan belt of Europe. Tectonophysics 126, 329–374. https://doi.org/10.1016/0040-1951(86)90237-4

McKenzie, D.P., Parker, R.L., 1967. The North Pacific: An example of tectonics on a sphere. Nature 216, 1276–1280. https://doi.org/10.1038/2161276a0

Mehl, L., Hirth, G., 2008. Plagioclase preferred orientation in layered mylonites: Evaluation of flow laws for the lower crust. Journal of Geophysical Research 113, B05202. https://doi.org/10.1029/2007JB005075

Menegon, L., Fusseis, F., Stünitz, H., Xiao, X., 2015. Creep cavitation bands control porosity and fluid flow in lower crustal shear zones. Geology 43, 227–230. https://doi.org/10.1130/G36307.1

Menegon, L., Pennacchioni, G., Heilbronner, R., Pittarello, L., 2008a. Evolution of quartz microstructure and c-axis crystallographic preferred orientation within ductilely deformed granitoids (Arolla unit, Western Alps). Journal of Structural Geology 30, 1332–1347. https://doi.org/10.1016/j.jsg.2008.07.007

Menegon, L., Pennacchioni, G., Spiess, R., 2008b. Dissolution-precipitation creep of K-feldspar in mid-crustal granite mylonites. Journal of Structural Geology 30, 565–579. https://doi.org/10.1016/j.jsg.2008.02.001

Menegon, L., Pennacchioni, G., Stünitz, H., 2006. Nucleation and growth of myrmekite during ductile shear deformation in metagranites. Journal of Metamorphic Geology 24, 553–568.

https://doi.org/10.1111/j.1525-1314.2006.00654.x

Meyersm, M.A., Ashworth, E., 1982. A model for the effect of grain size on the yield stress of metals. Philosophical Magazine A: Physics of Condensed Matter, Structure, Defects and Mechanical Properties 46, 737–759. https://doi.org/10.1080/01418618208236928

Miranda, E.A., Hirth, G., John, B.E., 2016. Microstructural evidence for the transition from dislocation creep to dislocation-accommodated grain boundary sliding in naturally deformed plagioclase. Journal of Structural Geology 92, 30–45. https://doi.org/10.1016/j.jsg.2016.09.002

Mitra, G., 1978. Ductile deformation zones and mylonites; the mechanical processes involved in the deformation of crystalline basement rocks. American Journal of Science 278, 1057–1084. https://doi.org/10.2475/ajs.278.8.1057

Miyazaki, T., Sueyoshi, K., Hiraga, T., 2013. Olivine crystals align during diffusion creep of Earth's upper mantle. Nature 502, 321–326. https://doi.org/10.1038/nature12570

Montési, L.G.J., 2013. Fabric development as the key for forming ductile shear zones and enabling plate tectonics. Journal of Structural Geology 50, 254–266. https://doi.org/10.1016/j.jsg.2012.12.011

Montési, L.G.J., 2007. A constitutive model for layer development in shear zones near the brittle-ductile transition. Geophysical Research Letters 34, 1–5. https://doi.org/10.1029/2007GL029250

Montési, L.G.J., Hirth, G., 2003. Grain size evolution and the rheology of ductile shear zones: from laboratory experiments to postseismic creep. Earth and Planetary Science Letters 211, 97–110. https://doi.org/10.1016/S0012-821X(03)00196-1

Morgan, W.J., 1968. Rises, trenches, great faults, and crustal blocks. Journal of Geophysical Research 73, 1959–1982. https://doi.org/10.1029/JB073i006p01959

Morley, W., L., 1964. Paleomagnetism as a means of dating geological events. Geochronology in Canada.

Murphy, M.A., Yin, A., Kapp, P., Harrison, T.M., Manning, C.E., Ryerson, F.J., Lin, D., Jinghui, G., 2002. Structural evolution of the Gurla Mandhata detachment system, southwest Tibet: Implications for the eastward extent of the Karakoram fault system. Bulletin of the Geological Society of America 114, 428–447. https://doi.org/10.1130/0016-7606(2002)114<0428:SEOTGM>2.0.CO; 2

Nabarro, F.R.N., 1948. Report on strength of solids. Physical Society, p.38.

Naziri, H., Pearce, R., Brown, M.H., Hale, K.F., 1975. Microstructural-mechanism relationship in the zinc/ aluminium eutectoid superplastic alloy. Acta Metallurgica 23, 489–496. https://doi.org/10.1016/0001-6160(75)90088-7

Newman, J., Lamb, W.M., Drury, M.R., Vissers, R.L.M., 1999. Deformation processes in a peridotite shear zone: reaction-softening by an H2O-deficient, continuous net transfer reaction. Tectonophysics 303, 193–222. https://doi.org/10.1016/S0040-1951(98)00259-5

Newman, J., Mitra, G., 1993. Lateral variations in mylonite zone thickness as influenced by fluid-rock interactions, Linville falls fault, North Carolina. Journal of Structural Geology 15, 849–863. https://doi.org/10.1016/0191-8141(93)90,180-I

Nicolas, A., Christensen, N.I., 1987. Formation of anisotropy in upper mantle peridotites: A review. American Geophysical Union (AGU), 111–123. https://doi.org/10.1029/GD016p0111

Okudaira, T., Jeřábek, P., Stünitz, H., Fusseis, F., 2015. High-temperature fracturing and subsequent grain-size-sensitive creep in lower crustal gabbros: Evidence for coseismic

loading followed by creep during decaying stress in the lower crust. Journal of Geophysical Research: Solid Earth 120, 3119–3141. https://doi.org/10.1002/2014JB011708

Okudaira, T., Shigematsu, N., Harigane, Y., Yoshida, K., 2017. Grain size reduction due to fracturing and subsequent grain-size-sensitive creep in a lower crustal shear zone in the presence of a CO2-bearing fluid. Journal of Structural Geology 95, 171–187. https://doi.org/10.1016/j.jsg.2016.11.001

Olgaard, D.L., 1990. The role of second phase in localizing deformation. Geological Society, London, Special Publications 54, 175–181. https://doi.org/10.1144/GSL.SP.1990.054.01.17

Olgaard, D.L., Evans, B., 1988. Grain growth in synthetic marbles with added mica and water. Contributions to Mineralogy and Petrology 100, 246–260. https://doi.org/10.1007/BF00373591

Olgaard, D.L., Evans, B., 1986. Effect of Second-Phase Particles on Grain Growth in Calcite. Journal of the American Ceramic Society 69, C-272-C—277. https://doi.org/10.1111/j.1151-2916.1986.tb07374.x

Oliot, E., Goncalves, P., Schulmann, K., Marquer, D., Lexa, O., 2014. Mid-crustal shear zone formation in granitic rocks: Constraints from quantitative textural and crystallographic preferred orientations analyses. Tectonophysics 612–613, 63–80. https://doi.org/10.1016/j.tecto.2013.11.032

Palazzin, G., Raimbourg, H., Stünitz, H., Heilbronner, R., Neufeld, K., Précigout, J., 2018. Evolution in H2O contents during deformation of polycrystalline quartz: An experimental study. Journal of Structural Geology 114, 95–110. https://doi.org/10.1016/J.JSG.2018.05.021

Panozzo, R., 1983. Two-dimensional analysis of shape-fabric using projections of digitized lines in a plane. Tectonophysics 95, 279–294. https://doi.org/10.1016/0040-1951(83)90073-2

Park, Y., Yoo, S.H., Ree, J.H., 2006. Weakening of deforming granitic rocks with layer development at middle crust. Journal of Structural Geology 28, 919–928. https://doi.org/10.1016/j.jsg.2006.02.005

Passchier, C., 1984. The generation of ductile and brittle shear bands in a low-angle mylonite zone. Journal of Structural Geology 6, 273–281. https://doi.org/10.1016/0191-8141(84)90051-8

Passchier, C., Trouw, R.A.J., 2005. Deformation Mechanisms. Microtectonics. Springer-Verlag, Berlin/Heidelberg, 25–66. https://doi.org/10.1007/3-540-29359-0_3

Paterson, M.S., 1995. A Granular Flow Approach to Fine-Grain Superplasticity. Plastic Deformation of Ceramics. Springer US, 279–283. https://doi.org/10.1007/978-1-4899-1441-5_24

Paterson, M. S., 2013. Materials science for structural geology, Springer Dordrecht Heidelberg New York London, p. 247, doi:10.1007/978-94-007-5545-1

Paterson, M.S., Luan, F.C., 1990. Quartzite rheology under geological conditions. Geological Society, London, Special Publications 54, 299–307. https://doi.org/10.1144/GSL.SP.1990.054.01.26

Pec, M., Stünitz, H., Heilbronner, R., 2012. Semi-brittle deformation of granitoid gouges in shear experiments at elevated pressures and temperatures. 38. https://doi.org/10.1016/j.jsg.2011.09.001

Pec, M., Stünitz, H., Heilbronner, R., Drury, M., 2016. Semi-brittle flow of granitoid fault rocks in experiments. Journal of Geophysical Research: Solid Earth 121, 1677–1705. https://doi.org/10.1002/2015JB012513

Petit, C., Burov, E., Tiberi, C., 2008. Strength of the lithosphere and strain localisation in the Baikal rift. Earth and Planetary Science Letters 269, 523–529. https://doi.org/10.1016/j.epsl.2008.03.012

Philippot, P., Kienast, J.R., 1989. Chemical-microstructural changes in eclogite-facies shear zones (Monviso, Western Alps, north Italy) as indicators of strain history and the mechanism and scale of mass transfer. LITHOS 23, 179–200. https://doi.org/10.1016/0024-4937(89)90004-2

Platt, J.P., 2015. Rheology of two-phase systems: A microphysical and observational approach. Journal of Structural Geology 77, 213–227. https://doi.org/10.1016/j.jsg.2015.05.003

Platt, J.P., Behr, W.M., 2011. Grainsize evolution in ductile shear zones: Implications for strain localization and the strength of the lithosphere. Journal of Structural Geology 33, 537–550. https://doi.org/10.1016/j.jsg.2011.01.018

Poirier, J.P., 1980. Shear localization and shear instability in materials in the ductile field. Journal of Structural Geology 2, 135–142. https://doi.org/10.1016/0191-8141(80)90043-7

Powell, R., Holland, T., 1999. Relating formulations of the thermodynamics of mineral solid solutions; activity modeling of pyroxenes, amphiboles, and micas. American Mineralogist 84, 1–14. https://doi.org/10.2138/am-1999-1-201

Precigout, J., Gueydan, F., Gapais, D., Garrido, C.J., Essaifi, A., 2007. Strain localisation in the subcontinental mantle—a ductile alternative to the brittle mantle. Tectonophysics 445, 318–336. https://doi.org/10.1016/j.tecto.2007.09.002

Précigout, J., Hirth, G., 2014. B-type olivine fabric induced by grain boundary sliding. Earth and Planetary Science Letters 395, 231–240. https://doi.org/10.1016/j.epsl.2014.03.052

Précigout, J., Prigent, C., Palasse, L., Pochon, A., 2017. Water pumping in mantle shear zones. Nature Communications 8, 15,736. https://doi.org/10.1038/ncomms15736

Précigout, J., Stünitz, H., 2016. Evidence of phase nucleation during olivine diffusion creep: A new perspective for mantle strain localisation. Earth and Planetary Science Letters 455, 94–105. https://doi.org/10.1016/j.epsl.2016.09.029

Précigout, J., Stünitz, H., Pinquier, Y., Champallier, R., Schubnel, A., 2018. High-pressure, High-temperature Deformation Experiment Using the New Generation Griggs-type Apparatus. Journal of Visualized Experiments : JoVE. https://doi.org/10.3791/56841

Précigout, J., Stünitz, H., Villeneuve, J., 2019. Excess water storage induced by viscous strain localization during high-pressure shear experiment. Scientific Reports 9. https://doi.org/10.1038/s41598-019-40020-y

Prigent, C., Guillot, S., Agard, P., Lemarchand, D., Soret, M., Ulrich, M., 2018. Transfer of subduction fluids into the deforming mantle wedge during nascent subduction: Evidence from trace elements and boron isotopes (Semail ophiolite, Oman). Earth and Planetary Science Letters 484, 213–228. https://doi.org/10.1016/J.EPSL.2017.12.008

Raimbourg, H., Toyoshima, T., Harima, Y., Kimura, G., 2008. Grain-size reduction mechanisms and rheological consequences in high-temperature gabbro mylonites of Hidaka, Japan. Earth and Planetary Science Letters 267, 637–653. https://doi.org/10.1016/j.epsl.2007.12.012

Raj, R., Ashby, M.F., 1971. On grain boundary sliding and diffusional creep. Metallurgical Transactions 2, 1113–1127. https://doi.org/10.1007/BF02664244

Ramsay, J.G., 1980. Shear zone geometry: A review. Journal of Structural Geology 2, 83–99. https://doi.org/10.1016/0191-8141(80)90038-3

Ree, J.H., Kim, H.S., Han, R., Jung, H., 2005. Grain-size reduction of feldspars by fracturing and neocrystallization in a low-grade granitic mylonite and its rheological effect.

Tectonophysics 407, 227–237. https://doi.org/10.1016/j.tecto.2005.07.010

Richter, B., Stünitz, H., Heilbronner, R., 2018. The brittle-to-viscous transition in polycrystalline quartz: An experimental study. Journal of Structural Geology 114, 1–21. https://doi.org/10.1016/j.jsg.2018.06.005

Richter, B., 2017. The brittle-to-viscous transition in experimentally deformed quartz gouge. Thesis, University of Basel.

Richter, B., Stünitz, H., Heilbronner, R., 2016. Stresses and pressures at the quartz-to-coesite phase transformation in shear deformation experiments. Journal of Geophysical Research: Solid Earth 121, 8015–8033. https://doi.org/10.1002/2016JB013084

Ringwood, A. E., Hart, P. J., 1969. The Earth's Crust and Upper Mantle. American Geophysical Union 13, 1–17.

Rosenberg, C.L., Handy, M.R., 2005. Experimental deformation of partially melted granite revisited: implications for the continental crust. Journal of Metamorphic Geology 23, 19–28. https://doi.org/10.1111/j.1525-1314.2005.00555.x

Rubie, D.C., 1983. Reaction-enhanced ductility: The role of solid-solid univariant reactions in deformation of the crust and mantle. Tectonophysics 96, 331–352. https://doi.org/10.1016/0040-1951(83)90225-1

Rudnick, R.L., Fountain, D.M., 1995. Nature and composition of the continental crust: A lower crustal perspective. Reviews of Geophysics 33, 267. https://doi.org/10.1029/95RG01302

Rudnick, R.L. and Gao, S., 2003. Composition of the continental crust. Treatise on geochemistry, 3, p.659.

Rudnick, R.L., Taylor, S.R., 1987. The composition and petrogenesis of the lower crust: A xenolith study. Journal of Geophysical Research: Solid Earth 92, 13981–14005. https://doi.org/10.1029/jb092ib13p13981

Rutter, E.H., Brodie, K.H., 1992. Rheology of the lower crust, *in Continental Lower Crust*, edited by D. M. Fountain, R. J. Arculus, and R. W. Kay, pp.201–267. Elsevier Sci., New York.

Rutter, E.H., Brodie, K.H., 1988. The role of tectonic grain size reduction in the rheological stratification of the lithosphere. Geologische Rundschau 77, 295–307. https://doi.org/10.1007/BF01848691

Rutter, E.H., Brodie, K.H., 1985. The Permeation of Water into Hydrating Shear Zones. 242–250. https://doi.org/10.1007/978-1-4612-5066-1_9

Rutter, E.H., Hackston, A.J., Yeatman, E., Brodie, K.H., Mecklenburgh, J., May, S.E., 2013. Reduction of friction on geological faults by weak-phase smearing. Journal of Structural Geology 51, 52–60. https://doi.org/10.1016/j.jsg.2013.03.008

Rutter, E.H., Holdsworth, R.E., Knipe, R.J., 2001. The nature and tectonic significance of fault-zone weakening: An introduction. Geological Society Special Publication 186, 1–11. https://doi.org/10.1144/GSL.SP.2001.186.01.01

Rybacki, E., Dresen, G., 2000. Dislocation and diffusion creep of synthetic anorthite aggregates. Journal of Geophysical Research: Solid Earth 105, 26017–26036. https://doi.org/10.1029/2000JB900223

Sawyer, D.S., 1985. Brittle failure in the Upper Mantle during extension of continental lithosphere. Journal of Geophysical Research, 90: 3021-3025. https://doi.org/10.1029/JB090iB04p03021

Scheuber, E., Gonzalez, G., 1999. Tectonics of the Jurassic-Early Cretaceous magmatic arc of the north Chilean Coastal Cordillera (22°-26 °S): A story of crustal deformation along a

convergent plate boundary. Tectonics 18, 895–910. https://doi.org/10.1029/1999TC900024

Schmid, S.M., 1982. Laboratory experiments on the rheology and deformation mechanisms in calcite rocks and their applications to studies in the field. Geol Inst ETH Univ Zürich, no 241, pp 1-62.

Schmid, S.M., Paterson, M.S., Boland, J.N., 1980. High temperature flow and dynamic recrystallization in carrara marble. Tectonophysics 65, 245–280. https://doi.org/10.1016/0040-1951(80)90077-3

Scholz, C.H., 1988. The brittle-plastic transition and the depth of seismic faulting. Geologische Rundschau 77, 319–328. https://doi.org/10.1007/BF01848693

Schroeder, T., John, B.E., 2004. Strain localization on an oceanic detachment fault system, Atlantis Massif, 30 °N, Mid-Atlantic Ridge. Geochemistry, Geophysics, Geosystems 5. https://doi.org/10.1029/2004GC000728

Shea, W.T., Kronenberg, A.K., 1993. Strength and anisotropy of foliated rocks with varied mica contents. Journal of Structural Geology 15, 1097–1121. https://doi.org/10.1016/0191-8141(93)90158-7

Shelley, D., 1994. Spider texture and amphibole preferred orientations. Journal of Structural Geology 16, 709–717. https://doi.org/10.1016/0191-8141(94)90120-1

Sibson, R.H., 1977. Fault rocks and fault mechanisms. Journal of the Geological Society 133, 191–213. https://doi.org/10.1144/gsjgs.133.3.0191

Sidman, D., Ferré, E.C., Teyssier, C., Jackson, M., 2005. Magnetic fabric and microstructure of a mylonite: Example from the Bitterroot shear zone, western Montana. Geological Society Special Publication 245, 143–163. https://doi.org/10.1144/GSL.SP.2005.245.01.07

Simpson, C., Wintsch, R.P., 1989. Evidence for deformation-induced K-feldspar replacement by myrmekite. Journal of Metamorphic Geology 7, 261–275. https://doi.org/10.1111/j.1525-1314.1989.tb00588.x

Skemer, P., Katayama, I., Jiang, Z., Karato, S., 2005. The misorientation index: Development of a new method for calculating the strength of lattice-preferred orientation. Tectonophysics 411, 157–167. https://doi.org/10.1016/J.TECTO.2005.08.023

Snyder, D.B., Kjarsgaard, B.A., 2013. Mantle roots of major precambrian shear zones inferred from structure of the great slave lake shear zone, northwest Canada. Lithosphere 5, 539–546. https://doi.org/10.1130/L299.1

Song, W.J., Ree, J.H., 2007. Effect of mica on the grain size of dynamically recrystallized quartz in a quartz-muscovite mylonite. Journal of Structural Geology 29, 1872–1881. https://doi.org/10.1016/j.jsg.2007.09.011

Stewart, M., Holdsworth, R.E., Strachan, R.A., 2000. Deformation processes and weakening mechanisms within the frictional—viscous transition zone of major crustal-scale faults: insights from the Great Glen Fault Zone, Scotland. Journal of Structural Geology 22, 543–560. https://doi.org/10.1016/S0191-8141(99)00164-9

Stipp, M., Stunitz, H., Heilbronner, R., Schmid, S.M., 2002. Dynamic recrystallization of quartz: correlation between natural and experimental conditions. Geological Society, London, Special Publications 200, 171–190. https://doi.org/10.1144/GSL.SP.2001.200.01.11

Stünitz, H., 1993. Transition from fracturing to viscous flow in a naturally deformed metagabbro. Defects and processes in the solid state: geoscience applications. Elsevier, Amsterdam, pp 121–150.

Stünitz, H., Fitz Gerald, J.D., 1993. Deformation of granitoids at low metamorphic grades: II. Granular flow in albite rich mylonites. Tectonophysics 221, 299–324.

https://doi.org/10.1016/0040-1951(93)90164-F

Stünitz, H., Fitz Gerald, J.D., Tullis, J., 2003. Dislocation generation, slip systems, and dynamic recrystallization in experimentally deformed plagioclase single crystals. Tectonophysics 372, 215–233. https://doi.org/10.1016/S0040-1951(03)00241-5

Stünitz, H., Tullis, J., 2001. Weakening and strain localization produced by syn-deformational reaction of plagioclase. International Journal of Earth Sciences 90, 136–148. https://doi.org/10.1007/s005310000148

Sundberg, M., Cooper, R.F., 2008. Crystallographic preferred orientation produced by diffusional creep of harzburgite: Effects of chemical interactions among phases during plastic flow. Journal of Geophysical Research: Solid Earth 113. https://doi.org/10.1029/2008JB005618

Svahnberg, H., Piazolo, S., 2013. Interaction of chemical and physical processes during deformation at fluid-present conditions: A case study from an anorthosite-leucogabbro deformed at amphibolite facies conditions. Contributions to Mineralogy and Petrology 165, 543–562. https://doi.org/10.1007/s00410-012-0822-9

Svahnberg, H., Piazolo, S., 2010. The initiation of strain localisation in plagioclase-rich rocks: Insights from detailed microstructural analyses. Journal of Structural Geology 32, 1404–1416. https://doi.org/10.1016/j.jsg.2010.06.011

Tackley, P.J., 1998. Self-consistent generation of tectonic plates in three-dimensional mantle convection. Earth and Planetary Science Letters 157, 9–22. https://doi.org/10.1016/S0012-821X(98)00029-6

Takeda, Y.T., Griera, A., 2006. Rheological and kinematical responses to flow of two-phase rocks. Tectonophysics 427, 95–113. https://doi.org/10.1016/j.tecto.2006.03.050

Tarantola, A., Diamond, L., Stünitz, H., 2010. Modification of fluid inclusions in quartz by deviatoric stress I: experimentally induced changes in inclusion shapes and microstructures. https://doi.org/10.1007/s00410-010-0509-z

Tartèse, R., Boulvais, P., 2010. Differentiation of peraluminous leucogranites “en route” to the surface. Lithos 114, 353–368. https://doi.org/10.1016/j.lithos.2009.09.011

Tartèse, R., Boulvais, P., Poujol, M., Chevalier, T., Paquette, J.L., Ireland, T.R., Deloule, E., 2012. Mylonites of the South Armorican Shear Zone: Insights for crustal-scale fluid flow and water-rock interaction processes. Journal of Geodynamics 56–57, 86–107. https://doi.org/10.1016/j.jog.2011.05.003

Tartèse, R., Boulvais, P., Poujol, M., Vigneresse, J.-L., 2011. Granite petrogenesis revealed by combined gravimetric and radiometric imaging. Tectonophysics 501, 98–103. https://doi.org/10.1016/J.TECTO.2011.02.003

Tasaka, M., Zimmerman, M.E., Kohlstedt, D.L., 2016. Evolution of the rheological and microstructural properties of olivine aggregates during dislocation creep under hydrous conditions. Journal of Geophysical Research: Solid Earth 121, 92–113. https://doi.org/10.1002/2015JB012134

Tasaka, M., Zimmerman, M.E., Kohlstedt, D.L., Stünitz, H., Heilbronner, R., 2017. Rheological Weakening of Olivine + Orthopyroxene Aggregates Due To Phase Mixing: Part 2. Microstructural Development. Journal of Geophysical Research: Solid Earth 122, 7597–7612. https://doi.org/10.1002/2017JB014311

Tokle, L., Hirth, G., Behr, W.M., 2019. Flow laws and fabric transitions in wet quartzite. Earth and Planetary Science Letters 505, 152–161. https://doi.org/10.1016/J.EPSL.2018.10.017

Trouw, A.J.R., Passchier, C.W., Wiersma, D.J., 2009. Atlas of Mylonites — and Related Microstructures. Springer-Verlag, Berlin Heidelberg.

Tsurumi, J., Hosonuma, H., Kanagawa, K., 2003. Strain localization due to a positive feedback of deformation and myrmekite-forming reaction in granite and aplite mylonites along the Hatagawa Shear Zone of NE Japan. Journal of Structural Geology 25, 557–574. https://doi.org/10.1016/S0191-8141(02)00048-2

Tullis, J., Wenk, H.R., 1994. Effect of muscovite on the strength and lattice preferred orientations of experimentally deformed quartz aggregates. Materials Science and Engineering A 175, 209–220. https://doi.org/10.1016/0921-5093(94)91,060-X

Tullis, J., Yund, R.A., 1985. Dynamic recrystallisation of feldspar: a mechanism for ductile shear zone formation. Geology 13, 238–241.

Turrillot, P., Augier, R., Faure, M., 2009. The top-to-the-southeast Sarzeau shear zone and its place in the late-orogenic extensional tectonics of southern Armorica. Bulletin de La Societe Geologique de France 180, 247–261. https://doi.org/10.2113/gssgfbull.180.3.247

Turrillot, Paul, Augier, R., Monié, P., Faure, M., 2011. Late orogenic exhumation of the Variscan high-grade units (South Armorican Domain, western France), combined structural and ^{40}Ar/^{39}Ar constraints. Tectonics 30, n/a-n/a. https://doi.org/10.1029/2010TC002788

Turrillot, P., Faure, M., Martelet, G., Chen, Y., Augier, R., 2011. Pluton-dyke relationships in a Variscan granitic complex from AMS and gravity modeling. Inception of the extensional tectonics in the South Armorican Domain (France). Journal of Structural Geology 33, 1681–1698. https://doi.org/10.1016/J.JSG.2011.08.004

Vauchez, A., Tommasi, A., Mainprice, D., 2012. Faults (shear zones) in the Earth's mantle., Tectonophysics. https://doi.org/10.1016/j.tecto.2012.06.006

Vernon, R.H., Johnson, S.E., Melis, E.A., 2004. Emplacement-related microstructures in the margin of a deformed pluton: the San José tonalite, Baja California, México. Journal of Structural Geology 26, 1867–1884. https://doi.org/10.1016/J.JSG.2004.02.007

Viegas, G., Menegon, L., Archanjo, C., 2016. Brittle grain-size reduction of feldspar, phase mixing and strain localization in granitoids at mid-crustal conditions (Pernambuco shear zone, NE Brazil). Solid Earth 7, 375–396. https://doi.org/10.5194/se-7-375-2016

Vigneresse, J.-L., Brun, J.-P., 1983. Les leucogranites armoricains marqueurs de la deformation regionale; apport de la gravimetrie. Bulletin de La Société Géologique de France S7-XXV. https://doi.org/10.2113/gssgfbull.S7-XXV.3.357

Vine, F.J., Matthews, D.H., 1963. Magnetic Anomalies Over Oceanic Ridges. Nature 199, 947–949. https://doi.org/10.1038/199947a0

Vissers, R.L.M., Drury, M.R., Newman, J., Fliervoet, T.F., 1997. Mylonitic deformation in upper mantle peridotites of the North Pyrenean Zone (France): implications for strength and strain localization in the lithosphere. Tectonophysics 279, 303–325. https://doi.org/10.1016/S0040-1951(97)00128-5

Warren, J.M., Hirth, G., 2006. Grain size sensitive deformation mechanisms in naturally deformed peridotites. Earth and Planetary Science Letters 248, 423–435. https://doi.org/10.1016/j.epsl.2006.06.006

Wassmann, S., Stöckhert, B., 2013. Rheology of the plate interface—Dissolution precipitation creep in high pressure metamorphic rocks., Tectonophysics. https://doi.org/10.1016/j.tecto.2013.09.030

Watts, M.J., Williams, G.D., 1979. Fault rocks as indicators of progressive shear deformation in the Guingamp region, Brittany. Journal of Structural Geology 1, 323–332. https://doi.org/10.1016/0191-8141(79)90007-5

Weaver, B.L., Tarney, J., 1984. Major and trace element composition of the continental

lithosphere. Physics and Chemistry of the Earth 15, 39–68. https://doi.org/10.1016/0079-1946(84)90004-1

Wegener, A., 1912. Die Entstehung der Kontinente. Geologische Rundschau 3, 276–292. https://doi.org/10.1007/BF02202896

Wehrens, P., Baumberger, R., Berger, A., Herwegh, M., 2017. How is strain localized in a meta-granitoid, mid-crustal basement section? Spatial distribution of deformation in the central Aar massif (Switzerland). Journal of Structural Geology 94, 47–67. https://doi.org/10.1016/J.JSG.2016.11.004

Wehrens, P., Berger, A., Peters, M., Spillmann, T., Herwegh, M., 2016. Deformation at the frictional-viscous transition: Evidence for cycles of fluid-assisted embrittlement and ductile deformation in the granitoid crust. Tectonophysics 693, 66–84. https://doi.org/10.1016/J.TECTO.2016.10.022

Wenk, H.-R., Christie, J.M., 1991. Comments on the interpretation of deformation textures in rocks. Journal of Structural Geology 13, 1091–1110. https://doi.org/10.1016/0191-8141(91)90,071-P

White, S., 1976. The Effects of Strain on the Microstructures, Fabrics, and Deformation Mechanisms in Quartzites. Philosophical Transactions of the Royal Society A: Mathematical, Physical and Engineering Sciences 283, 69–86. https://doi.org/10.1098/rsta.1976.0070

White, S.H., Burrows, S.E., Carreras, J., Shaw, N.D., Humphreys, F.J., 1980. On mylonites in ductile shear zones. Journal of Structural Geology 2, 175–187. https://doi.org/10.1016/0191-8141(80)90048-6

White, S.H., Knipe, R.J., 1978. Transformation- and reaction-enhanced ductility in rocks. Journal of the Geological Society 135, 513–516. https://doi.org/10.1144/gsjgs.135.5.0513

Whitmeyer, S.J., Wintsch, R.P., 2005. Reaction localization and softening of texturally hardened mylonites in a reactivated fault zone, central Argentina. Journal of Metamorphic Geology 23, 411–424. https://doi.org/10.1111/j.1525-1314.2005.00588.x

Wintsch, R.P., Christoffersen, R., Kronenberg, A.K., 1995. Fluid-rock reaction weakening of fault zones. Journal of Geophysical Research: Solid Earth 100, 13021–13032. https://doi.org/10.1029/94JB02622

Yonkee, W.A., Parry, W.T., Bruhn, R.L., 2003. Relations between progressive deformation and fluid-rock interaction during shear-zone growth in a basement-cored thrust sheet, Sevier orogenic belt, Utah. American Journal of Science 303, 1–59. https://doi.org/10.2475/ajs.303.1.1

Yund, R.A., Tullis, J., 1991. Compositional changes of minerals associated with dynamic recrystallizatin. Contributions to Mineralogy and Petrology 108, 346–355. https://doi.org/10.1007/BF00285942

Zhang, Y., Jessell, M.W., Hobbs, B.E., 1996. Experimental and numerical studies of the accommodation of strain incompatibility on the grain scale. Journal of Structural Geology 18, 451–460. https://doi.org/10.1016/0191-8141(95)00097-W

Appendix A

Experimental data were processed using a MATLAB-based program inspired from the "rig" program of Matej Pec (Pec et al., 2016). The source code for the rig program is given below and can be found at https://sites.google.com/site/jacquesprecigout/telechargements-downloads.

```
%-------------------------------------------------------------------------
%-------------------------------------------------------------------------
%                    Griggs-type experiment: data treatment
%-------------------------------------------------------------------------
%-------------------------------------------------------------------------


% Type of Griggs used

quest = "\fontsize{15} What lab?";
opts. Interpreter = 'tex';
opts. Default ='Orléans';
answer = questdlg(quest,'Apparatus','Tromso','Orléans',opts);

switch answer
    case "Tromso"
        Griggs = 1;
    case "Orléans"
        Griggs = 2;
end

if Griggs == 1;
    fid = fopen("./Data files/425JP.txt",'r'); % import in mV
    formatSpec = "%f %f %f %f\n";
    sizedata = [4 Inf];
    data=fscanf(fid,formatSpec,sizedata)';
    fclose(fid);
    [n,nc]= size(data);

    Time = data(:,1);
    Force = data(:,2);
    Stress_S3 = data(:,3);
    Displacement_S1 = data(:,4);


    quest = "\fontsize{15} What rig?";
    opts. Interpreter = "tex";
    opts. Default ='Rig 1';
    answer = questdlg(quest,'Rig','Rig 1','Rig 2',opts);

    switch answer
     case "Rig 1'
        Rig = 1;
     case "Rig 2'
        Rig = 2;
    end
```

```
    Options = {"Temperature of experiment?"};
    title = "Experiment temperature (C)";
    dims = [1 35];
    definput = {'800'};
    answer2 = inputdlg(Options,title,dims,definput);
    T = str2double(answer2{1});

    Temperature=ones(length(Time),1)*T; % experiment temperature (°C)
    [data,m] = size(Time);

% Convert V to kN, MPa and mm
% Conversion factors (from Matej Pec's Programm)
    if Rig == 1
        fconv=19.4871; % (N)
        pcconv=502.8742561; % (kPa)
        dxconv=4.047108340; % (m)
        rig_stiffness = 3.31e-3; %(micron/kN)
        Friction = 1.3; % (N/mm)
    end

    if Rig == 2
        fconv=22.0344; % (N)
        pcconv=251.6292997;
        dxconv=5.0431186; % (m)
        rig_stiffness = 5.04e-3; %(micron/kN)
        Friction = 1.3; % (N/mm)
    end

Force=Force*fconv*1e-3; %force (kN)
Stress_S3=Stress_S3*pcconv*1e-3; %confining pressure (MPa)
Displacement_S1=Displacement_S1*dxconv*1e-3; %displacement sigma 1 (mm)

%--------------------
% Filtering displacement and stress curve
%--------------------

if n <100
    no = 10;
else
    no = 1000;
end
b=linspace(1/no,1/no,no)";
Displacement_S1 = filtfilt(b,1,Displacement_S1);
Force = filtfilt(b,1,Force);
end

if Griggs == 2

% temps 1
C1_data = Channel_1_Data;
C1_unit = Channel_1_Header.Unit;
% Experience Temperature
C2_name = Channel_2_Header.SignalName;
```

```
C2_data = Channel_2_Data;
C2_unit = Channel_2_Header.Unit;
% LVDT ram
C3_name = Channel_3_Header.SignalName;
C3_data = Channel_3_Data;
C3_unit = Channel_3_Header.Unit;
% LVDT def
C4_name = Channel_4_Header.SignalName;
C4_data = Channel_4_Data;
C4_unit = Channel_4_Header.Unit;
% temps 2
C5_name = Channel_5_Header.SignalName;
C5_data = Channel_5_Data;
C5_unit = Channel_5_Header.Unit;
% P def
C6_name = Channel_6_Header.SignalName;
C6_data = Channel_6_Data;
C6_unit = Channel_6_Header.Unit;
% P ram
C7_name = Channel_7_Header.SignalName;
C7_data = Channel_7_Data;
C7_unit = Channel_7_Header.Unit;
% Force
C8_name = Channel_8_Header.SignalName;
C8_data = Channel_8_Data;
C8_unit = Channel_8_Header.Unit;
% Room temperature
C9_name = Channel_9_Header.SignalName;
C9_data = Channel_9_Data;
C9_unit = Channel_9_Header.Unit;
% Sigma 1
C10_name = Channel_10_Header.SignalName;
C10_data = Channel_10_Data;
C10_unit = Channel_10_Header.Unit;
% Sigma 3
C11_name = Channel_11_Header.SignalName;
C11_data = Channel_11_Data;
C11_unit = Channel_11_Header.Unit;
% Delta sigma
C12_name = Channel_12_Header.SignalName;
C12_data = Channel_12_Data;
C12_unit = Channel_12_Header.Unit;
% P_def_MPa
C13_name = Channel_13_Header.SignalName;
C13_data = Channel_13_Data;
C13_unit = Channel_13_Header.Unit;
% P_ram_MPa
C14_name = Channel_14_Header.SignalName;
C14_data = Channel_14_Data;
C14_unit = Channel_14_Header.Unit;
% Sigma 1_bar
C15_name = Channel_15_Header.SignalName;
C15_data = Channel_15_Data;
C15_unit = Channel_15_Header.Unit;
```

```
% Sigma 3_barC16_name = Channel_16_Header.SignalName;
C16_data = Channel_16_Data;
C16_unit = Channel_16_Header.Unit;
% Diff LVDT
C17_name = Channel_17_Header.SignalName;
C17_data = Channel_17_Data;
C17_unit = Channel_17_Header.Unit;

[data,m] = size(C1_data);

% Extract data every seconds
%---------------------------

s = round(data/C1_data(data));
r=round(data/s);
C1_data_s = linspace(0.,0.,r-1)";
C2_data_s = linspace(0.,0.,r-1)';
C3_data_s = linspace(0.,0.,r-1)';
C4_data_s = linspace(0.,0.,r-1)';
C5_data_s = linspace(0.,0.,r-1)';
C6_data_s = linspace(0.,0.,r-1)';
C7_data_s = linspace(0.,0.,r-1)';
C8_data_s = linspace(0.,0.,r-1)';
C9_data_s = linspace(0.,0.,r-1)';
C10_data_s = linspace(0.,0.,r-1)';
C11_data_s = linspace(0.,0.,r-1)';
C12_data_s = linspace(0.,0.,r-1)';
C13_data_s = linspace(0.,0.,r-1)';
C14_data_s = linspace(0.,0.,r-1)';
C15_data_s = linspace(0.,0.,r-1)';
C16_data_s = linspace(0.,0.,r-1)';
C17_data_s = linspace(0.,0.,r-1)';

k=0;
for i=1:data
    if i == k*s+1
        C1_data_s(k+1)=i;
        C2_data_s(k+1)=C2_data(i);
        C3_data_s(k+1)=C3_data(i);
        C4_data_s(k+1)=C4_data(i);
        C5_data_s(k+1)=C5_data(i);
        C6_data_s(k+1)=C6_data(i);
        C7_data_s(k+1)=C7_data(i);
        C8_data_s(k+1)=C8_data(i);
        C9_data_s(k+1)=C9_data(i);
        C10_data_s(k+1)=C10_data(i);
        C11_data_s(k+1)=C11_data(i);
        C12_data_s(k+1)=C12_data(i);
        C13_data_s(k+1)=C13_data(i);
        C14_data_s(k+1)=C14_data(i);
        C15_data_s(k+1)=C15_data(i);
        C16_data_s(k+1)=C16_data(i);
        C17_data_s(k+1)=C17_data(i);

        k=k+1;
```

```
    end
end
Time = C1_data_s;
%Temperature = C2_data_s;
Displacement_S3 = C2_data_s;
Displacement_S1 = C3_data_s;
Time_2 = C4_data_s;
Pressure_S1_bar = C5_data_s;
Pressure_S3_bar = C6_data_s;
Force = C7_data_s;
Room_temperature = C8_data_s;
Stress_S1 = C9_data_s;
Stress_S3 = C10_data_s;
Delta_stress = C11_data_s;
Pressure_S1_MPa = C12_data_s;
Pressure_S3_MPa = C13_data_s;
Stress_S1_bar = C14_data_s;
Stress_S3_bar = C15_data_s;
Diff_LVDT = C16_data_s;

%--------------------
% Filtering displacement and stress curve
%--------------------

if data <100
    no = 10;
else
    no = 1000;
end
b=linspace(1/no,1/no,no)';
Stress_S3 = filtfilt(b,1,Stress_S3);
Displacement_S1 = filtfilt(b,1,Displacement_S1);
Force = filtfilt(b,1,Force);

% Define rig stiffness as a function of pressure
%---------------

a = (15.1768-13.2476)/500;
c = 13.2476-(a*500);
rig_stiffness = (a*max(Stress_S3)+c)*1e-3; %(13.2476e-3 at 5 kbar; 15.1768e-3 at 10
kbar);
Friction = 1.3; % Value from Brown University (Matej/Renée's software)

end

% Temperature of experiment
%-----------

disp("<a href="matlab: Temperature_graph;">Temperature</a>")

% Force%-----------
```

```
disp("<a href="matlab : Force_graph;">Force</a>")
```

```
% Pressure
%-----------

disp("<a href="matlab : Stress_sigma_3;">Pressure (Stress sigma 3)</a>")

% Displacement
%-----------

disp('<a href="matlab : Displacement_sigma_1;">Displacement (Sigma 1)</a>')

if Griggs == 2

% Stress
%-----------

disp('<a href="matlab: Stress_sigma_1;">Stress (Sigma 1)</a>')

% Differential stress
%-----------

disp("<a href="matlab: Differential_stress;">Differential stress (Sigma 1–
Sigma 3)</a>")


% Ram pressure sigma 1
%-----------

disp("<a href="matlab : Ram_pressure_sigma_1;">Ram_pressure (Sigma 1)</a>")

% Ram pressure sigma 3
%-----------

disp('<a href="matlab : Ram_pressure_sigma_3;">Ram_pressure (Sigma 3)</a>')

% Displacement sigma 3
%-----------

disp('<a href="matlab: Displacement_sigma_3;">Displacement (Sigma 3)</a>')

end

% Regime of deformation, i.e., coaxial or non-coaxial
%------------------------
quest = "\fontsize{15} Deformation regime?";
opts. Interpreter = "tex";
opts. Default ='Coaxial';
answer = questdlg(quest,'Regime','Coaxial','Non-coaxial (shear)',opts);
switch answer
    case "Coaxial"
        Deformation_regime = 1;
    case "Non-coaxial (shear)"
        Deformation_regime = 2;
End
```

```
% Sample thickness and piston diameter
%-----------------------
if Griggs == 1
    if Deformation_regime == 1
        Options = {"Sample length (mm)",'Piston diameter (mm)'};
        title = "Contours options";
        dims = [1 35];
        definput = {"15","6,394'};
        answer = inputdlg(Options,title,dims,definput);
        Sample_thickness_coaxial = str2double(answer{1});
        Piston_diameter = str2double(answer{2});
    else
        Options = {"Sample thickness before (mm)",'Sample thickness after','Piston
diameter (mm)','Shear zone angle (°)'};
        title = "Contours options";
        dims = [1 35];
        definput = {"1.2","1','6,394','45'};
        answer = inputdlg(Options,title,dims,definput);
        Sample_thickness_before = str2double(answer{1});
        Sample_thickness_after = str2double(answer{2});
        Piston_diameter = str2double(answer{3});
        Shear_zone_angle = str2double(answer{4});
    end
else
    if Deformation_regime == 1
        Options = {"Sample length (mm)",'Piston diameter (mm)'};
        title = "Contours options";
        dims = [1 35];
        definput = {"15","8'};
        answer = inputdlg(Options,title,dims,definput);
        Sample_thickness_coaxial = str2double(answer{1});
        Piston_diameter = str2double(answer{2});
    else
        Options = {"Sample thickness before (mm)",'Sample thickness after','Piston
diameter (mm)','Shear zone angle (°)'};
        title = "Contours options";
        dims = [1 35];
        definput = {"1.2","1','8','45'};
        answer = inputdlg(Options,title,dims,definput);
        Sample_thickness_before = str2double(answer{1});
        Sample_thickness_after = str2double(answer{2});
        Piston_diameter = str2double(answer{3});
        Shear_zone_angle = str2double(answer{4});
    end
end

if Deformation_regime == 2
    quest = "\fontsize{15} What stress to plot?";
    opts. Interpreter = "tex";
```

```
    opts. Default ='Differential stress';
    answer = questdlg(quest,'Stress curve','Shear stress','Differential
stress',opts);

    switch answer
```

```
        case "Shear stress"
            Shear = 1;
        case "Differential stress"
            Shear = 2;
    end
end

% Pressure correction
%-----------------------------
if Griggs == 1
quest = "\fontsize{15} Apply pressure correction?";
opts. Interpreter = "tex";
opts. Default ='No';
answer = questdlg(quest,'Pressure correction','Yes','No',opts);

switch answer
    case "Yes"
        Pressure_correction = 1;
    case "No"
        Pressure_correction = 2;
end
end

%-------------------------------------------------
% starting and quenching points
%-------------------------------------------------

figure(1)
plot(Time,Force,'r')
hold on
xlabel("Time (s)")
ylabel("Force (kN)")
txt3 = ({"Start of experiment:" "Select the point" "where the deformation"
"started"});
hText = text(max(Time)/2,max(Force)/2,txt3,'FontSize',16);

% Start of deformation point
[x3,y3]=ginput(1);
for i=1:data
    if x3>= Time(i)
        start = i;
    end
end
delete(hText)
txt4 = ({"End of experiment:" "Select the point" "where the quenching" "started"});
hText = text(max(Time)/2,max(Force)/2,txt4,'FontSize',16);
% End of deformation point
[x4,y4]=ginput(1);
```

```
for i=1:data
    if x4>= Time(i)
        quench = i;
    end
end
delete(hText)
```

```
C4_new = linspace(0.,0.,quench-start+1)';
C7_new = linspace(0.,0.,quench-start+1)';
C1_new = linspace(0.,0.,quench-start+1)';
j = 1;
for i=start:quench
    C4_new(j) = Displacement_S1(i);
    C7_new(j) = Force(i);
    C1_new(j) = Time(i);
    j = j+1;
end

%-----------------------------------------
% To define the hit-point
%-----------------------------------------

figure(3)
plot(C1_new/3600,C7_new,'r')
hold on
xlabel("Time (h)")
ylabel("Force (kN)")
ylim([0 max(C7_new)+10])
txt5 = ({"Hit point (phase 1):" "Select 2 points" "on the "run-in"" "through lead
curve"});
hText = text(max(C1_new/3600)/2,max(C7_new)/3,txt5,'FontSize',16);

% regression "lead" curve
[x5,y5]=ginput(2);
for i = 1:j-1
    if C1_new(i)/3600 <= x5(1)
        lead_1 = i;
    end
    if C1_new(i)/3600 <= x5(2)
        lead_2 = i;
    end
end

Lead = [lead_1 lead_2];

X_tangent_lead = linspace(C1_new(min(Lead)),C1_new(max(Lead)),max(Lead)-
min(Lead)+1)';
Y_tangent_lead = linspace(C7_new(min(Lead)),C7_new(max(Lead)),max(Lead)-
min(Lead)+1)';

P1=polyfit(X_tangent_lead/3600,Y_tangent_lead,1);
Ys1 = P1(1)*(C1_new/3600)+P1(2);
plot(C1_new/3600,Ys1,'k-')
```

```
delete(hText)
```

```
txt6 = ({'Hit point (phase 2):' 'Select 2 points' 'on the elactic' 'curve'});
hText = text(max(C1_new/3600)/2,max(C7_new)/3,txt6,'FontSize',16);

% regression "elastic" curve
[x6,y6]=ginput(2);
for i = 1:j-1
```

```
    if C1_new(i)/3600 <= x6(1)
        elas_1 = i;
    end
    if C1_new(i)/3600 <= x6(2)
        elas_2 = i;
    end
end

Elas = [elas_1 elas_2];

X_tangent_elas = linspace(C1_new(min(Elas)),C1_new(max(Elas)),max(Elas)-
min(Elas)+1)';
Y_tangent_elas = linspace(C7_new(min(Elas)),C7_new(max(Elas)),max(Elas)-
min(Elas)+1)';

P2=polyfit(X_tangent_elas/3600,Y_tangent_elas,1);
Ys2 = P2(1)*(C1_new/3600)+P2(2);
plot(C1_new/3600,Ys2,'k-')
for i=1:quench-start
    if Ys2(i) < Ys1(i)
        Hit_point = C4_new(i);
        iter_HP = i;
    end
end
delete(hText)

txt1 = ["Hit point = ",num2str(Hit_point),' mm'];
text(max(C1_new/3600)/2,max(C7_new)/3,txt1,'FontSize',18)


%--------------------------------------------------
% Correction of rig extension/stiffness
%--------------------------------------------------

nsigma=quench-start-iter_HP+1;
Differential_force = linspace(0.,0.,nsigma)';
Displacement_total = C4_new(quench-start)-C4_new(iter_HP);
Displacement_from_HP_source = linspace(0.,0.,nsigma)';
Displacement_from_HP_temp = linspace(0.,0.,nsigma)';
Displacement_from_HP = linspace(0.,0.,nsigma)';
Time_from_HP = linspace(0.,0.,nsigma)';
Force_ini = linspace(0.,0.,nsigma)';
delta_sigma_HP = C7_new(iter_HP)-Ys2(iter_HP);
Pressure_from_HP = linspace(0.,0.,nsigma)';


h = 1;
for i = iter_HP:quench-start
    if Ys2(i) <C7_new(i)
        Differential_force(h) = Ys2(i)-Ys2(iter_HP);
    else
        Differential_force(h) = C7_new(i)-Ys2(iter_HP);
    end
    Time_from_HP(h) = C1_new(i)-C1_new(iter_HP);
```

```
    Pressure_from_HP(h) = Stress_S3(i)-Stress_S3(iter_HP);
    Displacement_from_HP_source(h) = C4_new(i)-C4_new(iter_HP);
    h=h+1;
end

for i = 1:nsigma
    if Differential_force(i) <0;
        Differential_force(i) = 0;
    end
end

for i=1:nsigma
    Displacement_from_HP_temp(i) = Displacement_from_HP_source(i)—
(Differential_force(i)*rig_stiffness);
end

figure
plot(Time_from_HP/3600,Displacement_from_HP_source,'k')
hold on
plot(Time_from_HP/3600,Displacement_from_HP_temp,'r')
legend('as-is','Stiffness corrected','Location','northwest')
hold off
xlabel('Time (h)')
ylabel('Displacement (mm)')

%--------------------------------------------------
% Correction of friction
%--------------------------------------------------

Differential_force_corr = linspace(0.,0.,nsigma);

for i=1:nsigma
    Differential_force_corr(i) = Differential_force(i)-
Displacement_from_HP_temp(i)*Friction;
end

% Filtering Differential_force curve

b=linspace(1/no,1/no,no)';

Differential_force = filtfilt(b,1,Differential_force);
Differential_force_corr = filtfilt(b,1,Differential_force_corr);

j = 1;
for i = iter_HP:quench-start
    Time_from_HP(j) = C1_new(i)-C1_new(iter_HP);
    j=j+1;
end
```

```
%--------------------------------------------------
% Correction of sample compaction
%--------------------------------------------------

if Deformation_regime == 2
```

```
Sample_thickness = linspace(0.,0.,nsigma)';


for i = 1:nsigma
        Sample_thickness(i) = Sample_thickness_before-(i-
1)*(Sample_thickness_before-Sample_thickness_after)/nsigma;
        Displacement_from_HP(i) = Displacement_from_HP_temp(i)-(i-
1)*((Sample_thickness_before-
Sample_thickness_after)/nsigma)/sind(Shear_zone_angle);
end
else
    Displacement_from_HP = Displacement_from_HP_temp;
end

if Deformation_regime == 2
    figure
    plot(Time_from_HP/3600,Displacement_from_HP_temp,'k')
    hold on
    plot(Time_from_HP/3600,Displacement_from_HP,'r')
    legend('as is','Compaction corrected','Location','northwest')
    xlabel('Time (h)')
    ylabel('Displacement (mm)')
    hold off
end

%-----------------------------------------
% Stress-strain curve as a fonction of changing sample surface
%-----------------------------------------

Poisson_coefficient = 0.5;
Chamber_diameter = 27;
Strain = linspace(0.,0.,nsigma)';
diff_stress_ante = linspace(0.,0.,nsigma)';
diff_stress_area = linspace(0.,0.,nsigma)';
diff_stress = linspace(0.,0.,nsigma)';
diff_stress_corr = linspace(0.,0.,nsigma)';
%Surface = pi*(Piston_diameter/2)*((Piston_diameter/2)/cosd(Shear_zone_angle));
Surface = pi*(Piston_diameter/2)^(2);
Shear_displacement = linspace(0.,0.,nsigma)';
Shear_surface = linspace(0.,0.,nsigma)';
surface_with_time = linspace(0.,0.,nsigma)';


if Deformation_regime == 2
    for i = 1:nsigma
        %Shear_displacement(i) = (Displacement_from_HP(i)-Displacement_from_HP(i-
1))/cosd(Shear_zone_angle);
        Shear_displacement(i) = Displacement_from_HP(i)/cosd(Shear_zone_angle);
        %Strain(i) = Strain(i-1)+Shear_displacement(i)/Sample_thickness(i);
        Strain(i) = Shear_displacement(i)/Sample_thickness(i);
        Shear_surface(i) =
2*(Piston_diameter/2)^2*acos((Displacement_from_HP(i)/Piston_diameter))-
Displacement_from_HP(i)*sqrt((Piston_diameter/2)^2-(Displacement_from_HP(i)/2)^2);
%Shear_surface(i) =
```

```
2*(Piston_diameter/2)*((Piston_diameter/2)/cosd(Shear_zone_angle))*(pi/2-
atan((Displacement_from_HP(i)/Piston_diameter)))-
Displacement_from_HP(i)*sqrt((Piston_diameter/2)*((Piston_diameter/2)/cosd(Shear_zo
ne_angle))-(Displacement_from_HP(i)/2)^2);
        diff_stress_ante(i) = (Differential_force(i)*1e3)/Surface;
        diff_stress_area(i) = (Differential_force(i)*1e3)/Shear_surface(i);
        diff_stress(i) = (Differential_force_corr(i)*1e3)/Surface;
        diff_stress_corr(i) = (Differential_force_corr(i)*1e3)/Shear_surface(i);
    end

%--------------------
% Filtering Diff stress curve
%--------------------

b=linspace(1/no,1/no,no)';

diff_stress_ante = filtfilt(b,1,diff_stress_ante);
diff_stress_area = filtfilt(b,1,diff_stress_area);
diff_stress = filtfilt(b,1,diff_stress);
diff_stress_corr = filtfilt(b,1,diff_stress_corr);

    figure
    if Shear == 2
        plot(Strain,diff_stress_ante,'b')
        hold on
        plot(Strain,diff_stress,'k')
        hold on
        plot(Strain,diff_stress_corr,'r')
        hold on
        plot(Strain,diff_stress_area,'-r')
        hold on
        if Griggs == 2
            legend('as-is','Friction corrected','Area corrected','no
friction','Location','southeast')
        else
        if Pressure_correction == 2
            legend('as-is','Friction corrected','Area corrected','no
friction','Location','southeast')
        end
        end
        xlabel('Strain (gamma)')
        ylabel('Differential stress (MPa)')
    else
        plot(Strain,diff_stress_ante/2,'b')
        hold on
        plot(Strain,diff_stress/2,'k')
        hold on
        plot(Strain,diff_stress_corr/2,'r')
        hold on
        plot(Strain,diff_stress_area/2,'-r')
        hold on
        if Griggs == 2
            legend('as-is','Friction corrected','Area corrected','no
friction','Location','southeast')
```

```
        else
        if Pressure_correction == 2
            legend('as-is','Friction corrected','Area corrected','no
friction','Location','southeast')
        end
        end
        xlabel('Strain (gamma)')
        ylabel('Shear stress (MPa)')
    end
else
    for i = 1:nsigma
        surface_with_time(i) = pi*(Piston_diameter/2*(1-
Poisson_coefficient*((Sample_thickness_coaxial-
Displacement_from_HP(i))/Sample_thickness_coaxial-1)))^(2);
        diff_stress_ante(i) =
(Differential_force(i)*1e3)/(pi*(Piston_diameter/2)^(2));
        diff_stress_area(i) = (Differential_force(i)*1e3)/surface_with_time(i);
        diff_stress(i) =
(Differential_force_corr(i)*1e3)/(pi*(Piston_diameter/2)^(2));
        diff_stress_corr(i) =
(Differential_force_corr(i)*1e3)/surface_with_time(i);
        Strain(i) = abs(((Sample_thickness_coaxial-Displacement_from_HP(i))-
Sample_thickness_coaxial)/Sample_thickness_coaxial*100);
    end

%--------------------
% Filtering Diff stress curve
%--------------------

b=linspace(1/no,1/no,no)';

diff_stress_ante = filtfilt(b,1,diff_stress_ante);
diff_stress_area = filtfilt(b,1,diff_stress_area);
diff_stress = filtfilt(b,1,diff_stress);
diff_stress_corr = filtfilt(b,1,diff_stress_corr);

    figure
    plot(Strain,diff_stress_ante,'b')
    hold on
    plot(Strain,diff_stress,'k')
    hold on
    plot(Strain,diff_stress_corr,'r')
    hold on
    plot(Strain,diff_stress_area,'—r')
    hold on
    if Griggs == 2
        legend('as-is','Friction corrected','Area corrected','Area corrected (no
friction)','Location','southeast')
```

```
    else
    if Pressure_correction == 2
        legend('as-is','Friction corrected','Area corrected','Area corrected (no
friction)','Location','southeast')
    end
    end
```

```
    xlabel('Strain (%)')
    ylabel('Differential stress (MPa)')
end

%-----------------------------------------
% Confining pressure correction
%-----------------------------------------

if Griggs == 1
if Pressure_correction == 1

diff_stress_corr_p = linspace(0.,0.,nsigma)';
diff_stress_area_p = linspace(0.,0.,nsigma)';

for i = 1:nsigma
    diff_stress_corr_p(i) = diff_stress_corr(i)-Pressure_from_HP(i);
    diff_stress_area_p(i) = diff_stress_area(i)-Pressure_from_HP(i);
end

b=linspace(1/no,1/no,no)';
diff_stress_corr_p = filtfilt(b,1,diff_stress_corr_p);
    if Deformation_regime == 2
        if Shear == 2
            plot(Strain,diff_stress_corr_p,'g')
            hold on
            plot(Strain,diff_stress_area_p,'-g')
        else
            plot(Strain,diff_stress_corr_p/2,'g')
            hold on
            plot(Strain,diff_stress_area_p/2,'-g')
        end
    else
            plot(Strain,diff_stress_corr_p,'g')
            hold on
            plot(Strain,diff_stress_area_p,'-g')
    end
            legend('as-is','Friction corrected','Area corrected','Area corrected
(no friction)','Pressure corrected','Pressure corrected (no
friction)','Location','southeast')
            hold off

end
end
```

Published with MATLAB® R2016b

Nicolas MANSARD

Le rôle des réactions métamorphiques pour la localisation de la déformation dans la croûte moyenne et inférieure : observations de terrain et expériences de déformation

Résumé :

Les zones de cisaillement résultent de la localisation de la déformation dans les roches de la croûte et du manteau supérieur au cours de la déformation de la lithosphère. En accommodant une importante quantité de déformation, ces zones de cisaillement exercent un contrôle direct sur la rhéologie et la dynamique de la lithosphère. En s'appuyant sur des observations de terrain et des expériences de déformation, cette étude aspire à élargir les connaissances actuelles sur la rhéologie et le développement des zones de cisaillement. Dans cette étude, nous mettons en évidence que le comportement rhéologique des matériaux polyphasés est extrêmement sensible à la composition minéralogique, dans la mesure où de faibles variations chimiques peuvent initier la localisation de la déformation – même à faible contrainte de cisaillement – et induire de larges différences de résistance. Nos résultats exposent également la capacité dont fait preuve la déformation pour faciliter les réactions minérales, la nucléation, la formation de mélange de phases à grains fins et, inversement, comment une telle évolution des microstructures aboutit à la localisation de la déformation et à l'affaiblissement des matériaux. La composition des phases minérales, dans la mesure où elles régissent la réactivité, participe grandement à l'initiation de l'affaiblissement et à l'évolution à long terme de la résistance des zones de cisaillement. Globalement, notre étude atteste que la rhéologie des roches ne peut se résumer au comportement rhéologique des matériaux monophasés. Afin de recourir à l'utilisation de modèles rhéologiques pour prédire la résistance de la lithosphère, il semble nécessaire de prendre en compte à la fois la complexité des structures régionales (comme les zones de cisaillement) et la nature complète des roches qui les composent, notamment la rhéologie des matériaux polyphasés en présence — ou non — de la rétroaction entre la déformation et les réactions.

Mots clés : Rétroaction entre déformation et réaction, localisation de la déformation, affaiblissement rhéologique.

The role of metamorphic reactions for strain localization in the middle and lower crust: Insights from field observations and deformation experiments

Abstract :

Shear zones arise from strain localization into rocks of the crust and uppermost mantle during deformation of the lithosphere. By accommodating a large amount of strain, these shear zones have a direct control on rheology and dynamics of the lithosphere. Based on field observations and deformation experiments, this study aims at extending the current knowledge about the rheological behavior and the development of shear zones. In this study, we highlight that the rheological behavior of polyphase materials is extremely sensitive to their mineralogical composition and that small chemical variations can initiate strain localization – even at small shear strain - and induce large differences in resistance. Our results also show the ability of deformation to enhance mineral reactions, nucleation, the development of fine-grained mixed zones and, conversely, how such an evolution in microstructures eventually results in strain localization and weakening of polyphase aggregates. Phase compositions, in as much they control the reactivity, play a first-order role on both the initiation of weakening but also on the long-term evolution and strength of shear zones. Overall, our study illustrates that the rheology of rocks cannot be summarized as being controlled by monophase materials. In order to further use the rheological models as a predictive tool for lithospheric rheology, it seems essential to take into account both the complexity of regional structures (such as shear zone areas) and the complete nature of rocks that compose them, including the rheology of polyphase material in presence—or in absence—of feedback between deformation and reactions.

Keywords : Feedback between deformation and reaction, strain localization, rheological weakening.

Earth Sciences Institute of Orléans
ISTO
Institut des Sciences de la Terre d'Orléans
cnrs

1A, rue de la Férollerie - 45071 Orléans Cedex 2